Kerr-enhanced optomechanics

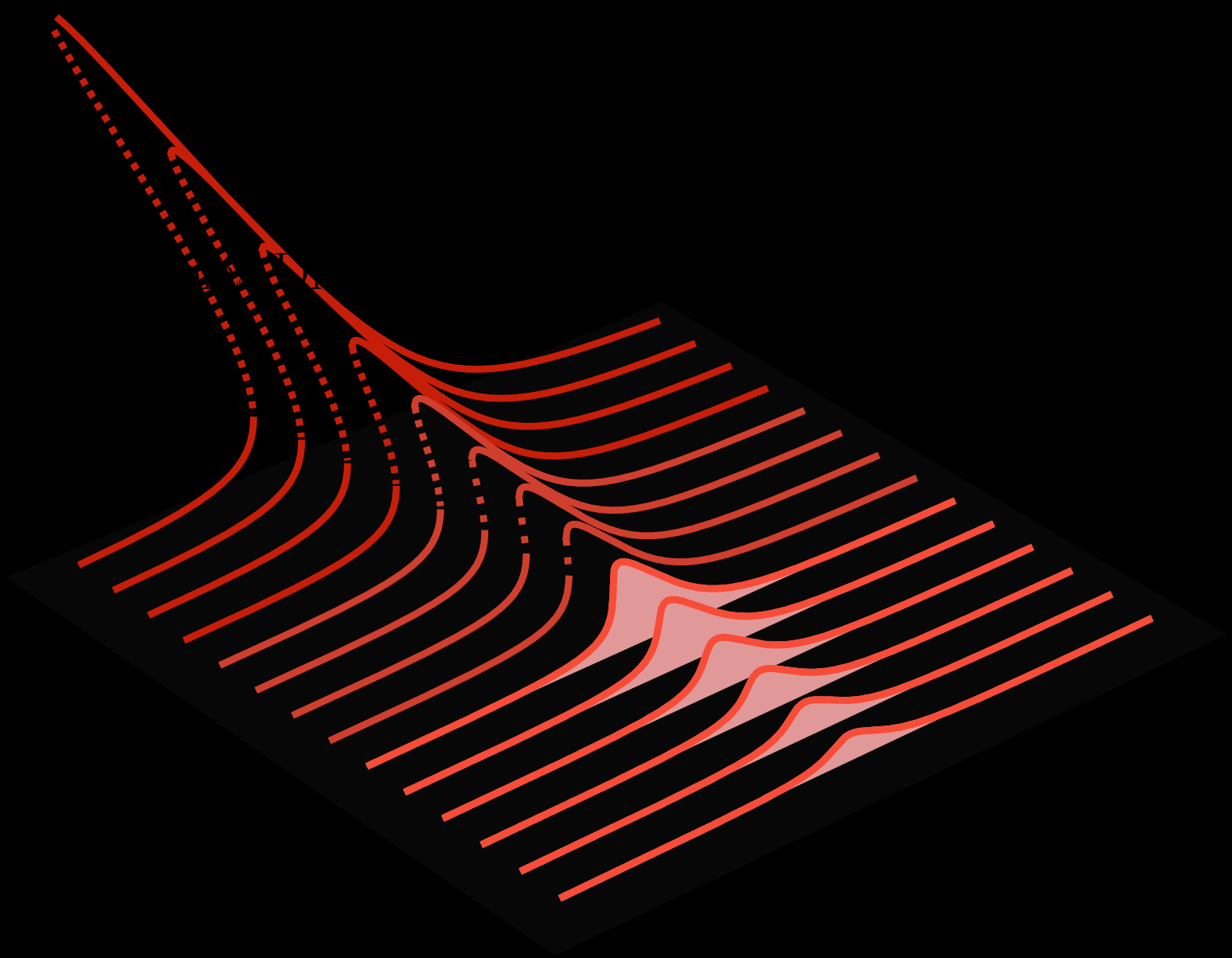

Nicolás Díaz Naufal

Karlsruher Institut für Technologie

Fakultät für Physik
Institut für Theorie der Kondensierten Materie

Kerr-enhanced optomechanics

Zur Erlangung des akademischen Grades eines

DOKTORS DER NATURWISSENSCHAFTEN (Dr. rer. nat.)

von der KIT-Fakultät für Physik
des Karlsruher Instituts für Technologie (KIT)

angenommene

DISSERTATION

von

M.Sc. Nicolás Díaz Naufal

Tag der mündlichen Prüfung: 06.12.2024

Referentin:
Prof. Dr. Anja Metelmann

Korreferent:
Prof. Dr. Gerhard Kirchmair

Erklärung:

Ich versichere wahrheitsgemäß, die Arbeit selbstständig verfasst, alle benutzten Hilfsmittel vollständig und genau angegeben und alles kenntlich gemacht zu haben, was aus Arbeiten anderer unverändert oder mit Abänderungen entnommen wurde sowie die Satzung des KIT zur Sicherung guter wissenschaftlicher Praxis in der Fassung vom 27 März 2017 beachtet zu haben.

Berlin, den 21. Oktober 2024

Nicolás Díaz Naufal

Abstract

The pursuit of ground state cooling a mechanical mode has been of significant interest for its fundamental relevance to numerous quantum science and technology applications. In recent years, optomechanical backaction cooling protocols have successfully achieved the motional quantum ground state of a mechanical oscillator in the *resolved sideband* regime, i.e. when the mechanical resonance frequency is significantly larger than the cavity decay rate [1]. However, as the size of these mechanical systems increases, their natural frequency generally decreases, pushing them into the *unresolved sideband* regime. Backaction cooling becomes less effective in this regime, limiting the ability to cool the mechanical mode to its ground state.

In this thesis, we theoretically study a novel optomechanical setup, where a nonlinear cavity and a mechanical cantilever are inductively coupled. Despite being initially proposed to achieve single-photon coupling strengths [2], this system has the particularity of being able to more efficiently backaction cool a mechanical mode in the unresolved sideband regime. We will demonstrate that the intrinsic nonlinearity of the cavity results in an enhancement of the cooling capabilities in the sideband unresolved regime as experimentally shown in [3]. The above arises due to the increased asymmetry between the cooling and heating processes, thereby improving the cooling efficiency.

Acknowledgements

Writing these lines has made me realise that I am coming to the end of a long period of my life. And like every ending, it deserves a farewell.

This thesis is nothing more than the sum of many collective efforts. Like everything in life, science is a team effort and this thesis is only the result of all the support I have received over the past years. For this reason, I would like to dedicate the following lines to those who have contributed most, both directly and indirectly, to completing this thesis.

Esta es mi tercer tesis, y la segunda que escribo fuera de México. Por fortuna, eso no ha significado sentirme lejos de casa, ya que mi familia siempre me ha apoyado incondicionalmente. Porque escribir una tesis de doctorado en mis condiciones es un privilegio, quisiera empezar agradeciéndole a mi familia, porque sin ella nada de esto sería posible. A ti mamá, gracias, por tu apoyo en todo momento. Por tus palabras de ánimo y cariño cuando más lo necesitaba. A mi papá, por haberme enseñado el camino del esfuerzo y la dedicación. A ti Inés, por escucharme siempre y darme la calma y el cariño necesario para seguir adelante.

Cause this work would otherwise not exist, I want to thank Prof. Anja Metelemann for her trust and support over the last five years. Thank you for allowing me to join your group and for always motivating me in my research process. Thank you for all the discussions, suggestions and insights you shared with me. For supporting me even when I was doubting myself, and pushing me to improve.

As this thesis is the result of an amazing collaboration, I would like to thank Prof. Gerhard Kirchmair for his great support throughout the project. For the many discussions and insights, and for making this collaboration so enjoyable. Special thanks go to Lukas Deeg and David Zoepfl because I could not imagine having better colleagues. Thank you both for your unlimited and unconditional support over the past years. Thank you for the many conversations about science, for the many nights out and for all the help you have given me. Thank you, David, for driving me around LA in your Mustang, for visiting me in Berlin, and for all the conversations and support. Thank you, Lukas, for your patience in explaining the experiment to me, for all the corrections you gave me, for your always great advice, for the dinner in Munich and for making these last years so fulfilling. But most of all, thank you both for your friendship.

I would like to thank Daniel Bothner, Inês Rodrigues, and Jakob Koenig for the valuable collaboration that led to the final chapter of this thesis. In particular, I am especially grateful to Jakob for his assistance in writing the simulations and for his patience in explaining the devices to me.

I would also like to thank AG Metelmann for the great time I have had over the past few years. Thank you for the great conversations, for supporting me with endless zoom meetings, but most of all for making my home office more bearable. Special thanks to Victor Bittencourt, for the great support over the past years and for the impressively detailed corrections of this work. Thank you for sharing your knowledge, mentoring me and keeping me motivated.

I would also like to thank Carlos González Ballestero for the final revision of this thesis and his great support over the last three years.

I would also like to thank the Instituto de Ciencias Nucleares at the UNAM in Mexico for inviting me to present my work. I would especially like to thank Prof. Eduardo Nahmad for his support and friendship for more than seven years now. For his trust, teaching and motivation over the years.

Diese Arbeit wäre ohne die Hilfe von Jörg und der gesamten Hackbarth's Gruppe überhaupt nicht möglich gewesen. Vielen Dank für eure liebevolle Unterstützung, die schönen Momente und vor allem dafür, dass ich in euch eine Familie gefunden habe. Ein besonderer Dank geht an dich, Frank, denn niemand hat mir in den letzten Jahren so viel beigebracht wie du. Vielen Dank für deine Lebensfreude, deine Solidarität und deine Freundschaft. Ich küsse deine Augen, Frank.

Because these years would not have been so enjoyable, I am deeply indebted to all my friends who have supported me over the years. Thanks to Manu, Theo, Fernanda, Juli, Huguette, Fernando, Rinat, Julia, Kevin, Emilia, Guadi, Andrés and the many people who made Berlin my home.

Last but not least, I want to thank the most important person in my life: my wife, Romi. No existen palabras para agradecerte lo suficiente, porque sin tu apoyo nada de esto sería

posible. Gracias por tu incondicional amor, por tu alegría, paciencia y confianza. Gracias por creer en mí y motivarme en todo momento. Porque todo esto y más te lo debo a ti. Te amo con todo mi corazón.

Contents

Acronyms

OQS	Open Quantum System
DBAE	Dynamical Backaction Evasion
QSDE	Quantum Stochastic Differential Equations
RWA	Rotating Wave Approximation
SQUID	Superconducting Quantum Interference Device
EoM	Equation of Motion
FDT	Fluctuation Dissipation Theorem
QND	Quantum Non Demolition
SQL	Standard Quantum Limit
OMIT	Optomechanically Induced Transparency
EIT	Electromechanically Induced Transparency
ZPF	Zero Point Fluctuation
VNA	Vector Network Analyzer
GSA	Gaussian-state Approximation
DPA	Degenerate Parametric Amplifier

List of Symbols

Symbol	**Meaning**
ω_m	Mechanical frequency
γ_m	Total mechanical damping rate
ω_c	Cavity frequency
Δ	Cavity detuning
$\mathcal{F}$	Optical finesse $\mathcal{F} = \omega_c/\kappa$
κ	Total cavity decay rate composed by external and internal losses $\kappa = \kappa_{\text{ext}} + \kappa_{\text{int}}$
$\bar{n}_c$	Intracavity photon number
ϕ_{c}	Driving phase
G_0	Optical frequency shift per displacement $G_0 = \partial\omega_c/\partial q$.
g_0	Optomechanical single-photon coupling strength $g_0 = G_0 x_{\text{zpf}}$
G	Light-enhanced optomechanical coupling for the linearized regime, $G = g_0\sqrt{\bar{n}_c}$
$\hat{F}$	Linearized radiation pressure force operator $\hat{F} = G\left(\hat{d} + \hat{d}^\dagger\right)$.
$\bar{n}_m^T$	Average phonon number in thermal equilibrium
$\hat{x}_m$	Position operator $\hat{x}_m \equiv \hat{b} + \hat{b}^\dagger$
$\hat{X}_m$	Position quadrature $\hat{X}_m = \hat{x}_m/\sqrt{2}$
$\mathcal{K}$	Kerr nonlinearity
$\mathcal{K}_m$	Optomechanically induced Kerr nonlinearity, here denoted *mechanical Kerr*: $\mathcal{K}_m = 2g_0^2\omega_m/(\omega_m^2 + \gamma^2/4)$
$\mathcal{K}_{\text{eff}}$	Effective Kerr nonlinearity: $\mathcal{K}_{\text{eff}} = \mathcal{K} + \mathcal{K}_m$
Λ	Photon enhanced Kerr nonlinearity: $\Lambda = \mathcal{K}\bar{n}_c e^{-2i\phi}$
$\tilde{\Delta}$	Modified cavity detuning: $\tilde{\Delta} = \Delta + 2\lvert\Lambda\rvert$
Δ_{bi}	Critical detuning: $\Delta_{\text{bi}} = -\sqrt{3}\kappa/2$
Δ_{eff}	Effective detuning: $\Delta_{\text{eff}} = \lvert\Lambda\rvert - \tilde{\Delta}$
$\bar{n}_{\text{in}}$	Cavity input power
$\bar{n}_{\text{bi}}$	Critical photon number: $\bar{n}_{\text{bi}} = \kappa/\sqrt{3}\mathcal{K}_{\text{eff}}$
$\bar{n}_{\text{in,bi}}$	Critical input power: $\bar{n}_{\text{in,bi}} = \kappa^2/3\sqrt{3}\mathcal{K}_{\text{eff}}$
$\Sigma_c[\omega]$	Linear cavity self-energy
$\Sigma_c^{\mathcal{K}}[\omega]$	Nonlinear cavity self-energy
$\mathcal{C}_{\text{eff}}$	Effective cooperativity $\mathcal{C}_{\text{eff}} = \Gamma_{\text{opt}}/\gamma_m = 2\Im\left\{\Sigma_c[\omega_m]\right\}/\gamma_m$.

$\Sigma_m[\omega]$	Mechanical self-energy
$\Gamma_{\mathrm{S/AS}}$	Stokes and anti-Stokes rates $\Gamma_{\mathrm{S/AS}} = \mathcal{S}_{FF}[\mp\omega_m] = g_0^2\mathcal{S}_{nn}[\mp\omega_m]$
$\mathcal{X}_{\mathcal{K}}[\omega]$	Driven Kerr cavity susceptibility

Chapter 1

Introduction

In my early years as a physics student, the idea of studying *quantum mechanics* seemed slightly absurd. At the time several quotes from renowned physicists came to my mind: *If you are not confused by quantum physics then you haven't really understood it* as Niels Bohr said. Even Richard Feynmann remarked: *I think I can safely say nobody understands quantum mechanics.* It appeared natural to fear a field that appeared both inaccessible and yet somehow provided the most accurate description of our universe.

The *fear* of quantum mechanics often arises not only from its complex mathematical description but also from a more fundamental aspect: its counter-intuitiveness, as applying classical concepts to quantum theory typically leads to paradoxes [4]. For instance, the *state* of a particle at a given time is entirely characterized by its position and its momentum, which both define a point in a six-dimensional *phase-space*. In quantum mechanics, however, the *state* of such a system is completely described by the *wave function*, $\psi(\boldsymbol{r})$, which is a complex function that lives in a *Hilbert space*[1]. In addition, the quantum state's momentum and position cannot be simultaneously measured with arbitrary precision due to the *Heisenberg's uncertainty principle* [5].

As in classical physics, the evolution of a quantum system can be studied within a deterministic framework, in this case using the time-dependent Schrödinger equation. Contrary to classical physics, the linearity of this equation allows a physical system to exist in a *superposition* state[2] [5]. It is then upon *measurement*[3] that the wave function undergoes a *collapse* into one of its possible states. In addition, one of the most striking manifestations of quantum mechanics is *entanglement*[4]. In particular, entangled states exhibit correlations that persist over large distances, leading to the appearance of instantaneous influence when one part of the system is measured. This *spooky action at a distance* [7], does not transmit information faster than light, but instead reveals pre-existing correlations established when the entangled state was created. With no classical equivalent, entanglement represents the embodiment of quantum mechanics.

With Planck's seminal work [8], the pursuit to describe the behaviour of physical systems at the microscopic level led to the rise of quantum mechanics. In recent years and alongside the development in experimental physics, the quantum theory has been pushed to larger scales, aiming to demonstrate quantum effects in the macroscopic world [9]. However, preparing and controlling quantum features, such as superposition or entangled states, in large-scale systems is particularly difficult, since such systems are more vulnerable to *decoherence*[5]. Beyond enabling us to explore fundamental aspects of quantum mechanics [10, 11], extending these boundaries has important technological applications in, for example, quantum information theory and quantum metrology.

[1] In fact, to represent a physical state the wave function has to be *normalized*, such that their collection constitutes the Hilbert space of square-integrable functions, which is equipped with an inner product and usually known as L_2. Nevertheless, for simplicity, it is often referred to only as *Hilbert space*.

[2] If ψ_1 and ψ_2 are solutions of the Schrödinger equation, then the superposition $\tilde{\psi} = \alpha\psi_1 + \beta\psi_2$, where $\alpha, \beta \in \mathbb{C}$ is also a solution.

[3] The theory of quantum measurement is a field of research on its own [6] and a consistent measurement-based interpretation of quantum mechanics led to the *measurement problem* [4].

[4] For instance, bi-partite pure entanglement can be defined by exclusion: all pure quantum states on a Hilbert space $\mathcal{H} = \mathcal{H}_1 \otimes \mathcal{H}_2$ that are not product states of the form $\psi = \psi_1 \otimes \psi_2$ are called *entangled states.*

[5] Since in reality such perfectly isolated systems do not exist, all systems have to be considered as *open*, and the larger the system, the more important is the interaction with its environment, leading to a faster *decoherence.* Such an interaction therefore converts a quantum superposition into a classical mixture.

Overcoming these difficulties has led to new fabrication techniques to create macroscopic systems that exhibit quantum behaviour, often referred to as *engineered quantum systems*. Among the most relevant examples are *optomechanical systems*, in which light interacts with a mechanical system through *radiation pressure* [1]. One of the main abilities of quantum optomechanics is to coherently control mechanical objects in a wide range of scales, which combined with its extremely high sensitivity to external forces and fields made them ideal for sensing applications [12]. Beyond this, optomechanical systems have shown great promise in preparing nonclassical quantum states [13–16], which further enhances their sensing capabilities [17]. This suggests that optomechanics could help explore fundamental questions in quantum mechanics at a macroscopic mass scale, where gravity may influence quantum behaviour [18].

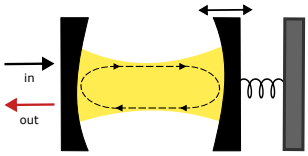

FIGURE 1.1: Sketch of an optomechanical system

Nevertheless, such promising features of optomechanics come at the expense of very challenging experimental requirements, which include, for instance, strong optomechanical coupling to observe quantum effects [19]. As a result, new ways of coupling and controlling mechanical systems have been examined in recent decades, such as superconducting circuits [20]. These platforms offer extremely high tunability and large coupling strengths, enabling the exploration of otherwise inaccessible parameter regimes.

Despite its name, the field of optomechanics is not limited to the optical domain but can be realized also in the microwave regime by capacitive [21] or inductive [22] coupling of a mechanical system to a superconducting microwave circuit. The prominent progress in such *electromechanical* platforms has succeeded in achieving *strong-single-photon* coupling strengths [23], a regime where the intrinsic nonlinear nature of the optomechanical interaction leads to the creation of mechanical non-Gaussian states [24].

Due to the difficulties of reaching the strong coupling regime, the majority of the optomechanical experiments to date operate in a regime where the optomechanical interaction is small compared to both the mechanical frequency and the cavity loss rate. To compensate for this drawback, the cavity is externally driven to enhance the interaction. This is the so-called *weak-coupling* regime, where many of the radiation-pressure effects have been observed, such as *optomechanical amplification* [1], *optomechanically induced transparency* [25] and *red-sideband cooling* [26].

In the classical limit, systems operate in a regime where thermal *fluctuations*[6] overcome quantum effects. In an optomechanical system, this implies that *Brownian motion* defines the position of the mechanical resonator. As the resonator's displacement decreases with temperature, approaching the quantum limit means nearing its lowest energy state, or its ground state. However, even at this state, quantum fluctuations cause the oscillator to retain some residual motion, referred to as *zero-point motion*, consistent with the Heisenberg uncertainty principle [27]. Achieving precise quantum control of the mechanical oscillator therefore requires cooling it to its ground state.

Even at cryogenic temperatures, low-frequency mechanical systems require additional cooling due to their high thermal occupation. Over the past decades, feedback cooling [28] and dynamical backaction cooling [21, 29] have successfully achieved ground state cooling. However, as the size of these mechanical systems increases, their natural frequency generally decreases, pushing them into the *unresolved sideband regime*. In this regime, sideband cooling becomes less effective, limiting the ability to cool the mechanical mode to its ground state.

FIGURE 1.2: Magnetomechanical platform used in [3].

To address the limitations of sideband cooling in the unresolved sideband regime, various approaches have been proposed, including the use of squeezed light [30–32] and dual-cavity modes [33, 34]. This work focuses on analyzing an alternative proposal that leverages intrinsic cavity nonlinearities to enhance the cooling performance of optomechanical systems

[6] This term indicates a stochastic process, normally related to the interaction between a system and its environment.

in the unresolved sideband regime. Despite being experimentally realized using a SQUID cavity inductively coupled to a cantilever with a magnetic tip, this analysis can be applied to nonlinear optomechanical systems in general. This work was carried out under the supervision of Anja Metelmann (KIT) and in collaboration with the experimental group of Gerhard Kirchmair (Universität Innsbruck, IQOQI), particularly with David Zoepfl and Lukas Deeg. This work resulted in the development of three articles [3, 35, 36].

> D. Zoepfl, M. L. Juan, N. Diaz-Naufal, C. M. F. Schneider, L. F. Deeg, A. Sharafiev, A. Metelmann, and G. Kirchmair, "Kerr enhanced backaction cooling in magnetomechanics," Phys. Rev. Lett., Jan 2023
>
> N. Diaz-Naufal, L. Deeg, D. Zoepfl, C. M. F. Schneider, M. L. Juan, G. Kirchmair and A. Metelmann, "Kerr enhanced optomechanical cooling in the unresolved sideband regime," 2024, arXiv:2410.15435
>
> L. F. Deeg, D. Zoepfl, N. Diaz-Naufal, M. L. Juan, A. Metelmann, and G. Kirchmair, "Optomechanical backaction in the bistable regime," 2024, Phys. Rev. Applied 23, 014082

1.1 Structure of the thesis

This thesis aims to highlight the advantages of two seemingly undesirable features: combining an optomechanical system in the unresolved sideband regime with an intrinsically nonlinear cavity. In the spirit of completeness, the thesis begins in Chapter 2 with a brief introduction to open quantum systems to provide the required machinery to address the fundamentals of optomechanical systems presented in Chapter 3.

In Chapter 3 we start with a brief introduction to the field of optomechanics and introduce *the quantum noise approach*, which will be essential throughout the whole thesis. In Chapter 3, we also present the Hamiltonian formulation of an optomechanical system and analyze the dynamical backaction effects of the radiation pressure interaction as well as its application in mechanical motion detection.

In Chapter 4, we show how the Hamiltonian description of an LC circuit with a Josephson junction is equivalent to that of a Duffing oscillator. Here, we analyze the dynamics of the nonlinear cavity and study its inherent properties, which exhibit promising features for optomechanical sideband cooling.

Chapter 5 consists of the theoretical description of the experimental work of D. Zoepfl *et al.* [3], in which we show the backaction cooling advantages arising from the interaction of a Kerr-cavity with a low-frequency mechanical mode. In Chapter 6 we loosen up the constraints imposed by the experimental setup and we follow M. Asjad *et al.* work [31], where squeezed vacuum is injected into the nonlinear cavity for improved optomechanical cooling in the unresolved sideband regime.

Finally, in Chapter 7 we study the quadratic *photon-pressure interaction* between two superconducting LC circuits of different frequencies that lead to both sideband cooling and OMIT via two-photon processes.

Chapter 2

Open Quantum Systems

In optomechanics, for instance, terms like *quantum fluctuations* and *quantum noise* commonly appear when we analyze the system's dynamics. Since the Schrödinger equation is purely deterministic, new methods emerged to address fluctuations and, more importantly, to handle *dissipation* in quantum mechanical systems. This led to the development of a theory that describes the evolution of an *open quantum system* (OQS) that is inevitably coupled to a much larger second system, normally referred to as a *bath, reservoir or environment*[1].

As with every other system, quantum mechanical systems can not be treated as completely isolated entities, since they are irremediably subjected to the non-negligible influence of the environment. Thus, the theory of OQS arises due to the need to describe these effects and obtain a more realistic understanding of the dynamics of quantum mechanical systems. Contrary to a closed system, OQS can no longer be described by a unitary time evolution. The formulation of a *quantum dissipative theory* will allow us to explain the effects that appear when the quantum system is in contact with its environment. Unfortunately, the coupling of the quantum system to its surroundings results in a loss of information causing an irreversible process, which is commonly known as *decoherence*.

In this Chapter, we examine the dynamics of an OQS following standard literature [37–39] as well as the introductory chapter of my master's thesis [40]. While this material may appear repetitive, its inclusion ensures completeness. The purpose of this Chapter is to equip the reader with the necessary theoretical tools for the subsequent analysis. Therefore, experienced readers may choose to skip this section. First, we will introduce the *density operator*, enabling us to perform an adequate statistical analysis of the open system. Next, we will analyze the dynamics of the OQS within *the master equation* framework. In addition to the master equation approach which treats the environment as a thermal bath, in the last section, we will introduce the *input-output* theory. The latter theory considers the environment as an external field to which the quantum system is coupled.

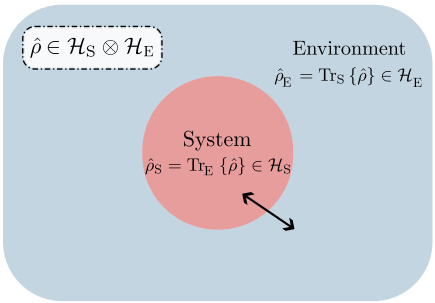

FIGURE 2.1: Diagram of an OQS, where $\mathcal{H}_S$ and $\hat{\rho}_\mathrm{S}$ are the Hilbert space and the density operator of the system, respectively; while the respective environment's counterparts are denoted by $\mathcal{H}_\mathrm{E}$ and $\hat{\rho}_\mathrm{E}$. The composite Hilbert space is given by $\mathcal{H} = \mathcal{H}_S \otimes \mathcal{H}_B$ with its density operator $\hat{\rho}$.

[1] These terms are often used interchangeably, but there can be subtle differences in their usage and implications. The term *environment* is the most general and encloses all other terms and refers to systems with a larger number of degrees of freedom compared to the OQS. Typically *bath* is used when the environment is in thermal equilibrium at a well-defined temperature. Conversely, *reservoir* not always imply thermal equilibrium

2.1 Density operator formalism

The formulation of quantum mechanics is typically expressed in the language of *state vectors*. However, a more general description that encodes all the statistical properties of quantum systems, whose state is not completely known, is given using the so-called *density operator* or *density matrix*. Introduced by John von Neumann in 1927 [41], the density operator formalism arises due to the need to describe the outcome of measurement upon a quantum system.

Given a physical system, there is a state vector $|\psi\rangle$, that contains all possible information about the system. Unfortunately, in many cases, we do not know $|\psi\rangle$, but only that the system is in a state $|\psi_\alpha\rangle$ taken from an ensemble $\{|\psi_1\rangle, |\psi_2\rangle, \dots |\psi_l\rangle\}$, whose associated probabilities are $\{p_1, p_2, \dots p_l\}$ satisfying the condition of unit total probability $\sum_i p_i = 1$. This indicates that we have a *statistical mixture* of the states $|\psi_\alpha\rangle$ weighted by the probability p_α. However, every single state $|\psi_\alpha\rangle$ is what we know as a *pure state*.

Consequently, the average of an arbitrary observable (Hermitian operator) $\hat{\mathcal{O}}$ is given by

$$\langle\hat{\mathcal{O}}\rangle = \sum_\alpha p_\alpha \langle\psi_\alpha|\hat{\mathcal{O}}|\psi_\alpha\rangle. \tag{2.1}$$

Here, p_α characterizes the individual probabilities of the state $|\psi_\alpha\rangle$. The factor $\langle\psi_\alpha|\hat{\mathcal{O}}|\psi_\alpha\rangle$ indicates the probability of measuring the observable $\hat{\mathcal{O}}$. If we define the *density operator* $\hat{\rho}$ by

$$\hat{\rho} \equiv \sum_\alpha p_\alpha |\psi_\alpha\rangle\langle\psi_\alpha|, \tag{2.2}$$

then Eq. (2.1) can be rewritten as

$$\langle\hat{\mathcal{O}}\rangle = \mathrm{Tr}\left\{\hat{\mathcal{O}}\hat{\rho}\right\}. \tag{2.3}$$

In this way, the density operator in Eq. (2.2) contains both the statistical and quantum mechanical information about the system given by the probability p_α and the state vector $|\psi_\alpha\rangle$, respectively.

Based on the representation of Eq. (2.2), we find the following properties of the density operator. We have that for $\mathrm{Tr}\{\hat{\rho}\} = 1$ the following is satisfied

$$\mathrm{Tr}\{\hat{\rho}\} = \sum_\alpha p_\alpha \langle\psi_\alpha|\psi_\alpha\rangle = \sum_\alpha p_\alpha = 1. \tag{2.4}$$

Furthermore, if all p_α are zero except for the one corresponding to the state $|\psi_0\rangle$, then

$$\hat{\rho} = |\psi_0\rangle\langle\psi_0|,$$

which is called a *pure state* and, from the conservation of probability, it follows that $\mathrm{Tr}\{\hat{\rho}\} = 1$. On the other hand, for any state $|\phi\rangle$ we have

$$\langle\phi|\hat{\rho}|\phi\rangle = \sum_\alpha p_\alpha |\langle\phi|\psi_\alpha\rangle|^2 \geq 0,$$

i.e. $\hat{\rho}$ is *positive semidefinite*.

While state vectors can only describe pure states, the density operator can describe *mixed states*. It is known as a mixed state a collection of pure states $|\psi_\alpha\rangle$ with probability p_α, where $p_\alpha \in [0, 1]$ and $\sum_\alpha p_\alpha = 1$ and it can be proven that

$$\mathrm{Tr}\left\{\hat{\rho}^2\right\} \leq 1$$

with equality only for a pure state. The above can then be easily summarized as follows:

$$\begin{aligned} \text{Pure State} &\iff \mathrm{Tr}\left\{\hat{\rho}^2\right\} = 1, \\ \text{Mixed State} &\iff \mathrm{Tr}\left\{\hat{\rho}^2\right\} < 1. \end{aligned}$$

The dynamics of the density operator can be derived from the Schrödinger equation,

$$\frac{d}{dt}|\psi\rangle = -\frac{i}{\hbar}\hat{H}|\psi\rangle, \tag{2.5}$$

where $\hat{H}$ is the time-independent Hamiltonian of the system. The time derivative of $\hat{\rho}$ in Eq. (2.2) yields

$$\frac{d}{dt}\hat{\rho} = \sum_{\alpha} p_\alpha \left(\frac{d|\psi_\alpha\rangle}{dt}\langle\psi_\alpha| + |\psi_\alpha\rangle\frac{d\langle\psi_\alpha|}{dt} \right),$$

where we assume that the probability p_α is time-independent. By inputting the Schrödinger Eq. (2.5) into the last equation we find

$$\frac{d}{dt}\hat{\rho} = -\frac{i}{\hbar}\left[\hat{H}, \hat{\rho}\right], \tag{2.6}$$

whose formal solution reads

$$\hat{\rho}(t) = \exp\left\{-\frac{i}{\hbar}\hat{H}t\right\}\hat{\rho}(0)\exp\left\{\frac{i}{\hbar}\hat{H}t\right\}. \tag{2.7}$$

Eq. (2.6) is the so-called *Liouville* or *Von Neumann* equation of motion for the density operator, which can also be written as

$$\frac{d}{dt}\hat{\rho} = \hat{\mathcal{L}}(t)\hat{\rho}, \tag{2.8}$$

where $\hat{\mathcal{L}}$ is known as the *Liouville superoperator* and is given by $\hat{\mathcal{L}} = -\frac{i}{\hbar}\left[\hat{H}, \bullet\right]$ with $\bullet$ a placeholder. It is regarded as a superoperator since it acts on an operator to yield another operator.

On the other hand, in the Heisenberg picture, the equation of motion for a dynamical operator differs in sign from Eq. (2.6) and reads

$$\frac{d}{dt}\hat{\mathcal{O}} = \frac{i}{\hbar}\left[\hat{H}, \hat{\mathcal{O}}\right]. \tag{2.9}$$

So far, we described the dynamics in the Schrödinger and Heisenberg picture, Eqs. (2.6) and (2.9), respectively. However, throughout this work, we will usually move to an the interaction frame, where the Hamiltonian of the system can be regarded as a sum of two parts

$$\hat{H} = \hat{H}_0 + \hat{H}_{\mathrm{I}}. \tag{2.10}$$

The first term, $\hat{H}_0$, generally represents the sum of the energies of the systems without concerning their interaction, usually called the *free* or *bare* Hamiltonian. The second term on the right, $\hat{H}_{\mathrm{I}}$, describes the interaction between the systems and is known as the *interaction Hamiltonian*. To transform Eq. (2.6) into the interaction frame we need to separate the rapid motion associated with the free Hamiltonian, $\hat{H}_0$, from the slow dynamics of the interaction, $\hat{H}_I$. We now define the interaction frame density operator as

$$\hat{\rho}'(t) \equiv e^{\frac{i}{\hbar}\hat{H}_0 t}\hat{\rho}(t)e^{-\frac{i}{\hbar}\hat{H}_0 t}, \tag{2.11}$$

and from Eq. (2.6), we obtain the corresponding von Neumann's equation in the interaction frame

$$\frac{d}{dt}\hat{\rho}'(t) = -\frac{i}{\hbar}\left[\hat{H}'_{\mathrm{I}}(t), \hat{\rho}'_{\mathrm{I}}(t)\right]. \tag{2.12}$$

After formally integrating this equation we find

$$\hat{\rho}'(t) = \hat{\rho}(0) - \frac{i}{\hbar}\int_0^t d\tau \left[\hat{H}'_{\mathrm{I}}(\tau), \hat{\rho}'_{\mathrm{I}}(\tau)\right], \tag{2.13}$$

where, from now on, the tilde indicates the interaction frame. Furthermore, note that $\hat{H}_{\mathrm{I}}(t)$ is explicitly time-dependent, namely,

$$\hat{H}'_{\mathrm{I}}(t) \equiv e^{\frac{i}{\hbar}\hat{H}_0 t}\hat{H}_{\mathrm{I}}e^{-\frac{i}{\hbar}\hat{H}_0 t}. \tag{2.14}$$

One of the key aspects of an OQS is its irreversibility, which is caused by the system's coupling to a larger complex system (see Fig. 2.1): its environment. In this way, the dynamics of the system can not be described by the unitary evolution of the state vector, but rather in terms of an equation of motion for its density operator, i.e. the so-called *quantum master equation*, which we will study in the next section.

2.2 Master equation approach

There are various methods analyzing the dynamics of OQS, with the most effective being the *system-bath* theory [37, 39, 42]. Essentially it means that, when the bath acts as a larger system in thermal equilibrium, it generates fluctuations in the system it's connected to, leading to energy exchange.

The decomposition of the whole ensemble into a system plus environment allows to write the composite Hilbert space as a tensor product:

$$\mathcal{H}_{\mathrm{total}} = \mathcal{H}_{\mathrm{S}} \otimes \mathcal{H}_{\mathrm{B}}, \tag{2.15}$$

where $\mathcal{H}_{\mathrm{S}}$ and $\mathcal{H}_{\mathrm{B}}$ are the system and environment individual Hilbert spaces, respectively. Recalling Eq. (2.10), the composite Hamiltonian is then given by

$$\hat{H} = \hat{H}_{\mathrm{S}} \otimes I_{\mathrm{B}} + I_{\mathrm{S}} \otimes \hat{H}_{\mathrm{B}} + \hat{H}_{\mathrm{SB}}, \tag{2.16}$$

where the first term constitutes the free Hamiltonian $\hat{H}_0$, which consists of the system and bath individual energies. On the other hand, the last Hamiltonian describes the interaction between them. The study of time-dependent Hamiltonians, which requires additional techniques, are beyond the scope of this work.

Using the composite Hamiltonian, we have, in the Schrödinger picture as in Eq. (2.5), the following equation of motion for the density operator ($\hbar = 1$ onwards)

$$\frac{d}{dt}\hat{\rho}(t) = -i\left[\hat{H}_{\mathrm{S}} + \hat{H}_{\mathrm{B}} + \hat{H}_{\mathrm{SB}}, \hat{\rho}(t)\right] \tag{2.17}$$

with $\hat{\rho}(t) \in \mathcal{H}_{\mathrm{S}} \otimes \mathcal{H}_{\mathrm{B}}$. Our primary aim is to characterize the effective dynamics of *the system*. Hence, we introduce the *reduced density operator*

$$\hat{\rho}_{\mathrm{S}}(t) \equiv \mathrm{Tr}_B\left\{\hat{\rho}(t)\right\}, \tag{2.18}$$

which describes the system's dynamics by tracing out the reservoir's degrees of freedom. Likewise, for an arbitrary operator $\hat{\mathcal{O}} \in \mathcal{H}_{\mathrm{S}}$, we have that its expectation reads

$$\langle\hat{\mathcal{O}}\rangle = \mathrm{Tr}_{\mathrm{total}}\left\{\hat{\mathcal{O}}\,\hat{\rho}(t)\right\} = \mathrm{Tr}_{\mathrm{S}}\left\{\hat{\mathcal{O}}\,\mathrm{Tr}_B\left\{\hat{\rho}(t)\right\}\right\} = \mathrm{Tr}_{\mathrm{S}}\left\{\hat{\mathcal{O}}\,\hat{\rho}_{\mathrm{S}}(t)\right\}. \tag{2.19}$$

We aim to obtain an expression for $\hat{\rho}_{\mathrm{S}}(t)$, which includes the information of its coupling to the bath. First, we move to the interaction frame as in Eq. (2.11), which implies doing

$$\hat{\rho}'(t) = e^{i(\hat{H}_S + \hat{H}_B)t}\hat{\rho}(t)e^{-i(\hat{H}_S + \hat{H}_B)t}. \tag{2.20}$$

Therefore, following Eq. (2.12), using Eqs. (2.17) and (2.20), we find

$$\frac{d}{dt}\hat{\rho}'(t) = -i[\hat{H}'_{\mathrm{SB}}(t), \hat{\rho}'(t)] \tag{2.21}$$

and consequently

$$\hat{\rho}'(t) = \hat{\rho}(0) - i\int_{t_0}^{t} d\tau \left[\hat{H}'_{\mathrm{SB}}(\tau), \hat{\rho}'(\tau)\right]. \tag{2.22}$$

So far, this derivation has been equivalent to the one yielding Eq. (2.13), but with Eq. (2.16). Thus, $\hat{H}'_{\mathrm{SB}}(t)$ is given by Eq. (2.14) with $\hat{H}_0 = \hat{H}_{\mathrm{S}} + \hat{H}_{\mathrm{B}}$.

We can now substitute Eq. (2.22) into Eq. (2.21), which leads us to the exact equation

$$\frac{d}{dt}\hat{\rho}'(t) = -i\left[\hat{H}'_{SB}, \hat{\rho}(0)\right] - \int_0^t d\tau \left[\hat{H}'_{SB}(t), \left[\hat{H}'_{SB}(\tau), \hat{\rho}'(\tau)\right]\right], \tag{2.23}$$

This integro-differential equation is the starting point for a series of approximations that we will explain below.

2.2.1 Initial Conditions

In the study of OQSs, a crucial consideration is the initial state of the composite system, comprising both the system and its bath. The formulation of this initial composite density operator plays a fundamental role in determining the system's evolution and the validity of various approximations.

We will assume that no correlation exists between the system and the bath at the initial time $t = 0$. That means $\hat{\rho}(0) = \hat{\rho}'(0)$ can be factorized as

$$\hat{\rho}(0) = \hat{\rho}_{\mathrm{S}}(0) \otimes \hat{\rho}_{\mathrm{B}}(0) \tag{2.24}$$

with $\hat{\rho}_{\mathrm{B}}(0) = \mathrm{Tr}_S\{\hat{\rho}(0)\}$ the initial bath density operator, and $\hat{\rho}_{\mathrm{S}}(0) = \mathrm{Tr}_B\{\hat{\rho}(0)\}$ the initial system density operator.

2.2.2 Weak Coupling

We will now assume the bath is sufficiently large, and its coupling to the system *weak* enough to neglect the system's backaction on the bath. Consequently, the statistical properties of the bath remain unaffected by the weak coupling, thus

$$\hat{\rho}'(t) \approx \hat{\rho}'_S(t) \otimes \hat{\rho}_{\mathrm{B}}, \quad t > 0 \tag{2.25}$$

with $\hat{\rho}_{\mathrm{B}} \equiv \hat{\rho}_{\mathrm{B}}(0)$. The last assumption supposes that the total density operator remains a product of the initial bath state density operator and $\hat{\rho}'_S(t)$.

Up to this point, we have first assumed that there are no correlations between the system and bath as in Eq. (2.24) at $t = 0$. Additionally, we have presumed that the bath density operator remains relatively unchanged by the weak interaction, in contrast to the system's density operator. This is due to the system's smaller size compared to the bath, resulting in stronger fractional effects of the interaction on the system.

Hence assuming Eq. (2.24) and Eq. (2.25) are valid, Eq. (2.23) allows us to describe the dynamics of the quantum system by

$$\frac{d}{dt}\hat{\rho}'_S(t) = -i\mathrm{Tr}_B\left\{[\hat{H}'_{SB}, \hat{\rho}_{\mathrm{S}}(0) \otimes \hat{\rho}_{\mathrm{B}}]\right\} - \int_0^t d\tau\, \mathrm{Tr}_B\left\{[\hat{H}'_{SB}(t), [\hat{H}'_{SB}(\tau), \hat{\rho}'_S(\tau) \otimes \hat{\rho}_{\mathrm{B}}]\,]\right\}, \tag{2.26}$$

where the first term can be set to zero – an assumption that can always be fulfilled with a properly shifted system Hamiltonian [38]. Hence, we have

$$\frac{d}{dt}\hat{\rho}'_S(t) = -\int_0^t d\tau \,\mathrm{Tr}_B\left\{[\hat{H}'_{SB}(t),[\hat{H}'_{SB}(\tau),\hat{\rho}'_S(\tau)\otimes\hat{\rho}_\mathrm{B}]\,]\right\}. \tag{2.27}$$

We now continue denoting the system operators by $\hat{S}_k$ and the bath operators by $\hat{B}_k$, such that the most general form of $\hat{H}_\mathrm{SB}$ reads

$$\hat{H}_\mathrm{SB} = \sum_k \hat{S}_k \otimes \hat{B}_k. \tag{2.28}$$

Since $\hat{S}_k \in \mathcal{H}_\mathrm{S}$ and $\hat{B}_k \in \mathcal{H}_\mathrm{B}$ in the interaction frame we have $\hat{H}'_\mathrm{SB} = \sum_k \hat{S}'_k \otimes \hat{B}'_k$. The substitution of $\hat{H}'_\mathrm{SB}$ into Eq. (2.27) results in

$$\frac{d}{dt}\hat{\rho}'_S(t) = -\int_0^t d\tau \sum_{kl} \mathrm{Tr}_B\left\{\left[\hat{S}'_k(t)\otimes\hat{B}'_k(t),[\hat{S}_l(\tau)\otimes\hat{B}'_l(\tau),\hat{\rho}'_S(\tau)\otimes\hat{\rho}_\mathrm{B}\right]\right\},$$

which can be rewritten as

$$\begin{aligned}\frac{d}{dt}\hat{\rho}'_S(t) = &-\sum_{kl}\int d\tau\, C_{kl}(t,\tau)\left[\hat{S}'_k(t)\hat{S}'_l(\tau)\hat{\rho}'_S(\tau) - \hat{S}'_l(\tau)\hat{\rho}'_S(\tau)\hat{S}'_k(t)\right]\\ &-\sum_{kl}\int d\tau\, C_{lk}(\tau,t)\left[\hat{\rho}'_S(\tau)\hat{S}'_l(\tau)\hat{S}'_k(t) - \hat{S}'_k(t)\hat{\rho}'_S(\tau)\hat{S}'_l(\tau)\right],\end{aligned}$$

where we used the cyclic property of the trace and we have introduced the *correlation function*

$$C_{kl}(t,t') \equiv \mathrm{Tr}_B\left\{\hat{B}'_k(t)\hat{B}'_l(\tau)\hat{\rho}_\mathrm{B}\right\} = \langle \hat{B}'_k(t)\hat{B}'_l(\tau)\rangle, \tag{2.29}$$

that describes the properties of the reservoir.

To obtain Eq. (2.27) we dropped the first term in Eq. (2.26), which can also be done by assuming that the bath is in thermal equilibrium, i.e. $\left[\hat{\rho}_\mathrm{B},\hat{H}_B\right] = 0$ and consequently writing $C_{kl}(t,\tau) \equiv C_{kl}(t-\tau)$ with $C_{kl}(t,\tau)$ given by Eq. (2.29). Using these results, Eq. (2.27) becomes

$$\begin{aligned}\frac{d}{dt}\hat{\rho}'_S(t) = &-\int_0^t d\tau \sum_{kl}\left(C_{kl}(t-\tau)\left\{\hat{S}'_k(t)\hat{S}'_l(\tau)\hat{\rho}'_S(\tau) - \hat{S}'_l(\tau)\hat{\rho}'_S(\tau)\hat{S}'_k(t)\right\}\right)\\ &-\int_0^t d\tau \sum_{kl}\left(C_{lk}(\tau-t)\left\{\hat{\rho}'_S(\tau)\hat{S}'_l(\tau)\hat{S}'_k(t) - \hat{S}'_k(t)\hat{\rho}'_S(\tau)\hat{S}'_l(\tau)\right\}\right).\end{aligned} \tag{2.30}$$

The next approximation arises from the distinct time scales corresponding to the bath correlations and the time needed for the system to change.

2.2.3 Markov Approximation

This assumption is crucial as it implies a clear separation between the time-scale evolution of the system and the bath in the interaction picture. Indeed, the bath correlation functions are generally characterized by a correlation time, which is typically shorter than the time constant associated with the system's density operator. Consequently, the system's density operator changes almost insignificantly over the time it takes for the correlation function given in Eq. (2.30) to vanish. Thus, in the interaction and under this approximation, the replacement of $\hat{\rho}'(\tau) \to \hat{\rho}'(t)$ is valid since we can take $C_{kl}(t-\tau) \propto \delta(t-\tau)$ suggesting the existence of these two widely separated times scales. This has also a *deeper* implication: we are neglecting the reservoir's memory because we are unable to resolve its effects. Hence,

under this approximation, Eq. (2.30) reads

$$\frac{d}{dt}\hat{\rho}'_S(t) = -\int_0^t d\tau \sum_{kl}\left(C_{kl}(t-\tau)\left\{\hat{S}'_k(t)\hat{S}'_l(\tau)\hat{\rho}'(t) - \hat{S}'_l(\tau)\hat{\rho}'(t)\hat{S}'_k(t)\right\}\right) \\ -\int_0^t d\tau \sum_{kl}\left(C_{lk}(\tau-t)\left\{\hat{\rho}'(t)\hat{S}'_l(\tau)\hat{S}'_k(t) - \hat{S}'_k(t)\hat{\rho}'(t)\hat{S}'_l(\tau)\right\}\right).$$

The transformation of the last equation back into the Schrödinger picture yields

$$\begin{aligned}\frac{d}{dt}\hat{\rho}_{\mathrm{S}}(t) &= -i[\hat{H}_S, \hat{\rho}_{\mathrm{S}}(t)] \\ &-\int_0^t d\tau \sum_{kl} C_{kl}(t-\tau)\left\{\hat{S}_k\hat{S}'_l(\tau-t)\hat{\rho}_{\mathrm{S}}(t) - \hat{S}'_l(\tau-t)\hat{\rho}_{\mathrm{S}}(t)\hat{S}_k\right\} \\ &-\int_0^t d\tau \sum_{lk} C_{lk}(\tau-t)\left\{\hat{\rho}_{\mathrm{S}}(t)\hat{S}'_l(\tau-t)\hat{S}_k - \hat{S}_k\hat{\rho}_{\mathrm{S}}(t)\hat{S}'_l(\tau-t)\right\}.\end{aligned} \tag{2.31}$$

The integral over τ can be carried out in the limit of $t \to \infty$ and defining

$$\begin{aligned}\hat{D}_k &:= \lim_{t\to\infty}\int_0^t d\tau \sum_l C_{kl}(\tau)\hat{S}'_l(-\tau), \\ \hat{E}_k &:= \lim_{t\to\infty}\int_0^t d\tau \sum_l C_{lk}(-\tau)\hat{S}'_l(-\tau)\end{aligned} \tag{2.32}$$

we finally find

$$\frac{d}{dt}\hat{\rho}_{\mathrm{S}}(t) = -i[\hat{H}_S, \hat{\rho}(t)] - \sum_k\left[\hat{S}_k\hat{D}_k\hat{\rho}(t) - \hat{D}_k\hat{\rho}(t)\hat{S}_k + \hat{\rho}(t)\hat{E}_k\hat{S}_k - \hat{S}_k\hat{\rho}(t)\hat{E}_k\right]. \tag{2.33}$$

From the derivation leading to Eq. (2.33), it follows (see [39, 42]) that the master equation for a Markovian system can be expressed in the *Lindblad form* [43]:

$$\frac{d}{dt}\hat{\rho}_{\mathrm{S}}(t) = -i[\hat{H}, \hat{\rho}_{\mathrm{S}}(t)] + \sum_j \gamma_j\left[\hat{L}_j\hat{\rho}_{\mathrm{S}}(t)\hat{L}_j^\dagger - \frac{1}{2}\left\{\hat{L}_j^\dagger\hat{L}_j, \hat{\rho}_{\mathrm{S}}(t)\right\}\right], \tag{2.34}$$

where $\hat{H}$ is the system's Hamiltonian. Here, γ_j is a decay rate, and $\hat{L}_j$ is a *Lindblad operator*, representing the dissipation channels through which energy can either enter into or leak out of the system to its environment. It describes the nature of the energy loss or decoherence process. Without the second term on the right, Eq.(2.34) would be the von Neumann Eq. (2.6) describing the system's unitary dynamics. The second term to the right corresponds then to the dissipative processes causing the dynamics to be irreversible. Lastly, often Eq. (2.34) is found as

$$\frac{d}{dt}\hat{\rho}_{\mathrm{S}}(t) = -i\left[\hat{H}, \hat{\rho}_{\mathrm{S}}(t)\right] + \sum_j \gamma_j\mathcal{D}[\hat{L}_j]\,\hat{\rho}_{\mathrm{S}}(t),$$

where the dissipative term, also known as *dissipator* or *jump operator* is usually written in superoperator form:

$$\mathcal{D}[\hat{o}]\bullet \equiv \hat{o}\bullet\hat{o}^\dagger - \frac{1}{2}\left\{\hat{o}^\dagger\hat{o}, \bullet\right\}. \tag{2.35}$$

Here, in general, the Hamiltonian $\hat{H}$ does not necessarily refer to the system's free Hamiltonian, since it might contain additional terms induced by the coupling to the bath.

Let us now consider the composite system $\mathcal{S}\otimes\mathcal{B}$ of a damped harmonic oscillator. This example is particularly important since many physical systems, such as an optical cavity or a mechanical oscillator, can be modelled as quantum harmonic oscillators. The Hamiltonian of

a harmonic oscillator is $\hat{\mathcal{H}}_{\rm S} = \omega_0 \hat{a}^\dagger \hat{a}$ with ω_0 its frequency and where $\hat{a}$ and $\hat{a}^\dagger$ are the creation and annihilation operators of the bosonic mode, respectively. The system is in contact with a thermal bath modelled as a collection of harmonic oscillators, whose Hamiltonian reads

$$\hat{\mathcal{H}}_{\rm B} = \sum_j \omega_j \hat{b}_j^\dagger \hat{b}_j, \tag{2.36}$$

with frequencies ω_j and associated annihilation and creation operators $\hat{b}_j^\dagger$ and $\hat{b}_j$, respectively. In addition, the system-bath interaction is given by

$$\hat{\mathcal{H}}_{\rm SB} = \sum_j \left(\kappa_j \hat{a} \hat{b}_j^\dagger + \kappa_j^* \hat{a}^\dagger \hat{b}_j \right) \tag{2.37}$$

with coupling constants k_j in the RWA. Hence, the master equation of a damped harmonic oscillator reads (see derivation in [42])

$$\frac{d}{dt}\hat{\rho} = -i\omega_0' \left[\hat{a}^\dagger \hat{a}, \hat{\rho}\right] + \gamma \left(\bar{n}^T + 1\right) \mathcal{D}[\hat{a}]\hat{\rho} + \bar{n}^T \mathcal{D}[\hat{a}^\dagger]\hat{\rho} \tag{2.38}$$

where γ is the decay rate, $\omega_0' = \omega_0 + \Delta$ and $\bar{n}^T = [\exp\{\omega_0/k_{\rm B}T\} - 1]^{-1}$ with $k_{\rm B}$ the Boltzmann constant. This equation will be fundamental throughout this work. Nevertheless, the derivation yielding Eq. (2.38) is valid within the RWA, but for low-frequency oscillators (strong damping $\gamma \sim \omega_0$) this approximation is no longer valid. The frequency shift[2], Δ, is small and usually neglected.

So far, we have presented the formulation of OQSs in the Schrödinger picture using the master equation formalism. In the next section, we will introduce the *input-output* formalism, developed by Gardiner and Collett [44]. This approach, within the Heisenberg picture, employs quantum stochastic differential equations to describe the reservoir theory. Within this theory, the environment dictates the system's dynamics through input fields and output fields as we will see below.

2.3 Input-output theory

In the preceding section, we employed the quantum master equation approach to analyze the dynamics of a dissipative system in the Schrödinger picture. This approach treats the field, to which the system is weakly coupled, as the environment. In the context of quantum optics, this environment refers to a field surrounding the open system, typically considered a passive system assumed to be in equilibrium. In contrast, in this section, the environment is viewed as an external field coupled to the system. This approach enables the assessment of how the *input field* influences the system dynamics, subsequently impacting the quantum statistics of the *output field*. Thus, in this section, we will discuss Gardiner's and Collett's seminal work [44] and introduce the so-called input-output formalism which analyzes the system dynamics in the Heisenberg picture.

Similarly, as in Sec. 2.2, we will consider the system-bath model with a composite Hamiltonian as in Eq. (2.16). In the frequency domain, this Hamiltonian is given by

$$\begin{aligned} \hat{H}_{\rm B} &= \int_{-\infty}^{\infty} d\omega\, \omega\, \hat{b}^\dagger[\omega]\hat{b}[\omega], \\ \hat{H}_{\rm SB} &= i \int_{-\infty}^{\infty} d\omega\, k[\omega] \left(\hat{a}\hat{b}^\dagger[\omega] - \hat{a}^\dagger \hat{b}[\omega] \right), \end{aligned}$$

where $\hat{b}[\omega]$ are the bath's bosonic annihilation operators, which satisfy $[\hat{b}[\omega], \hat{b}^\dagger[\omega']] = \delta[\omega - \omega']$. On the other hand, $\hat{a}$ is a system's operator and $k[\omega]$ is a frequency-dependent coupling. Here, the RWA is again valid since we are once more assuming a weak coupling between the system and the large environment.

[2] For the case of a damped two-level atom this frequency shift is known as the *Lamb shift* and is particularly important [37].

To derive the *quantum Langevin equations* we start with the Heisenberg equation of motion given in Eq. (2.9) for the b-mode that reads

$$\frac{d}{dt}\hat{b}[\omega] = -i\omega\hat{b}[\omega] + k[\omega]\hat{a} \tag{2.39}$$

and analogously for the a-mode

$$\frac{d}{dt}\hat{a}(t) = -i\left[\hat{a}, \hat{H}_S\right] - \int_{-\infty}^{\infty} d\omega\, k[\omega]\hat{b}[\omega]. \tag{2.40}$$

To solve equations as Eq. (2.39), we will use the method of *variation of constants*, which we will explain below.

Variation of constants: Let us first consider an equation of the form

$$\frac{db}{dx} = ab(x) + \xi(x).$$

Here, using the *Ansatz* $b(x) = e^{ax}v(x)$, we get

$$\frac{d}{dx}b = ae^{ax}v(x) + e^{ax}v'(x) \stackrel{!}{=} av(x) + \xi(x).$$

The last equality results in

$$\frac{dv(x)}{dx} = e^{-ax}\xi(x),$$

whose solution is

$$v(x) = v(0) + \int_{x_0}^{x} dx' e^{-ax'}\xi(x').$$

If we multiply the last equation from both sides by e^{ax} we finally obtain

$$b(x) = e^{ax}v(0) + \int_{x_0}^{x} dx' e^{-a(x'+x)}\xi(x'). \tag{2.41}$$

We can now associate Eq. (2.41) with Eq. (2.39) and

$$b[\omega] = e^{-i\omega(t-t_0)}b_0[\omega] + \kappa[\omega]\int_{t_0}^{t} dt' e^{-i\omega(t-t')}\hat{a}(t'), \tag{2.42}$$

where $\hat{b}_0[\omega]$ is the value of the operator $\hat{b}[\omega]$ at an initial time $t = t_0$ and has the same commutation relations as $\hat{b}[\omega]$. Here, the first term has the information of the initial conditions, whereas the second is a memory term, which can be seen from the integration limits. The substitution of this result into Eq. (2.40) gives

$$\begin{aligned}\frac{d}{dt}\hat{a}(t) = &-i\left[\hat{a}(t), \hat{H}_S\right] - \int_{-\infty}^{\infty} d\omega\, k[\omega]e^{-i\omega(t-t_0)}b_0[\omega] \\ &- \int_{-\infty}^{\infty} d\omega \int_{t_0}^{t} dt'\, k^2[\omega]e^{-i\omega(t-t')}\hat{a}(t').\end{aligned} \tag{2.43}$$

Now, similar to what we did in Sec. 2.2, we make the *first Markov approximation*:

$$\kappa[\omega] = \sqrt{\frac{\gamma}{2\pi}},. \tag{2.44}$$

As discussed in Sec. 2.2.3, Markovian processes are defined by the absence of memory effects, meaning that the future state of the system depends only on its current state, not its past. In the context of OQS, the Markovian approximation assumes the environment relaxes much

faster than the system dynamics. This is reflected in the last equation by assuming a constant coupling to the environment, implying that the environment lacks memory and responds instantaneously to the system. Note, due to the last expression, Eq. (2.43) has the form of a damping equation. Since the following relation

$$\frac{1}{2\pi}\int_{-\infty}^{\infty} d\omega\, e^{-i\omega(t-t')} = \delta(t-t') \tag{2.45}$$

is achieved as the limit of an integral of a function going smoothly to zero at $\pm\infty$, then the following result is also valid

$$\int_{t_0}^{t} dt'\, \hat{a}(t')\delta(t-t') = \frac{1}{2}\hat{a}(t). \tag{2.46}$$

We now define the *in-field* by

$$\hat{a}_{\rm in}(t) \equiv \frac{1}{\sqrt{2\pi}}\int d\omega\, e^{-i\omega(t-t_0)}\hat{b}_0[\omega], \tag{2.47}$$

which satisfies the bosonic commutation relations and finally, using Eqs. (2.44-2.47) in Eq. (2.43), we find

$$\frac{d}{dt}\hat{a}(t) = -i\left[\hat{a}(t), \hat{H}_S\right] - \frac{\gamma}{2}\hat{a}(t) - \sqrt{\gamma}\hat{a}_{\rm in}(t), \tag{2.48}$$

which is a *quantum stochastic differential equation* (QSDE) for the intracavity field $\hat{a}(t)$. Note, if $\gamma = 0$, we would recover the Heisenberg equation of motion given in Eq. (2.9). As expected, when $\gamma \neq 0$, the interaction with the bath introduces a damping term proportional to $\frac{\gamma}{2}\hat{a}(t)$, that has no particular specification of the state of the reservoir. Moreover, from Eq. (2.44), this damping term depends only on the system operators at time t and does not take into account previous times. On the other hand, the *quantum noise term* enters as the input field to the cavity given in Eq. (2.47).

Analogously, we can obtain the time-reversed QSDE as

$$\frac{d}{dt}\hat{a}(t) = -i\left[\hat{a}(t), \hat{H}_S\right] + \frac{\gamma}{2}\hat{a}(t) - \sqrt{\gamma}\hat{a}_{\rm out}(t),$$

with

$$\hat{a}_{\rm out}(t) = \frac{1}{\sqrt{2\pi}}\int d\omega\, e^{-i\omega(t-t')}\hat{b}_1[\omega]. \tag{2.49}$$

The definition of the input and output fields are related by the *input-output relation*

$$\hat{a}_{\rm out}(t) - \hat{a}_{\rm in}(t) = \sqrt{\gamma}a(t). \tag{2.50}$$

This relation describes how the system alters the incoming field, generating an outgoing field that encodes information about the system's current state.

As discussed in this Chapter, the Heisenberg equations of motion in Eq. (2.9) play a central role in deriving the quantum Langevin equations. In these equations, the evolution of the system's operator experiences dissipation at a rate $\gamma/2$, where γ represents the decay constant. Simultaneously, quantum fluctuations are reintroduced by the quantum noise entering the system from different ports. Therefore, the quantum Langevin equation essentially constitutes a formulation of reservoir theory within the Heisenberg picture.

Throughout this chapter, we introduced the necessary tools to handle OQSs using the system-plus-reservoir approach, which leads to the master equation. Additionally, we discussed input-output theory, which models the environment as an external field coupled to the cavity. In the next Chapter, we will apply this theory to explore the fundamentals of optomechanical systems.

Chapter 3

Fundamentals of Optomechanical Systems

In the 17th century, Kepler recognized that light carries momentum which led to the concept of radiation pressure force [45]. Centuries later, in 1909, Einstein analyzed the statistics of these radiation pressure force fluctuations acting on a movable mirror [46]. It was through the mediation of the radiation pressure force that the interaction between two seemingly distinct yet scientifically rich subjects, namely optical cavities [47] and mechanical resonators [48], established the foundations of the field of *optomechanics*.

One of the fundamental consequences of the quantum fluctuations of the radiation pressure force is that they impose a limit on the accuracy of position measurement, which gives rise to the *standard quantum limit* (SQL) [49, 50], crucial for gravitational wave detectors such as LIGO [51] or VIRGO [52]. Additionally, the pioneering works of V.B. Braginsky and A.B. Manukin [53, 54] revealed that the retarded nature of the radiation pressure of light confined in a cavity or resonator leads to the effect of *dynamical backaction*. This effect provides damping or anti-damping to the mechanical mode, resulting in *optomechanical backaction cooling* and mechanical amplification (parametric instability), respectively. Moreover, it has also been shown that the radiation pressure force results in the modification of the mechanical oscillator stiffness, a phenomenon called *optical spring effect* [55].

The theoretical development in the field of optomechanics goes hand in hand with the improvement in the realization of optical cavities and mechanical resonators. Experimentally, radiation pressure in the microwave domain dates back to Braginsy's work in 1977 [54]. Years later, in 1983 Dorsel *et al.* observed the bistability of the radiation pressure force on a macroscopic end-mirror [56], being the first experiment in the optical regime. Although the dynamical backaction effects of the radiation pressure force were among the first phenomena predicted in optomechanics, it was only recently that these *dynamical* effects were experimentally observed in micro- and nano-mechanical systems. Interestingly, although dynamical backaction was motivated by the position measurement of gravitational waves using large masses, it was first observed in a completely different size scale using microtoroid cavities [57–59]. This is an example of *parametric amplification* induced by the optomechanical interaction. Contrary, the opposite effect has been used to backaction cool, for instance, cantilevers [60, 61], microtoroids [62], macroscopic mirror modes [63] and mechanical nano-membranes [64].

The rapid development of optomechanics lies not only in the construction of accurate position detectors but also in the possibility of being used as a light-mechanics interface due to the controllable interaction between light and mechanics. Thus, optomechanics is a fundamental resource to realize hybrid quantum devices of otherwise incompatible degrees of freedom for numerous applications in quantum technologies [65]. For these reasons, optomechanics has also been able to shine a light on the quantum-to-classical transition [66]. Nevertheless, a deeper understanding of the quantum nature of macroscopic mechanical systems is hindered by the difficulty of cooling a mechanical mode to its quantum ground state [67]. The fabrication improvement in recent years has also enabled the possibility to backaction cool a mechanical mode to the ground state [29, 68]. These achievements using dynamical backaction cooling have been realized in the so-called *resolved sideband* or *good cavity* regime, where the mechanical resonant frequency (ω_m) exceeds the cavity decay rate (κ), i.e. when $\omega_m \gg \kappa$. However, as mechanical systems increase in size, their frequency naturally decreases which

brings them into the *unresolved sideband* or *bad cavity* regime ($\omega_m \ll \kappa$). In this regime, dynamical backaction cooling is less effective, and other protocols, such as *measurement feedback cooling* have proven to be a more successful strategy [69].

Before dynamical backaction, *optomechanical feedback cooling* was already proposed. Such protocols use the high sensitivity of the cavity readout to measure the oscillator's position via a phase-sensitive detection of the classical cavity's output signal. This information is then turned into negative feedback on the oscillator, i.e. a force proportional to the time derivative of the output signal. The above finally translates into enhancing the mechanical damping rate without increasing the thermal noise (cold damping). This constitutes what is known as *active feedback cooling*. Experimentally, it is precisely the radiation pressure force that is used as the feedback force in optomechanical devices [70, 71]. Due to its nature, the cooling efficiency in such protocols is limited by the imprecision of the readout, whereas their quantum limits have been discussed in [72, 73]. However, in quantum physics, any measurement not only reads out the system's state but also irreversibly modifies it. Contrary to active feedback, *coherent feedback* protocols avoid this problem by coherently processing quantum signals, without measuring the system, and then feeding them back. In this way, coherent feedback would enable the preparation of nonclassical states [74] and facilitate cooling of the mechanics close to its ground state even in the unresolved sideband regime. While J. Guo *et al.* [75] theoretically propose a scheme to achieve ground state cooling in this regime, M. Ernzer *et al.* [76] provide experimental evidence demonstrating significant cooling improvements.

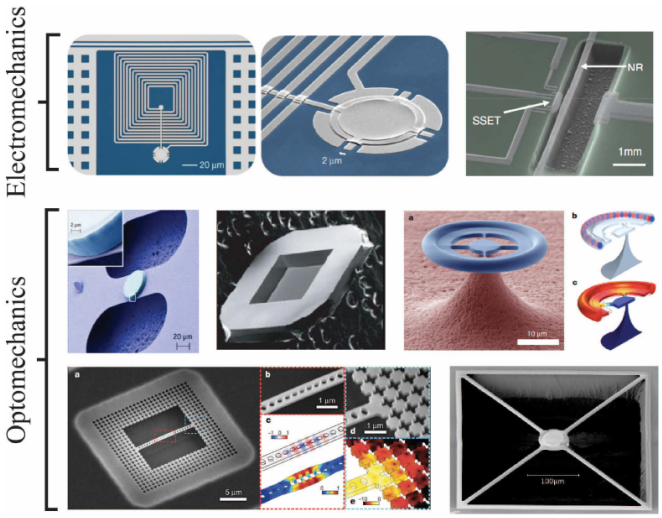

Figure 3.1: Some examples of electromechanical and optomechanical devices. Electromechanical devices Left & middle: aluminium drum mechanical resonator coupled to a superconducting lumped element microwave resonator [68]. *Right*: nanomechanical beam coupled to a superconducting single-electron transistor [77]. Optomechanical devices *Clockwise from top left*: microscale end-mirror from a Fabry-Pérot cavity optomechanical system [19], silicon nitride membrane used in membrane-in-the-middle type system [64], microtoroidal integrated cavity optomechanical system [78], phononic-photonic crystal integrated optomechanical system [29], trampoline microscale end-mirror from a Fabry-Pérot cavity optomechanical system [79]. Figure taken from [80].

The theoretical and experimental progress in the field of optomechanics led to many achievements, such as the detection of displacements below the SQL [81], which enabled the detection of gravitational waves [82, 83]; the demonstration of nonclassical states of motion [84, 85] as well as the development of novel protocols for their generation [86], and the demonstration of strong optomechanical coupling in both the microwave and optical regimes [23, 68, 87]. Additionally, it has also been demonstrated that the radiation pressure interaction enables the entanglement of macroscopic oscillators [88–90]. Furthermore, optomechanics plays also a singular role in studying fundamental aspects of quantum mechanics, such as testing local realism [91].

The rapid advancements in optical cavity and mechanical resonator technologies have also driven growing interest in cavity optomechanics. Such improvement has made it possible to operate in a regime in which optical forces are dominant [60–63]. For this regime to hold, considerable progress has been made in the manufacturing of mechanical devices as illustrated in Fig 3.1. Nevertheless, optomechanical interaction is not only limited to the optical regime. In the microwave regime, the realization of optomechanical coupling has also been possible with microfabricated superconducting resonators, by inserting a nanomechanical beam inside a superconducting transmission line microwave cavity [92]. Moreover, it has been proposed that the inductive coupling between a superconducting microcantilever and a flux-dependent microwave quantum circuit can reach the strong coupling regime [93–96]. On the other hand, in acoustic devices strong coupling has been shown [97]. Alternatively, single-photon strong coupling has also been realized by incorporating a flexible aluminium membrane into a lumped element superconducting resonator [68] and proposed in circuit optomechanical devices [98]. These advancements demonstrate the integration of electrical and non-optical techniques in optomechanical systems, enabling the coupling of mechanical oscillators to single-electron transistors [77, 99] or quantum point contacts [100]. Such electromechanical devices provide also the ability to realize hybrid quantum devices [20, 101] when they are coupled to two-level quantum systems [102–104].

To understand the components of the optomechanical coupling it is convenient to study the basic geometry depicted in Fig. 3.2, which has been used to describe the vast majority of the experiments to date. Here, we have an optomechanical system composed of a Fabry-Pérot optical cavity with a movable mirror that also serves as a mass-on-a-spring. The optical cavity, with resonant frequency ω_c, is populated with photons injected by an external driving field at frequency ω_p. This high circulating intracavity photon number exerts a force upon the movable *mass-spring* mirror, thereby displacing it. This movement gives rise to a parametric interaction, where the motion of the mechanical mode modifies the cavity resonance.

Since a thorough review of optomechanics is beyond the scope of this work, the reader is referred to the numerous reviews published in recent years on cavity optomechanics, which offer a broader picture of this interesting and growing field [1, 27, 105–107]. In this chapter, we will first discuss optical cavities and mechanical oscillators. We will then use the methods introduced in Chapter 2 and derive the basic dynamical consequences of this interaction and present the quantum theory of optomechanical cooling. Next, using a quantum noise approach, we will study how an optomechanical system can be used for position detection. Finally, we will present the theory of optomechanically induced transparency.

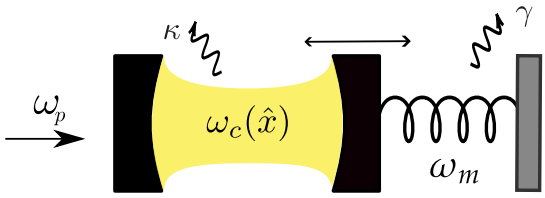

FIGURE 3.2: Diagram of an optomechanical system. Here, we depict a driven optical cavity with resonant frequency ω_c with a movable mirror that acts as a mass-on-a-spring. The driving (at frequency ω_p) populates the cavity with photons that circulate and impinge on the mirror, thereby exerting a force on it and ultimately displacing it. This movement also modifies the cavity resonance yielding a parametric interaction between the modes.

3.1 Optical resonators

To begin, let's briefly introduce the concept of an optical and a mechanical resonator. The optical resonator is typically depicted as a Fabry-Pérot resonator as illustrated in Fig. 3.2. At the two ends of the optical cavity, two highly reflective mirrors separated by a distance L are located. It is precisely this separation that determines the cavity resonant frequencies given by $\omega_n \approx n\pi c/L$, where n represents the integer mode number and c denotes the speed of light in vacuum. Although there are multiple optical modes, we will primarily focus on a single mode, commonly denoted by ω_c. This single-mode approximation is particularly

valid for high-finesse cavities, where the large spectral separation between modes, compared to their individual linewidths, ensures that each mode is well-resolved. Due to construction imperfection, both the mirror transparencies and the internal absorption or photon leakage out of the cavity result in a finite photon cavity decay rate denoted κ. Another useful value is the *optical finesse*, $\mathcal{F}$, which quantifies the average number of round-trips of a photon before leaving the cavity: $\mathcal{F} \equiv \omega_n/\kappa$. Additionally, the *quality factor* is given by $\mathcal{Q}_{\text{opt}} = \omega_c \tau$ with $\tau = \kappa^{-1}$ the *photon lifetime*.

Usually, the cavity decay rate is composed of two components

$$\kappa = \kappa_{\text{ext}} + \kappa_{\text{int}}, \tag{3.1}$$

where κ_{ext} is related to the loss rate associated with the input coupling and κ_{int} to the remaining internal losses. If the external coupling κ_{ext} dominates the cavity losses then the cavity is considered *overcoupled* resulting in pump photons emerging from the cavity without being absorbed or lost via internal losses.

Since our focus lies in the light field emitted by and reflected from the cavity, it is natural to adopt the input-output formalism outlined in Chapter 2. This theory offers the advantage of modelling quantum fluctuations introduced from any coupling channel into the cavity, as well as the presence of any coherent laser drive. Thus, derived from Eq. (2.48), we obtain the following equation of motion for the field amplitude $\hat{a}$ inside the cavity:

$$\frac{d}{dt}\hat{a} = i\Delta\hat{a} - \frac{\kappa}{2}\hat{a} - \sqrt{\kappa}\hat{a}_{\text{in}}, \tag{3.2}$$

where $\hat{a}$ is the bosonic annihilation operator of the optical mode, κ is the decay rate of the cavity and $\hat{a}_{\text{in}}$ the input field. The latter should be regarded as a stochastic quantum field, typically representing the fluctuating vacuum electric field coupling to the cavity at time t along with an additional laser drive. Here, we have assumed that the cavity is coherently populated through a driving field at frequency ω_p and we have chosen a frame rotating with the drive's frequency, such that $\Delta = \omega_p - \omega_c$. Moreover, the total cavity loss rate given in Eq. (3.1) results in the following decomposition $\sqrt{\kappa}\hat{a}_{\text{in}} \to \sqrt{\kappa_{\text{int}}}\hat{f}_{\text{in}} + \sqrt{\kappa_{\text{ext}}}\hat{a}_{\text{in}}$, where the $\hat{f}_{\text{in}}$ represents the *unwanted* stochastic quantum field associated with internal cavity losses. This detrimental loss port for an optical cavity at room temperature can be approximated as a vacuum state resulting in $\langle \hat{f}_{\text{in}} \rangle = 0$.

The dynamics of $\hat{a}$ are described by Eq. (3.2), which shows its decay at a rate $\kappa/2$, but simultaneously driven by the quantum noise entering through various cavity input ports. Moreover, the Fourier transform of Eq. (3.2) yields an expression linking both the input and intracavity fields, which is known as the *cavity susceptibility*

$$\mathcal{X}_c[\omega] = \frac{1}{-i\,(\omega + \Delta) + \frac{\kappa}{2}}. \tag{3.3}$$

The susceptibility then quantifies the system's response to external drives as a function of frequency.

Leaving aside the quantum dynamics for now and focusing entirely on the classical average quantities, we find from Eq. (3.2) that the average steady state is given by

$$\langle \hat{a} \rangle = -\frac{\sqrt{\kappa_{\text{ext}}}\langle \hat{a}_{\text{in}} \rangle}{-i\Delta + \frac{\kappa}{2}}. \tag{3.4}$$

The last equation together with the input-output relation given in Eq. (2.50) allows us to introduce the *reflection amplitude* which reads

$$R \equiv \frac{\langle \hat{a}_{\text{out}} \rangle}{\langle \hat{a}_{\text{in}} \rangle} = \frac{(\kappa_{\text{int}} - \kappa_{\text{ext}})/2 - i\Delta}{(\kappa_{\text{int}} + \kappa_{\text{ext}})/2 - i\Delta}. \tag{3.5}$$

The probability of reflection from the cavity is

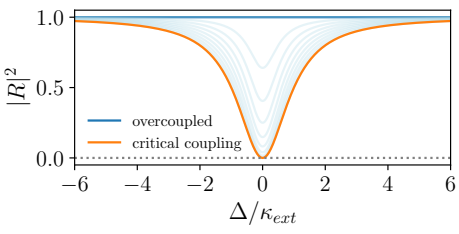

FIGURE 3.3: Reflection's probability as a function of the cavity detuning for $\kappa_{\text{int}}/\kappa_{\text{ext}} = [10^{-4}, 10]$.

then given by $|R|^2$, from which also the transmission probability can be obtained. The last expression allows us to distinguish different regimes which we show in Fig. 3.3. If the external coupling dominates the cavity losses ($\kappa_{\text{ext}} \approx \kappa \gg \kappa_{\text{int}}$) then the cavity is said to be *overcoupled* ($|R|^2 \approx 1$), which results in pumped photons emerging from the cavity without being absorbed or lost through the second mirror. If $\kappa_{\text{ext}} = \kappa_{\text{int}}$ then it is in the *critical coupling* regime, such that for $\Delta = 0$ we find $R = 0$. Hence, the input power is fully dissipated within the resonator or completely transmitted through the second mirror. Finally, *undercoupled* refers to internal losses dominating $\kappa_{\text{ext}} \ll \kappa_{\text{int}}$, which leads to an unwanted information loss.

The multiplication of Eq. (3.4) by its complex conjugate yields the number of photons circulating in the cavity

$$\bar{n}_c = |\langle \hat{a} \rangle|^2 = \frac{\kappa_{\text{ext}}}{\Delta^2 + \frac{\kappa^2}{4}} \frac{P}{\omega_p}, \tag{3.6}$$

where P is the power injected into the cavity.

One of the key advantages of optical cavities is that the thermal equilibrium bath for the field at room temperature is nearly in the vacuum state, owing to the high frequency of the optical fields. Furthermore, since the optical wavelength is approximately 1 μm, optical cavities can be fabricated within the micrometer or nanometer scales, enabling stronger optomechanical coupling strengths. Optical cavities have proven to be highly efficient for constructing detectors that operate across a wide range of intensities, from watts to single-photon levels.

3.2 Microwave resonators

As discussed before, quantum optomechanics is not exclusively limited to the optical domain, but also to the microwave domain as shown in Fig. 3.1. For optomechanical systems in this regime, the optical cavity is replaced by a microwave resonator, which can be described by LC circuits consisting of an *inductance* L and a *capacitance* C, as illustrated in Fig. 3.4. The capacitance represents the ability of a circuit element to store energy in the form of an electric field when voltage is applied across it. The inductance, on the other hand, represents the ability of a circuit element to store energy in a magnetic field when current flows through it and to generate voltage when this current changes. Thus, in an LC circuit we have two different kind of energy: electrical energy in the capacitor C and magnetic energy in the inductor L.

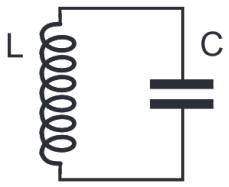

FIGURE 3.4: LC circuit with inductance L and capacitance C

Mathematically, the inductivity, L, is related the voltage, $U(t)$, and current, $I(t)$, via

$$U(t) = L\dot{I}. \tag{3.7}$$

On the other hand, the capacitor stores its energy in the electric field between two conductive plates separated by an insulating material. The charge on a capacitor, Q is given by $Q = CU$, where C is the capacitance. Taking the time derivative it yields

$$\dot{Q}(t) = I(t) = C\dot{U}(t). \tag{3.8}$$

Using Eqs. (3.7) and (3.8) with Kichhoff's laws [108] we find

$$C\ddot{U} = -\frac{1}{LU}. \tag{3.9}$$

This equation can be solved using an Ansatz of the form $A = U \sin(\omega_c t)$ yielding the resonance frequency of the resonator

$$\omega_c = \sqrt{\frac{1}{LC}}, \tag{3.10}$$

which was constructed by placing a capacitance and an inductance in parallel. In typical realization, a resonator for electromagnetic radiation can be build in the microwave regime, that is $\omega_c/2\pi \approx$ GHz.

Now, we will briefly derive the Hamiltonian of such resonators following [109–112]. From electrodynamics [108] the energy stored in the capacitor and inductor is given by

$$E_C = \frac{Q^2}{2C}, \tag{3.11}$$

$$E_L = \frac{\Phi^2}{2L}, \tag{3.12}$$

respectively. Thus, the corresponding Hamiltonian for an LC circuit is then given by

$$H_{\mathrm{LC}} = \frac{Q^2}{2C} + \frac{\Phi^2}{2L}, \tag{3.13}$$

where Q is the charge at the capacitor and Φ is the magnetic flux at the inductor.

For a quantum description of such circuits, we must perform a quantization and replace the classical variables with the corresponding quantum operators. Hence, we impose the commutation relation $[\hat{\Phi}, \hat{Q}] = i$ and express $\hat{\Phi}$ and $\hat{Q}$ using bosonic creation, $\hat{a}^\dagger$, and annihilation, $\hat{a}$, operators [109]. Thus, we do

$$\begin{aligned} \hat{\Phi} &= \Phi_{\mathrm{zpf}} \left(\hat{a} + \hat{a}^\dagger\right), \quad \Phi_{\mathrm{zpf}} \equiv \sqrt{\frac{Z_0}{2}}, \\ \hat{Q} &= iQ_{\mathrm{zpf}} \left(\hat{a}^\dagger - \hat{a}\right), \quad Q_{\mathrm{zpf}} \equiv \sqrt{\frac{1}{2Z_0}}, \end{aligned} \tag{3.14}$$

with Φ_{zpf} and Q_{zpf} the zero point fluctuations of flux and charge, respectively. In the last equation, we have also introduced the *impedance* of the circuit $Z_0 = \sqrt{L/C}$. Using these operators it is straightforward to rewrite the Hamiltonian in Eq. (3.13) resulting in

$$\hat{H} = \omega_c \left(\hat{a}^\dagger \hat{a} + \frac{1}{2}\right), \tag{3.15}$$

where the constant factor of $1/2$ is usually neglected. This equation describes the typical Hamiltonian of a harmonic oscillator whose frequency is given by Eq. (3.10). Later, we will show how the motion of a mechanical oscillator can be coupled capacitively to such LC resonators resulting in a shift of capacitance and consequently of its resonant frequency. In this way, we recover the standard radiation pressure interaction.

3.3 Mechanical resonator

Quantum mechanics offers a highly accurate description of very small physical systems. However, as they increase in size, the applicability of a quantum mechanical description has been a persistent challenge. This arises since macroscopic physical systems often have stronger damping rates and large masses, making the zero-point motion smaller. In addition, testing the *quantumness* of such mechanical systems is hindered by the difficulty of cooling them down to their ground state.

The application of a quantum theory to massive mechanical objects could explain, for instance, why quantum superposition does not seem to occur in macroscopic objects [10] or might shine a light on the long-standing challenge of the incompatibility between the quantum theory and relativity. This highlights the importance of testing quantum mechanics on macroscopic systems, but also the quest to achieve quantum control of such massive systems.

A way to reach quantum control of macroscopic mechanical systems is through their strong interaction with a second system, which can be well controlled in the quantum regime. The field of optomechanics represents an attractive scheme that could offer such a strong interaction between photons and mechanical motion.

Due to the wide variety of optomechanical systems, this interaction can be established not only in the optical but also in the microwave domain. The mechanical systems used in experiments span from the meter scale, such as in gravitational wave detectors, to the nanometer scale, including devices like single-electron transistors or SQUIDs [113]. In this work, we will discuss the interaction of a cavity with an embedded SQUID that is sensitive to magnetic fields and consequently coupled to a cantilever with an attached magnet on its tip. Such cantilever (see Fig. 3.5) was proposed in [93] and realized in [3, 94].

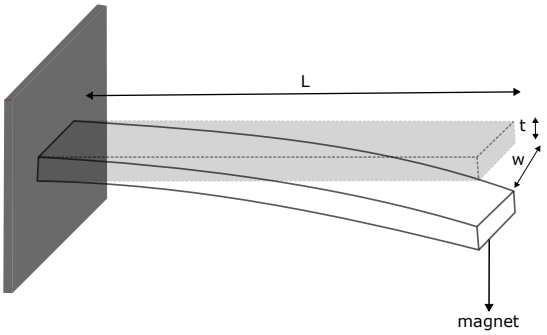

FIGURE 3.5: Illustration of a cantilever of length L, width w and thickness t. Here, a magnetic force leads to the vertical oscillation of the cantilever.

3.3.1 Cantilever

A cantilever (see Fig. 3.5) is a great example of a mechanical resonator that has been broadly studied in the literature [113]. In recent years such mechanical devices have been inductively coupled to microwave quantum circuits [94, 95, 114] to improve the resulting optomechanical coupling strength [93].

A cantilever is a beam of length L clamped solely on one side and free on the other. Depending on its material and boundary conditions, a cantilever has different torsional and bending modes [113], but we will only focus on its first. Its geometry, however, characterizes its resonance frequency given by

$$\omega_m = 1.02 \frac{t}{L^2} \sqrt{\frac{E}{\rho}}, \tag{3.16}$$

where E is the Young's modulus, ρ the material density, and t the thickness of the beam as illustrated in Fig. 3.5. Assuming negligible contributions from higher-order modes, a cantilever in the limit of small displacements can be approximated as a harmonic oscillator.

Hook's law describes the restoring force, that exerts the motion of the cantilever and is given by $F = k\Delta z$, with Δz the displacement of the tip and

$$k = \frac{Ewt^3}{4L^3} \tag{3.17}$$

is the constant that characterizes the stiffness of the beam. The motion of the cantilever-free end can be then well-approximated by the EoM of a harmonic oscillator with $\omega_m = \sqrt{k/m_{\text{eff}}}$, where the *effective mass* is defined by the material and geometric properties of the cantilever: $m_{\text{eff}} = \rho L \omega t/4$.

We are interested in the interaction of this cantilever with a magnetic field-sensitive cavity. For this, the cantilever is equipped with a magnet on the tip of its free end as depicted in Fig. 3.5. This additional weight modifies its resonance frequency

$$\tilde{\omega}_m = \omega_m \sqrt{\frac{m_{\text{eff}}}{m_{\text{eff}} + m_{\text{magnet}}}}. \tag{3.18}$$

Another important characteristic of the cantilever is its damping rate: γ_m. The quality factor of the cantilever is then given by $Q_{\text{mech}} = \tilde{\omega}_m/\gamma_m$.

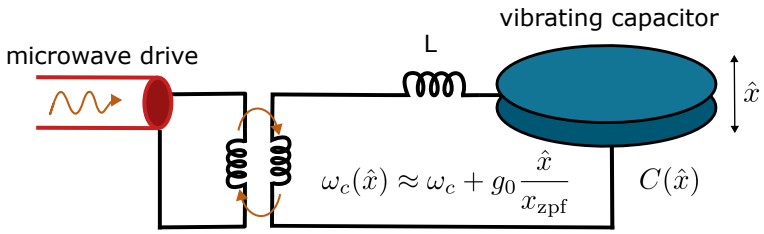

FIGURE 3.6: Microwave resonator composed by an LC circuit inductively coupled to a driven transmission line. A displacement in the vibrating capacitor modifies the circuit's resonance frequency, resulting in a dispersive interaction. A Taylor expansion of modulated resonance frequency of the LC circuit leads to the usual optomechanical interaction with $g_0 = x_{\mathrm{zpf}}\partial\omega_c/\partial\hat{x}$. Inspired by [1].

As we mentioned before, the inductive interaction between the cantilever and the cavity with a SQUID appears due to the magnetic tip at the beam's end. In this way, the motion of the cantilever changes the magnetic flux through the SQUID loop, which is converted to a voltage [115]. An alternative method to achieve optomechanical interaction in superconducting circuits is a displacement-sensitive capacitance, as illustrated in Fig. 3.6. In such experimental realizations, one plate of the capacitor is made to be a movable mechanical element, e.g. a suspended mirror. The displacement of this plate translates to a change in capacitance, resulting in a modification of the resonance frequency of the circuit. In the following, we will discuss how such parametric interaction leads to an optomechanical interaction.

Quantum regime

In this work we will focus solely on a single vibrational mode of frequency ω_m, which is valid under the assumption of a sparse mode spectrum, avoiding any spectral overlap. Similarly as Eq. (3.15), the quantum mechanical description of a mechanical resonator is characterized by the following Hamiltonian

$$\hat{\mathcal{H}} = \omega_m \left(\hat{b}^\dagger \hat{b} + \frac{1}{2}\right), \tag{3.19}$$

where the second term inside the brackets corresponds to the zero-point energy and is normally neglected. The quantity $\hat{n}_m = \hat{b}^\dagger \hat{b}$ is the phonon number operator, whose average is denoted by $\langle \hat{n}_m \rangle$. Here, we have also introduced the creation ($\hat{b}^\dagger$) and annihilation ($\hat{b}$) operators, defined as

$$\hat{q} = x_{\mathrm{zpf}} \left(\hat{b} + \hat{b}^\dagger\right), \tag{3.20}$$

$$\hat{p} = i m_{\mathrm{eff}} \omega_m x_{\mathrm{zpf}} \left(\hat{b}^\dagger - \hat{b}\right), \tag{3.21}$$

which fulfil the commutation relation $[\hat{q}, \hat{p}] = i$. Here, m_{eff} is the effective mass and

$$x_{\mathrm{zpf}} = \sqrt{\frac{1}{2 m_{\mathrm{eff}} \omega_m}} \tag{3.22}$$

represents the zero-point fluctuation amplitude. The zero-point fluctuation is the quantum uncertainty in the position (or any other observable) of a system in its ground state. For the position coordinate, if $|0\rangle$ represents the ground state, then the zero-point fluctuation is given by:

$$\langle 0|\hat{q}^2|0\rangle = x_{\mathrm{zpf}}^2. \tag{3.23}$$

Quantum control is achieved experimentally if coupling or detecting the zero-point fluctuations is possible. For instance, for a cantilever, this value ranges from 10^{-5} to 10^{-14} m.

Furthermore, to analyze the average mechanical occupation it is convenient to recall Chapter 2.2 and work within the master equation framework. If the mechanical oscillator is coupled

to a bath, its *Liouvillian* reads

$$\hat{\mathcal{L}}_m = -i\left[\hat{\mathcal{H}}, \bullet\right] + \gamma_m\left(\bar{n}_m^T + 1\right)\hat{\mathcal{D}}[\hat{b}]\bullet + \gamma_m \bar{n}_m^T \hat{\mathcal{D}}[\hat{b}^\dagger]\bullet, \tag{3.24}$$

where $\hat{\mathcal{H}}$ is the mechanical Hamiltonian in Eq. (3.19) and γ_m denotes the mechanical decay rate. There are numerous sources of mechanical dissipation which are extensively reviewed in [116, 117], for instance, viscous damping [118] and clamping losses [119, 120]. Using the last expression in Eq. (2.19) we can compute the dynamics of the average phonon number:

$$\frac{d}{dt}\langle \hat{n}_m \rangle = \mathrm{Tr}\left\{\hat{n}_m \frac{d\hat{\rho}_m}{dt}\right\} = \mathrm{Tr}\left\{\hat{n}_m \hat{\mathcal{L}}_m\right\} \tag{3.25}$$

with $\hat{\rho}_m$ the mechanical density operator and $\bar{n}_m^T$ is the average phonon number of the environment. The substitution of Eq. (3.24) into Eq. (3.25) gives us the dynamics of the average phonon number

$$\frac{d}{dt}\langle \hat{n}_m \rangle = -\gamma_m \langle \hat{n}_m \rangle + \gamma_m \bar{n}_m^T, \tag{3.26}$$

where we used that $\mathrm{Tr}\{\hat{b}^\dagger \hat{b}\,\mathcal{D}[\hat{b}]\hat{\rho}_m\} = -\langle \hat{b}^\dagger \hat{b}\rangle$ and $\mathrm{Tr}\{\hat{b}^\dagger \hat{b}\,\mathcal{D}[\hat{b}^\dagger]\hat{\rho}_m\} = \langle \hat{b}^\dagger \hat{b}\rangle + 1$. If the oscillator is initially in the ground state then we find $\langle \hat{n}_m \rangle(t) = \bar{n}_m^T(1 - e^{-t/\gamma})$. Moreover, the rate at which the oscillator heats from the ground state ($t = 0$) is called the *thermal decoherence rate* and is given by

$$\frac{d}{dt}\langle \hat{n}_m(0) \rangle = \gamma_m \bar{n}_m^T \approx \frac{k_\mathrm{B} T}{\mathcal{Q}_m}, \tag{3.27}$$

with k_B, T and $\mathcal{Q}_m = \omega_m/\gamma_m$ the Boltzmann constant, the bath's temperature and the mechanical quality factor, respectively. For high temperature, we find from the last expression that the bath's temperature becomes a function of the oscillator's frequency: $\bar{n}_m^T \approx k_\mathrm{B} T/\omega_m$.

3.3.2 Quantum noise spectra

In addition to oscillating at its eigenfrequencies, the motion of a harmonic oscillator in thermal equilibrium is also influenced by damping and fluctuating thermal forces, leading to variations in amplitude and phase. The relation between damping and noise was already pointed out in 1905 by Einstein while studying Brownian motion [121]. For stationary noise, the analysis of the fluctuations is typically performed in the frequency domain. For instance, let $I(t)$ be a Gaussian random variable with zero mean, then its Fourier transform is defined as

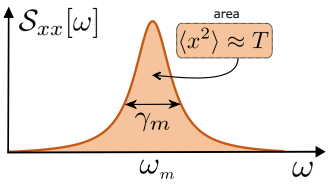

FIGURE 3.7: Power spectrum density of a damped harmonic oscillator, indicating the relation of the area with the variance, which for weak damping is set by the equipartition theorem $\langle x^2 \rangle \approx k_\mathrm{B} T/m_\mathrm{eff}\omega_m^2$.

$$I[\omega] = \frac{1}{\sqrt{T}} \int_{-T/2}^{T/2} dt\, e^{i\omega t} I(t), \tag{3.28}$$

where T is the interval of integration and the prefactor ensures a well-defined limiting value.

To measure the amount of noise at a given frequency, one introduces the so-called *spectral density of the noise* or simply *power spectrum* defined as

$$S_{II}[\omega] \equiv \lim_{T\to\infty} \left\langle |I[\omega]|^2 \right\rangle = \lim_{T\to\infty} \langle I[\omega] I[-\omega] \rangle\,. \tag{3.29}$$

In addition, the Wiener-Khinchin theorem relates this power spectrum to the Fourier transform of the autocorrelation function [122]

$$S_{II}[\omega] = \int_{-\infty}^{\infty} dt e^{i\omega t} \langle I(t) I(0) \rangle. \tag{3.30}$$

These last two equations indicate that the area under the noise spectrum yields the variance of the measured variable. As illustrated in Fig. 3.7, for the analysis of mechanical displacement this would read

$$\int_{-\infty}^{\infty} \frac{d\omega}{2\pi} S_{xx}[\omega] = \langle x^2 \rangle. \tag{3.31}$$

Classically the dynamics of a noise quantity, I, usually involves its spectral density $S_{II}[\omega]$ given in Eq. (3.30), which gives the intensity of the noise at a given frequency. Analogously, the analysis of quantum noise is connected to the study of the quantum noise spectral densities, which look like the classical case

$$S[\omega] = \int_{-\infty}^{\infty} dt e^{i\omega t} \langle x(t)x(0) \rangle \quad \underbrace{\longrightarrow}_{\text{quantum}} \quad \mathcal{S}[\omega] = \int_{-\infty}^{\infty} dt e^{i\omega t} \langle \hat{q}(t)\hat{q}(0) \rangle. \tag{3.32}$$

In this way, the quantum description of the noise spectra exchanges the classical variable, $x(t)$, by a quantum operator, $\hat{q}(t)$, whose noise we are interested in, and where the average is obtained using the quantum density operator (see Chapter 2.1).

However, the seemingly straightforward translation of exchanging classical variables by quantum operators leads to important differences. As a simple illustration, we will consider the case of a harmonic oscillator with mass m and frequency Ω, which is in contact with a reservoir at temperature T. In the classical case, we find

$$x(t) = x(0)\cos(\Omega t) + \frac{p(0)}{m\Omega}\sin(\Omega t) \quad \longrightarrow \quad G_{xx}(t) = \langle x(t)x(0) \rangle = \frac{k_{\mathrm{B}}T}{m\Omega^2}\cos(\Omega t), \tag{3.33}$$

where $G_{xx}(t)$ is the *autocorrelation function*. To obtain the last result, we use the *equipartition theorem* [123] and $\langle x(0)p(0) \rangle = 0$. Conversely, in the quantum case, the canonical commutation relation between the position and momentum operators applies leading to a complex autocorrelation function

$$G_{xx}(t) = x_{\mathrm{zpf}}^2 \left[\bar{n}^T e^{i\Omega t} + \left(\bar{n}^T + 1 \right) e^{-i\Omega t} \right] \tag{3.34}$$

with x_{zpf} defined in Eq. (3.22). Since the quantum autocorrelation function in Eq. (3.34) is complex the spectral density is not symmetric in frequency, i.e.

$$\mathcal{S}_{xx}[\omega] = 2\pi x_{\mathrm{zpf}}^2 \left[\bar{n}^T \delta[\omega + \Omega] + \left(\bar{n}^T + 1 \right) \delta[\omega - \Omega] \right]. \tag{3.35}$$

A classical noise spectral density, being real-valued, is symmetric in frequency, in contrast to its quantum counterpart, which exhibits asymmetry due to the fundamental differences in how noise behaves at the quantum level. Nevertheless, in the high-temperature limit, where $k_{\mathrm{B}}T \gg \Omega$ and therefore $\bar{n}^T \approx \bar{n}^T + 1$, $\mathcal{S}_{xx}[\omega]$ becomes symmetric as in the classical regime. The Bose-Einstein factors allow us to understand this asymmetry: the positive part is related to the stimulated emission of energy into the oscillator, whereas the negative-frequency part is linked to the ability of the oscillator to emit energy. Thus, the frequency-asymmetry of the quantum noise spectra gives us the magnitude of the *Fermi golden rule* transition rates for emission and absorption. This expression also shows that at zero temperature, emission events are not possible. The latter becomes particularly important if we consider the noise source as a force $\hat{F}$ that is weakly coupled to a harmonic oscillator, as we will see below.

Let us consider a quantum harmonic oscillator coupled to a noise source, where the Hamiltonian describing such interaction is given by

$$\hat{H}_{\mathrm{int}} = -\hat{q}\hat{F} \tag{3.36}$$

with $\hat{q}$ the position operator given in Eq. (3.20) and $\hat{F}$ the operator describing the fluctuating noise. Using the master equation framework (see Chapter 2), it can be shown that the equation for the average energy $\langle E \rangle$ of the oscillator (see [122, 123]) reads

$$\frac{d}{dt}\langle E \rangle = -\gamma \langle E \rangle + \frac{\bar{\mathcal{S}}_{FF}[\Omega]}{2m} \tag{3.37}$$

with the force spectral density

$$\mathcal{S}_{FF}[\omega] = \int_{-\infty}^{\infty} \frac{d\omega'}{2\pi} \langle \hat{F}[\omega]\hat{F}[\omega'] \rangle. \tag{3.38}$$

Here, we defined the symmetrized noise spectra

$$\bar{\mathcal{S}}_{FF}[\Omega] \equiv x_{\mathrm{zpf}}^2 \left(\mathcal{S}_{FF}[\Omega] + \mathcal{S}_{FF}[-\Omega] \right) \tag{3.39}$$

which, as a classical noise spectrum, heats the oscillator. On the other hand,

$$\gamma = x_{\mathrm{zpf}}^2 \left(\mathcal{S}_{FF}[\Omega] - \mathcal{S}_{FF}[-\Omega] \right) \tag{3.40}$$

is directly related to the damping rate. Due to the asymmetry of the noise spectral density, such that the imbalance between the absorption and emission rates results in a net energy exchange between the oscillator and the noise source.

From the definitions (3.39) and (3.40), we can derive the quantum version of the *fluctuation-dissipation theorem* (FDT) [124, 125]:

$$\bar{\mathcal{S}}_{FF}[\Omega] = m\gamma[\Omega]\Omega \coth\left(\frac{\Omega}{2k_{\mathrm{B}}T} \right) = m\gamma[\Omega]\Omega \left(1 + 2\bar{n}^T[\Omega] \right), \tag{3.41}$$

which for $k_{\mathrm{B}}T \gg \Omega$ yields the classical limit $\bar{\mathcal{S}}_{FF}[\Omega] = 2m\gamma k_{\mathrm{B}}T$. Furthermore, in thermal equilibrium, the FDT can also be expressed in terms of the susceptibility (3.3)

$$\mathcal{S}_{FF}[\omega] = \frac{2k_{\mathrm{B}}T}{\omega} \mathrm{Im}\left\{ \mathcal{X}_{\mathrm{FF}}[\omega] \right\}, \tag{3.42}$$

where $\mathcal{X}_{\mathrm{FF}}[\omega]$ denotes the susceptibility.

Using the last expression, we can also define an effective temperature denoted $T_{\mathrm{eff}}[\Omega]$ given by

$$k_{\mathrm{B}}T_{\mathrm{eff}}[\Omega] \equiv \Omega \left[\ln\left(\frac{\mathcal{S}_{FF}[\Omega]}{\mathcal{S}_{FF}[-\Omega]} \right) \right]^{-1}, \tag{3.43}$$

such that for non-equilibrium systems $\mathcal{S}_{FF}[\Omega]$ will be frequency dependent. For a system with a very high-quality factor, only the noise at $\pm\Omega$ is significant. This will be particularly important later on when discussing backaction cooling techniques.

3.4 Hamiltonian formulation

The exchange of momentum between the cavity and mechanical modes is a fundamental aspect of radiation pressure interaction. In quantum optomechanics, the parametric interaction between the optical cavity or microwave resonator and mechanical motion arises from the transfer of momentum carried by photons. One of the simplest examples of radiation-pressure interaction is the momentum transfer through the reflection of photons in a Fabry-Pérot cavity. A single intracavity photon transfers the momentum $|\Delta p| = 2h/\lambda$, with λ the photon wavelength, and consequently the *radiation pressure force* reads

$$\langle \hat{F} \rangle = G_0 \langle \hat{a}^\dagger \hat{a} \rangle, \quad G_0 = \frac{\omega}{L}. \tag{3.44}$$

This represents the radiation pressure force caused by a single intracavity photon, where G_0 describes the modification of the cavity resonance frequency with position. Let us now consider a Fabry-Pérot cavity of length L, where one of the mirrors is movable and connected to a mechanical oscillator. If the mechanical oscillator undergoes a displacement q, it causes a corresponding shift in the cavity's length: $L(q) = L - q$. Thus, the cavity optical modes are given as a function of this displacement as

$$\lambda_n(q) = \frac{2L(q)}{n} = \frac{2(L-q)}{n}$$

where n is the mode number. The corresponding mode frequencies are given by

$$\omega_n(q) = \frac{2\pi c}{\lambda_n} = \frac{\pi c n}{L-q} \sim \omega_n(0)(1+\frac{q}{L}), \tag{3.45}$$

where c is the speed of light, $\omega_n(0)$ is the optical resonance frequency of the cavity and is valid only if $q \ll L$. Note that to first order the displacement of the mechanical oscillator induces a linear shift of the optical resonance frequency.

In this work, we will restrict our attention to the optical mode closest to resonance with the driving laser and consider a single mode of the mechanical resonator. The uncoupled optical and mechanical system is described by the Hamiltonian of two harmonic oscillators

$$\hat{H}_0 = \omega_c\, \hat{a}^\dagger \hat{a} + \omega_m \hat{b}^\dagger \hat{b}, \tag{3.46}$$

with $\hat{a}$ ($\hat{a}^\dagger$) and $\hat{b}$ ($\hat{b}^\dagger$) the cavity and mechanical annihilation (creation) operators, respectively. Here, the resonance frequencies are given by ω_c for the cavity and ω_m for the mechanical oscillator.

In a Fabry-Pérot cavity, the parametric interaction between the optical and mechanical modes originates from the radiation pressure force displacing the end and movable cavity mirror. Thus, the mechanical motion modulates the cavity resonance frequency. As mentioned before, since the cavity has a movable end mirror, the coupling of both, optical and mechanical, systems is parametric, because the mechanical amplitude modulates the cavity resonance frequency (3.45). For this introductory section, we will assume weak coupling, such that it is sufficient to consider up to the linear order to obtain

$$\omega_c(q) \approx \omega_c + G_0 q + \mathcal{O}(q^2), \tag{3.47}$$

with the optical frequency shift per displacement given by $G_0 = \partial\omega_c/\partial q$.

Hence, for the uncoupled system, from Eqs. (3.46) and (3.47), we find

$$\begin{aligned} \hat{H} &= (\omega_c + G_0 \hat{q})\, \hat{a}^\dagger \hat{a} + \omega_m \hat{b}^\dagger \hat{b} \\ &= \omega_c \hat{a}^\dagger \hat{a} + \omega_m \hat{b}^\dagger \hat{b} + g_0 \hat{a}^\dagger \hat{a} \left(\hat{b} + \hat{b}^\dagger\right), \end{aligned} \tag{3.48}$$

where we have defined the *vacuum optomechanical coupling rate*

$$g_0 = G_0 x_{\mathrm{zpf}}. \tag{3.49}$$

From the last equation into Eq. (3.44) we find that the radiation pressure force is given by

$$\hat{F} = \frac{g_0}{x_{\mathrm{zpf}}} \hat{a}^\dagger \hat{a}. \tag{3.50}$$

The vacuum optomechanical coupling strength, g_0, is central in the study of such systems. From Eq. (3.20), it can be interpreted as the optical frequency shift induced by the mechanical displacement, equal to the mechanical zero-point fluctuation. In essence, it quantifies the interaction between single photons and phonons. Conversely, the radiation pressure force from intracavity photons impinging on the end and movable cavity mirror displaces the mechanical oscillator. Moreover, the last term in Eq. (3.48) indicates the nonlinear nature of the optomechanical Hamiltonian [86, 126]. A detailed analysis of this aspect will be reserved for the upcoming chapters.

3.4.1 Coherent Enhancement

Given that the coupling rate g_0 is typically much smaller than the optical decay rate, an external drive is necessary to enhance the interaction and yield observable effects. Hence, the Hamiltonian description of a coherent drive coupled to the optomechanical system (3.48) is given by

$$\hat{\mathcal{H}}_{\mathrm{d}} = -i\sqrt{\kappa_{\mathrm{ext}}} \left(\alpha_{\mathrm{in}} e^{-i\omega_p t} \hat{a}^\dagger + \alpha_{\mathrm{in}}^* e^{i\omega_p t} \hat{a}\right), \tag{3.51}$$

where ω_p and $\alpha_{\rm in}$ are the drive frequency and classical driving amplitude, respectively. Consequently, from Eq. (3.48), the driven optomechanical Hamiltonian becomes

$$\hat{\mathcal{H}} = \omega_c \hat{a}^\dagger \hat{a} + \omega_m \hat{b}^\dagger \hat{b} + g_0 \hat{a}^\dagger \hat{a} \left(\hat{b} + \hat{b}^\dagger\right) + \hat{\mathcal{H}}_{\rm d}. \tag{3.52}$$

Typically, the optical cavity's resonance frequency, ω_c, is larger compared with all other system parameters. For this reason, it is convenient to change to a description in the frame rotating with the laser frequency ω_L. For this we use the *Baker-Hausdorff formula* [127] given by

$$e^{\hat{A}} \hat{B} e^{-\hat{A}} = \sum_{n=0}^{\infty} \frac{1}{n!} \left[{}^n\hat{A}, \hat{B}\right], \quad \left[{}^n\hat{A}, \hat{B}\right] \equiv \underbrace{\left[\hat{A}, \ldots \left[\hat{A}, \left[\hat{A}, \hat{B}\right]\right] \ldots\right]}_{\text{n-times}} \tag{3.53}$$

which leads us to

$$\hat{\mathcal{H}} = \hat{U}^\dagger \hat{H} \hat{U} - \hat{A}, \tag{3.54}$$

with $\hat{A} = \omega_p \hat{a}^\dagger \hat{a}$, $\hat{U} = e^{-i\hat{A}t}$ and $\hat{\mathcal{H}}$ given by Eq. (3.52). Finally, the corresponding driven optomechanical Hamiltonian in a frame rotating with the drive frequency reads

$$\hat{\mathcal{H}} = -\Delta \hat{a}^\dagger \hat{a} + \omega_m \hat{b}^\dagger \hat{b} + g_0 \hat{a}^\dagger \hat{a} \left(\hat{b} + \hat{b}^\dagger\right) - i\sqrt{\kappa_{\rm ext}} \left(\alpha_{\rm in} \hat{a}^\dagger + \alpha_{\rm in}^* \hat{a}\right) \tag{3.55}$$

with the detuning $\Delta = \omega_p - \omega_c$. In addition, the unitary transformation also makes the driving terms time-independent. Usually, the last term associated with the drive is ignored in the analysis of the system's dynamics since it leads to constant terms.

3.4.2 Equations of motion

In this section, we will derive the dynamics of a dispersive optomechanical system using the input-output formalism as discussed in Chapter 2. First, let us introduce the mechanical position and momentum oeprators

$$\hat{q} = \frac{\hat{b} + \hat{b}^\dagger}{\sqrt{2}}, \qquad \hat{p} = \frac{i(\hat{b}^\dagger - \hat{b})}{\sqrt{2}} \tag{3.56}$$

respectively. Using the Hamiltonian in Eq. (3.55) we find that the system's dynamics are given by

$$\frac{d}{dt}\hat{a} = \left(i\left[\Delta - \sqrt{2} g_0 \hat{q}\right] - \frac{\kappa}{2}\right) \hat{a} - \sqrt{\kappa}\hat{a}_{\rm in} - \sqrt{\kappa_{\rm ext}}\alpha_{\rm in}, \tag{3.57}$$

for the cavity. Here, the input field $\hat{a}_{\rm in}$, is stochastic and represents the input noise associated with external noise, the coherent drive or even intrinsic losses. In terms of the oscillator's operators given in Eq. (3.56), the dynamics of the mechanical mode read

$$\frac{d}{dt}\hat{q} = \omega_m \hat{p} - \frac{\gamma_m}{2}\hat{q} - \sqrt{\gamma_m}\hat{q}_{\rm in}, \tag{3.58}$$

$$\frac{d}{dt}\hat{p} = -\omega_m \hat{q} - \frac{\gamma_m}{2}\hat{p} - \sqrt{2} g_0 \hat{a}^\dagger \hat{a} - \sqrt{\gamma_m}\hat{p}_{\rm in}, \tag{3.59}$$

where we have also introduced the mechanical decay rate γ_m. The vacuum noise operator $\hat{a}_{\rm in}$ satisfies

$$\begin{aligned} \langle \hat{a}_{\rm in}(t) \hat{a}_{\rm in}^\dagger(t') \rangle &= \delta(t - t'), \\ \langle \hat{a}_{\rm in}^\dagger(t) \hat{a}_{\rm in}(t') \rangle &= 0. \end{aligned} \tag{3.60}$$

Here, we assumed that the cavity field has zero thermal occupation ($k_{\rm B}T/\hbar\omega_c \approx 0$), valid for optical fields at room temperatures. However, this approximation might only be valid for microwave fields if the setup is sufficiently cooled down. Analogously, the noise operator $\hat{b}_{\rm in}$

describes coupling to a Markovian reservoir at temperature T, as represented by the following correlators

$$\begin{aligned}\langle \hat{b}_{\rm in}(t)\hat{b}^{\dagger}_{\rm in}(t')\rangle &= (\bar{n}^{T}_{m}+1)\delta(t-t')\\ \langle \hat{b}^{\dagger}_{\rm in}(t)\hat{b}_{\rm in}(t')\rangle &= \bar{n}^{T}_{m}\delta(t-t').\end{aligned} \tag{3.61}$$

Furthermore, in the absence of any other coupling, the bath leads to the emergence of a thermal state, characterized by a mean occupation number $\bar{n}^{T}_{m} = [\exp\{\hbar\omega_m/k_BT\}-1]^{-1}$ for the mechanical oscillator. This means that the mechanical mode is coupled to a hot bath, whose average number of quanta is described by the Boltzmann distribution and is generally $\bar{n}^{T}_{m} \gg 1$. The noise correlators given above with Eqs. (3.57) and (3.59) describe the evolution of the cavity and mechanical mode.

In Eq. (3.57) it can be observed that the optomechanical interaction results in a modification of the cavity detuning, whereas in Eq. (3.59) the interaction leads to a radiation pressure force acting on the mechanical oscillator. However, note that these equations form a nonlinear system of quantum differential equations, which typically cannot be solved analytically.

However, for sufficiently large intracavity photon number and phonon number, it is useful to analyze the classical average of these equations within the *semiclassical* limit: $\alpha(t) = \langle \hat{a}(t)\rangle$ and $q(t) = \langle \hat{q}(t)\rangle$. Hence, from Eqs. (3.57-3.59) the classical differential equations of motion read:

$$\frac{d}{dt}\alpha = \left(i\Delta - \frac{\kappa}{2}\right)\alpha - i\sqrt{2}g_0 q\alpha - \sqrt{\kappa_{\rm ext}}\alpha_{\rm in}, \tag{3.62}$$

and

$$\begin{aligned}\frac{d}{dt}q &= \omega_m p - \frac{\gamma_m}{2}q,\\ \frac{d}{dt}p &= -\omega_m q - \frac{\gamma_m}{2}p - \sqrt{2}g_0|\alpha|^2,\end{aligned} \tag{3.63}$$

respectively. Since the oscillation of the mechanical position is small enough to weakly modulate the cavity field, we solve Eq. (3.63) in the long time limit and find the steady state of the mechanical position operator

$$\hat{q}_{\rm st} = -\frac{\sqrt{2}g_0\omega_m|\alpha|^2}{\omega_m^2 + \frac{\gamma_m^2}{4}}, \tag{3.64}$$

which we insert into the equation for the classical cavity amplitude given by Eq. (3.62) and obtain

$$\frac{d}{dt}\alpha = \left(i\Delta - \frac{\kappa}{2}\right)\alpha + i\mathcal{K}_{\rm m}\alpha|\alpha|^2 - \sqrt{\kappa_{\rm ext}}\alpha_{\rm in}, \tag{3.65}$$

where $\mathcal{K}_{\rm m}$ is an optomechanically-induced nonlinearity which we will denote *mechanical Kerr* nonlinearity [128] and is given by

$$\mathcal{K}_{\rm m} = \frac{2g_0^2\omega_m}{\omega_m^2 + \frac{\gamma_m^2}{4}}. \tag{3.66}$$

The multiplication of the steady state solution of Eq. (3.65) with its complex conjugate yields ultimately the average cavity photon number

$$\bar{n}_c\left[(\Delta + \mathcal{K}_{\rm m}\bar{n}_c)^2 + \left(\frac{\kappa}{2}\right)^2\right] = \kappa_{\rm ext}\bar{n}_{\rm in} \tag{3.67}$$

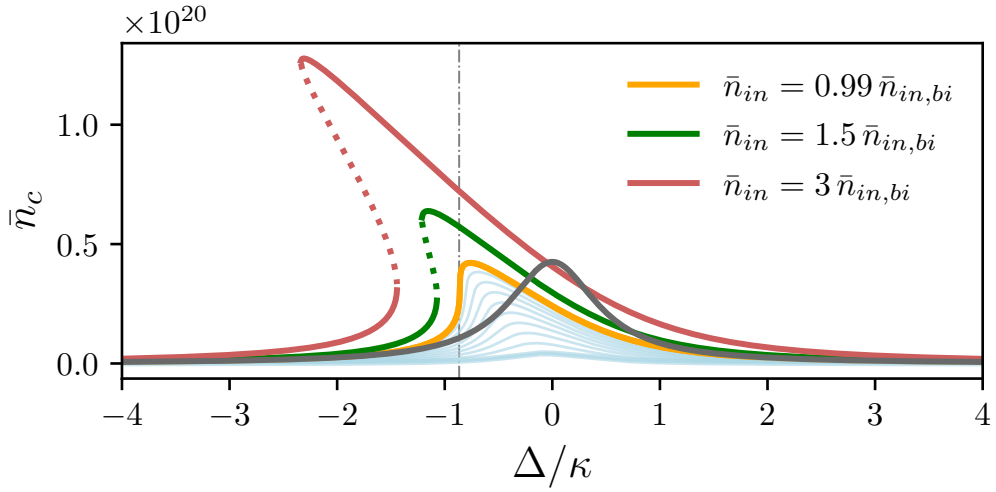

FIGURE 3.8: Intracavity photon number as a function of the optical detuning for increasing drive strength. Blue lines show the number of photons for a driving strength approaching the critical value $\bar{n}_{\mathrm{in}} = \bar{n}_{\mathrm{in,bi}}$. The orange line shows the result obtained slightly before the critical input power: $\bar{n}_{\mathrm{in}} = 0.99\bar{n}_{\mathrm{in,bi}}$. Above this value, the system becomes bistable, where the middle solution (dotted lines) is unstable and typically neglected. The vertical dashed line shows the position of the critical detuning Δ_{bi}, where the slope of the curve reaches a maximum. The grey line results from assuming a Lorentzian distribution, regardless of the optomechanical interaction, which is commonly assumed for weak input power $\bar{n}_{\mathrm{in}} \ll \bar{n}_{\mathrm{in,bi}}$. For this plots $g_0/2\pi = 1.7$ kHz, $\omega_m/\kappa = 0.1$, $\gamma_m/2\pi = 0.5$ Hz and $\kappa/2\pi = 3$ MHz. These parameters are similar to those used in [3].

with $\bar{n}_{\mathrm{in}} = |\alpha_{\mathrm{in}}|^2$. The possible values of the intracavity photon number can be explicitly calculated yielding

$$|\alpha|_1^2 = \frac{1}{3\mathcal{K}_{\mathrm{m}}}\left\{-2\Delta - \Sigma + \frac{\Lambda_0}{\Sigma}\right\}, \tag{3.68}$$

$$|\alpha|_{2,3}^2 = \frac{1}{3\mathcal{K}_{\mathrm{m}}}\left\{-2\Delta + e^{\mp i\frac{\pi}{3}}\Sigma - e^{\pm i\frac{\pi}{3}}\frac{\Lambda_0}{\Sigma}\right\} \tag{3.69}$$

where we introduced the following definitions $\Sigma = \sqrt[3]{\sqrt{\Lambda_0^3 + \Lambda_1^2} + \Lambda_1}$ with $\Lambda_0 = \frac{3\kappa^2}{4} - \Delta^2$ and $\Lambda_1 = -\left(\frac{9\kappa^2}{4} + \Delta^2\right)\Delta - \frac{27}{2}\kappa\mathcal{K}_{\mathrm{m}}\bar{n}_{\mathrm{in}}$. The bifurcation line in the drive and detuning parameter space that delineates between the single solution and bistable solution regions occur where the first derivative with respect to $\bar{n}_c$ diverges:

$$(\Delta + \mathcal{K}_{\mathrm{m}}\bar{n}_c)^2 + \left(\frac{\kappa}{2}\right)^2 + 2\mathcal{K}_{\mathrm{eff}}\left(\Delta + \mathcal{K}_{\mathrm{m}}\bar{n}_c\right)\bar{n}_c = 0. \tag{3.70}$$

If we further impose the condition that the transition between the two regions is continuous, we get

$$2\mathcal{K}_{\mathrm{m}}^2\bar{n}_c + 4\mathcal{K}_{\mathrm{m}}\left(\Delta + \mathcal{K}_{\mathrm{m}}\bar{n}_c\right) = 0, \tag{3.71}$$

such that the imposition of the last two conditions yields

$$\Delta_{\mathrm{bi}} = -\frac{\sqrt{3}\kappa}{2}, \quad \bar{n}_{\mathrm{bi}} = \frac{\kappa}{\sqrt{3}\mathcal{K}_{\mathrm{m}}}, \tag{3.72}$$

which correspond to the universal values at bifurcation. Upon substituting the aforementioned relations into Eq. (3.67), the critical drive amplitude $\bar{n}_{\mathrm{in,bi}}$ at which bifurcation occurs can

be obtained:

$$\bar{n}_{\mathrm{in,bi}} = \frac{\kappa^2}{3\sqrt{3}\mathcal{K}_{\mathrm{m}}}. \tag{3.73}$$

The average number of photons circulating in the cavity is described by Eq. (3.67) and illustrated in Fig. 3.8. Here, we show the cavity's behaviour at different drive strengths. For weak driving, a single real solution exists as depicted by the light-blue lines. However, for stronger drive power ($\bar{n}_{\mathrm{in}} > \bar{n}_{\mathrm{in,bi}}$) a bifurcation occurs and a regime of bistability arises, where two stable states appear within a certain range of detunings. Conversely, for drive amplitudes slightly below the critical driving threshold, given by Eq. (3.73), the average photon number exhibits a single-valued solution with respect to the cavity detuning, with a significant gradient at Δ_{bi}, as represented by Eq. (3.72) and illustrated in Fig. 3.8 by the blue-dashed vertical line.

The cubic equation for the intracavity photon number, given in Eq. (3.67), highlights the intrinsic nonlinearity of the optomechanical interaction. Nevertheless, for a high-Q oscillator, the strength of the nonlinearity given in Eq. (3.66) can be approximated by $\mathcal{K}_m \approx 2g_0^2/\omega_m$ which is typically small. Consequently, entering the bistable regime generally requires either very strong input power or a significant optomechanical coupling strength. Later, we will show that this effect resembles intrinsic nonlinear optical behaviour, such as the Kerr effect.

In the next section, we will study how, when the coherent driving field is strong enough, the system's dynamics can be effectively described by *linearizing* around the semi-classical steady-state solution. As we will see, this approach captures small quantum fluctuations of the system around the classical steady-state, offering a simplified yet accurate description under appropriate conditions.

3.4.3 Displacement transformation

As discussed in Sec. 3.4.1, the optomechanical coupling strength, g_0, is typically significantly smaller than the decay rate of the cavity. Therefore, coherent driving is necessary to enhance the radiation pressure interaction yielding Eq. (3.52). We will now introduce the *linearized* approximation of cavity optomechanics in which the cavity field is split into an average coherent amplitude given by the semiclassical solution $\langle\hat{a}\rangle = \alpha$ and a fluctuating term:

$$\hat{a} = \alpha + \hat{d}. \tag{3.74}$$

The reason behind this approximation originates from the fact that due to the cavity driving, the cavity reaches an average value for the cavity field operator $\hat{a}$. In addition, since the average photon number is a static force acting on the mechanical oscillator, its equilibrium position through the radiation pressure interaction is also displaced. Consequently, a displacement transformation is useful to separate the dynamics of the classical mean values from the fluctuations around them. These fluctuations arise through the noise operators $\hat{a}_{\mathrm{in}}$ and $\hat{b}_{\mathrm{in}}$, which include both classical and quantum noise driving the system. In this way, the operator $\hat{d}$ is *designed* to capture only the fluctuations around the classical mean value α. Since these fluctuations are random, their average value is zero, i.e. $\langle\hat{d}\rangle = 0$.

Using Eq. (3.74), the interaction Hamiltonian $\hat{\mathcal{H}}_{\mathrm{int}} = g_0\hat{a}^\dagger\hat{a}\left(\hat{b}+\hat{b}^\dagger\right)$ becomes

$$\hat{H}_{\mathrm{int}} = \underbrace{g_0|\alpha|^2(\hat{b}^\dagger+\hat{b})}_{\bar{F}=G|\alpha|^2} + g_0(\alpha^*\hat{d}+\alpha\hat{d}^\dagger)(\hat{b}^\dagger+\hat{b}) + \underbrace{g_0\hat{d}^\dagger\hat{d}\,(\hat{b}^\dagger+\hat{b})}_{\text{smaller by a factor of }|\alpha|}. \tag{3.75}$$

The first term on the right implies the presence of an average radiation pressure force $\bar{F} = \hbar G|\alpha|^2$, which can be omitted after implementing an appropriate shift of the displacement's origin $\delta\bar{q} = \bar{F}/m_{\mathrm{eff}}\omega_m^2$. The second-order nonlinear term is a *quadrature-to-quadrature* interaction between the quadratures of the optical amplitude and the mechanical dimensionless displacement, which is enhanced by the coherent amplitude of the cavity field. The last term, on the other hand, keeps the third-order nonlinearity, but it is not amplified by the coherent amplitude, thereby it is smaller by a factor of α and can be omitted. Hence, from

this observation, we find that the linearized optomechanical Hamiltonian reads[1]

$$\hat{H}_{\text{lin}} = -\Delta\hat{d}^\dagger\hat{d} + \omega_m\hat{b}^\dagger\hat{b} + G\left(\hat{d}+\hat{d}^\dagger\right)\left(\hat{b}+\hat{b}^\dagger\right) \tag{3.76}$$

where the first two terms represent the free Hamiltonian. Here, we also introduced

$$G = g_0\sqrt{\bar{n}_{\text{c}}}, \tag{3.77}$$

often known as the *linearized optomechanical coupling strength* or the *multiphoton optomechanical coupling strength* with $\bar{n}_c \in \mathbb{R}$ given by Eq. (3.67) and where we assumed without loss of generality that $\alpha = \sqrt{\bar{n}_{\text{c}}} \in \mathbb{R}$. Note that, the explicit solutions for $\bar{n}_c$ in Eqs. (3.68) and (3.69) suggest that if the input power is set according to the critical value in Eq. (3.73), the multiphoton coupling strength G becomes independent of g_0.

Alternatively, the derivation yielding Eq. (3.76) can be done more rigorously using the master equation formalism. Recalling Chapter 2, we will consider the cavity as a reservoir responsible for inducing both heating and cooling processes in the mechanical mode, specifically referred to as Stokes and anti-Stokes processes, respectively. The master equation reads

$$\frac{d}{dt}\hat{\rho} = -i\left[\hat{\mathcal{H}},\hat{\rho}\right] + \kappa\hat{\mathcal{D}}\left[\hat{a}\right]\hat{\rho} + \gamma_m\left(\bar{n}_m^T+1\right)\hat{\mathcal{D}}\left[\hat{b}\right]\hat{\rho} + \gamma_m\bar{n}_m^T\hat{\mathcal{D}}\left[\hat{b}^\dagger\right]\hat{\rho}, \tag{3.78}$$

where $\hat{\rho} \in \mathcal{H}_c \otimes \mathcal{H}_m$ is the density operator of the composite system with $\mathcal{H}_{c(m)}$ the Hilbert space of the optical(mechanical) mode, $\hat{\mathcal{H}}$ is the Hamiltonian in Eq. (3.55) and $\hat{\mathcal{D}}[\hat{o}]\bullet$ as in Eq. (2.35).

To study both classical and quantum dynamics we introduce the displacement operator $\hat{\mathcal{D}}(\eta) = \exp\left(\eta\hat{o}^\dagger - \eta^*\hat{o}\right)$ with $\eta = \langle\hat{o}\rangle$ an average amplitude and $\hat{o}$ the fluctuations around it [127], which allows transforming the dynamics given by Eq. (3.55) to a displaced frame of the optical and mechanical mode. For the optical mode, for example, we have $\hat{\mathcal{D}}^\dagger(\alpha)\hat{\mathcal{D}}(\alpha) = \hat{\mathcal{D}}(-\alpha)\hat{\mathcal{D}}(\alpha) = 1$. Furthermore, recalling the Baker-Hausdorff Eq. (3.53) and noting that $\left[\alpha^*\hat{a} - \alpha\hat{a}^\dagger, \hat{a}\right] = \alpha$ we find the action of the displacement operator:

$$\hat{\mathcal{D}}^\dagger(\alpha)\hat{a}\hat{\mathcal{D}}(\alpha) = \alpha + \hat{d} \tag{3.79}$$

Here, the amplitude α is time-dependent and $\hat{d}$ describes solely the vacuum fluctuations as in Eq. (3.74). Similarly, we introduce the displacement operator for the mechanical $\hat{\mathcal{D}}^\dagger(\beta)$, whose action yields $\hat{\mathcal{D}}^\dagger(\beta)\hat{b}\hat{\mathcal{D}}(\beta) = \beta + \hat{b}$, with the time-dependent classical amplitude $\beta = \beta(t)$ and where, for simplicity, we kept the operator $\hat{b}$ to describe the fluctuations in the mechanics.

We proceed transforming Eq. (3.78) to a displaced frame by doing $\hat{\rho} \to \hat{\rho}' = \hat{P}\hat{\rho}\hat{P}^\dagger$ with the unitary $\hat{P}(t) = \hat{\mathcal{D}}^\dagger(\alpha)\hat{\mathcal{D}}^\dagger(\beta)$ which results in

$$\frac{d}{dt}\hat{\rho}' = -i\left[\hat{\mathcal{H}}',\hat{\rho}'\right] + \kappa\hat{\mathcal{D}}\left[\alpha+\hat{d}\right]\hat{\rho}' + \gamma_m\left(\bar{n}_m^T+1\right)\hat{\mathcal{D}}\left[\beta+\hat{b}\right]\hat{\rho}' + \gamma_m\bar{n}_m^T\hat{\mathcal{D}}\left[\beta^*+\hat{b}^\dagger\right]\hat{\rho}'. \tag{3.80}$$

Similar to Eq. (3.54), the displacement transformation through $\hat{P}$ induces a frame change in the Hamiltonian. The transformed Hamiltonian in this new frame depends solely on the unitary transformation and the original Hamiltonian. In the following, we will outline the calculation of this transformed Hamiltonian for a general case.

[1] For simplicity and without loss of generality we will assume $\alpha = \sqrt{\bar{n}_c} \in \mathbb{R}$, which removes the phase-dependence of the interaction.

Derivation of $\hat{\mathcal{H}}'$ under a frame transformation: For completeness, we will stop for a couple of lines and address the derivation of the Hamiltonian in Eq. (3.80). First, let us recall the Schrödinger equation

$$\frac{d}{dt}\psi = -i\hat{\mathcal{H}}\psi \tag{3.81}$$

with ψ an arbitrary system's wave function and $\hat{\mathcal{H}}$ the time-dependent system's Hamiltonian. Using an unitary operator $\hat{U}$, such that $\hat{U}^\dagger\hat{U} = 1$, we find

$$\hat{U}\dot{\psi} = -i\left(\hat{U}\hat{\mathcal{H}}\hat{U}^\dagger\right)\hat{U}\psi. \tag{3.82}$$

On the left-hand-side we can use the product rule, namely $\frac{d}{dt}(\hat{U}\psi) = \dot{\hat{U}}\psi + \hat{U}\dot{\psi}$, which leads us to

$$\hat{U}\dot{\psi} = \frac{d}{dt}\left(\hat{U}\psi\right) - \dot{U}\hat{U}^\dagger\hat{U}\psi. \tag{3.83}$$

The combination of the last two equations results in

$$\frac{d}{dt}\left(\hat{U}\psi\right) = -i\left[\hat{U}\hat{\mathcal{H}}\hat{U}^\dagger + i\dot{U}\hat{U}^\dagger\right]\left(\hat{U}\psi\right), \tag{3.84}$$

which multiplied by $\hat{U}^\dagger$ from the right becomes

$$\frac{d}{dt}\left(\hat{U}\psi\hat{U}^\dagger\right) = -i\left[\hat{U}\hat{\mathcal{H}}\hat{U}^\dagger + i\dot{U}\hat{U}^\dagger\right]\left(\hat{U}\psi\hat{U}^\dagger\right). \tag{3.85}$$

Expressing the last equation as

$$\frac{d}{dt}\psi' = -i\hat{\mathcal{H}}'\psi', \quad \hat{\mathcal{H}}' = \hat{U}\hat{\mathcal{H}}\hat{U}^\dagger + i\dot{U}\hat{U}^\dagger \quad \square \tag{3.86}$$

with $\psi' = \hat{U}\psi\hat{U}^\dagger$ and where $\hat{\mathcal{H}}'$ shows precisely the transformed Hamiltonian in Eq. (3.87).

Using the derivation yielding Eq. (3.86), the transformed Hamiltonian in Eq. (3.80) is given by

$$\hat{\mathcal{H}}' = \hat{P}(t)\hat{\mathcal{H}}\hat{P}^\dagger(t) + i\frac{\partial\hat{P}(t)}{\partial t}\hat{P}^\dagger(t), \tag{3.87}$$

where the second term does not vanish due to the time dependence of the classical mode amplitudes. Hence, using the product rule it follows that

$$i\frac{\partial\hat{P}(t)}{\partial t}\hat{P}^\dagger(t) = -i\left[\frac{\partial\alpha}{\partial t}\hat{d}^\dagger - \frac{\partial\alpha^*}{\partial t}\hat{d}\right] - i\left[\frac{\partial\beta}{\partial t}\hat{b}^\dagger - \frac{\partial\beta^*}{\partial t}\hat{b}\right]. \tag{3.88}$$

These time derivatives are explicitly given by

$$i\frac{\partial\hat{D}^\dagger(\alpha)}{\partial t}\hat{D}(\alpha) = -i\left[\frac{\partial\alpha}{\partial t}\hat{d}^\dagger - \frac{\partial\alpha^*}{\partial t}\hat{d}\right]\hat{\mathcal{D}}^\dagger(\alpha)\hat{\mathcal{D}}(\alpha) = -i\left[\frac{\partial\alpha}{\partial t}\hat{d}^\dagger - \frac{\partial\alpha^*}{\partial t}\hat{d}\right] \tag{3.89}$$

for the cavity mode and

$$i\frac{\partial\hat{\mathcal{D}}^\dagger(\beta)}{\partial t}\hat{\mathcal{D}}(\beta) = -i\left[\frac{\partial\beta}{\partial t}\hat{b}^\dagger - \frac{\partial\beta^*}{\partial t}\hat{b}\right] \tag{3.90}$$

for the mechanics. Note, that in these equations the analysis of the classical dynamics is crucial. Thus, recalling the dynamical analysis of the classical equations of motion done before in Eq. (3.62) we find that the cavity's mode amplitude follows

$$\frac{d}{dt}\alpha = \left(i\Delta - \frac{\kappa}{2}\right)\alpha - i\frac{g_0}{x_{\mathrm{zpf}}}\langle\hat{q}\rangle\alpha - i\alpha_p \tag{3.91}$$

with $\langle\hat{q}\rangle = x_{\text{zpf}}\langle\hat{b}+\hat{b}^\dagger\rangle$. Analogously, for the mechanics we find

$$\frac{d\beta}{dt} = -\left(i\omega_m + \frac{\gamma_m}{2}\right)\beta - ig_0|\alpha|^2. \tag{3.92}$$

Using Eq. (3.91) into Eq. (3.89) we find

$$\begin{aligned} i\frac{\partial\hat{D}^\dagger(\alpha)}{\partial t}\hat{D}(\alpha) = &-i\left(i\Delta - \frac{\kappa}{2}\right)\alpha\hat{d}^\dagger + i\left(-i\Delta - \frac{\kappa}{2}\right)\alpha^*\hat{d} \\ &- \frac{g_0}{x_{\text{zpf}}}\langle\hat{q}\rangle\left[\alpha^*\hat{d} + \alpha\hat{d}^\dagger\right] - \left(\alpha_p^*\hat{d} + \alpha_p\hat{d}^\dagger\right) \end{aligned} \tag{3.93}$$

and similarly for the mechanics

$$i\frac{\partial\hat{\mathcal{D}}^\dagger(\beta)}{\partial t}\hat{\mathcal{D}}(\beta) = -i\left[-\left(i\omega_m + \frac{\gamma_m}{2}\right)\beta - ig_0|\alpha|^2\right]\hat{b}^\dagger + i\left[-\left(-i\omega_m + \frac{\gamma_m}{2}\right)\beta^* + ig_0|\alpha|^2\right]\hat{b}. \tag{3.94}$$

We can now plug these results into Eq. (3.87) to find

$$\begin{aligned} \hat{\mathcal{H}}' = &-\Delta\left[|\alpha|^2 + \alpha^*\hat{d} + \alpha\hat{d}^\dagger + \hat{d}^\dagger\hat{d}\right] + \omega_m\left[|\beta|^2 + \beta^*\hat{b} + \beta\hat{b}^\dagger + \hat{b}^\dagger\hat{b}\right] + \alpha_p^*\left(\alpha + \hat{d}\right) + \alpha_p\left(\alpha^* + \hat{d}^\dagger\right) \\ &+ g_0\Bigg[|\alpha|^2\left[\beta+\beta^*\right] + |\alpha|^2\left[\hat{b}+\hat{b}^\dagger\right] + \left[\alpha^*\hat{d} + \alpha\hat{d}^\dagger\right]\left[\beta+\beta^*\right] + \left[\alpha^*\hat{d} + \alpha\hat{d}^\dagger\right]\left[\hat{b}+\hat{b}^\dagger\right] \\ &+ \hat{d}^\dagger\hat{d}\left[\beta+\beta^*\right] + \hat{d}^\dagger\hat{d}\left[\hat{b}+\hat{b}^\dagger\right]\Bigg] \\ &- i\left(i\Delta - \frac{\kappa}{2}\right)\alpha\hat{d}^\dagger + i\left(-i\Delta - \frac{\kappa}{2}\right)\alpha^*\hat{d} - \frac{g_0}{x_{\text{zpf}}}\langle\hat{q}\rangle\left[\alpha^*\hat{d} + \alpha\hat{d}^\dagger\right] - \left(\alpha_p^*\hat{d} + \alpha_p\hat{d}^\dagger\right) \\ &- i\left[-\left(i\omega_m + \frac{\gamma_m}{2}\right)\beta - ig_0|\alpha|^2\right]\hat{b}^\dagger + i\left[-\left(-i\omega_m + \frac{\gamma_m}{2}\right)\beta^* + ig_0|\alpha|^2\right]\hat{b}. \end{aligned} \tag{3.95}$$

Note that the blue terms involve only classical components, depending solely on the amplitudes α and β, and represent the average energy of the system. These classical terms ensure a correct value for the expectation value $\langle\hat{H}'\rangle$. In contrast, the last term in the third line consists of a nonlinear (non-quadratic) component, which is normally neglected since it is smaller by a factor of $|\alpha|$ (see Eq. (3.75)). The remaining orange terms, except for black, will cancel out. Furthermore, since we are interested in the dynamics of the fluctuations, we will neglect both the purely classical (blue) and nonlinear terms in this analysis. Thus, the resulting Hamiltonian becomes

$$\begin{aligned} \hat{\mathcal{H}} = &-\Delta\hat{d}^\dagger\hat{d} + \omega_m\hat{b}^\dagger\hat{b} + g_0\left[\alpha^*\hat{d} + \alpha\hat{d}^\dagger\right]\left[\hat{b}+\hat{b}^\dagger\right] + \frac{g_0}{x_{\text{zpf}}}\langle\hat{q}\rangle\hat{d}^\dagger\hat{d} \\ &- i\frac{\kappa}{2}\left[\alpha^*\hat{d} - \alpha\hat{d}\right] - i\frac{\gamma_m}{2}\left[\beta^*\hat{b} - \beta\hat{b}\right]. \end{aligned} \tag{3.96}$$

However, we can see that in the second line of the last equation the decay rates κ and γ_m appear, which arises due to the differential Eqs. (3.91) and (3.92). To account for the dissipation, the transformation of the dissipators $\hat{\mathcal{D}}[\hat{o}]\bullet$ given by (2.35) is still required. Following the same approach we find

$$\begin{aligned} \kappa\hat{\mathcal{D}}^\dagger(\alpha)\hat{\mathcal{D}}[\hat{a}]\bullet\hat{\mathcal{D}}(\alpha) &= \kappa\hat{\mathcal{D}}[\alpha+\hat{d}]\bullet \\ &= \kappa\hat{\mathcal{D}}[\hat{d}]\bullet - i\frac{\kappa}{2}\left[i\alpha^*\hat{d} - i\alpha\hat{d}^\dagger, \bullet\right] \end{aligned} \tag{3.97}$$

and similarly for the mechanics

$$\gamma\hat{\mathcal{D}}[\beta+\hat{b}]\bullet = \gamma_m\hat{\mathcal{D}}[\hat{b}]\bullet - i\frac{\gamma_m}{2}\left[i\beta^*\hat{b} - i\beta\hat{b}^\dagger, \bullet\right]. \tag{3.98}$$

Note, the second term in Eqs. (3.97) and (3.98) can be written as $-i\left[\hat{\mathcal{H}}_\kappa, \bullet\right]$, where $\hat{\mathcal{H}}_\kappa$ can then enter the Hamiltonian given in Eq. (3.96), yielding the effective Hamiltonian

$$\hat{\mathcal{H}}_{\text{eff}} = \hat{\mathcal{H}} + \hat{\mathcal{H}}_\kappa = -\left(\Delta - \frac{g_0}{x_{\text{zpf}}}\langle\hat{q}\rangle\right)\hat{d}^\dagger\hat{d} + \omega_m\hat{b}^\dagger\hat{b} + g_0\left[\alpha^*\hat{d} + \alpha\hat{d}^\dagger\right]\left[\hat{b} + \hat{b}^\dagger\right]. \tag{3.99}$$

Since typically g_0 is small then $1 \gg g_0\langle\hat{q}\rangle/x_{\text{zpf}}$ and $\langle\hat{q}\rangle/x_{\text{zpf}}$ can be neglected. Furthermore, assuming that $\alpha = \sqrt{\bar{n}_c}$, we find that the effective Hamiltonian obtained from the transformation of Eq. (3.78) is precisely the linearized Hamiltonian given in Eq. (3.76).

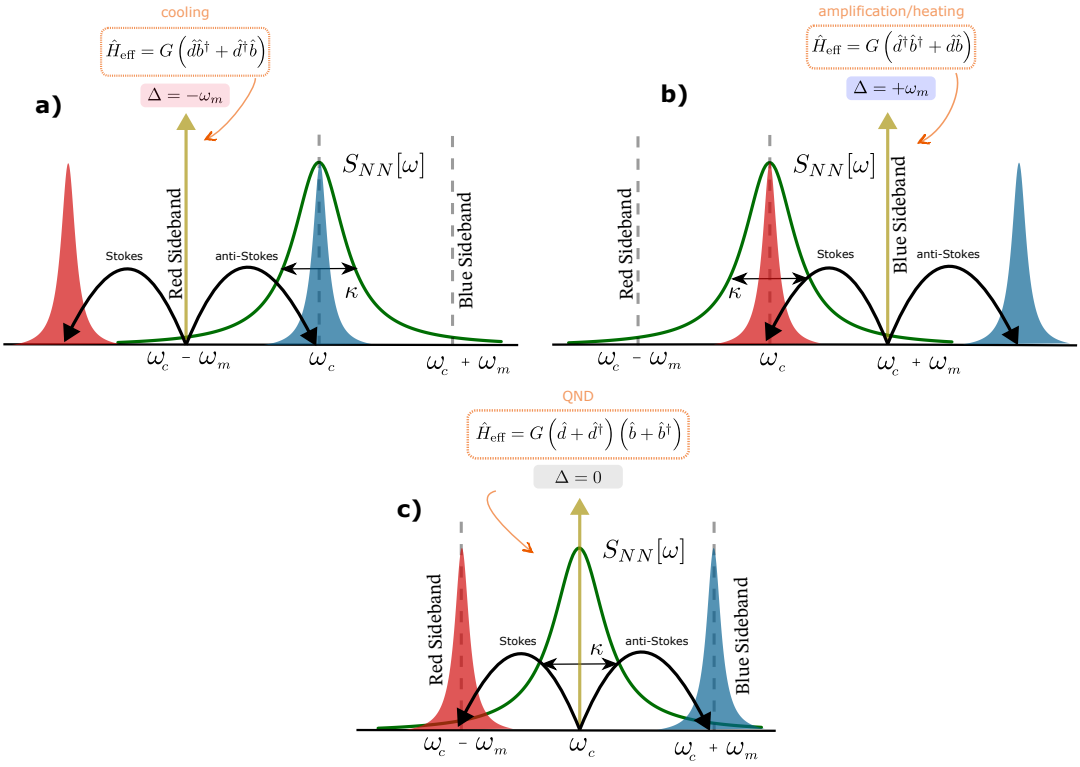

FIGURE 3.9: Illustration of an optomechanical system's different cavity driving schemes. In the linearized regime, the choice of cavity detuning leads to distinct optomechanical effects due to the resonant interactions. a) A red-detuned laser leads to an exchange of quanta between the cavity and mechanical modes, ideal for sideband cooling. b) A blue-detuned laser results in a *two-mode squeezing* Hamiltonian, which may lead to the observation of entanglement and self-sustained optomechanical oscillations. c) At zero detuning the cavity experiences a shift proportional to the displacement, which will be encoded in the transmitted/reflected cavity field that can be used for mechanical motion detection. In this regime, the cavity effectively works as an interferometer.

3.5 Driving schemes

The term *linearized Hamiltonian* dues its name from the resulting linear equations of motion within this approximation. It serves as the foundation for describing the majority of quantum optomechanical experiments.

In the interaction frame for both the cavity and the mechanics, the Hamiltonian in Eq. (3.76) reads

$$\hat{\mathcal{H}}'_{\text{int}} = G\left(\hat{d}\hat{b}e^{i\delta_- t} + \hat{d}^\dagger\hat{b}^\dagger e^{-i\delta_- t}\right) + G\left(\hat{d}\hat{b}^\dagger e^{i\delta_+ t} + \hat{d}^\dagger\hat{b}e^{-i\delta_+ t}\right), \tag{3.100}$$

where $\delta_\pm \equiv \Delta \pm \omega_m$. This Hamiltonian gives rise to interesting optomechanical effects, which are selected by the choice of the cavity detuning Δ as illustrated in Fig. 3.9.

If $\Delta \approx -\omega_m$, one obtains two oscillators of similar frequency. Neglecting the fast rotating terms in Eq. (3.100), i.e. applying the *rotating wave approximation* [2] (RWA), yields

$$\hat{\mathcal{H}}_{\rm BS} = G\left(\hat{d}\hat{b}^\dagger + \hat{d}^\dagger\hat{b}\right), \tag{3.101}$$

which is denoted as the *beam-splitter* interaction due to the exchange of quanta between the mechanical and optical modes. Consequently, this interaction leads to the cooling effect of the mechanical system, since the process excites photons by a Raman scattering process leading to the absorption of phonons as we will later study.

For $\Delta = \omega_m$, within the RWA, the first term on the right of (3.100) survives:

$$\hat{\mathcal{H}}_{\rm S} = G\left(\hat{d}\hat{b} + \hat{d}^\dagger\hat{b}^\dagger\right). \tag{3.102}$$

This type of Hamiltonian represents a *two-mode squeezing* interaction, central in the study of *parametric amplification*. Neglecting dissipation, this interaction causes an exponential accumulation of the energy in both, optical and mechanical, modes with high correlations between them.

In the original frame, for $\Delta = 0$, the interaction can be written as

$$\hat{\mathcal{H}}_{\rm QND} = G\left(\hat{d} + \hat{d}^\dagger\right)\left(\hat{b} + \hat{b}^\dagger\right), \tag{3.103}$$

which can be regarded as the mechanical position $\hat{q} \propto \hat{b} + \hat{b}^\dagger$ shifts the cavity phase. Later in this Chapter, we will show that for zero detuning the cavity mode does not modify the coherent dynamics of the mechanical mode, usually referred as *dynamical backaction evasion*.

3.6 Dynamical backaction effects

To study the implications of the optomechanical interaction, we will next analyze the dynamics of the fluctuations. We begin by deriving the dissipative dynamics of the fluctuations described by the quantum Langevin equation from the linearized Hamiltonian given in Eq. (3.76).

$$\frac{d}{dt}\vec{\hat{A}} = \mathbf{M}\vec{\hat{A}} - \mathbf{K}\vec{A}_{\rm in}, \tag{3.104}$$

where we defined the vector containing all mode operators $\vec{\hat{A}} = [\hat{d}, \hat{d}^\dagger, \hat{b}, \hat{b}^\dagger]^T$ and the dynamical matrix $\mathbf{M}$ as

$$\mathbf{M} = \begin{pmatrix} i\Delta - \frac{\kappa}{2} & 0 & -iG & -iG \\ 0 & -i\Delta - \frac{\kappa}{2} & iG & iG \\ -iG & -iG & -i\omega_m - \frac{\gamma_m}{2} & 0 \\ iG & iG & 0 & i\omega_m - \frac{\gamma_m}{2} \end{pmatrix}, \tag{3.105}$$

with G given in Eq. (3.77). In Eq. (3.104), the vector $\vec{A}_{\rm in} = [\hat{d}_{\rm in}, \hat{d}^\dagger_{\rm in}, \hat{b}_{\rm in}, \hat{b}^\dagger_{\rm in}]^T$ represents the cavity and mechanical input noises. In contrast, the decay rates are encoded in the diagonal matrix $\mathbf{K} = \mathrm{diag}(\sqrt{\kappa}, \sqrt{\kappa}, \sqrt{\gamma_m}, \sqrt{\gamma_m})$. Here, the input noise correlators for the cavity fluctuation, $\hat{d}_{\rm in}$, look like those given in Eq. (3.60). The mechanical correlators are given in Eq. (3.61).

[2] In the resolved sideband regime ($\kappa \ll \omega_m$) the intracavity photons remain longer than one period of the mechanics. This leads to intracavity photons interacting equally with both quadratures of the mechanics. Through the RWA we neglect the fast oscillating processes, i.e. $\hat{a}\hat{b}\,(\hat{a}^\dagger\hat{b}^\dagger)$, which for $\kappa \ll \omega_m$ are off-resonance, thereby suppressed. Contrary, in the sideband unresolved regime, the RWA fails to deliver an accurate description of the dynamics.

To solve the system of differential equations we move to the frequency domain by applying the Fourier transform defined

$$\hat{\mathcal{O}}[\omega] = \int_{-\infty}^{\infty} dt e^{i\omega t}\hat{\mathcal{O}}(t), \quad \hat{\mathcal{O}}^\dagger[\omega] = \int_{-\infty}^{\infty} dt e^{i\omega t}\hat{\mathcal{O}}^\dagger(t), \tag{3.106}$$

such that $\hat{\mathcal{O}}^\dagger[\omega] = (\hat{\mathcal{O}}[-\omega])^\dagger$, where $\hat{\mathcal{O}}$ is an arbitrary operator. This yields yielding

$$-i\omega\vec{\hat{A}}[\omega] = \mathbf{M}\vec{\hat{A}}[\omega] - \mathbf{K}\vec{A}_{\rm in}[\omega] \tag{3.107}$$

with the vectors $\vec{\hat{A}}[\omega] = [\hat{d}[\omega], \hat{d}^\dagger[\omega], \hat{b}[\omega], \hat{b}^\dagger[\omega]]^T$ and $\vec{\hat{A}}_{\rm in}[\omega] = [\hat{d}_{\rm in}[\omega], \hat{d}^\dagger_{\rm in}[\omega], \hat{b}_{\rm in}[\omega], \hat{b}^\dagger_{\rm in}[\omega]]^T$.

The last equation can be solved for $\hat{b}[\omega]$ and $\hat{b}^\dagger[\omega]$ to find the effective dynamics of the mechanical mode

$$\begin{pmatrix} \mathcal{X}_m^{-1}[\omega] - i\Sigma_c[\omega] & -i\Sigma_c[\omega] \\ i\Sigma_c[\omega] & \mathcal{X}_m^{*-1}[-\omega] + i\Sigma_c[\omega] \end{pmatrix} \begin{bmatrix} \hat{b}[\omega] \\ \hat{b}^\dagger[\omega] \end{bmatrix} = -\sqrt{\gamma_m} \begin{bmatrix} \hat{B}_{\rm in}[\omega] \\ \hat{B}^\dagger_{\rm in}[\omega] \end{bmatrix} \tag{3.108}$$

with the modified mechanical noise is given by $\hat{B}_{\rm in}[\omega] = \hat{b}_{\rm in}[\omega] - iG\sqrt{\frac{\kappa}{\gamma_m}}\hat{F}[\omega]$ with the radiation pressure force noise given explicitly below

$$\hat{F}[\omega] = \mathcal{X}_c[\omega]\hat{d}_{\rm in}[\omega] + \mathcal{X}_c^*[-\omega]\hat{d}^\dagger_{\rm in}[\omega], \tag{3.109}$$

where the cavity susceptibility given in Eq. (3.3).

In addition, as we see in Eq. (3.108), due to the optomechanical interaction, a modification of the oscillator's coherent dynamics arises through the *cavity self-energy*

$$\Sigma_c[\omega] \equiv \frac{-2G^2\Delta}{(-i\omega + \frac{\kappa}{2})^2 + \Delta^2} \equiv -\delta\omega_m[\omega] + 2i\Gamma[\omega], \tag{3.110}$$

which acts as an additional force. In other words, the interaction with the cavity alters the mechanical susceptibility via the cavity's self-energy. This, in turn, affects how the mechanical mode emits energy to and absorbs energy from the thermal bath.

Therefore, the real part of the self-energy introduces the *frequency dependent mechanical frequency shift*

$$\delta\omega_m[\omega] = G^2\left(\frac{\Delta+\omega}{(\Delta+\omega)^2 + \frac{\kappa^2}{4}} + \frac{\Delta-\omega}{(\Delta-\omega)^2 + \frac{\kappa^2}{4}}\right), \tag{3.111}$$

whereas the imaginary part the optomechanical damping given by

$$\Gamma[\omega] = G^2\left(\frac{\kappa}{(\Delta+\omega)^2 + \frac{\kappa^2}{4}} - \frac{\kappa}{(\Delta-\omega)^2 + \frac{\kappa^2}{4}}\right). \tag{3.112}$$

At strong enough coupling the frequency dependence of $\Sigma_c[\omega]$, which is generally described by a non-Lorentzian lineshape for the susceptibility, will turn into a double-peak structure [1]. For sufficient weak coupling ($\kappa \gg g_0$) and a high-Q mechanical oscillator, the cavity self-energy can be evaluated at the mechanical resonance frequency, namely $\Sigma_c[\omega] \approx \Sigma_c[\omega_m]$. This leads to the so-called *optical spring effect* and the *optomechanical damping rate*.

The optical spring effect

The *optical spring effect* occurs when the frequency shift induced by the cavity for $\delta\omega_m[\omega]$ is evaluated at ω_m:

$$\delta\omega_m[\omega_m] = G^2\left(\frac{\Delta+\omega_m}{(\Delta+\omega_m)^2 + \frac{\kappa^2}{4}} + \frac{\Delta-\omega_m}{(\Delta-\omega_m)^2 + \frac{\kappa^2}{4}}\right). \tag{3.113}$$

This effect owns its name due to the modification of the resonance frequency of the mechanical mode due to the interaction with the cavity, which can be thought of as modifying the oscillator's spring constant. Note, from Eq. (3.113), the vanishing frequency shift for $\Delta = 0$, as depicted in Fig. 3.10. In addition, by evaluating the last equation at the mechanical sidebands we find

$$\delta\omega_m[\Delta = \pm\omega_m] = \pm\frac{2G^2\omega_m}{\frac{\kappa^2}{4} + 4\omega_m^2}. \tag{3.114}$$

As depicted in Fig. 3.10 a) in the unresolved sideband regime ($\kappa \gg \omega_m$) this effect becomes

$$\delta\omega_m[\Delta]|_{\kappa\gg\omega_m} = G^2\frac{2\Delta}{\Delta^2 + \frac{\kappa^2}{4}}. \tag{3.115}$$

This implies that for a red-detuned laser ($\Delta < 0$) the mechanical oscillator will be *spring-softened*, resulting in a decrease of the mechanical frequency. Conversely, for a blue-detuned laser ($\Delta > 0$), there will be *spring-hardened*, leading to an increase in the mechanical frequency.

However, in the resolved sideband regime ($\kappa \ll \omega_m$) the effect is significantly distinct as depicted in Fig. 3.10 c) and is effectively described by

$$\delta\omega_m[\Delta]|_{\kappa\ll\omega_m} = G^2\frac{2\Delta}{(\Delta - \omega_m)(\Delta + \omega_m)}, \tag{3.116}$$

which vanishes for $\Delta = 0$. Conversely, for $\Delta = \pm\omega_m$ we have $\delta\omega_m[\Delta] \to \infty$, which leads to unstable dynamics. In the unresolved sideband regime, the system becomes increasingly sensitive to small perturbations when $\Delta = \pm\omega_m$

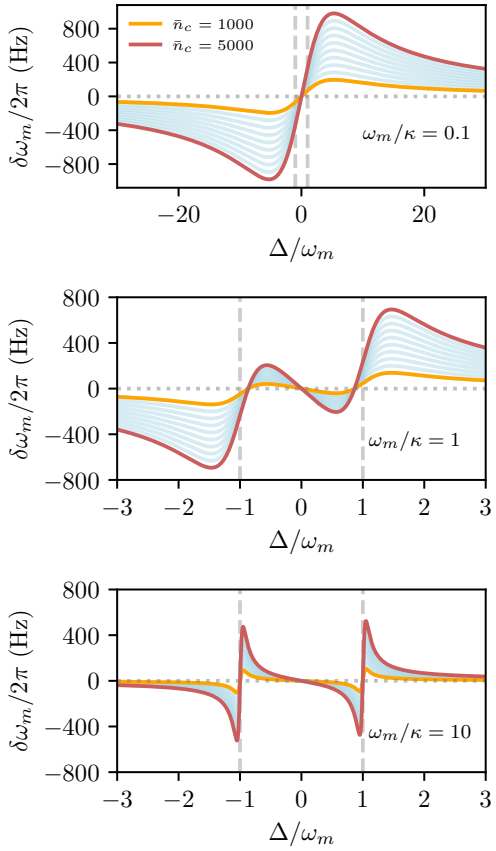

FIGURE 3.10: Mechanical frequency shift $\delta\omega_m[\omega_m]$ as a function of the optical detuning Δ/ω_m for different intracavity photon number. From left to right the sideband resolved parameter is increased: $\omega_m/\kappa = 0.1$, $\omega_m/\kappa = 1$, $\omega_m/\kappa = 10$, respectively, setting the parameters from the unresolved to the resolved sideband regime. For these plots we used: $\kappa/2\pi = 1\,\text{MHz}$ and $g_0/2\pi = 100\,\text{Hz}$.

The optomechanical damping

On the other hand, the optical damping is defined as

$$\Gamma_{\text{opt}} \equiv \Gamma[\omega_m] = G^2 \left(\frac{\kappa}{(\Delta + \omega_m)^2 + \frac{\kappa^2}{4}} - \frac{\kappa}{(\Delta - \omega_m)^2 + \frac{\kappa^2}{4}} \right), \tag{3.117}$$

such that the full effective mechanical damping rate is given by

$$\Gamma_{\text{tot}} = \gamma_m + \Gamma_{\text{opt}}. \tag{3.118}$$

From the last expression, we see that $\Gamma_{\text{opt}} > 0$ leads to an increase in the mechanical damping rate, whereas $\Gamma_{\text{opt}} < 0$ yields anti-damping. Extra damping results in cooling, while amplification is a consequence of anti-damping. As illustrated in Fig. 3.11, depending on the resolved sideband parameter, ω_m/κ, the cavity backaction on the mechanics leads to distinct features.

In the resolved sideband regime ($\omega_m \gg \kappa$) the optical damping exhibits highly peaked maxima and minima near the lower and upper sideband, i.e. at $\Delta = \pm\omega_m$ as shown in Fig. 3.11 c). The maximum rate occurs for a red-detuned drive at $\Delta = -\omega_m$:

$$\Gamma_{\text{opt}}|_{\kappa \ll \omega_m} = \frac{4G^2}{\kappa}. \tag{3.119}$$

Recalling the intracavity photon number given by (3.67), note that for a weakly coupled cavity

with $\mathcal{K}_m \approx 0$ (see Eq. (3.66)), the photon number within the resolved sideband parameter is given by

$$\bar{n}_c|_{\kappa \ll \omega_m} = \frac{\kappa \bar{n}_{\text{in}}}{\omega_m^2} \tag{3.120}$$

with $\bar{n}_{\text{in}}$ the input power. With this last equation substituted into Eq. (3.119) we find

$$\Gamma_{\text{opt}}|_{\kappa \ll \omega_m} = \frac{4g_0^2\, \bar{n}_{\text{in}}}{\omega_m^2}, \tag{3.121}$$

which shows that the cooling rate in the sideband limit does not depend on the cavity linewidth.

Contrary, in the unresolved sideband regime we find that the optomechanical damping rate (3.117) becomes

$$\Gamma_{\text{opt}}[\Delta]|_{\kappa \gg \omega_m} = \frac{-4G^2 \Delta \kappa}{\left(\Delta^2 + \frac{\kappa^2}{4}\right)^2}, \tag{3.122}$$

such that for $\Delta = \pm\kappa/2$ we find

$$\Gamma_{\text{opt}}[\Delta = \pm\frac{\kappa}{2}]|_{\kappa \gg \omega_m} = \mp\frac{8G^2\omega_m}{\kappa^2}, \tag{3.123}$$

where the backaction effects are most relevant.

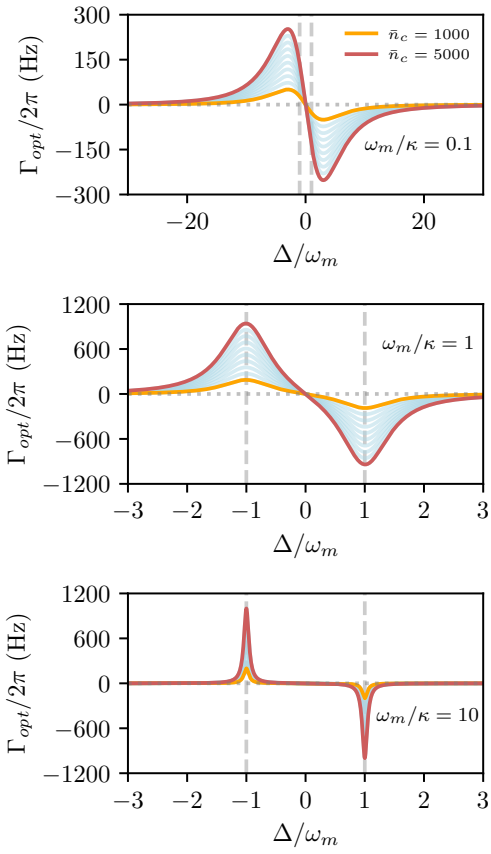

FIGURE 3.11: Optomechanical damping rate $\Gamma_{\text{opt}}[\omega_m]$ as a function of the optical detuning Δ/ω_m for different intracavity photon number. From left to right the sideband resolved parameter is increased: $\omega_m/\kappa = 0.1$, $\omega_m/\kappa = 1$, $\omega_m/\kappa = 10$, respectively, setting the parameters from the unresolved to the resolved sideband regime. For these plots we used: $\kappa/2\pi = 1\,\text{MHz}$ and $g_0/2\pi = 100\,\text{Hz}$.

3.7 Dynamical backaction cooling

The ability to prepare a system in a well-defined state is fundamental for quantum control. In the case of a harmonic oscillator, this corresponds to preparing it in its ground state, which is characterized by a minimal average number of excitations. However, mechanical resonators often exhibit a large number of quanta, far away from that of the ground state and therefore unsuitable for quantum control. In addition, typically mechanical resonators have resonant frequencies between $1 - 100$ MHz, and since these frequencies generally scale inversely with the size of the oscillator, passive cooling (e.g. dilution refrigerator) methods remain insufficient for macroscopic systems to achieve the ground state.

An alternative method to reach the ground state involves the interaction of the mechanical oscillator with another system. Optical cavities are ideal candidates for *backaction cooling* due to their negligible thermal occupation at room temperature and well-understood quantum behaviour. The radiation pressure interaction between these resonators and an optical cavity provides a method to approach the ground state and ultimately achieve quantum control [30]. This technique employs an optical drive to induce transitions that absorb phonons while generating photons in an optical or microwave cavity, resulting in irreversible energy extraction from the mechanical mode. This process effectively cools the mechanical oscillator towards its quantum ground state, representing a promising approach for precise quantum manipulation of macroscopic objects.

In this section, we will study dynamical backaction cooling, which can be understood with the help of Fig. 3.12. In the unresolved sideband regime, where the cavity decay rate far exceeds the mechanical frequency ($\kappa \gg \omega_m$), the cavity field adapts *almost* instantaneously to the oscillator's position. However, when we consider the cavity's finite response time, a phase lag arises between the radiation pressure force and the mechanical motion. This retardation effect causes the force to become out of sync with the oscillator's displacement, resulting in a net energy extraction from the mechanical mode [67].

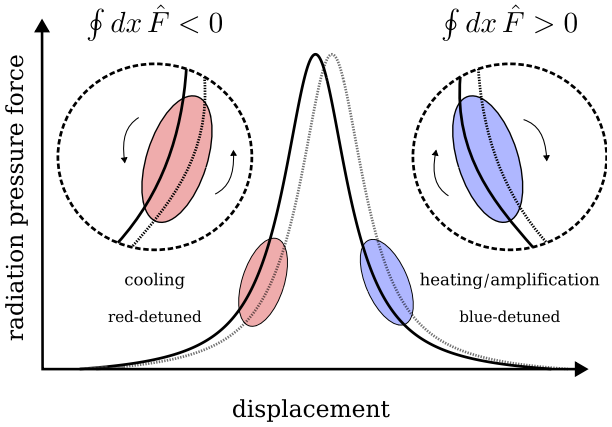

FIGURE 3.12: Schematic diagram of the radiation pressure force against displacement, which illustrates the work done during one cycle of oscillation. The work done is given by the finite area (shaded area) swept, which is due to the retardation of the force (finite cavity decay rate). For a red-detuned drive, this work is negative leading to energy extraction from the mechanical mode, thereby cooling it. Contrary, for a blue-detuned drive, heating and amplification are the result of positive work. Figure inspired by [129].

Within the weak-coupling limit ($g \ll \kappa$) a perturbative treatment of the radiation-pressure interaction is valid. In this regime, optomechanical sideband cooling, also known as backaction cooling, can be better explained using a Raman-scattering picture. Here, photons from below the cavity frequency (red-detuned) are preferentially scattered via the radiation-pressure interaction to higher frequencies taking energy from the mechanical mode to reach the cavity resonance. This is commonly known as the *anti-Stokes* process and describes the absorption of one phonon from the mechanical mode via optomechanical interaction. Conversely, the *Stokes* process describes the effect when blue-detuned photons via the optomechanical interaction add a phonon to the mechanical mode and return red-shifted. The upward transitions

(absorption) described by the anti-Stokes process happen at a rate denoted $\Gamma_{\rm AS}$, whereas the Stokes (emission) process occurs at a rate $\Gamma_{\rm S}$. Hence, the cooling of the mechanical mode can be regarded to originate from the imbalance between the absorption and emission rates, such that the net damping (cooling) rate is given by

$$\Gamma_{\rm opt} = \Gamma_{\rm AS} - \Gamma_{\rm S}. \tag{3.124}$$

Recalling the analysis of the quantum noise in Chapter 3.3.2, we know that the rates $\Gamma_{\rm AS,S}$ can be obtained using Fermi's Golden Rule applied to the photon-pressure interaction between the mechanical oscillator and the photonic cavity, namely $\hat{H}_{\rm int} = \hat{F}\hat{q}$ with the radiation pressure force $\hat{F} = g_0\hat{a}^\dagger\hat{a}$ [122]. Hence, within the weak coupling limit, the Stokes and anti-Stokes rates are given by

$$\Gamma_{\rm S/AS} = \mathcal{S}_{FF}[\mp\omega_m] = g_0^2\mathcal{S}_{nn}[\mp\omega_m], \tag{3.125}$$

with the *photon number noise spectrum*

$$\mathcal{S}_{nn}[\omega] = \int_{-\infty}^{\infty} dt\, e^{i\omega t}\langle(\hat{a}^\dagger\hat{a})(t)(\hat{a}^\dagger\hat{a})(0)\rangle. \tag{3.126}$$

As discussed before, most of the optomechanical experiments can be explained in the linearized regime (see Eq. (3.74)) with the associated Hamiltonian given in Eq. (3.76). Recalling Eq. (3.104), we will only consider terms involving cavity fluctuations, whose dynamics read

$$\begin{bmatrix}\hat{d}[\omega]\\ \hat{d}^\dagger[\omega]\end{bmatrix} = -\sqrt{\kappa}\begin{pmatrix}\mathcal{X}_c[\omega] & 0\\ 0 & \mathcal{X}_c^*[-\omega]\end{pmatrix}\begin{bmatrix}\hat{d}_{\rm in}[\omega]\\ \hat{d}_{\rm in}^\dagger[\omega]\end{bmatrix} \tag{3.127}$$

As we did before, assuming delta correlated noise as in Eq. (3.60) we find that the only non-zero contribution comes from the correlator $\langle\hat{d}_{\rm in}[\omega']\hat{d}_{\rm in}^\dagger[\omega]\rangle$, such that the spectrum of the radiation pressure force reads

$$\mathcal{S}_{FF}[\omega] = G^2\kappa\int\frac{d\omega'}{2\pi}\,\mathcal{X}_c[\omega]\mathcal{X}_c^*[-\omega']\langle\hat{d}_{\rm in}[\omega]\hat{d}_{\rm in}^\dagger[\Omega']\rangle = \frac{G^2\kappa}{(\omega+\Delta)^2+\frac{\kappa^2}{4}}. \tag{3.128}$$

Finally, note that using the last result in Eq. (3.125) we recover exactly the optical damping rate given in Eq. (3.117) obtained using the linearized equations of motion. This is precisely the relation of the noise and the dissipative part of the linear response established by the FDT in Eq. (3.42).

Similarly, as in Chapter 3.3, the average number of phonons, $\langle\hat{n}_m\rangle$, can be computed within the master equation framework (see Eq. (3.24)). Given γ_m and ω_m, the mechanical loss rates and resonant frequency, respectively, if they satisfy $\gamma_m \ll g_0 \ll \kappa, \omega_m$ then the dynamics of the mechanical mode can be approximated by truncating the cavity degrees of freedom at the lowest relevant order in the coupling parameter g_0. The resulting average mechanical occupation is given

$$\frac{d}{dt}\langle\hat{n}_m\rangle = -\left(\gamma_m + \Gamma_{\rm AS} - \Gamma_{\rm S}\right)\langle\hat{n}_m\rangle + \gamma_m\bar{n}_m^T + \Gamma_{\rm S}, \tag{3.129}$$

where we have introduced the extra transition rates induced by the optomechanical coupling strength. From this equation, we find the steady-state final phonon number which reads

$$\langle\hat{n}_m\rangle = \frac{\gamma_m\bar{n}_m^T}{\gamma_m + \Gamma_{\rm AS} - \Gamma_{\rm S}} + \frac{\Gamma_{\rm S}}{\gamma_m + \Gamma_{\rm AS} - \Gamma_{\rm S}}. \tag{3.130}$$

Note that, in the absence of the radiation pressure interaction, the last equation yields $\langle\hat{n}_m\rangle = \bar{n}_m^T$. In this way, the first term can be understood as a modified thermal occupation due to the optomechanical damping rate of Eq. (3.117) $\Gamma_{\rm opt} = \Gamma_{\rm AS} - \Gamma_{\rm S}$. The second term, on the other hand, represents the unwanted cavity backaction heating, such that the minimal phonon

number ($\gamma_m = 0$) is

$$\langle \hat{n}_m \rangle = \frac{\Gamma_{\rm S}}{\Gamma_{\rm AS} - \Gamma_{\rm S}} = \left(\frac{(\omega_m - \Delta)^2 + \frac{\kappa^2}{4}}{(\omega_m + \Delta)^2 + \frac{\kappa^2}{4}} - 1 \right)^{-1}. \tag{3.131}$$

From the denominator of Eq. (3.130) it is possible to notice that cooling is only possible if $\Gamma_{\rm opt} > 0$, thereby for large asymmetry between the Stokes and anti-Stokes processes. As illustrated in Fig. 3.11 in the resolved sideband regime the optical damping is largest and cooling is therefore more efficient. This is also consistent with the cooling limits shown in Fig. 3.13 for different resolved sideband parameters and driving strengths.

Nevertheless, there is still one variable that we can experimentally vary to minimize this expression: the optical detuning. The minima occupation occurs for optimal detuning, such that the backaction (3.131) becomes

$$\langle \hat{n}_m \rangle = \frac{1}{2} \left(\frac{\sqrt{\omega_m^2 + \frac{\kappa^2}{4}}}{\omega_m} - 1 \right), \quad \Delta_{\rm opt} = -\sqrt{\omega_m^2 + \kappa^2/4}. \tag{3.132}$$

This equation indicates that ground state cooling is only possible if $\kappa/\omega_m < 4\sqrt{2}$. In the resolved sideband regime where $\omega_m \gg \kappa$ we find that $\Delta_{\rm opt} \approx -\omega_m$ and therefore the minimum photon number becomes

$$\langle \hat{n}_m \rangle_{\rm min} = \left(\frac{\kappa}{4\omega_m} \right)^2 < 1, \quad \omega_m \gg \kappa, \tag{3.133}$$

as shown in Fig. 3.13. The above means that in the resolved sideband equation backaction cooling can lead to ground-state cooling of the mechanical mode as illustrated in Fig. 3.13. However, in the opposite regime, $\omega_m \ll \kappa$, we find

$$\langle \hat{n}_m \rangle_{\rm min} = \frac{\kappa}{4\omega_m} \gg 1, \quad \omega_m \ll \kappa, \tag{3.134}$$

for which the optimal detuning becomes $\Delta_{\rm opt} \approx -\kappa/2$. From the last equation, note that ground state cooling is impossible in the unresolved sideband regime as depicted by the orange line in the upper plot in Fig. 3.13.

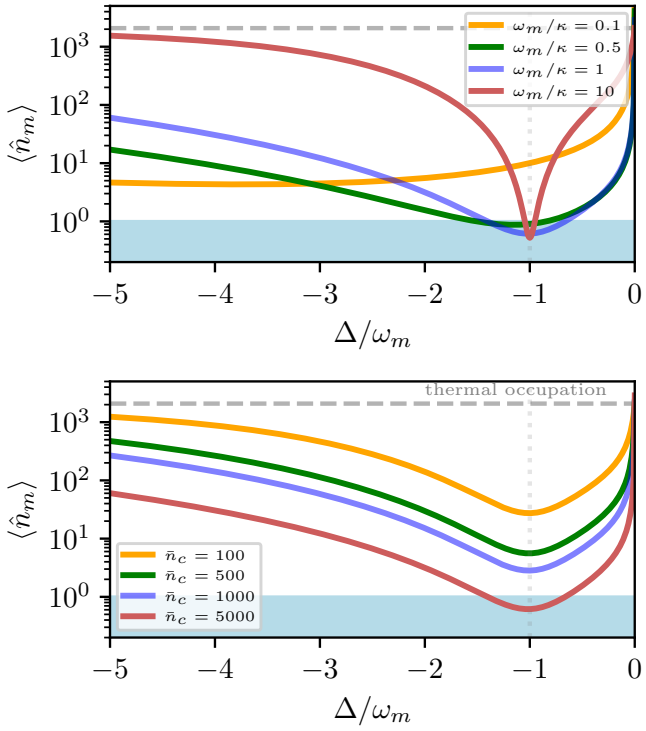

FIGURE 3.13: Phonon number as a function of the optical detuning. The upper plot shows the average mechanical occupation for varying sideband parameter ω_m/κ but fixed drive strength $\bar{n}_c = 5000$. As ω_m/κ increases the system approaches the resolved sideband regime, where ground state cooling (blue-shaded area) for $\Delta = -\omega_m$ is possible as depicted by the red and blue lines. The lower plot shows the phonon number for increasing drive power. In this case, ground state cooling is possible for higher drive strength resulting in increased optical damping (3.117). However, in this plot, the same resolved parameter $\omega_m/\kappa = 1$, hence best cooling is found at the same optical detuning. For both plots the dashed grey line shows the thermal occupation and the following parameters were used: $\kappa/2\pi = 1\,\mathrm{MHz}$, $\gamma_m/2\pi = 0.5\,\mathrm{Hz}$, $T = 0.1\,\mathrm{K}$ and $g_0/2\pi = 100\,\mathrm{Hz}$.

So far our analysis of the mechanical occupation has been done using the quantum noise spectral density of the radiation pressure force resulting in the derivation of the emission and absorption rates given in Eq. (3.125). However, the analysis of the quantum Langevin equations within the input-output formalism also enables the computation of the phonon number. First, we defined the mechanical noise spectrum as

$$\mathcal{S}_{bb}[\omega] = \int \frac{d\Omega}{2\pi} \langle \hat{b}^\dagger[\Omega]\hat{b}[\omega]\rangle, \tag{3.135}$$

where the correlator can be obtained using the effective dynamics of the mechanical mode given by (3.108), which here we will rewrite as

$$\begin{pmatrix} \mathcal{X}_m^{-1}[\omega] - i\Sigma_c[\omega] & -i\Sigma_c[\omega] \\ i\Sigma_c[\omega] & \mathcal{X}_m^{*-1}[-\omega] + i\Sigma_c[\omega] \end{pmatrix} \begin{bmatrix} \hat{b}[\omega] \\ \hat{b}^\dagger[\omega] \end{bmatrix} = -\sqrt{\gamma_m} \begin{bmatrix} \hat{b}_{\mathrm{in}}[\omega] \\ \hat{b}^\dagger_{\mathrm{in}}[\omega] \end{bmatrix} + \frac{i}{\sqrt{\gamma_m}} \begin{bmatrix} \hat{F}[\omega] \\ \hat{F}[\omega] \end{bmatrix} \tag{3.136}$$

with the radiation pressure force noise given in Eq. (3.109). Eq. (3.136) indicates that, besides the intrinsic mechanical noise, there is additional noise, whose source is precisely the radiation pressure force as indicated in the second term on the right-hand side.

At strong enough coupling the frequency dependence of $\Sigma_c[\omega]$, which is generally described by a non-Lorentzian lineshape for the susceptibility, will turn into a double-peak structure [1]. Yet, for sufficient weak coupling ($\kappa \gg g_0$), the cavity self energy given in Eq. (3.110) can be evaluated at the mechanical resonance frequency, namely $\Sigma_c[\omega] \approx \Sigma_c[\omega_m]$. Contrary, in

the strong coupling regime ($\kappa \sim g_0$), the interaction hybridizes the mechanical and optical modes, forming new normal modes (polaritons) [87]. As a consequence, the self energy becomes frequency-dependent leading to frequency-dependent optical backaction effects. Hence, assuming a high-Q mechanical oscillator the mechanical noise spectrum takes the rather simple form

$$\begin{aligned}\mathcal{S}_{bb}[\omega] = &\frac{\gamma_m \left|\mathcal{X}_{\mathrm{m}}^{*-1}[-\omega] + i\Sigma_c[\omega_m]\right|^2}{\left|(\omega-\Omega_{m,+})(\omega-\Omega_{m,-})\right|^2}\bar{n}_m^T + \frac{\gamma_m\left|\Sigma_c[\omega_m]\right|^2}{\left|(\omega-\Omega_{m,+})(\omega-\Omega_{m,-})\right|^2}\left(\bar{n}_m^T+1\right)\\ &+\frac{\left|\mathcal{X}_m^{*-1}[-\omega]\right|^2}{\left|(\omega-\Omega_{m,+})(\omega-\Omega_{m,-})\right|^2}\Gamma_{\mathrm{S}},\end{aligned} \tag{3.137}$$

with the poles $\Omega_{m,\pm} = -i\gamma_m/2 \pm \sqrt{\omega_m^2 - 2\omega_m\Sigma_c[\omega_m]}$ and the Stokes rate given by (3.125). The first two terms of the last expression are associated to the noise correlators of the mechanical mode (3.61). Nevertheless, the contribution proportional to $\bar{n}_m^T + 1$ arises exclusively due to the optomechanical interaction yielding the squeezing of the mechanics. The last line, on the other hand, exhibits the thermal occupation introduced uniquely by the cavity, namely the so-called *cavity backaction*. Note that, even at a zero-temperature bath $\bar{n}_m^T = 0$, the interaction with the cavity introduces unwanted heating.

Using the Wiener-Khinchin theorem [27], the occupation of the mechanical mode can be obtained by calculating

$$\langle \hat{n}_m \rangle = \int \frac{d\omega}{2\pi}\mathcal{S}_{bb}[\omega] \tag{3.138}$$

with the noise spectrum given in Eq. (3.137). Furthermore, in the weak coupling regime ($g_0 \ll \kappa$) we can Taylor expand mechanical noise spectra poles, i.e.

$$\Omega_{m,\pm} = -i\frac{\gamma_m}{2} \pm \sqrt{\omega_m^2 - 2\omega_m\Sigma_c[\omega_m]} \approx -i\frac{\gamma_m}{2} \pm \omega_m\left(1 - \frac{\Sigma_c[\omega_m]}{\omega_m}\right). \tag{3.139}$$

This allows us to analytically perform Eq. (3.138), where we identified the following integrals

$$\begin{aligned}\mathcal{I}_1 &= \int_{-\infty}^{\infty}\frac{d\omega}{2\pi}\,\frac{1}{\left|(\omega-\Omega_+)(\omega-\Omega_-)\right|^2} \approx \frac{\mathcal{C}_{\mathrm{eff}}}{2\omega_m^2\gamma_m\left[\mathcal{C}_{\mathrm{eff}}^2-1\right]},\\ \mathcal{I}_2 &= \int_{-\infty}^{\infty}\frac{d\omega}{2\pi}\,\frac{\omega}{\left|(\omega-\Omega_+)(\omega-\Omega_-)\right|^2} \approx \frac{1}{2\omega_m\gamma_m\left[1-\mathcal{C}_{\mathrm{eff}}^2\right]},\\ \mathcal{I}_3 &= \int_{-\infty}^{\infty}\frac{d\omega}{2\pi}\,\frac{\omega^2}{\left|(\omega-\Omega_+)(\omega-\Omega_-)\right|^2} \approx \frac{\mathcal{C}_{\mathrm{eff}}}{2\gamma_m\left[\mathcal{C}_{\mathrm{eff}}^2-1\right]}\left[1-\left(\frac{\gamma_m}{2\omega_m}\right)^2\right],\end{aligned} \tag{3.140}$$

where we introduced the *effective cooperativity* $\mathcal{C}_{\mathrm{eff}} = \Gamma_{\mathrm{opt}}/\gamma_m$ with the imaginary part of the susceptibility given in Eq. (3.110). Using these integrals it can be shown that the occupation takes the rather simple form

$$\langle \hat{n}_m \rangle \approx \frac{\bar{n}_m^T}{1+\mathcal{C}_{\mathrm{eff}}} + \left(\frac{|\Sigma_c[\omega_m]|}{\omega_m}\right)^2\frac{\mathcal{C}_{\mathrm{eff}}}{[\mathcal{C}_{\mathrm{eff}}^2-1]}\left(\bar{n}_m^T+1\right) + \frac{1/\gamma_m}{1+\mathcal{C}_{\mathrm{eff}}}\Gamma_{\mathrm{S}}. \tag{3.141}$$

Furthermore, for sufficiently weak coupling $g \ll \kappa$ the term $|\Sigma_c[\omega_m]|/\omega_m \ll 1$, such that we can further simplify the last expression and neglect the term proportional to $\bar{n}_m^T + 1$. Finally, the mechanical occupation reads

$$\langle \hat{n}_m \rangle \approx \frac{\bar{n}_m^T}{1+\mathcal{C}_{\mathrm{eff}}} + \frac{1/\gamma_m}{1+\mathcal{C}_{\mathrm{eff}}}\Gamma_{\mathrm{S}} = \frac{1}{1+\mathcal{C}_{\mathrm{eff}}}\left[\bar{n}_m^T + \frac{\Gamma_{\mathrm{S}}}{\gamma_m}\right], \tag{3.142}$$

which is equivalent to Eq. (3.130).

Throughout this section, we have computed the average mechanical occupation using different approaches. First, we derived the radiation pressure force spectrum—closely related to the photon number spectrum—to determine the Stokes and anti-Stokes rates. These rates

describe the emission and absorption of phonons and characterize the effective damping of the mechanical mode. To calculate the steady-state average mechanical occupation, we employed the master equation framework (see Chapter 2), leading to the result shown in Eq. (3.130).

Alternatively, we derived the effective dynamics of the mechanics in Eq. (3.136) and computed the mechanical noise spectrum Eq. (3.135). Finally, the integration of the power spectrum as in Eq. (3.138) results in the average mechanical occupation. Nevertheless, to arrive at an analytical result we assumed the oscillator to be high-quality and weak enough coupling. Since they scale as $\sim \Sigma_c[\omega_m]$, these approximations allowed us to neglect the parametric coupling indicated by the off-diagonal elements of the Langevin matrix in Eq. (3.136). These terms are responsible of unwanted heating associated to single-mode squeezing and leading to the second term in Eq. (3.141). Hence, under these specific conditions, namely a high mechanical quality factor and weak enough coupling strength, the analytical integration of the mechanical noise spectrum leads also to Eq. (3.130).

In Fig. 3.14, we illustrate how, in the resolved sideband regime, the approximated result no longer accurately captures the mechanical occupation as the optomechanical coupling increases. This deviation arises because, with stronger interaction, the optomechanically induced parametric coupling in the mechanical mode becomes more significant, leading to a substantial contribution to the average mechanical occupation.

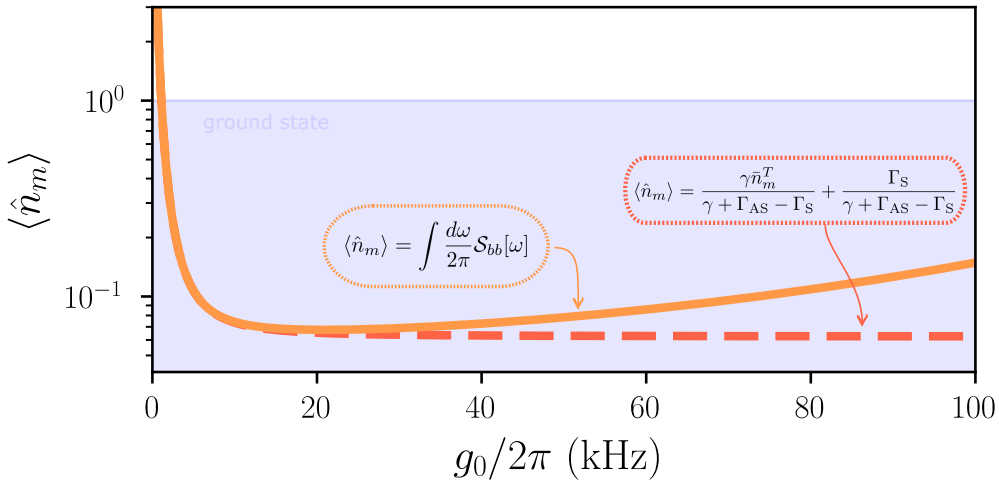

FIGURE 3.14: Average mechanical occupation as a function of the bare optomechanical coupling strength. The solid orange line represents the exact result, obtained through the numerical integration of the mechanical power spectrum $\mathcal{S}_{bb}[\omega]$. In contrast, the dashed red line corresponds to the approximate result from the calculation of the Stokes and anti-Stokes rates. For sufficiently strong optomechanical coupling, off-resonant processes introduced by the radiation-pressure interaction—neglected in the approximate result—become more significant. For this plot: $\omega_m/\kappa = 1$, $\Delta = -\omega_m$, and $\bar{n}_m^T \approx 277$.

3.8 Measuring the mechanical motion

In the field of optomechanics, the optical cavity functions as an interferometer, directly measuring the motion of the mechanical oscillator through the phase shift in the transmitted or reflected light field. The optomechanical interaction allows the optical field to acquire information about the oscillator's position, which can be extracted using linear detection methods such as homodyne or heterodyne techniques, with a precision constrained by quantum mechanics. In addition, since the radiation pressure interaction is linear in the oscillator's displacement, it allows to continuously measure the position of the mechanical mode. As a result, mechanical motion readout has emerged as a primary application of cavity optomechanics.

The sensitivity of this measurement depends on how effectively the oscillator's position influences the optical field and how accurately that influence can be detected. Intuitively,

one might think that stronger optomechanical coupling and lower optical readout noise would lead to more precise position measurements. However, the fluctuating radiation pressure force introduces an inevitable *disturbance* in the mechanical motion, since each photon delivers a random *push*, whose overall effect scales with $\sqrt{\bar{n}_c}$, with $\bar{n}_c$ being the number of photons circulating in the cavity. This is known as *backaction noise* and counteracts the increased precision in phase readout at higher photon numbers. However, by carefully selecting the photon number, one can find a *sweet spot* where the combined effects of measurement precision and backaction noise are minimized, leading to optimal detection.

Below we will analyze the imprecision and backaction noise contributions to the total measurement error in terms of the noise spectra (see Chapter 3.3.2). The total noise registered at the detector for an optomechanical system described by the Hamiltonian given in Eq. (3.76) will have the following form [130]

$$\begin{aligned}\bar{\mathcal{S}}_{uu}^{\mathrm{out}}[\omega] &= \bar{\mathcal{S}}_{uu}[\omega] + |\mathcal{G}[\omega]|^2 \left(\bar{\mathcal{S}}_{xx}^{0}[\omega] + \bar{\mathcal{S}}_{\mathrm{BA}}[\omega]\right) \\ &\equiv |\mathcal{G}[\omega]|^2 \left(\bar{\mathcal{S}}_{xx}^{0}[\omega] + \bar{\mathcal{S}}_{uu}^{\mathrm{add}}[\omega]\right)\end{aligned} \tag{3.143}$$

with the oscillator's spectral density, $\bar{\mathcal{S}}_{xx}^{0}[\omega]$ and where we defined the measurement *gain* $\mathcal{G}[\omega]$. Here, we also introduced the *total added noise* given by

$$\bar{\mathcal{S}}_{uu}^{\mathrm{add}}[\omega] = \bar{\mathcal{S}}_{\mathrm{BA}}[\omega] + \bar{\mathcal{S}}_{uu}^{\mathrm{imp}}[\omega] \equiv \bar{\mathcal{S}}_{\mathrm{BA}}[\omega] + \frac{\bar{\mathcal{S}}_{uu}[\omega]}{|\mathcal{G}[\omega]|^2}. \tag{3.144}$$

In Eq. (3.143) the cavity spectral density, $\bar{\mathcal{S}}_{uu}[\omega]$, represents the intrinsic noise contribution of the cavity, which when referred back to the oscillator leads to the *imprecision noise*, $\bar{\mathcal{S}}_{uu}^{\mathrm{imp}}[\omega]$, defined in Eq. (3.144). As its name suggests, this noise characterizes how precisely a measurement can be done and arises from the fundamental fluctuations in the measurement device. From its dependence on the measurement gain, below we will see that the reduction of the imprecision noise is tied to an increase in the coupling (or the response) to the oscillator. This arises since it allows for more efficient transduction of the mechanical motion into detectable changes in the optical field.

The backaction noise contribution, $\bar{\mathcal{S}}_{\mathrm{BA}}[\omega]$, results from fluctuations in the cavity field that probes the mechanical oscillator. These fluctuations induce additional motion in the oscillator, beyond its intrinsic thermal and quantum fluctuations. We will show that the backaction noise scales with the photon-enhanced optomechanical coupling strength, contrary to the imprecision noise. This creates a trade-off between the two contributions: increasing the measurement strength reduces imprecision noise, but simultaneously raises backaction noise. Together, the imprecision and the backaction noises form what we denote as the total added noise, $\bar{\mathcal{S}}_{uu}^{\mathrm{add}}[\omega]$, whose reduction is crucial for an accurate measurement. Without backaction noise, a large optomechanical coupling strength would result in negligible imprecision noise. However, due to the presence of backaction noise, the coupling strength must be carefully adjusted to balance these two noise contributions.

To derive an expression for the SQL on position detection we will first define the spectral density of the total measured noise referred back at the oscillator. From Eq. (3.143), this is given by [130]

$$\begin{aligned}\bar{\mathcal{S}}_{\mathrm{tot}}[\omega] &\equiv \frac{\bar{\mathcal{S}}_{uu}^{\mathrm{out}}[\omega]}{|\mathcal{G}[\omega]|^2} \\ &= \bar{\mathcal{S}}_{xx}^{0}[\omega] + \bar{\mathcal{S}}_{uu}^{\mathrm{add}}[\omega],\end{aligned} \tag{3.145}$$

where the last term is the added noise introduced in Eq. (3.144). The standard quantum limit (SQL) occurs then at the point of optimal balance between imprecision and backaction noises, i.e. where the added noise reaches a minimum. The *quantum limit* on continuous position detection at each frequency must satisfy the following fundamental inequality

$$\bar{\mathcal{S}}_{uu}^{\mathrm{add}}[\omega] \geq \bar{\mathcal{S}}_{xx}^{\mathrm{zdf}}[\omega] \tag{3.146}$$

where $\bar{\mathcal{S}}_{xx}^{\mathrm{zdf}}[\omega]$ is the spectral density of mechanical zero-point fluctuations[3]. This implies that the measurement process adds at least the zero-point noise on top of the intrinsic fluctuations, thereby cannot be arbitrarily small. The SQL, however, only coincides with Eq. (3.146) at $\omega = \omega_m$, whereas for all distinct frequencies, it does not represent any quantum bound. Different approaches have been done to surpass the SQL as a backaction-evading scheme proposed by Tsang and Caves [131, 132] and the exploitation of squeezed light [133, 134].

We now calculate the standard quantum limit on mechanical position measurement in optomechanics. Using the linearized Hamiltonian from Eq. (3.76), we consider an optical cavity driven on resonance ($\Delta = 0$), coupled to a mechanical oscillator via radiation pressure. Under this driving scheme, the interaction is described by Eq. (3.103). From Eq. (3.104), the dynamics of the cavity field fluctuations read

$$\mathcal{X}_c^{-1}[\omega]\hat{d}[\omega] = -iG\hat{x}_m[\omega] - \sqrt{\kappa}\hat{d}_{\mathrm{in}}[\omega] \tag{3.147}$$

with the cavity susceptibility given in Eq. (3.3), $\hat{x}_m \equiv \hat{b} + \hat{b}^\dagger$ and where we will assume $G \in \mathbb{R}$.

Next, we determine the detected power spectral density of the cavity's output field. To do this, we apply the input-output relation from Eq. (2.50), which gives

$$\hat{d}_{\mathrm{out}}[\omega] = (1 - \kappa\mathcal{X}_c[\omega])\,\hat{d}_{\mathrm{in}}[\omega] - i\sqrt{\kappa}G\mathcal{X}_c[\omega]\hat{x}_m[\omega]. \tag{3.148}$$

Through the interference of the detected field given by the last equation with a local oscillator field of the same carrier frequency, homodyne detection provides a measurement of an arbitrary quadrature $\hat{U}_{\mathrm{out}}$ of the detected optical field (see [27] for the mathematical treatment). Expressing the output field in the quadrature basis yields:

$$\hat{U}_{\mathrm{out}}[\omega] \equiv \frac{1}{\sqrt{2}}\left(\hat{d}_{\mathrm{out}}[\omega]e^{-i\theta} + \hat{d}_{\mathrm{out}}^\dagger[\omega]e^{i\theta}\right) \tag{3.149}$$

$$= (1 - \kappa\mathcal{X}_c[\omega])\,\hat{U}_{\mathrm{in}}[\omega] - \sqrt{2\kappa}G\mathcal{X}_c[\omega]\sin(\theta)\hat{x}_m[\omega], \tag{3.150}$$

where we used that in the zero detuning case $\mathcal{X}_c[\omega] = \mathcal{X}^*[-\omega]$. Here, we also introduced the input noise quadratures $\sqrt{2}\hat{U}_{\mathrm{in}}[\omega] = \hat{d}_{\mathrm{in}}[\omega]e^{-i\theta} + \hat{d}_{\mathrm{in}}^\dagger[\omega]e^{i\theta}$ and $\sqrt{2}\hat{V}_{\mathrm{in}}[\omega] = i(\hat{d}_{\mathrm{in}}^\dagger[\omega]e^{i\theta} - \hat{d}_{\mathrm{in}}[\omega]e^{-i\theta})$, where θ is the quadrature angle. Note, for $\sin(\theta) = 0$ this quadrature decouples from the mechanical mode, therefore the oscillator's information will be encoded in its orthogonal quadrature.

The frequency-symmetrized output noise spectral density is then defined as

$$\bar{\mathcal{S}}_{\mathrm{out}}[\omega] = \frac{1}{2}\left(\mathcal{S}_{\mathrm{out}}[\omega] + \mathcal{S}_{\mathrm{out}}[-\omega]\right), \quad \mathcal{S}_{\mathrm{out}}[\omega] = \int \frac{d\omega'}{2\pi}\langle\hat{U}_{\mathrm{out}}[\omega]\hat{U}_{\mathrm{out}}[\omega']\rangle, \tag{3.151}$$

where, from Eq. (3.60), we find that the noise correlators are given by

$$\begin{aligned}\langle\hat{U}_{\mathrm{in}}[\omega]\hat{U}_{\mathrm{in}}[\omega']\rangle &= \langle\hat{V}_{\mathrm{in}}[\omega]\hat{V}_{\mathrm{in}}[\omega']\rangle = \pi\delta[\omega + \omega'],\\ \langle\hat{U}_{\mathrm{in}}[\omega]\hat{V}_{\mathrm{in}}[\omega']\rangle &= -\langle\hat{V}_{\mathrm{in}}[\omega]\hat{U}_{\mathrm{in}}[\omega']\rangle = i\pi\delta[\omega + \omega'].\end{aligned} \tag{3.152}$$

Hence, using Eq. (3.150) into Eq. (3.151), we get

$$\mathcal{S}_{uu}^{\mathrm{out}}[\omega] = \mathcal{S}_{11}[\omega] + 2\kappa G^2|\mathcal{X}_c[\omega]|^2\sin^2(\theta)\mathcal{S}_{xx}[\omega], \tag{3.153}$$

with the bare cavity's response $\bar{\mathcal{S}}_{11}[\omega] = 1/2$ and where the last term in Eq. (3.153) is defined by the oscillator's position spectral density.

The oscillator's position spectral density is defined by

$$\mathcal{S}_{xx}[\omega] = \int_{-\infty}^{\infty}\frac{d\omega'}{2\pi}\langle\hat{x}_m[\omega]\hat{x}_m[\omega']\rangle \tag{3.154}$$

[3]Here, following the derivation of Eq. (3.42), we used the FDT at $T = 0$ to introduce $\bar{\mathcal{S}}_{xx}^{\mathrm{zdf}}[\omega] = |\mathrm{Im}\{\mathcal{X}_{xx}[\omega]\}|$ with the oscillator's susceptibility $m_{\mathrm{eff}}\mathcal{X}_{xx}^{-1}[\omega] = \left[(\omega_m^2 - \omega^2) - i\gamma_m\omega\right]^{-1}$.

and quantifies the oscillator's ability to absorb and emit phonons into its environment for different frequencies. For an uncoupled oscillator ($G = 0$) in thermal equilibrium, the last equation reads

$$\mathcal{S}^0_{xx}[\omega] = \gamma_m \left(|\mathcal{X}_m[\omega]|^2 \left(\bar{n}^T_m + 1 \right) + |\mathcal{X}_m[-\omega]|^2 \bar{n}^T_m \right). \quad (3.155)$$

Moreover, for a high-quality mechanical oscillator ($\omega_m \gg \gamma_m$) coupled to a zero temperature bath $\bar{n}^T_m = 0$, the oscillator's spectrum becomes simply $\mathcal{S}^0_{xx}[\omega_m] \approx 2/\gamma_m$.

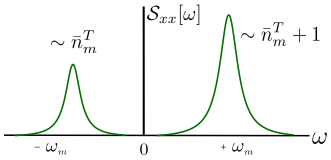

FIGURE 3.15: Oscillator's position spectrum

From the quantum Langevin equations of motion given in Eq. (3.104) we find the effective dynamics of the mechanical position operator

$$\hat{x}_m[\omega] = -\sqrt{\gamma_m} \left(\mathcal{X}_m[\omega] \hat{b}_{\rm in}[\omega] + \mathcal{X}^*_m[-\omega] \hat{b}^\dagger_{\rm in}[\omega] \right) - \frac{\Sigma_m[\omega]}{|G|^2} \hat{F}[\omega], \quad (3.156)$$

where we introduced the *mechanical self-energy*

$$\Sigma_m[\omega] \equiv \frac{2|G|^2 \omega_m}{(-i\omega + \frac{\gamma_m}{2})^2 + \omega_m^2}. \quad (3.157)$$

The first term in Eq. (3.156) corresponds to the intrinsic noise contribution of the mechanical mode, whereas the second term is the hermitian contribution of the cavity, where we introduced the *linearized force operator* defined

$$\hat{F} \equiv G \left(\hat{d} + \hat{d}^\dagger \right). \quad (3.158)$$

Under the zero detuning assumption the cavity self-energy given in Eq. (5.13) vanishes and the force operator becomes

$$\hat{F}[\omega] = -\sqrt{\kappa} \mathcal{X}_c[\omega] \left(\hat{d}_{\rm in}[\omega] + \hat{d}^\dagger_{\rm in}[\omega] \right), \quad (3.159)$$

which features no dynamical backaction contribution from the mechanics. The oscillator's spectral density defined in Eq. (3.154) then reads

$$\mathcal{S}_{xx}[\omega] = \mathcal{S}^0_{xx}[\omega] + \left| \frac{\Sigma_m[\omega]}{G^2} \right|^2 \mathcal{S}_{FF}[\omega] \quad (3.160)$$

with the uncoupled oscillator's spectrum given in Eq. (3.155) and the force noise spectral density given by Eq. (3.128) for $\Delta = 0$.

Moreover, for a high-quality factor oscillator at $\bar{n}^T_m = 0$ we have that $\Sigma_m[\omega_m]/G^2 = i\mathcal{S}^0_{xx}[\omega_m]$, such that Eq. (3.160) becomes

$$\mathcal{S}_{xx}[\omega_m] = \mathcal{S}^0_{xx}[\omega_m] + \left(\mathcal{S}^0_{xx}[\omega] \right)^2 \mathcal{S}_{FF}[\omega_m]. \quad (3.161)$$

From Eqs. (3.153) and (3.161) we find the following expression

$$\mathcal{S}^{\rm out}_{uu}[\omega_m] = 2\mathcal{S}_{FF}[\omega_m] \sin^2(\theta) \left(\mathcal{S}^0_{xx}[\omega_m] + \underbrace{\left(\mathcal{S}^0_{xx}[\omega] \right)^2 \mathcal{S}_{FF}[\omega_m] + \mathcal{S}_{\rm imp}[\omega_m]}_{\text{added noise}} \right), \quad (3.162)$$

where the added noise is given by the last two terms inside the parenthesis. For a *quantum-limited detector* we have $\mathcal{S}_{\rm imp}[\omega_m]\mathcal{S}_{FF}[\omega_m] = 1/4$, such that the added noise becomes [130]

$$\mathcal{S}_{\rm add}[\omega_m] = \left(\mathcal{S}^0_{xx}[\omega] \right)^2 \mathcal{S}_{FF}[\omega_m] + \frac{1}{4\mathcal{S}_{FF}[\omega_m]}. \quad (3.163)$$

Hence, the backaction is proportional to the coupling of the oscillator to the detector and the intensity of the drive on the cavity. The added noise given by the last equation is minimized

when the drive is tuned such that the following is satisfied

$$\mathcal{S}_{FF}^{\mathrm{opt}}[\omega_m] = \left(2\mathcal{S}_{xx}^{0}[\omega_m]\right)^{-1}. \tag{3.164}$$

Under optimal driving conditions, the added noise is minimized, leading to $\mathcal{S}_{\mathrm{add}}^{\mathrm{opt}}[\omega_m] = \mathcal{S}_{xx}^{0}[\omega_m]$, and consequently to $\mathcal{S}_{uu}^{\mathrm{out}}[\omega_m] = 2\sin^2(\theta)$.

In Fig. 3.16 we show the imprecision and backaction noise contributions as a function of the input power using a linear cavity operating at zero detuning. Under optimal conditions, namely when Eq. (3.164) is satisfied, the added noise is minimized and the SQL on position detection is reached as shown in Fig. 3.16.

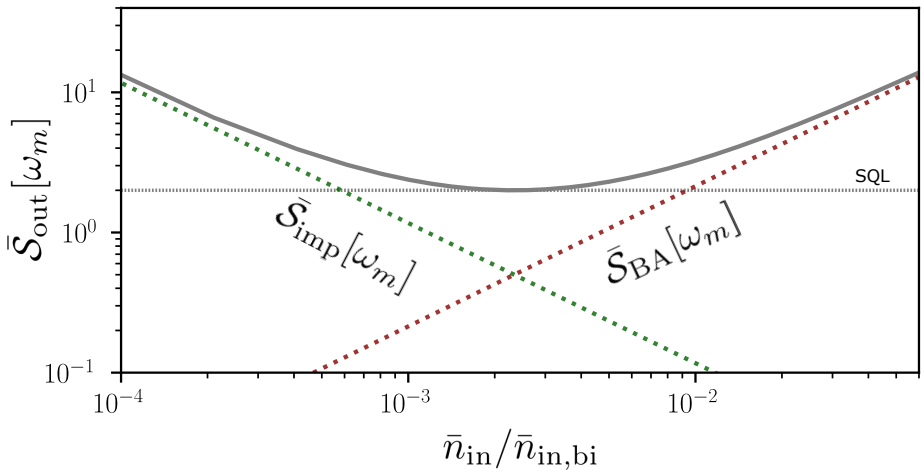

FIGURE 3.16: The measured noise spectral density at the detector, evaluated at the mechanical resonance frequency, is plotted as a function of the cavity's input power. This spectral density includes the intrinsic noise contribution of the linear cavity, along with the added noise due to measurement imprecision (dashed-green) and backaction heating (dashed-red) of the oscillator. For weak driving powers, imprecision noise dominates. Conversely, as driving power increases, the imprecision noise decreases while backaction noise becomes more significant. The intersection of these two contributions marks the point of minimum added noise, corresponding to the standard quantum limit.

3.9 Optomechanically induced transparency (OMIT)

So far we have described optomechanical effects that occur when the cavity is driven coherently by a single tone. Nevertheless, the use of multiple optical drives enables more complicated phenomena, such as *optomechanically induced transparency* (OMIT) [25]. Similarly to *electromagnetically induced transparency* (EIT) [135, 136], in OMIT a cavity is simultaneously driven by a weak *probe field* and a strong *control field*, where the former is set at a frequency near the cavity resonance frequency and the latter is set at the lower mechanical sideband as illustrated in Fig. 3.17. The field of OMIT has led to several applications such as *slow light* [137, 138] and the enhancement of Kerr-nonlinearities [139]. As we will see later in this work, recently OMIT has also been realized using photon-pressure interaction between superconducting circuits to measure the single-photon coupling rate of the system [140].

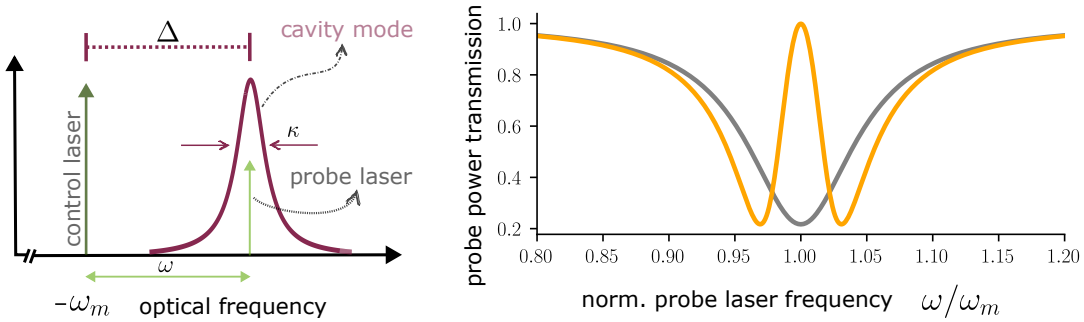

FIGURE 3.17: (left) Schematic for optomechanically induced transparency. A strong control field on the red mechanical sideband ($\Delta = -\omega_m$) drives the optomechanical system. Additionally, a weak probe laser scans across the cavity's resonant frequency and analyses the response (right) of the driven system. The transparency window appears when the probe laser is tuned at the cavity resonance, whose decay rate is $\kappa = \kappa_{\rm ext} + \kappa_{\rm int}$.

Recalling the linearized optomechanical system described by the Hamiltonian given in Eq. (3.76), we know from Section 3.5 that the resonant Hamiltonian for a red-detuned driven optomechanical system within the resolved sideband regime is effectively given by

$$\hat{\mathcal{H}}_{\rm eff} = -\Delta \hat{d}^\dagger \hat{d} + \omega_m \hat{b}^\dagger \hat{b} + G\left(\hat{d}\hat{b}^\dagger + \hat{d}^\dagger \hat{b}\right). \tag{3.165}$$

The quantum Langevin equations of motion of the cavity are given by

$$\frac{d}{dt}\hat{d} = \left(i\Delta - \frac{\kappa}{2}\right)\hat{d} - iG\hat{b} - \sqrt{\kappa\eta}\hat{d}_{\rm in} - \sqrt{\kappa(1-\eta)}\xi_{\rm in} \tag{3.166}$$

with the coupling parameter

$$\eta \equiv \frac{\kappa_{\rm ext}}{\kappa_{\rm ext} + \kappa_{\rm int}}, \tag{3.167}$$

where $\kappa_{\rm int}$ and $\kappa_{\rm ext}$ denote the intrinsic and external loss rates, respectively. Note that, due to the two driving fields, here we are explicitly separating the decay rate into the internal and external contributions as explained in Eq. (3.1). On the other hand, for the mechanics we have

$$\frac{d}{dt}\hat{b} = -\left(i\omega_m + \frac{\gamma_m}{2}\right)\hat{b} - iG\hat{d} - \sqrt{\gamma_m}\hat{b}_{\rm in} \tag{3.168}$$

In the frequency domain, the equations of motion of the modes become

$$\mathcal{X}_c^{-1}[\omega]\hat{d}[\omega] = -iG\hat{b}[\omega] - \sqrt{\kappa\eta}\hat{d}_{\rm in}[\omega] - \sqrt{\kappa(1-\eta)}\xi_{\rm in}[\omega], \tag{3.169}$$

$$\mathcal{X}_m^{-1}[\omega]\hat{b}[\omega] = -iG\hat{d}[\omega] - \sqrt{\gamma_m}\hat{b}_{\rm in}[\omega], \tag{3.170}$$

with the cavity susceptibility, $\mathcal{X}_c[\omega]$, given in Eq. (3.3) and the mechanical susceptibility given by $\mathcal{X}_m^{-1}[\omega] = -i(\omega - \omega_m) + \gamma_m/2$. This system of equations can be easily solved yielding

$$\mathcal{X}_c^{-1}[\omega]\hat{d}[\omega] = -G^2\mathcal{X}_m[\omega]\hat{d}[\omega] + iG\sqrt{\gamma_m}\mathcal{X}_m[\omega]\hat{b}_{\rm in}[\omega] - \sqrt{\kappa\eta}\hat{d}_{\rm in}[\omega] - \sqrt{\kappa(1-\eta)}\xi_{\rm in}[\omega], \tag{3.171}$$

which can be rewritten as

$$\hat{d}[\omega] = \mathcal{X}_{aa}[\omega]\hat{d}_{\rm in}[\omega] + \mathcal{X}_{ab}[\omega]\hat{b}_{\rm in}[\omega] + \mathcal{X}_{aa}^{\rm int}[\omega]\xi_{\rm in}[\omega] \tag{3.172}$$

with

$$\mathcal{X}_{aa}[\omega] = -\frac{\sqrt{\kappa\eta}}{\mathcal{X}_c^{-1}[\omega] + G^2\mathcal{X}_m[\omega]}, \qquad \mathcal{X}_{ab}[\omega] = \frac{iG\sqrt{\gamma_m}\mathcal{X}_m[\omega]}{\mathcal{X}_c^{-1}[\omega] + G^2\mathcal{X}_m[\omega]} \tag{3.173}$$

and the internal-loss susceptibility

$$\mathcal{X}_{aa}^{\text{int}}[\omega] = -\frac{\sqrt{\kappa(1-\eta)}}{\mathcal{X}_c^{-1}[\omega] + G^2\mathcal{X}_m[\omega]} \tag{3.174}$$

Here, $\mathcal{X}_{aa}[\omega]$ is the *cavity-to-cavity*, whereas $\mathcal{X}_{ab}[\omega]$ corresponds to the *cavity-to-oscillator* susceptibilities. Note that the full optical susceptibility leads no longer to the usual Lorentzian describing a bare optical resonance, but is modified by the radiation pressure interaction with the mechanical mode. Additionally, the optomechanical interaction introduces a second input noise given by the second term in Eq. (3.172).

Finally, using the input-output relation given in Eq. (2.50) we find from Eq. (3.172)

$$\hat{d}_{\text{out}}[\omega] = \mathcal{T}[\omega]\hat{d}_{\text{in}}[\omega] + \mathcal{L}[\omega]\hat{b}_{\text{in}}[\omega] \tag{3.175}$$

with

$$\mathcal{T}[\omega] = 1 - \sqrt{\kappa\eta}\mathcal{X}_{aa}[\omega], \quad \mathcal{L}[\omega] = -\sqrt{\kappa\eta}\mathcal{X}_{ab}[\omega], \quad |\mathcal{T}[\omega]|^2 + |\mathcal{L}[\omega]|^2 = 1 \tag{3.176}$$

where $\mathcal{T}[\omega]$ is a complex, frequency-dependent transmission coefficient representing the portion of the incident field that persists in the output field of the optomechanical system, and $\mathcal{L}[\omega]$ represents the fraction of the mechanical bath fluctuations that are transferred onto the output field. Since $\Delta = -\omega_m$, the interaction is described by a beam-splitter type of coupling, hence $\mathcal{T}[\omega]$ and $\mathcal{L}[\omega]$ can be considered as scattering amplitudes, with $\mathcal{L}[\omega]$ not only quantifying the level of mechanical fluctuations imprinted on the output field but also the loss (or absorption) of the optical field by the mechanical bath [27].

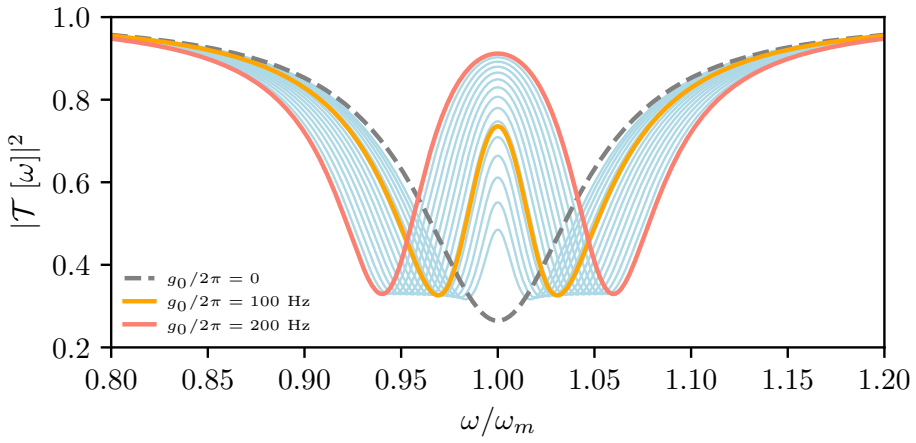

FIGURE 3.18: Optomechanically induced transparency. Transmissivity as a function of the driving frequency ω for different optomechanical coupling strengths. In the absence of optomechanical coupling strength, the response of the cavity depicts the usual Lorentzian. However, turning on the interaction leads to the emergence of the transparency window, which approaches the unity as the coupling strength increases. For this plot: $\omega_m/\kappa = 10$, $\omega_c/2\pi = 7$ GHz, $\Delta = -\omega_m$, $\kappa_{\text{ext}}/2\pi = 85$ kHz and $\kappa_{\text{int}}/2\pi = 265$ kHz.

Explicitly the transmissivity is given by which for $\Delta = -\omega_m$ it becomes

$$\mathcal{T}[\omega] = 1 - \frac{\kappa_{\text{ext}}}{-i(\omega-\omega_m) + \frac{\kappa}{2} + \frac{G^2}{-i(\omega-\omega_m)+\frac{\gamma_m}{2}}}, \tag{3.177}$$

such that for $\omega = \omega_m$ it yields

$$\mathcal{T}[\omega_m] = 1 - \frac{\kappa_{\text{ext}}}{\frac{\kappa}{2} + \frac{2G^2}{\gamma_m}} \equiv 1 - \frac{2\eta}{1+\mathcal{C}}, \tag{3.178}$$

where we introduced $\eta = \kappa_{\text{ext}}/\kappa$ and the *optomechanical cooperativity* $\mathcal{C} = 4G^2/\kappa\gamma_m$. Furthermore, for the critical value $\eta = 1/2$ we find

$$|\mathcal{T}[\omega_m]|^2 = \frac{\mathcal{C}^2}{(1+\mathcal{C})^2}, \tag{3.179}$$

such that for $\mathcal{C} \to \infty$ the on-resonance transmissivity approaches the unity, while for $\mathcal{C} = 1$ the optomechanical system acts as a balanced but lossy beam-splitter since it changes the transmission to 50%.

Additionally one can linearize the mechanical susceptibility around $\Delta' = \omega - \omega_m$ such that the transmissivity in Eq. (3.177) becomes

$$\mathcal{T}[\omega] = 1 - \frac{\kappa\eta}{-i\Delta' + \frac{\kappa}{2} + \frac{g^2}{-i\Delta' + \frac{\gamma}{2}}}, \tag{3.180}$$

Again, for the critical coupling, $\eta = 1/2$, under the assumption that the optical losses are stronger than the optomechanical coupling, one approximate $-i\Delta' + \kappa/2 \approx \kappa/2$, such that the last equation yields

$$|\mathcal{T}|^2 = \frac{16G^4/\kappa^2}{4\Delta'^2 + \Gamma_{\text{omit}}^2} = \frac{\mathcal{C}^2}{\left(\frac{2\Delta'}{\gamma_m}\right)^2 + (1+\mathcal{C})^2} \tag{3.181}$$

with $\Gamma_{\text{omit}} \equiv \gamma_m + 4G^2/\kappa$. The last equation describes the optomechanically induced transparency window, which results in a Lorentzian with width given by Γ_{omit} and peak when $\Delta' = 0$ resulting in Eq. (3.179). Nevertheless, the underlying approximations leading to these results require two coherent fields, which maintain their coherence for times longer than the mechanical damping time.

The appearance of the transparency window illustrated in Fig. 3.18 for $g_0 \neq 0$ can be understood in a sideband picture. In this case, the probe and control fields both generate a radiation pressure oscillating at the frequency difference ω. If this driving force oscillates near the mechanical resonance frequency ω_m, then the mechanical mode starts to oscillate coherently creating a sideband on the intracavity field. This leads to Stokes and anti-Stokes scattering processes originating from the control field. Furthermore, if the system is deep in the resolved sideband regime $\kappa \ll \omega_m$ then the Stokes scattering is suppressed due to being far off-resonant with the cavity resonance. In contrast, the anti-Stokes process builds up inside the cavity, since it is resonant and phase-coherent with the probe field. This leads to destructive interference between these driving waves that cancel the intracavity field on resonance, giving rise to the transparency window of width Γ_{omit}. Note that, at stronger driving power this effect evolves into a normal mode splitting [1].

Furthermore, if we consider a field injected into the upper sideband ($\Delta = \omega_m$) instead of having a red-detuned control field, an additional optical signal in the probe field gets amplified, resulting in the so-called optomechanically induced amplification [137, 138]. While this is an interesting effect, it is beyond the scope of this work.

Throughout this Chapter, we have explored the fundamental aspects of optomechanical interactions. We began by introducing optical, mechanical, and microwave resonators—key components in the field of optomechanics. Additionally, with the advancements in optomechanics, we clarified that experiments are not limited to the optical regime but can also be conducted in the microwave domain. We introduced the concept of quantum noise, essential for characterizing systems through their signal's power spectral density. Moving forward, we outlined the Hamiltonian formulation of an optomechanical system, which serves as the foundation for describing the interaction between a cavity and a vibrational mode. We derived the system's dynamics in a displaced frame, leading to the linearized Hamiltonian and the corresponding linearized equations of motion for both modes. This linearized framework allowed us to explore various driving schemes, resulting in different phenomena, including optomechanical cooling, amplification, and quantum non-demolition measurements. Furthermore, by analyzing the mechanical mode dynamics, we introduced key effects mediated by radiation pressure interactions: backaction cooling and the optical spring effect.

In this chapter, we also reviewed one of the primary applications of optomechanical systems: their use as highly sensitive detectors. By employing a quantum noise approach, we analyzed the various contributions to the measurement of mechanical motion and demonstrated that, under optimal conditions, an optical cavity can reach the SQL in position detection.

Additionally, we studied sideband cooling, also known as dynamical backaction, which has been employed to cool a mechanical mode to its ground state [141]. We reviewed two distinct approaches to determine the average mechanical occupation. The first method used the emission and absorption rates given in Eq. (3.125) within the master equation formalism. In the second method, we used the input-output formalism to derive the mechanical occupation through the effective dynamics of the mechanical mode. Both approaches concluded that ground-state cooling is achievable only when the system is in the resolved sideband regime, where $\kappa/\omega_m < 4\sqrt{2}$. This regime maximizes the asymmetry between the Stokes and anti-Stokes rates, resulting in higher optical damping, $\Gamma_{\rm opt} > 0$, as shown in Fig. 3.11.

We also clarified that the mechanical occupation given in Eq. (3.130) deviates from the numerical solution of Eq. (3.138) at higher optomechanical coupling strengths. In such cases, nonlinear effects of the radiation pressure interaction become significant, introducing additional heating into the mechanical mode, as illustrated in Fig. 3.14.

Last but not least, we introduced optomechanically induced transparency (OMIT), a phenomenon that arises from the destructive interference of intracavity fields when both strong control and weak probe fields are present.

Up to this point, we have concentrated solely on optomechanical systems with linear cavities. However, in the next Chapter, we will shift our focus to nonlinear cavities and explore how their intrinsic nonlinearity plays a crucial role in enhancing sideband cooling protocols.

Chapter 4

Nonlinear Kerr cavities

In Chapter 3 we introduced the basic aspects of optomechanics, where an optical cavity interacts with a vibrational mode through radiation pressure. In that Chapter, we revisited some dynamical effects that arise due to the optomechanical interaction, including dynamical backaction cooling and the optical spring effect. Additionally, the optomechanical interaction also gives rise to some static phenomena such as optical bistability [142]. This effect arises from the nonlinear nature of the optomechanical interaction, where the radiation pressure force displaces the mechanical element, shifting the cavity resonance, which in turn affects the intracavity light intensity. In the presence of sufficiently strong enough driving, this feedback loop triggers a nonlinear behaviour, which depending on the input power and optical detuning, can result into two stable system configurations.

Under specific conditions, the radiation pressure interaction leads to nonlinear effects, this is because the optomechanical interaction is inherently nonlinear. For sufficiently strong input power and blue-detuned driving, it has been shown that optomechanics results, for instance, into chaotic motion [143], multisability [144] and instability [60]. For a red-detuned drive, however, this nonlinear nature leads to the emergence of a bistable regime in the circulating photon number as shown in Fig. 3.8. Moreover, this effect is not limited to the optical domain but has also been demonstrated in the microwave regime [145].

The steady-state solution of the average cavity amplitude led us to the cubic Eq. (3.67) describing the average number of photons inside the cavity. This cubic equation also allows us to compute the values at bifurcation analytically given in Eq. (3.72). In the early months of 1994 both C. Fabre *et. al.* [146], and S. Mancini and P. Tombesi [147] showed that close to these critical values, the squeezing of the cavity mode due to the optomechanical interaction is maximized resulting in a significant reduction of quantum noise in one quadrature at the expense of increased noise in the orthogonal quadrature. In addition, it has also been demonstrated that near the bifurcation point entanglement is maximized [72, 148].

The emergence of two stable solutions in the intracavity photon number for specific input powers and optical detuning, resulting from the optomechanical interaction, is analogous to the behaviour of a Kerr medium, an equivalence that has already been studied [149]. The optical Kerr effect dates back to 1956 with the classical formulation in liquids done by Buckingham [150]. A decade later, its quantum theory using the density matrix formalism was presented [151]. Due to their application, for instance, in squeezing generation [152, 153], QND measurements [154] and photonic-based quantum technology [155, 156], devices containing a Kerr medium have been extensively studied [157]. Moreover, Kerr-nonlinear resonators have also been shown to be promising for quantum-limited amplification [158, 159] and in the creation of photonic cat states [160]. For the latter, the consideration of higher-order anharmonicities as found in superconducting devices leads to shorter cat state preparation time [161].

The Kerr effect is a nonlinear process involving the third-order nonlinear polarizability of a medium. In such a nonlinear medium, the field undergoes a phase shift that depends on its intensity. Consequently, the refractive index of the medium scales with the intensity of the field. The Hamiltonian describing a Kerr nonlinear cavity is given by [162, 163]

$$\hat{\mathcal{H}} = \omega_c \hat{a}^\dagger \hat{a} - \frac{\mathcal{K}}{2} \hat{a}^\dagger \hat{a}^\dagger \hat{a} \hat{a}, \tag{4.1}$$

where ω_c and $\mathcal{K}$ denote the cavity resonance frequency and the Kerr constant, respectively, where the latter is typically considered to be $\mathcal{K} > 0$. Here, $\hat{a}$ and $\hat{a}^\dagger$ are the cavity mode

bosonic annihilation and creation operators.

As we discussed earlier, nonlinear optical phenomena, such as the Kerr effect, have a wide range of applications. In optical cavities, the Kerr effect arises from the refractive index's dependence on the medium, while in optomechanics, bistability emerges due to the optomechanical interaction. However, these nonlinear effects are not confined to the optical domain; they also occur in the microwave domain, where the nonlinearity can be engineered by incorporating superconducting devices, like a Josephson junction, into a circuit, as we will explore below.

4.1 Superconducting nonlinear cavities

In Chapter 3, we demonstrated that an optomechanical system exhibits bistability at certain drive powers. This is a nonlinear effect, as indicated by Eq. (3.67) and illustrated in Fig. 3.8, resembling the behaviour of an optical cavity with inherent nonlinearity, such as a Kerr medium. Motivated by the applications of nonlinear optical phenomena discussed earlier, the quest to engineer such anharmonicities has led researchers to explore various experimental platforms. Next, we will show how quantum systems based on superconducting circuits enable the possibility of engineering such nonlinearities for specific purposes.

As the name suggests, *superconducting* materials allow current to flow without resistance by forming *Cooper pairs*. The formation of Cooper pairs creates an energy gap between the ground state and the next available energy state. This gap inhibits small excitations and electron scattering, which are the primary sources of electrical resistance in normal conductors. Furthermore, at low temperatures, Cooper pairs *condense* into the lowest energy state, preventing scattering from lattice vibrations and significantly reducing resistance. The superconductive state of Cooper pairs is linked to phenomena like Bose-Einstein condensation, making it inherently quantum. Superconductivity is observed in certain materials when their temperature drops below a critical threshold[1].

Besides being perfect conductors, superconductors have also another property: their internal magnetic field vanishes. Superconductors act as perfect diamagnets because of the Meissner-Ochsenfeld effect, which causes them to repel magnetic fields. Nevertheless, depending on the material, superconductivity breaks down for certain critical magnetic fields and temperatures. Furthermore, in a closed superconducting loop, the internal magnetic field can be quantized via the flux quantum

$$\Phi_0 = \frac{h}{2e}, \tag{4.2}$$

where e is the electron charge.

In Chapter 3, we showed that the Hamiltonian describing an LC circuit in Eq. 3.15 is equivalent to that of a quantum harmonic oscillator with frequency $\omega_c = \sqrt{1/LC}$. Due to their extremely high-quality factors and long coherence times, superconducting microwave cavities represent a promising platform for quantum information applications [164]. However, for quantum information processing, the equidistant energy levels of the quantum harmonic oscillator pose a limitation in terms of frequency selectivity, as individual transitions cannot be addressed separately. To overcome this, engineered nonlinearities are introduced into the system, modifying the energy spacing for specific applications. In LC circuits a Josephson junction is often employed to introduce nonlinearity into the system.

A Josephson junction is a device that is composed by a non-superconducting thin layer placed between two superconductors as shown in Fig. 4.2. Below a specific critical temperature, Cooper pairs can tunnel across the barrier without resistance, leading to a *supercurrent*. The first Josephson junction relation reads

$$I(t) = I_\mathrm{c} \sin(\delta), \tag{4.3}$$

where I_c is the critical current of the junction and δ is the phase difference across the junction. The phase δ is often referred to as the *reduced flux* defined as $\delta = 2\pi\Phi/\Phi_0$, which represents

[1] In the experiments conducted by D. Zoepfl *et al.* [3] and L. Deeg *et al.* [35], niobium and aluminium were commonly used, with critical temperatures of $T_c = 9.25$ K and $T_c = 1.19$ K, respectively.

a good quantum number associated with quantum or thermal fluctuations in the magnetic flux through the junction. The last equation describes the supercurrent that flows through the junction, which indicates that the superconductivity in the junction breaks if the current flowing across it surpasses the critical value I_c. The second Josephson relation characterises the time evolution of its phase difference when a voltage is applied

$$\frac{d}{dt}\delta = \frac{2\pi}{\Phi_0}U, \tag{4.4}$$

with U being the voltage across the junction. This equation will be fundamental to many applications of Josephson junctions such as extremely sensitive magnetometers.

Recalling Eqs. (3.7) and (3.8), it is now possible to combine them with the Josephson relations Eqs. (4.3) and (4.4) and obtain

$$U = \frac{L_{j0}}{\cos(\delta)}\dot{I}, \tag{4.5}$$

where we introduced the Josephson inductance

$$L_{j0} = \frac{\Phi_0}{2\pi I_c}. \tag{4.6}$$

As described by Eq. (4.5), the Josephson junction behaves like a nonlinear inductor, since its inductance depends on the current that flows through it, unlike the linear ones whose inductance is constant. Additionally, since it behaves like an inductor it consequently stores energy, which is given by

$$E_j(\delta) = -\frac{I_c\Phi_0}{2\pi}\cos(\delta) \equiv -E_{j0}\cos(\delta). \tag{4.7}$$

Furthermore, since δ is small, we can Taylor expand this potential yielding

$$E_{j0}\cos(\delta) = 1 - \frac{1}{2}E_{j0}\delta^2 - \frac{1}{24}E_{j0}\delta^4 + \mathcal{O}\left(\delta^6\right), \tag{4.8}$$

where the first term is usually neglected as it represents a constant energy shift. Taking only the quadratic term in the last equation would lead us to the Hamiltonian in Eq. (3.15) of a harmonic oscillator. However, the quartic term given by the second term gives rise to a modification of the energy structure of the harmonic oscillator, thereby represents the nonlinearity in the system.

By replacing the linear inductor of the LC circuit with a Josephson junction, we can ultimately make the microwave cavity effectively nonlinear. This replacement modifies the Hamiltonian given in Eq. (3.15), which by including terms up to fourth order in Eq. (4.8) becomes

$$\hat{\mathcal{H}} = \frac{Q^2}{2C} - \frac{1}{2}E_{j0}\delta^2 + \frac{1}{24}E_{j0}\delta^4. \tag{4.9}$$

Now, rescaling the operators introduced in Eq. (3.14) in terms of the reduced flux, δ, one find that the Hamiltonian resembles that of a Duffing oscillator [110, 165]

$$\hat{\mathcal{H}} = \omega_c\hat{a}^\dagger\hat{a} + \frac{\mathcal{K}}{2}\hat{a}^\dagger\hat{a}^\dagger\hat{a}\hat{a}, \tag{4.10}$$

where we have ignored fast-rotating terms and

$$\mathcal{K} = -\frac{\omega_c Z_0 e^2}{2}\left(\frac{L_j}{L_{tot}}\right)^3. \tag{4.11}$$

With the Hamiltonian in Eq. (4.10), we have shown that a microwave resonator can be made intrinsically nonlinear by replacing the linear inductor by a Josephson junction. Next, we will present one of the main applications of Josephson junctions and how they can be used as magnetic field detectors.

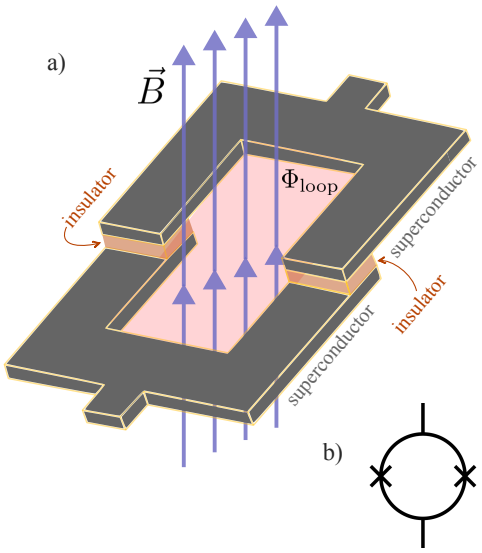

FIGURE 4.1: Both a) and b) show an illustration of a SQUID. a) shows the two Josephson junctions connected in parallel, which can be regarded as a single junction with a critical current that depends on the magnetic field. b) illustrates how a SQUID is typically pictured in circuits.

4.1.1 SQUID and SQUID resonators

We will now consider a superconducting loop containing two Josephson junctions in parallel as illustrated in Fig. 4.1. This architecture describes what is called a *superconducting quantum interference device* (SQUID) [166]. Under the assumption that the critical currents for the two junctions are equal, the use of Kirchhoff's law allows us to calculate the total current as

$$I = I_1 + I_2 = 2I_c \cos\left(\frac{\delta_1 - \delta_2}{2}\right) \sin\left(\frac{\delta_1 + \delta_2}{2}\right). \tag{4.12}$$

Assuming that only an external flux Φ_{ext} penetrates the loop, from the quantization of the magnetic flux in Eq. (4.2), we obtain

$$\delta_2 - \delta_1 = 2\pi \frac{\Phi_{\text{ext}}}{\Phi_0}, \tag{4.13}$$

such that the phase difference between the junctions has to be equal to the external flux. Using this expression in Eq. (4.12) we find the critical current of the SQUID

$$I_c^{\text{SQUID}} = 2I_c \left|\cos\left(\frac{\pi\Phi_{\text{ext}}}{\Phi_0}\right)\right|. \tag{4.14}$$

This implies that the critical value can be adjusted by varying the external flux. The last equation enables us to calculate the SQUID's inductance. Using Eq. (4.6), we find that the inductance is also dependent on the external flux, specifically:

$$L^{\text{SQUID}} = \frac{L_{\text{j0}}}{2} \left|\cos\left(\frac{\pi\Phi_{\text{ext}}}{\Phi_0}\right)\right|^{-1}. \tag{4.15}$$

So far we have conveniently assumed that the flux $\Phi_{\text{loop}} = \Phi_{\text{ext}}$. However, generally, they differ due to flux generated by currents flowing in the geometric inductance of the SQUID. To account for these additional magnetic fields that penetrate the loop one has to consider the so-called *screening factor*. Additional information about this can be found in [111, 112, 167].

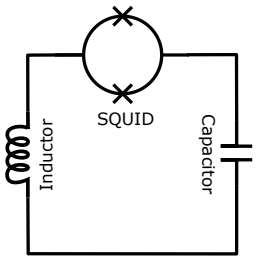

FIGURE 4.2: SQUID resonator composed by an LC circuit with a SQUID in series. This behaves like a nonlinear resonator due to the nonlinear inductance of the SQUID. In the presence of the SQUID, the resonance frequency is also flux-dependent.

Recalling our analysis in Chapter 3.2, the frequency of an LC resonator is described by Eq. (3.10). Placing a SQUID in the LC resonator makes its resonance frequency tunable, due to the SQUID's flux dependence as we shown in Eq. (4.15). Hence, the resonance frequency of an LC resonator with an embedded SQUID as illustrated in Fig. 4.2 is given by

$$\omega_c(\Phi) = \frac{1}{\sqrt{[L + L^{\mathrm{SQUID}}(\Phi)]\, C}} \tag{4.16}$$

with the SQUID inductance given in Eq. (4.15). Due to the flux dependence of the resonance frequency, the SQUID can be used as a highly sensitive magnetic field sensor with important applications in medicine.

To this point, we have discussed how the optomechanical interaction leads to bistability, an optical nonlinear effect that resembles a cavity with a Kerr medium. As mentioned before, such nonlinear effects have a wide range of applications, not only in the optical domain but also in the microwave regime. In the latter, the ability to engineer the interaction in high-Q microwave resonators enables its use in quantum information applications. Optomechanical bistability, however, is a static optical phenomenon observed in the steady-state regime when the system has settled into a stable configuration. In the next section, we will explore the dynamics arising from the nonlinear Hamiltonian in Eq. (4.1), which describes a Duffing oscillator.

4.2 Dynamics

The Hamiltonian describing a driven nonlinear cavity is given below

$$\hat{\mathcal{H}} = -\Delta \hat{a}^\dagger \hat{a} - \frac{\mathcal{K}}{2} \hat{a}^\dagger \hat{a}^\dagger \hat{a}\hat{a} - i\sqrt{\kappa}\left(\alpha_{\mathrm{in}} \hat{a}^\dagger + \alpha_{\mathrm{in}}^* \hat{a}\right), \tag{4.17}$$

which is in a frame rotated with respect to the drive frequency, ω_p, and where $\Delta = \omega_p - \omega_c$ denotes the cavity detuning. Similarly, as in Chapter 3.4.2, the dynamics of a nonlinear Kerr cavity can be obtained using the input-output formalism (see Chapter 2.3) yielding

$$\frac{d}{dt}\hat{a} = \left(i\Delta - \frac{\kappa}{2}\right)\hat{a} + i\mathcal{K}\hat{a}^\dagger \hat{a}\hat{a} - \sqrt{\kappa}\hat{a}_{\mathrm{in}}, \tag{4.18}$$

where κ is the cavity decay rate comprising internal and external losses. To solve the equations of motion of such a nonlinear system, we will coherently drive the system with an external pump and linearize its dynamics, as we did in Chapter 3.

Assuming a strong coherent drive, we can proceed following Chapter 3, and derive the equation of motion of the classical cavity amplitude

$$\frac{d}{dt}\alpha = \left(i\Delta - \frac{\kappa}{2}\right)\alpha + i\mathcal{K}\alpha|\alpha|^2 - \sqrt{\kappa}\alpha_{\mathrm{in}}. \tag{4.19}$$

This equation is equivalent to the result obtained in Eq. (3.65) with the only distinction arising from the origin of the Kerr nonlinearity. In Eq. (3.65), the Kerr nonlinearity emerges from the optomechanical interaction. Contrary, in Eq. (4.19) it results from the intrinsic cavity

nonlinearity. Proceeding similarly as in Chapter 3, we multiply the steady-state solution of the last equation by its complex conjugate to obtain an equation describing the circulating intracavity photon number. Hence, we find

$$\bar{n}_c \left[(\Delta + \mathcal{K}\bar{n}_c)^2 + \left(\frac{\kappa}{2}\right)^2 \right] = \kappa \bar{n}_{\text{in}} \tag{4.20}$$

with $\bar{n}_{\text{in}} = |\alpha_{\text{in}}|^2$, and which is equivalent to Eq. (3.67) for $\mathcal{K}_m \to \mathcal{K}$. The average photon number in the cavity described by the last equation is illustrated in Fig. 4.3.

Comparing the results obtained in Chapter 3 with the analysis leading to Eq. (4.20) demonstrates the equivalence between an optomechanical system and a Kerr medium. However, as mentioned also in Chapter 3, for a high-Q oscillator, the optomechanically induced Kerr nonlinearity, $\mathcal{K}_m \approx 2g_0^2/\omega_m$, is generally small. As a result, either a very strong input power or a significant coupling strength is necessary to observe substantial nonlinear effects. Otherwise, the intracavity photon number can be approximated by a Lorentzian distribution, as shown by the grey line in Fig. 4.3.

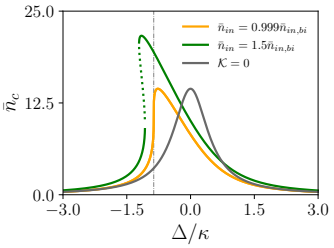

FIGURE 4.3: Intracavity photon number as a function of the optical detuning. For strong enough input power and certain detunings, the system shows bistability.

So far we studied the classical dynamics of a driven Kerr-cavity described by the Hamiltonian in Eq. (4.17). However, to analyze the dynamics of the quantum fluctuations we require to linearize the equations of motion using Eq. (3.74). Therefore, if we now assume that the system is strongly driven at frequency ω_p, we can perform the displacement transformation of the cavity field operators around the steady state mean value.

Similarly as in Eq. (3.87), we find that under the displacement transformation given in Eq. (3.74) the Hamiltonian in Eq. (4.17) becomes

$$\hat{\mathcal{H}}_{\text{eff}} = -\left(\Delta + 2\mathcal{K}|\alpha|^2\right)\hat{d}^\dagger\hat{d} - \frac{\mathcal{K}}{2}\left(\alpha^2\hat{d}^{2\dagger} + \alpha^{*2}\hat{d}^2\right) + \hat{\mathcal{H}}_{\text{NL}}, \tag{4.21}$$

where the last term includes all non-quadratic terms

$$\hat{\mathcal{H}}_{\text{NL}} = -\frac{\mathcal{K}}{2}\hat{d}^{2\dagger}\hat{d}^2 - \mathcal{K}\left[\alpha^*\hat{d}^\dagger\hat{d}\hat{d} + \alpha\hat{d}^\dagger\hat{d}^\dagger\hat{d}\right]. \tag{4.22}$$

Finally, by keeping only quadratic terms in Eq. (4.21) we obtain the linearized Kerr-cavity Hamiltonian given by

$$\hat{\mathcal{H}}_{\text{eff}} = -\tilde{\Delta}\hat{d}^\dagger\hat{d} - \frac{1}{2}\left(\Lambda\hat{d}^{2\dagger} + \Lambda^*\hat{d}^2\right), \tag{4.23}$$

where we introduced the *effective detuning* $\tilde{\Delta} = \Delta + 2|\Lambda|$ and the single-mode squeezing strength $\Lambda = \mathcal{K}\bar{n}_c e^{2i\phi_c}$. Here, the average coherent amplitude of the cavity field is given by $\alpha = \sqrt{\bar{n}_c}e^{i\phi_c}$ with its phase ϕ_c and the intracavity photon number $\bar{n}_c$.

The linearized Hamiltonian in Eq. (4.23) describes a detuned *degenerate parametric amplifier* (DPA), which is well-known to produce squeezed states [168, 169]. Furthermore, within the input-output formalism, the dynamics of the fluctuations of a driven Kerr-cavity are described by the following equations of motion

$$\frac{d}{dt}\hat{\vec{R}}(t) = \boldsymbol{\mathcal{A}}\hat{\vec{R}}(t) - \sqrt{\boldsymbol{\kappa}}\hat{\vec{R}}_{\text{in}}(t) \tag{4.24}$$

where we defined the vectors of the cavity operators $\vec{R} = \left(\hat{d}, \hat{d}^\dagger\right)$ and of the input noise operators $\vec{R}_{\text{in}}$, the diagonal matrix $\boldsymbol{\kappa} = \text{diag}(\kappa, \kappa)$ and $\boldsymbol{\mathcal{A}}$ is a time independent dynamical

matrix given by

$$\boldsymbol{\mathcal{A}} = \begin{pmatrix} i\tilde{\Delta} - \frac{\kappa}{2} & i\Lambda \\ -i\Lambda^* & -i\tilde{\Delta} - \frac{\kappa}{2} \end{pmatrix}. \tag{4.25}$$

The eigenvalues of the dynamical matrix $\boldsymbol{\mathcal{A}}$ are given by $\lambda_\pm = -\kappa/2 \pm \sqrt{|\Lambda|^2 - \tilde{\Delta}^2}$ and indicate the stability regime, i.e. as long as it is real part is negative. Nevertheless, an analytical expression for the stability condition is not straightforward since the intracavity photon number is also a function of the cavity's bare detuning as shown in Eq. (4.20). Note that the presence of the cavity nonlinearity introduces idler noise, which corresponds to the off-diagonal elements of Eq. (4.25). Furthermore, the noise correlators satisfy Eq. (3.60). $\langle \hat{d}_{\text{in}}(t)\hat{d}^\dagger_{\text{in}}(t')\rangle = \delta(t-t')$ and $\langle \hat{d}^\dagger_{\text{in}}(t)\hat{d}_{\text{in}}(t')\rangle = 0$.

The quantum Langevin equations of motion (3.104) can be solved in frequency space under a Fourier transform. Thus, we find

$$-i\omega\hat{\vec{R}}[\omega] = \boldsymbol{\mathcal{A}}\hat{\vec{R}}[\omega] - \sqrt{\boldsymbol{\kappa}}\hat{\vec{R}}_{\text{in}}(t), \tag{4.26}$$

which finally leads us to

$$\hat{d}[\omega] = -\sqrt{\kappa}\,\mathcal{X}_{\mathcal{K}}[\omega]\left(\hat{d}_{\text{in}}[\omega] + i\Lambda\mathcal{X}_c^*[-\omega]\hat{d}^\dagger_{\text{in}}[\omega]\right), \tag{4.27}$$

where we defined the *driven Kerr cavity susceptibility* as

$$\mathcal{X}_{\mathcal{K}}[\omega] = \frac{\mathcal{X}_c[\omega]}{1 - |\Lambda|^2\,\mathcal{X}_c[\omega]\mathcal{X}_c^*[-\omega]}, \tag{4.28}$$

with $\mathcal{X}_c^{-1}[\omega] = -i(\omega + \tilde{\Delta}) + \kappa/2$.

So far, we derived the Kerr cavity's semiclassical dynamics, resulting in the cubic Eq. (4.20), which describes the intracavity photon number (see Fig. 4.3). Subsequently, to fully understand the implications of the Kerr nonlinearity we also analyzed the dynamics of the fluctuations within the input-output formalism using the Hamiltonian in Eq. (4.23) yielding Eq. (4.27). From the dynamics of the fluctuations, it is possible to note the importance of the classical analysis that we carried out initially, given that the single-mode squeezing strength is enhanced by the intracavity photon number, which also induces a frequency shift.

Next, we will see how the added idler noise and the modification of the cavity susceptibility due to the cavity nonlinearity will result in an asymmetrical shape of the photon number spectrum, which will be fundamental when the cavity is coupled to a mechanical mode.

4.3 Photon number spectrum

The dynamical analysis done in the last section, allows us to derive the photon number spectrum defined in Eq. (3.126). Following the linearization yielding the effective Hamiltonian Eq. (4.23), we find that the photon number spectrum of the corresponding Kerr cavity is explicitly given by

$$\mathcal{S}_{nn}[\omega] = \frac{\bar{n}_c\kappa\left(\left[-\tilde{\Delta} + \omega + |\Lambda|\right]^2 + \frac{\kappa^2}{4}\right)}{\left[\tilde{\Delta}^2 - \omega^2 + \frac{\kappa^2}{4} - |\Lambda|^2\right]^2 + \kappa^2\omega^2}. \tag{4.29}$$

Note that for $\mathcal{K} = 0$ and therefore $\Lambda = 0$ we recover the results derived in Chapter 3.7.

Since the photon number spectrum given in Eq. (4.29) describes the system's ability to emit or absorb energy at various frequencies, analyzing its *asymmetry* is essential. This asymmetry indicates whether emission or absorption is more favourable, which is critical when the cavity couples to a vibrational mode, as it characterizes the cavity's ability to backaction cool the mechanical mode.

In this section, we will examine how operating near the bifurcation point enhances the asymmetry in the photon number spectrum. This enhancement will play a crucial role in improving the backaction cooling of a mechanical oscillator through radiation pressure.

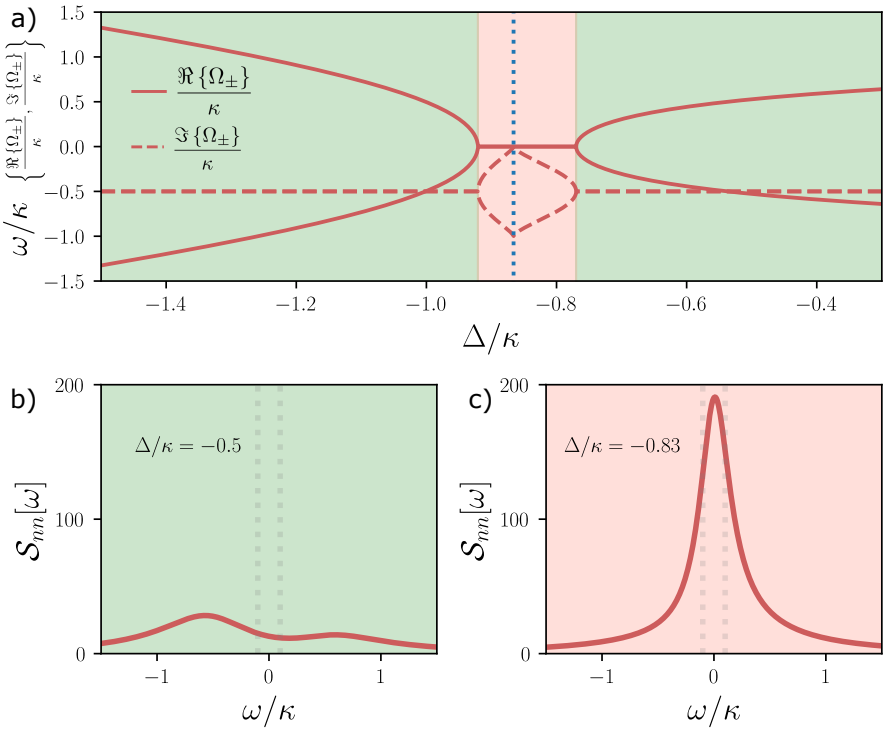

FIGURE 4.4: **a)** The imaginary (dashed) and real (solid) components of the poles of the driven Kerr cavity are plotted as functions of detuning. The exceptional points (EPs) mark the boundaries between regions with two resonant frequencies and a single decay rate (green-shaded, **b)**) and region with distinct decay rates but a single resonant frequency (red-shaded, **c)**). **b)** In the green-shaded region, the two resonant frequencies lead to a double-peak structure in the photon number spectrum. **c)** In the red-shaded region, where the system has split decay rates, the maxima and minima of $\Im\{\tilde{\Omega}_\pm\}$ occur at the bifurcation detuning, $\Delta_{\rm bi}$, indicated by the vertical blue line. The dotted-vertical lines in the lower plots show the position of the mechanical sidebands. For this plot $\kappa/2\pi = 3.5$ MHz, $\mathcal{K}/2\pi = 1.6$ MHz and $\bar{n}_{\rm in} = 0.99\bar{n}_{\rm in,bi}$, which are similar parameters to those in [3].

For convention, in this study, we will analyze the dynamics of the fluctuations in terms of the poles[2], or, in other words, the roots of the denominator of the photon number spectrum [26] Eq. (4.29):

$$\Omega_{c,\pm} = -i\frac{\kappa}{2} \pm \sqrt{(\Delta + 3|\Lambda|)\,(\Delta + |\Lambda|)}. \tag{4.30}$$

From these poles, we can extract information about the dynamical behaviour of the system. Here, the real (imaginary) part of the poles is associated to the resonance frequencies (damping rates) of the system. In Fig. 4.4 and Fig. 4.5 the poles are plotted as a function of the bare detuning Δ, and two distinct regions can be identified.

For detunings $\Delta < -3|\Lambda|$ and $\Delta > -|\Lambda|$ (green shaded area), the system is characterized by two resonant frequencies $\Re\{\tilde{\Omega}_\pm\}$ and a single decay rate, leading to the appearance of two peaks in the photon number spectrum, as shown in the lower-left plots of Fig. 4.4 and Fig. 4.5. Conversely, within the range $-3|\Lambda| < \Delta < -|\Lambda|$ (red shaded area), the situation reverses: the poles exhibit degenerate real parts and split dissipation rates $\Im\{\tilde{\Omega}_\pm\}$, as seen in the lower-right plots of Fig. 4.4 and Fig. 4.5. These two regions are separated by exceptional

[2] An equivalent description can be done using the cavity eigenvalues. These eigenvalues, denoted as $\lambda_{c,\pm}$, can be computed using the dynamical matrix in Eq. (3.104), leading to the following relation with the poles: $\lambda_{c,\pm} = -i\Omega_\pm$.

points (EPs), which are characteristic degeneracies in open quantum systems [170]. At an EP the system eigenvalues become degenerate and both eigenvectors coalesce due to the vanishing square root of Eq. (4.30). These EP's occur for the condition $\Delta_\pm = -(2 \pm 1)|\Lambda|$, however, the exact detuning points are not straightforwardly determined as $|\Lambda|$ is also a function of the average photon number in Eq. (4.20) which itself depends on the detuning.

Typically, for low input powers $\bar{n}_{\mathrm{in}} \ll \bar{n}_{\mathrm{in,bi}}$ the intracavity photon number is well described by a Lorentzian distribution (see Fig. 4.3), since the asymmetric response caused by the Kerr nonlinearity is weak. This behaviour is depicted by the vertical blue line in Fig. 4.3, which shows that as the input power increases, the nonlinear response becomes more pronounced. As the input power approaches the critical value $\bar{n}_{\mathrm{in}} \approx \bar{n}_{\mathrm{in,bi}}$, the asymmetry in the cavity response is more prominent. This results in a significant change in the photon number with even small variations in cavity detuning, which will have a remarkable effect in the asymmetry of the photon number spectrum, and consequently in the dynamics of the cavity fluctuations.

As mentioned before, when the input power approaches $\bar{n}_{\mathrm{in}} \approx \bar{n}_{\mathrm{in,bi}}$ the nonlinearity dominates the intracavity photon number given in Eq. (4.20), making it extremely steep around the bifurcation point. To examine the effect of performing the semiclassical description of the cavity dynamics, we can simply *ignore* the nonlinearity in Eq. (4.20) and model the intracavity photon number as a Lorentzian distribution regardless of the input power. This approach allows us to analyze the effects that emerge solely from the correct description of the semiclassical dynamics resulting in the cubic equation given in Eq. (4.20). Keep in mind that this is, by all means, a mathematical tool to highlight the effects of nonlinearity, as in reality, we cannot simply decide to *ignore* certain aspects of the experiment.

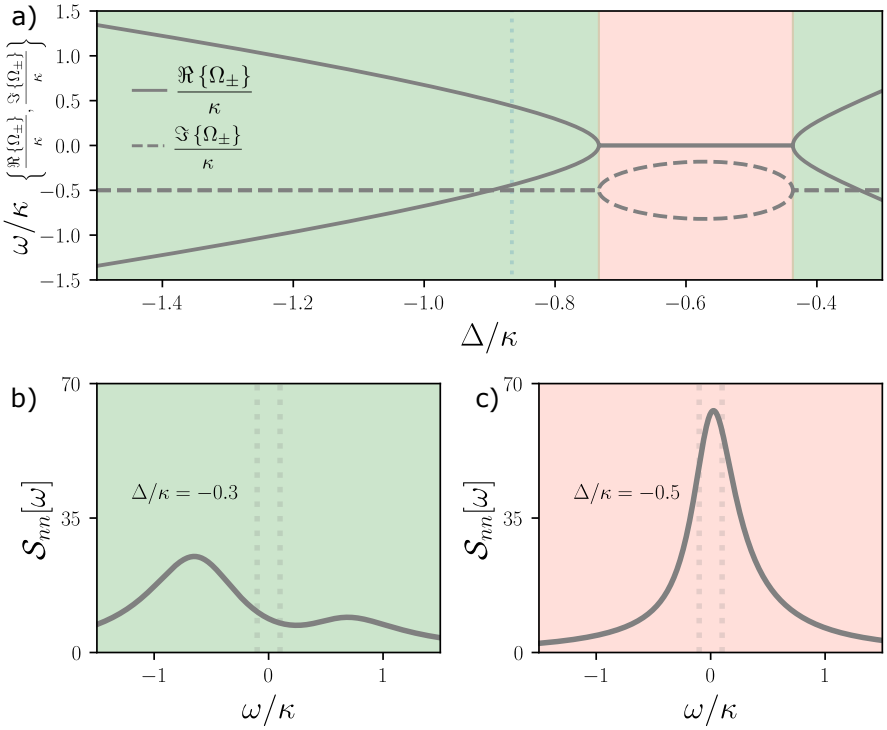

FIGURE 4.5: A linear description of the photon number, modelled by a Lorentzian distribution, results in the distinct dynamical behaviour of the fluctuations, characterized by symmetric broadening around the resonant frequency. This symmetry contrasts with the nonlinearity-driven dynamics observed near the bifurcation point, where asymmetries play a more prominent role. **a)** The imaginary (dashed) and real (solid) components of the poles of the driven Kerr cavity are plotted as functions of detuning. The exceptional points (EPs) mark the boundaries between regions with two resonant frequencies and a single decay rate (green-shaded, **b)**) and region with distinct decay rates but a single resonant frequency (red-shaded, **c)**). For this plot $\kappa/2\pi = 3.5$ MHz, $\mathcal{K}/2\pi = 1.6$ MHz and $\bar{n}_{\mathrm{in}} = 0.99\bar{n}_{\mathrm{in,bi}}$.

The nonlinear response of the cavity photon number leads to an overall frequency shift of the poles $\Omega_{c,\pm}$, which can be deduced from a direct comparison of Fig. 4.4 and Fig. 4.5. Nevertheless, in the red-shaded area, where the system has split decay rates, the presence of the nonlinearity in the photon number leads to one imaginary part of the pole approaching zero and the other to $\omega/\kappa \to -1$. Interestingly this effect occurs at the critical detuning, which is illustrated by the blue-dotted vertical line in Fig. 4.4. Note that, this asymmetry arises due to the pronounced change in the photon number as we approach the critical detuning Δ_{bi} from the left. Conversely, approaching this critical value from the right does not lead to an abrupt photon change, due to the positive skewness of the cavity response. Here, the decay rate approaching zero leads to an enhancement in the lifetime of the cavity's photon number, which is normally referred to as *cavity slow down*. The reduced decay rate translates into a narrowing of the photon number spectrum, reminiscent of the gain-bandwith limitation of a parametric amplifier [122]. Performing an extrema analysis, we can find

$$\frac{d}{d\bar{n}_c}\Im\left\{\tilde{\Omega}_{\pm}\right\} = 0 \quad \Rightarrow \quad \frac{\bar{n}_c}{\Delta} = -\frac{2}{3\mathcal{K}}, \tag{4.31}$$

which is equivalent to $\bar{n}_{\mathrm{bi}}/\Delta_{\mathrm{bi}}$ given in Eq. (3.72) for $\mathcal{K}_m \to \mathcal{K}$. This indicates that, due to the cavity nonlinearity, the decay rate reaches its extremum at the critical detuning, a result of the sharp variation in photon number with detuning, as shown in Fig. 4.4.

If we assume instead that the cavity response is described by a Lorentzian distribution at these input power levels, the characteristic asymmetry of the nonlinear system disappears. This is prominent in the region where the decay rates split as depicted in Fig. 4.5. In this region, we also observe that these decay rates no longer approach the values of 0 and -1, as was noted in the purely nonlinear description, thus losing the effects that this entails.

In this section, we analyzed the photon number spectrum of a nonlinear cavity, as described by Eq. (4.29). Specifically, we highlighted the influence of the average photon number, given by the nonlinear expression in Eq. (4.20). We demonstrated that at the point of bifurcation, marked by the critical detuning in Eq. (3.72), the nonlinearity results in a slowing down of the cavity, which leads to longer coherence times. Additionally, we observed in the red-shaded area of Fig. 4.4, where there is a single resonant frequency, that the system exhibits asymmetrical behaviour. This asymmetry is directly linked to the nonlinear characteristics of the circulating photon number shown in Fig. 4.3. In the next section, we will investigate this asymmetry and explore its potential applications.

4.4 Asymmetrical behaviour

In the last section, we noticed that the system becomes asymmetric in the red-shaded area in Fig. 4.4, an effect that is associated to the nonlinear behaviour of the average photon number. In addition, we also demonstrated that this asymmetry is more prominent as the system approaches the bifurcation point. Here, we will quantify this asymmetry by introducing the *skewness*, a statistical measure typically used to describe the asymmetry of a probability distribution.

The skewness quantifies how much a distribution deviates from symmetry around its mean. A positive (negative) skewness indicates a longer or fatter tail on the right (left) side as illustrated in Fig. 4.6. Thus, zero skewness *suggests* the distribution is symmetric around its mean. As shown in the last section, the photon number spectrum resembles a Lorentzian distribution for certain detuning (cf. Figs. 4.4 and 4.5). Nevertheless, since a Lorentzian distribution doesn't have finite moments of order one or higher, including the mean and variance, then its skewness is not well defined. A way to overcome this limitation is by truncating the distribution at its tails, which helps reduce the influence of extreme values on the average. This truncated skewness is what we use to measure the asymmetry of the photon number spectrum and what we denote the *effective skweness*.

Definition of the effective skewness: To define γ_{eff} we numerically obtained the *moment-based skewness* using the following function

$$\gamma_1 = \frac{\sum_{i=1}^{n}(x_i - \mu)^3}{n\sigma^3}, \tag{4.32}$$

where x is an array of data points with length n from the distribution, and μ and σ are the mean and standard deviation of the distribution, respectively. Furthermore, since the Lorentz distribution is heavy-tailed and therefore does not have finite moments, i.e. well-defined mean and variance, here we calculated the *truncated moment-based skewness*. This involves truncating the data set to a finite interval, calculating the moments of the truncated distribution, and then using these moments to determine the skewness of the truncated distribution. Using the description given above, for a certain interval of detunings Δ, we calculated the skewness of the photon number spectrum in Eq. (4.29) over a truncated set of driving frequencies ω. That means, for a $\Delta/\omega_m \in [-12, 0]$ the array x is given by the set of elements fulfilling $x = \{\mathcal{S}_{nn}[\omega] \mid \omega/\kappa \in [-10, 10]\}$. In addition, in Fig. 4.7 we show the *effective skewness*, which results from subtracting the constant skewness obtained using a linear cavity to the associated one of a nonlinear cavity, that is we do $\gamma_{\text{eff}}(\Delta) = \gamma_1^{\mathcal{K}\neq 0}(\Delta) - \gamma_1^{\mathcal{K}=0}$ with $\gamma_1^{\mathcal{K}=0} = 3.48$.

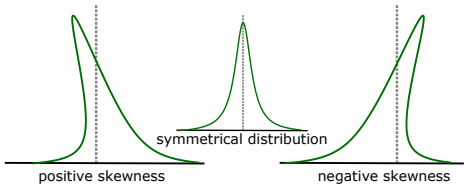

FIGURE 4.6: Skewness of a distribution

Using the effective skewness defined above, we calculate the asymmetry of the photon number spectrum described by Eq. (4.29). In Fig. 4.7, we present the effective skewness as a function of cavity detuning for a nonlinear cavity defined by the Hamiltonian in Eq. (4.23). To illustrate how the intracavity photon number affects the asymmetry of cavity fluctuations, we also analyzed the scenario where the nonlinearity in Eq. (3.67) is neglected. Operating just below the threshold power, the photon number spectrum becomes highly asymmetrical at the bifurcation point, as indicated by the orange line in Fig. 4.7. In contrast, when the correct description of the intracavity photon number is ignored, and a simple Lorentzian is assumed, the photon number spectrum shows considerably less asymmetry, as depicted by the grey line in Fig. 4.7.

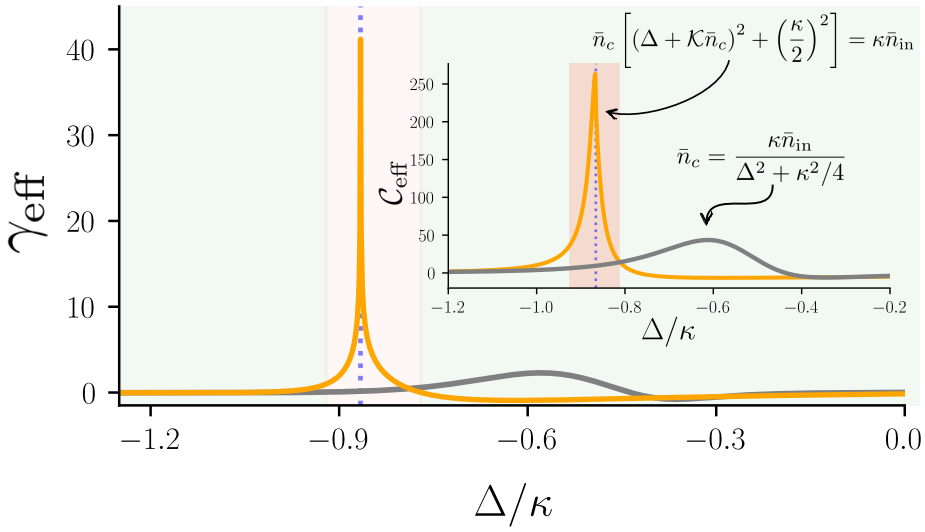

FIGURE 4.7: Effective skewness of the photon number spectrum and effective cooperativity (see inset) of a nonlinear cavity as a function of the cavity detuning. The orange line shows the result obtained when the circulating photon number is treated fully nonlinear, i.e. using Eq. (4.20). The grey line shows the result obtained when we measured this asymmetry with the photon number described by a Lorentztian. When operating close to the power threshold, the full nonlinear treatment (orange) shows maximum asymmetry when the cavity is located at $\Delta = \Delta_{\rm bi}$ (vertical blue line). Thus, as the cavity is driven close to the critical detuning the photon number spectrum becomes increasingly peaked and asymmetric. The asymmetry of the photon spectrum is significantly reduced when assuming a linear description of the photon occupancy. This, in turn, leads to a substantial decrease in the effective cooperativity and consequently weakens the cooling capabilities, as shown in the inset. The parameters of these plots are given in Table 5.1.

The maximum asymmetry occurs exactly at the critical detuning $\Delta_{\rm bi}$, where the largest fluctuations are also expected due to the steep slope in the average photon number (cf. Fig. 4.3). A positive skewness corresponds to a steeper decline in the photon number spectrum for negative frequencies and an extended tail for positive frequencies. In other words, for $\gamma_{\rm eff} > 0$, we have $\mathcal{S}_{nn}[\Omega] > \mathcal{S}_{nn}[-\Omega]$ with $\Omega > 0$.

As we will explore later in this study, this effect is crucial for cooling a mechanical mode when coupled via radiation pressure. The reason lies in the interpretation of the spectrum's positive and negative frequency components: the positive frequency part, $\mathcal{S}_{nn}[+\Omega]$, reflects the system's ability to absorb energy, while the negative frequency part, $\mathcal{S}_{nn}[-\Omega]$, represents its tendency to emit energy [122]. This distinction between absorption and emission is key to understanding the cooling dynamics in such systems.

For effective cooling, we want the cavity to absorb energy from the mechanical mode, which is indicated by a positive skewness in the photon number spectrum. This positive skewness reveals the detuning regime where cooling occurs. Specifically, we can identify the necessary conditions for the nonlinear cavity to absorb energy as:

$$\mathcal{S}_{nn}[\Omega] - \mathcal{S}_{nn}[-\Omega] > 0 \quad \text{for} \quad \Delta < -|\Lambda|, \tag{4.33}$$

In summary, the photon number spectrum $\mathcal{S}_{nn}[\omega]$ given in Eq. (4.29) deviates significantly from the typical Lorentzian form of a linear cavity [1]. While a Lorentzian is completely symmetric around its peak, the spectrum for a nonlinear cavity exhibits asymmetry, which plays a crucial role in enabling efficient cooling of the mechanical system. In the following Chapter, we will demonstrate how the cavity's nonlinearity can enhance the cooling efficiency of a mechanical resonator in the unresolved sideband regime by taking advantage of this asymmetrical response.

Chapter 5

Kerr-enhanced optomechanics in the unresolved sideband regime

In Chapter 3 we studied how the radiation pressure interaction in optomechanical systems enables dynamical backaction cooling of the mechanical mode. However, for systems at cryogenic temperatures, low-frequency mechanical systems require additional cooling due to their high thermal occupation. Since dynamical backaction works best in the resolved sideband regime ($\omega_m \gg \kappa$), the above represents a limitation for sideband cooling protocols aiming to bring large mechanical systems to their ground state. To overcome this limitation different schemes have already been proposed, which include two cavity modes [33, 34], two mechanical modes [171], or using squeezed light which can be generated either externally [31, 172] or internally within the cavity [32, 173–175]. The advantages and disadvantages of these approaches have been discussed in [176]. The latter strategies are very promising but require fine-tuning of the squeezing parameters to suppress the Stokes scattering process and thus enhance cooling.

Motivated by earlier work [177, 178], we will show how an intrinsic nonlinear cavity, introduced in Chapter 4, can be beneficial for backaction cooling of a mechanical mode. Hence, in this Chapter, we will use the theory of optomechanics presented in Chapter 3 but extend it to the nonlinear case. Particularly, we will demonstrate how the Kerr-nonlinearity allows for a significant improvement in the cooling efficiency deep in the unresolved sideband regime. This Chapter stems from our work [36], where we presented a theoretical description of our experimental collaboration on the enhancement of backaction cooling using a Kerr-cavity in magnetomechanics [3, 35]. Our experimental work is based on a flux-mediated optomechanical coupling scheme [94, 95, 114, 140, 179], where a mechanical oscillator is coupled magnetically to microwave photons in a superconducting LC circuit. In such a setup, the displacement of the mechanical oscillator is converted into a magnetic flux that changes a superconducting quantum-interference device (SQUID), serving as flux-dependent inductance [177, 180].

Crucially, besides being a magnetic field-sensitive element, the SQUID is also a nonlinear element since its inductance depends on the number of photons circulating in the cavity, resulting in a typically unwanted Kerr nonlinearity within the optomechanical system. First, we will focus our analysis on the cooling below the driving power threshold, to prevent the emergence of a bistable regime (see Chapter 4). Here, we will show how a nonlinear cavity enables more efficient cooling than an identical linear system, particularly in the unresolved sideband regime. Finally, we will loosen up the constraint imposed by the driving power and discuss cooling above bistability, where our theory shows a great agreement with the experimental data.

5.1 Kerr-cavity optomechanical system

So far, in Chapter 3, we reviewed key aspects of optomechanics, demonstrating how the optomechanical interaction gives rise to static nonlinear effects in the intracavity photon number. We also discussed the dynamical backaction effects of radiation-pressure interaction, such as sideband cooling of the mechanical mode. Given the bistability phenomenon in cavity optomechanics and its resemblance to an optical cavity with a Kerr medium, in Chapter 4, we examined nonlinear cavities. Additionally, we showed that such cavities can be engineered in

the microwave regime using superconducting circuits, which offer extremely high-Q factors, making them promising for quantum information applications. Furthermore, we highlighted how the characteristic asymmetry of nonlinear cavities has distinctive properties, with potential applications for backaction cooling of a mechanical mode in optomechanics.

In this section, we will introduce a novel optomechanical setup based on a theoretical proposal to enhance the optomechanical coupling strength [93], which has recently been realized experimentally [95, 179, 181]. In this setup displayed in Fig. 5.1, the interaction is achieved inductively, making the cavity inherently nonlinear. This intrinsic nonlinearity leads to an enhanced backaction cooling efficiency compared to traditional linear systems that rely on capacitive couplings [35, 94].

The setup shown in Fig. 5.1 consists of a superconducting microstrip cavity coupled to a single-clamped beam (a cantilever) with a magnetic tip [35, 94, 181]. To mediate the optomechanical interaction, a SQUID (cf. Chapter 4) is integrated into the cavity, making it effectively a microwave cavity sensitive to magnetic fields. In this architecture, the single-photon coupling strength given in Eq. (3.49) reads

$$g_0 = \frac{\partial \omega_c}{\partial x} x_{\mathrm{ZPF}} = \frac{\partial \omega_c}{\partial \phi_{\mathrm{ext}}} \times \frac{\partial \phi_{\mathrm{ext}}}{\partial x} x_{\mathrm{ZPF}}, \tag{5.1}$$

where ϕ_{ext} is the external magnetic flux. Due to the inaccessibility of the $\partial\omega_c/\partial x$, we expressed the optomechanical coupling in terms of the external magnetic flux. In the last equality, the first factor describes the cavity frequency dependence on the flux through the SQUID loop (see Fig. 4.1), thereby providing the ability to control the coupling strength. On the other hand, the second factor gives the flux change induced by a zero-point motion of the mechanical cantilever.

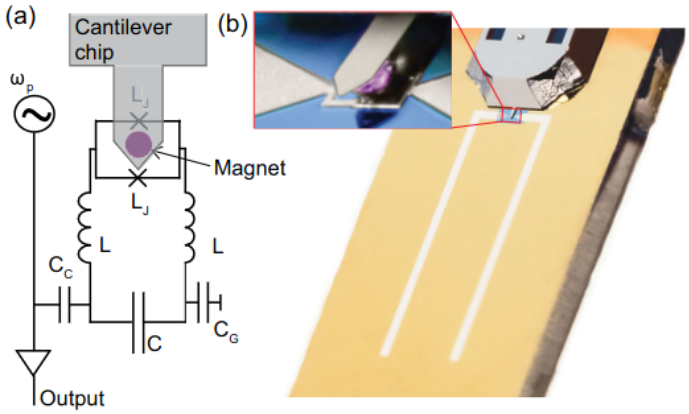

Figure 5.1: A) Circuit diagram of the setup with the junction and cavity inductances, L_J and L, respectively. The self, coupling and ground capacitances are given by C, C_c and C_g, respectively. B) Picture of the sample: silicon substrate in gold, u-shaped cavity in silver, cantilever in grey and magnet false coloured in purple. Both Figures were taken with permission from [3].

As shown in Fig. 5.1a), the device is mounted on the base plate of a dilution refrigerator, which is kept at a temperature of 100 mK. Most of the experiments are performed at the given temperature and when the system shows both stability and the mechanical mode is well thermalized. The dependence of the cavity frequency on the magnetic field characterizes the coupling strength. This setup allows for single-photon coupling strength of 7.4 kHz, whereas the sensitivity of the cavity enables coupling exceeding 90 kHz [3]. However, excessive flux noise due to mechanical vibrations does not allow for stable operations at such flux sensitivities.

The motion of the cantilever is measured by taking the homodyne noise spectrum of the probe tone, where the cantilever's motion appears as an amplitude (phase) modulation sideband. This sideband is then compared with the model of a damped harmonic oscillator [182]. In addition, the backaction effects are studied by measuring the mechanical cantilever for different detunings between the probe tone and the cavity resonance frequency. In this

Parameter	Value
Mechanical frequency	$\omega_m/2\pi = 0.3$ MHz
Mechanical linewidth	$\gamma_m/2\pi = 0.5$ Hz
Cavity linewidth	$\kappa/2\pi = 3$ MHz
Kerr strength	$\mathcal{K}/2\pi = 0.16$ MHz/ photon
Optomechanical coupling	$g_0/2\pi = 1.7$ kHz
Drive amplitude	$\bar{n}_{\mathrm{in,crit}} \equiv 0.9999999\bar{n}_{\mathrm{in,bi}}$

TABLE 5.1: Default values chosen for the parameters in the figures throughout the paper, if not otherwise indicated. These values are similar to those used in our recent experimental work [3].

way, by taking such cooling traces for various input powers up to bistability, the cooling enhancement due to the intrinsic nonlinearity of the cavity is revealed.

One of the most important aspects of this setup is the intrinsic nonlinearity of the SQUID with respect to the input power since its inductance depends on the intracavity photon number. This implies that, as the number of photons injected into the cavity increases, the frequency shifts to lower values consequently leading to the nonlinear response illustrated in Fig. 4.3. As explained in Chapter 4, one of the crucial aspects of a nonlinear cavity is the emergence of a bistable regime for a certain input power.

Throughout this chapter, we will use parameters similar to those employed in the experimental work of D. Zoepfl *et al.* [3], as listed in Table 5.1. This parameter regime places the optomechanical setup in the unresolved sideband regime, where sideband cooling is generally less effective. However, we will demonstrate that a nonlinear cavity can achieve more efficient cooling than an equivalent linear system, with the improvement being especially pronounced in the unresolved sideband regime. Despite being based on the setup provided in the work of D. Zoepfl *et al.* [3], our theoretical analysis is not limited to this system and can also be extended to other configurations.

5.2 Hamiltonian formulation

We will start the analysis with the Hamiltonian describing a mechanical oscillator parametrically coupled to a nonlinear Kerr-resonator (see Chapter 4), which can be driven into a bistable regime as depicted in Fig. 5.2. The Hamiltonian associated with such a system reads [177]:

$$\hat{\mathcal{H}}_{\mathrm{tot}} = \omega_c \hat{a}^\dagger \hat{a} + \omega_m \hat{b}^\dagger \hat{b} - \frac{\mathcal{K}}{12}\left(\hat{a}+\hat{a}^\dagger\right)^4 + \frac{g_0}{2}\left(\hat{a}+\hat{a}^\dagger\right)^2\left(\hat{b}+\hat{b}^\dagger\right) + \hat{H}_{\mathrm{d}}, \tag{5.2}$$

where $\hat{a}(\hat{b})$ and $\hat{a}^\dagger(\hat{b}^\dagger)$ are the bosonic annihilation and creation operators of the cavity (mechanical) mode, respectively. Here, we also introduced the resonance frequencies, ω_c and ω_m, for the cavity and mechanical mode, respectively. Furthermore, the Kerr constant, $\mathcal{K}$, is generally[1] assumed to be $\mathcal{K} > 0$, and $g_0 = g x_{\mathrm{ZPF}}$ denotes the bare optomechanical coupling strength introduced in Chapter 3. In addition, we include an external drive associated with the term $\hat{H}_{\mathrm{d}} = \alpha_p e^{-i\omega_p t}\hat{a}^\dagger + \mathrm{h.c}$, where ω_p is the drive frequency and α_p the classical amplitude. Moreover, if we assume that both the coupling g_0 and nonlinearity $\mathcal{K}$ are weak enough, we can simplify the system by neglecting counter-rotating terms resulting in the

[1] The sign depends on the architecture of the circuit [110].

time-independent Hamiltonian [2]

$$\hat{\mathcal{H}} = -\Delta\hat{a}^\dagger\hat{a} + \omega_m\hat{b}^\dagger\hat{b} - \frac{\mathcal{K}}{2}\hat{a}^\dagger\hat{a}^\dagger\hat{a}\hat{a} + g_0\hat{a}^\dagger\hat{a}\left(\hat{b}+\hat{b}^\dagger\right) + \hat{\mathcal{H}}_d, \tag{5.3}$$

with the cavity mode rotated with respect to the drive frequency ω_p, where $\Delta = \omega_p - \omega_c$ denotes the detuning and $\hat{\mathcal{H}}_d = \alpha_p\hat{a}^\dagger + \text{h.c.}$.

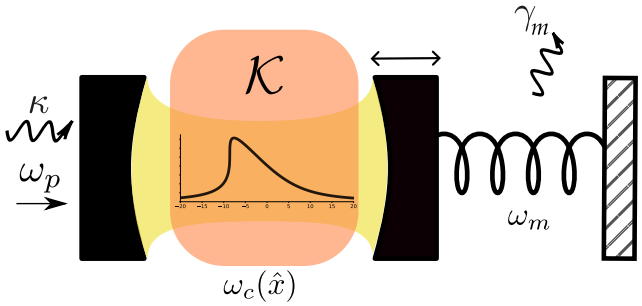

FIGURE 5.2: Dispersive optomechanical setup consisting of a driven Kerr-cavity at frequency ω_p, coupled via radiation pressure to a mechanical resonator. Due to the cavity's nonlinearity, the average photon number circulating in the cavity shows a notable asymmetry at specific driving powers and cavity detunings. The cavity and mechanical loss rates are denoted by κ and γ_m, respectively. The position-dependent cavity frequency is represented as $\omega_c(\hat{x})$, while ω_m is the resonator's resonant frequency.

As we did in Chapter 3, we will linearize Eq. (5.3) to study both classical and quantum dynamics. Hence, under the assumption that the system is driven strongly at the drive's frequency ω_p, its dynamics can be well studied as only small fluctuations in the vicinity of the steady state mean values. Therefore, we introduce the displacement operator $\hat{\mathcal{D}}(\eta) = \exp\left(\eta\hat{\mathcal{O}}^\dagger - \eta^*\hat{\mathcal{O}}\right)$ with $\eta = \langle\hat{\mathcal{O}}\rangle$ as an average amplitude and $\hat{\mathcal{O}}$ the fluctuations around it. This allows us to transform the Hamiltonian in Eq. (5.3) to a displaced frame of the cavity and mechanical mode. This results in an effective description of the coherent dynamics of the fluctuations given by the Hamiltonian

$$\hat{\mathcal{H}}_{\text{eff}} = -\tilde{\Delta}\hat{d}^\dagger\hat{d} + \omega_m\hat{b}^\dagger\hat{b} - \frac{1}{2}\left[\Lambda\hat{d}^\dagger\hat{d}^\dagger + \Lambda^*\hat{d}\hat{d}\right] + \left(G\hat{d}^\dagger + G^*\hat{d}\right)\left(\hat{b}+\hat{b}^\dagger\right), \tag{5.4}$$

with the effective detuning $\tilde{\Delta} = \Delta + 2|\Lambda|$. This time-independent Hamiltonian is characterized by the single-mode squeezing strength $\Lambda = \mathcal{K}\bar{n}_c e^{2i\phi_c}$, and the photon enhanced optomechanical coupling strength $G = g_0\sqrt{\bar{n}_c}\,e^{i\phi_c}$ with $\phi_c \in [0, 2\pi)$. Here, the average coherent amplitude of the cavity field is given by $\alpha = \sqrt{\bar{n}_c}e^{i\phi_c}$ with its phase ϕ_c and the intracavity photon number $\bar{n}_c$.

The first two terms in $\hat{\mathcal{H}}_{\text{eff}}$ describe the effective free Hamiltonian, where the presence of the Kerr nonlinearity introduces a photon-dependent frequency shift encoded in the effective detuning. The third term describes a parametric amplification process induced by the Kerr nonlinearity, which plays a crucial role in squeezing generation [183]. The final term describes the usual linearized optomechanical interaction, which combines both the process of swapping excitations and of two-mode squeezing between both modes. In the resolved sideband regime it is possible to select either of these processes depending on the drive's frequency. However, in the unresolved regime, both processes contribute to our analysis, hence we account for both of them. Furthermore, for a sufficiently weak Kerr nonlinearity, $\Lambda < |\Delta|$, the dynamics

[2] The Hamiltonian in Eq. (5.2) can be written as $\hat{\mathcal{H}} = \hat{\mathcal{H}}_0 + \hat{\mathcal{H}}_{\mathcal{K}} + \hat{\mathcal{H}}_{\text{om}} + \hat{\mathcal{H}}_d$, where the explicit expression of the Kerr-Hamiltonian reads

$$\hat{H}_{\mathcal{K}} = -\frac{\mathcal{K}}{12}\left(\hat{a}+\hat{a}^\dagger\right)^4 = -\frac{\mathcal{K}}{12}\left(\hat{a}^4+\hat{a}^{4\dagger}\right) - \frac{\mathcal{K}}{2}\left(\hat{a}^2+\hat{a}^{2\dagger}\right) - \frac{\mathcal{K}}{3}\left[\hat{a}^\dagger\hat{a}^\dagger\hat{a}+\hat{a}^\dagger\hat{a}\hat{a}\hat{a}\right] - \frac{\mathcal{K}}{2}\hat{a}^\dagger\hat{a}^\dagger\hat{a}\hat{a} - \mathcal{K}\hat{a}^\dagger\hat{a} - \frac{\mathcal{K}}{4}$$

and the optomechanical interaction is described by

$$\hat{H}_{\text{om}} = \frac{g_0}{2}\left(\hat{a}^2+\hat{a}^{2\dagger}+2\hat{a}^\dagger\hat{a}+2\right)\left(\hat{b}+\hat{b}^\dagger\right).$$

governed by Eq. (5.4) become equivalent to those of a standard optomechanical system driven by a squeezed reservoir [32, 176]. This equivalence can be seen when the Hamiltonian of the nonlinear cavity given in Eq. (4.23) is diagonalized via a Bogoliubov transformation, as detailed in Appendix A.

In the following, we will analyze the system's equations of motion, as governed by the Hamiltonian in Eq. (5.4), to investigate the radiation-pressure-induced dynamical backaction phenomena within this nonlinear optomechanical system.

5.3 System's dynamics

To achieve a sufficiently large cooling rate, we are interested in driving strengths that lead to a large average number of intracavity photons $\bar{n}_c$, but simultaneously do not result in multistable solutions in the classical cavity dynamics [178]. Therefore, our first focus is on understanding the classical dynamics of the system, as we will do below.

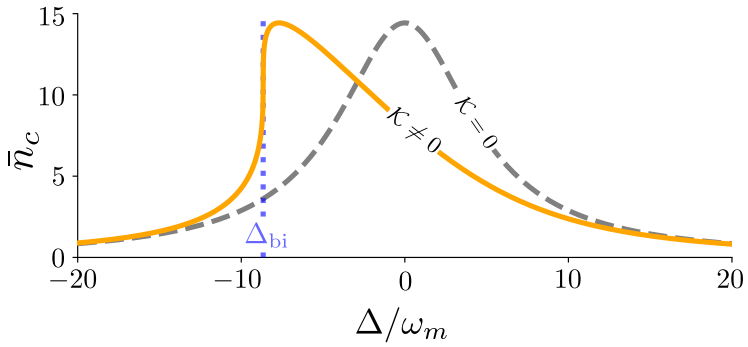

FIGURE 5.3: Average cavity photon number as a function of the detuning $\Delta = \omega_p - \omega_c$. The orange solid line shows the intracavity photon number obtained using a nonlinear cavity ($\mathcal{K} \neq 0$) near the point of bifurcation, namely at a drive amplitude of $\bar{n}_{\mathrm{in}} = \bar{n}_{\mathrm{in,crit}}$. In contrast, the grey-dashed line results from the linear cavity setup ($\mathcal{K} = 0$) at the same input power. The vertical dotted line denotes the critical detuning Δ_{bi}, where the system becomes bistable.

5.3.1 Semiclassical dynamics

For this we will start from the nonlinear Hamiltonian of Eq. (5.3) and assume that the cavity is coupled to an external waveguide with rate κ. We use standard *input-output* theory [152] to obtain the equation of motion for the average coherent cavity amplitude α. The steady-state solution of this coherent amplitude allows us to deduce the average cavity photon number

$$\bar{n}_c \left[(\Delta + \mathcal{K}_{\mathrm{eff}} \bar{n}_c)^2 + \left(\frac{\kappa}{2}\right)^2 \right] = \kappa \bar{n}_{\mathrm{in}}, \tag{5.5}$$

with the effective Kerr constant

$$\mathcal{K}_{\mathrm{eff}} \equiv \mathcal{K} + \frac{2 g_0^2 \omega_m}{\omega_m^2 + \frac{\gamma_m^2}{4}}, \tag{5.6}$$

and the input photon flux $\bar{n}_{\mathrm{in}}$ (in units of photons per second). Here, the cavity and mechanical decay rates are labelled as κ and γ_m, respectively. Here, it is important to note that the effective Kerr in Eq. (5.6) includes both, the intrinsic cavity and optomechanically-induced nonlinearities [128, 142], respectively. From now on, we will refer to the latter as the *mechanical Kerr*. Nevertheless, for the parameters given in Table 5.1, we have $\mathcal{K}_m \approx 2g_0^2/\omega_m = 121$ Hz, which makes it way smaller than the intrinsic Kerr-nonlinearity of the cavity, such that $\mathcal{K}_{\mathrm{eff}} \approx \mathcal{K}$. This suggests that without the cavity nonlinearity and considering the small mechanical Kerr, the intracavity photon number would follow a Lorentzian distribution for low input powers.

The average number of photons circulating in the cavity described by the cubic Eq. (5.5) provides insight into the cavity's behaviour. For low drive strengths, a single real solution

exists. However, for increasing drive power a bifurcation occurs, thus a regime of bistability arises, where two stable solutions (also called *branches*) appear within a certain range of detunings.

The bifurcation takes place at a point in parameter space, where the first derivative of $\bar{n}_c$ with respect to Δ diverges, which happens at a single point $\Delta = \Delta_{\mathrm{bi}}$. By requiring continuity in the transition between the two regions, we arrive at

$$\Delta_{\mathrm{bi}} = -\frac{\sqrt{3}\kappa}{2}, \quad \bar{n}_{\mathrm{bi}} = \frac{\kappa}{\sqrt{3}\mathcal{K}_{\mathrm{eff}}}, \tag{5.7}$$

which correspond to the universal values at bifurcation. Upon substituting the aforementioned relations into Eq. (5.5), we can derive the critical drive amplitude $\bar{n}_{\mathrm{in,bi}}$ at which bifurcation occurs:

$$\bar{n}_{\mathrm{in,bi}} = \frac{\kappa^2}{3\sqrt{3}\mathcal{K}_{\mathrm{eff}}}. \tag{5.8}$$

Consequently, for drive amplitudes slightly below the critical driving threshold, given by Eq. (5.8), the average photon number exhibits a single-valued solution with respect to the cavity detuning, with a significant gradient at Δ_{bi}, as represented by Eq. (5.7) and illustrated in Fig. 5.3. Moreover, for the chosen parameters (see Table 5.1), an identical linear cavity ($\mathcal{K} = 0$) driven at the same input power would show the conventional Lorentzian distribution for the average photon number, despite the presence of the mechanical Kerr given in Eq. (5.6). Hence, for weak coupling strengths, the intrinsic nonlinearity of the cavity dominates over the mechanical Kerr nonlinearity, as we see in Fig. 5.4.

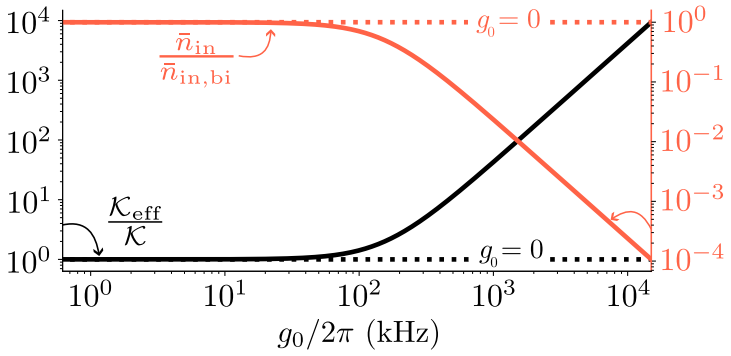

FIGURE 5.4: The black solid line depicts the effective Kerr nonlinearity given in Eq. (5.6) normalized by $\mathcal{K}$ as a function of the optomechanical coupling strength $g_0/2\pi$. For given parameters (see Table 5.1), the intrinsic cavity nonlinearity dominates for weak coupling strengths, and the critical input power (red line) is dominated by $\mathcal{K}$. As the coupling strength increases, the mechanical Kerr effect becomes significant, leading to a decrease in the critical input power as the effective Kerr nonlinearity is enhanced. Dashed lines (color) correspond to the case without the induced mechanical Kerr, i.e. $g_0 = 0$.

5.3.2 Dynamics of the fluctuations

To fully understand the consequences of the interaction between the mechanical and cavity modes, and to determine the cooling limit of the mechanical resonator, we will now analyze the dynamics of the fluctuations. We begin with the effective Hamiltonian of Eq. (5.4) to derive the dissipative dynamics of the fluctuations, which are described by the quantum Langevin equation

$$\frac{d}{dt}\hat{\vec{R}} = \boldsymbol{\mathcal{A}}\hat{\vec{R}} - \boldsymbol{\mathcal{K}}\hat{\vec{R}}_{\mathrm{in}}, \tag{5.9}$$

where we defined the vector containing all mode operators $\vec{R} = [\hat{d}, \hat{d}^\dagger, \hat{b}, \hat{b}^\dagger]^T$ and the dynamical matrix $\boldsymbol{\mathcal{A}}$ as

$$\boldsymbol{\mathcal{A}} = \begin{pmatrix} i\tilde{\Delta} - \frac{\kappa}{2} & i\Lambda & -iG & -iG \\ -i\Lambda^* & -i\tilde{\Delta} - \frac{\kappa}{2} & iG^* & iG^* \\ -iG^* & -iG & -i\omega_m - \frac{\gamma_m}{2} & 0 \\ iG^* & iG & 0 & i\omega_m - \frac{\gamma_m}{2} \end{pmatrix}. \tag{5.10}$$

In Eq. (5.9), the vector $\hat{\vec{R}}_{\rm in} = [\hat{d}_{\rm in}, \hat{d}^\dagger_{\rm in}, \hat{b}_{\rm in}, \hat{b}^\dagger_{\rm in}]^T$ represents the cavity and mechanical input noises characterized by the noise correlators given in Eqs.(3.60) and (3.61). On the other hand, the decay rates are included in the diagonal matrix $\boldsymbol{\mathcal{K}} = \text{diag}(\sqrt{\kappa}, \sqrt{\kappa}, \sqrt{\gamma_m}, \sqrt{\gamma_m})$.

As we did in Chapter 3, we will use the system's equations of motion to analyze the dynamical backaction effects arising from the radiation pressure interaction. In the following, we will focus on the impact of the intrinsic nonlinearity of the cavity on these effects. Using the parameters listed in Table 5.1, we will first discuss dynamical backaction cooling and then explore how the nonlinearity influences the detection sensitivity of mechanical motion in optomechanical systems.

5.4 Dynamical backaction cooling

In Chapter 3, we explored how radiation pressure interaction can be employed to cool a mechanical mode via dynamical backaction cooling. We observed that in the weak-coupling regime, a perturbative approach to the optomechanical interaction enables the derivation of the Stokes ($\Gamma_{\rm S}$) and anti-Stokes ($\Gamma_{\rm AS}$) rates, representing the heating and cooling rates, respectively, as given in Eq. (3.125). From this analysis, we concluded that cooling arises from the asymmetry between these rates, with the total optomechanical damping being the net downward rate, $\Gamma_{\rm opt} = \Gamma_{\rm AS} - \Gamma_{\rm S}$.

In addition, in Chapter 4, we examined how the presence of Kerr nonlinearity in the cavity leads to a pronounced asymmetry in the photon number spectrum, as described by Eq. (4.29) and depicted in Fig. 4.7. In this section, we will demonstrate how this asymmetry results in a substantial imbalance between the Stokes and anti-Stokes rates, thereby increasing the effective cooperativity and ultimately enhancing the cooling performance of the system.

Despite providing valuable insights into the advantages of using a nonlinear cavity and enabling a more straightforward derivation of the steady state phonon number in Eq. (3.130), the perturbative method, as studied in Chapter 3, relies on several approximations. As a result, it does not fully align with the complete numerical integration of the mechanical noise spectra, as shown in Fig. 3.14.

Because of the above, we will make a thorough analysis of the effective dynamics of the mechanical mode to explore the cooling limits of the system. We will demonstrate that this nonlinear approach is particularly advantageous for backaction cooling in the unresolved sideband regime, making it highly appealing for numerous applications involving massive mechanical systems.

5.4.1 Radiation pressure force spectrum

In Chapter 3.7, we discussed how a phase lag emerges between the radiation pressure force and the mechanical displacement due to the finite response time of the cavity. This out-of-phase force consistently opposes the oscillator's motion, acting as a damping force that extracts energy with each cycle, as illustrated in Fig. 3.12. In the absence of this retardation, the force would follow the oscillator's motion instantaneously, and no net cooling would occur. This explains why sideband cooling in the unresolved sideband regime is less effective.

In Chapter 4, we demonstrated that due to the intrinsic Kerr nonlinearity, the retardation of the cavity becomes more pronounced in the region where the decay rate splits as depicted in the red-shaded region in Fig. 4.4. As a result, the cavity ring-down time reaches its maximum at the bifurcation point, $\Delta_{\rm bi}$, leading to a longer coherence time of intracavity photons. The

effective cavity linewidth narrows as the detuning approaches this critical value, pushing the system into the resolved sideband regime.

Recalling the discussion in Chapter 3, the rates $\Gamma_{\mathrm{AS,S}}$ can be obtained using Fermi's Golden Rule applied to the radiation-pressure interaction between the mechanical oscillator and the cavity, namely $\hat{H}_{\mathrm{int}} = \hat{F}\hat{x}$ with the radiation pressure force $\hat{F} = g_0\hat{a}^\dagger\hat{a}$ [122]. Hence, within the weak coupling limit, the Stokes and anti-Stokes rates are given by Eq. (3.125) with the photon number spectrum given in Eq.(4.29). Hence, the optical damping introduced in Eq. (3.124) for a nonlinear cavity becomes

$$\Gamma_{\mathrm{opt}} = \frac{4g_0^2\bar{n}_c\kappa\left(|\Lambda| - \tilde{\Delta}\right)\omega_m}{\left[\tilde{\Delta}^2 - \omega_m^2 + \frac{\kappa^2}{4} - |\Lambda|^2\right]^2 + \kappa^2\omega_m^2}. \tag{5.11}$$

Optomechanical cooling is driven by the imbalance between the Stokes and anti-Stokes scattering processes as we discussed in Chapter 3. This imbalance is closely tied to the asymmetry of the photon number spectrum of the nonlinear cavity given in Eq. (4.29), which we measured using the effective skewness, γ_{eff}, which we introduced in Chapter 4. When we operate the nonlinear cavity close to the threshold power set by Eq. (5.8), maximum asymmetry is obtained close to the bifurcation point, Δ_{bi}, as shown in Fig. 4.7. Precisely under these conditions we also find maximum net optomechanical damping, which we measured in terms of the effective cooperativity $\mathcal{C}_{\mathrm{eff}} = \Gamma_{\mathrm{opt}}/\gamma_m$ as illustrated in Fig. 5.5. Experimentally, this effect was also pointed out in the work of D. Zoepfl *et al.* [3].

In addition, we also showed that this increased asymmetry and overall damping is closely tied to the asymmetrical shape of the intracavity photon number described by Eq. (4.20). By *ignoring* the asymmetry in the semiclassical dynamics, we observe a substantial reduction of the effective skewness, resulting in a decrease in optomechanical damping, as shown by the grey lines in Fig. 4.7.

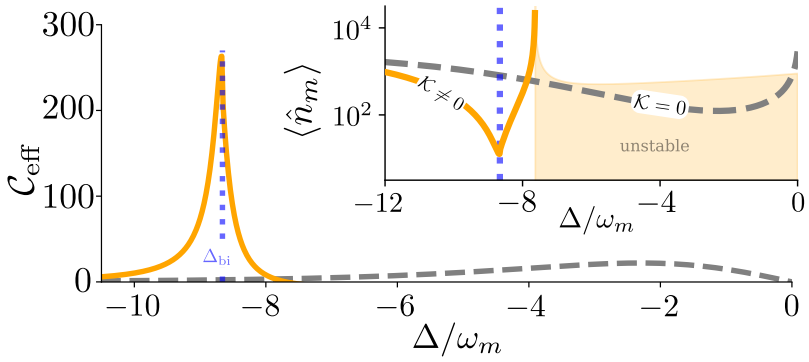

FIGURE 5.5: Effective cooperativity as a function of the optical detuning for a nonlinear (orange) and linear (dashed grey) cavity. Here, the asymmetric shape of the photon spectrum (see Fig. 4.7) caused by the presence of the Kerr nonlinearity results in the imbalance between the Stokes and anti-Stokes rates increasing the cavity damping, primarily around the critical detuning. Inset shows the average phonon number as a function of the cavity detuning, where the minimum occupation occurs at the point of maximum induced damping. For the parameters given in Table 5.1, we find that the cooling capabilities of a nonlinear system outperform an equivalent but linear system by more than an order of magnitude.

In the following, we will analyze the limits of cooling by deriving the effective dynamics of the mechanical mode. As we demonstrated in Chapter 3, this approach provides a more accurate description of the average mechanical occupation, which will be essential as we explore optimal backaction cooling for larger optomechanical coupling strengths.

5.4.2 Cooling limits

To investigate the cooling limits, we will analyze how the nonlinear cavity influences the dynamics of the mechanical mode by deriving the effective average mechanical occupation. Revisiting our study of dynamical backaction cooling in Sec. 3.7, here we aim to derive the

average mechanical occupation while considering the cavity's nonlinearity. Similarly as in our approach yielding Eq. (3.108), we start by transforming to frequency space the equation of motion given in Eq. (5.9) and solving them for $\hat{b}[\omega]$ and $\hat{b}^\dagger[\omega]$. This allows us to obtain an effective dynamical description of the mechanical oscillator given by the following equations of motion

$$\begin{pmatrix} \mathcal{X}^{-1}_{\mathrm{m,eff}}[\omega] & -i\Sigma^{\mathcal{K}}_c[\omega] \\ i\Sigma^{\mathcal{K}}_c[\omega] & \mathcal{X}^{*-1}_{\mathrm{m,eff}}[-\omega] \end{pmatrix} \begin{bmatrix} \hat{b}[\omega] \\ \hat{b}^\dagger[\omega] \end{bmatrix} = -\sqrt{\gamma_m} \begin{bmatrix} \hat{B}_{\mathrm{in}}[\omega] \\ \hat{B}^\dagger_{\mathrm{in}}[\omega] \end{bmatrix} \tag{5.12}$$

with the nonlinear cavity self-energy defined below

$$\Sigma^{\mathcal{K}}_c[\omega] = \frac{2|G|^2\left(|\Lambda| - \tilde{\Delta}\right)}{\tilde{\Delta}^2 - |\Lambda|^2 + \left(\frac{\kappa}{2} - i\omega\right)^2}. \tag{5.13}$$

Here, the modified mechanical noise is given by

$$B_{\mathrm{in}}[\omega] = \hat{b}_{\mathrm{in}}[\omega] + i\frac{1}{\sqrt{\gamma_m}}\hat{F}_{\mathrm{in}}[\omega] \tag{5.14}$$

with

$$\hat{F}_{\mathrm{in}}[\omega] = \eta^*[-\omega]\hat{d}_{\mathrm{in}}[\omega] + \eta[\omega]\hat{d}^\dagger_{\mathrm{in}}[\omega], \quad \eta[\omega] = -\frac{\sqrt{\kappa}}{\mathcal{N}[\omega]}\left(G\mathcal{X}_c^{-1}[\omega] + iG^*\Lambda\right). \tag{5.15}$$

with the denominator $\mathcal{N}[\omega] = \mathcal{X}_c^{*-1}[-\omega]\mathcal{X}_c^{-1}[\omega] - |\Lambda|^2$. Unlike the approach in Lau and Clerk's work [32], our single-drive system cannot cancel the backaction noise terms and associated unwanted heating, as we cannot leverage the interplay between two drives that would allow independent squeezing transformations to annihilate each other. Additionally, the response of the mechanical mode is encoded in the susceptibility matrix of the last equation with the cavity self-energy described in Eq. (5.13). Due to the optomechanical interaction, the effective susceptibility in Eq. (5.12) contains a modified mechanical frequency and damping $\omega_m - \Re\{\Sigma_c[\omega]\}$ and $\gamma_m + 2\Im\{\Sigma_c[\omega]\}$, respectively. The cavity also induces single-mode squeezing in the mechanical oscillator. Unlike the linear case described in Eq. (3.110), the dynamical modification due to the cavity interaction persists even on resonance ($\Delta = 0$) due to the presence of the cavity Kerr nonlinearity.

At sufficiently strong coupling, the cavity self-energy can be approximated as $\Sigma_c[\omega] \approx \Sigma_c[\omega_m]$. Consequently, for a high-Q mechanical oscillator, the mechanical noise spectrum simplifies to the following form:

$$\begin{aligned} \mathcal{S}_{bb}[\omega] = &\frac{\gamma_m\left|\mathcal{X}_m^{*-1}[-\omega] + i\Sigma_c[\omega_m]\right|^2}{\left|(\omega - \Omega_{m,+})(\omega - \Omega_{m,-})\right|^2}\bar{n}_m^T \\ &+ \frac{\gamma_m\left|\Sigma_c[\omega_m]\right|^2}{\left|(\omega - \Omega_{m,+})(\omega - \Omega_{m,-})\right|^2}\left(\bar{n}_m^T + 1\right) \\ &+ \frac{\left|\mathcal{X}_m^{*-1}[-\omega]\right|^2}{\left|(\omega - \Omega_{m,+})(\omega - \Omega_{m,-})\right|^2}\Gamma_{\mathrm{S}}, \end{aligned} \tag{5.16}$$

with the Stokes rate given in Eq. (3.125) and the poles

$$\Omega_{m,\pm} = -i\frac{\gamma_m}{2} \pm \sqrt{\omega_m^2 - 2\omega_m\Sigma_c[\omega_m]} = \pm\left[\mathcal{W}_R - i\mathcal{Z}_\pm\right], \tag{5.17}$$

where we defined $\mathcal{W}_R - i\mathcal{W}_I \equiv \sqrt{\omega_m^2 - 2\omega_m\Sigma_c[\omega_m]}$ and $\mathcal{Z}_\pm \equiv \pm\gamma_m/2 + \mathcal{W}_I$.

In this expression, note that the first two terms arise due to the mechanical noise correlators $\langle\hat{b}^\dagger_{\mathrm{in}}(t)\hat{b}_{\mathrm{in}}(t')\rangle = \bar{n}_m^T\delta(t-t')$ and $\langle\hat{b}^\dagger_{\mathrm{in}}(t)\hat{b}_{\mathrm{in}}(t')\rangle = (\bar{n}_m^T+1)\delta(t-t')$, respectively. The latter is associated with the off-diagonal terms of the Langevin matrix in Eq. (5.12), thereby with the induced single-mode squeezing. This implies that the term proportional to $\bar{n}_m^T + 1$ arises solely from the optomechanical interaction. In contrast, the last line represents the thermal

occupation introduced exclusively by the cavity backaction.

The poles of the mechanical noise spectra given in Eq. (5.17) are related to the effective mechanical eigenvalues via $\lambda_{m,\pm} = -i\Omega_{m,\pm}$. Thus, similarly as in Chapter 3.7, if we assume that $\Sigma_c[\omega] \approx \Sigma_c[\omega_m]$ and Taylor expand around $\Sigma_c[\omega_m]$ we find the effective eigenvalues of the mechanical mode

$$\lambda_{m,\pm} \approx -i\left(\omega_m \mp \Re\{\Sigma_c[\omega_m\}\right) - \frac{1}{2}\left(\gamma_m \pm \Im\{\Sigma_c[\omega_m\}\right), \tag{5.18}$$

which agree with the modified frequency shift and damping, $\omega_m[\omega_m]$ and $\gamma_m[\omega_m]$.

The occupation of the mechanical mode can be obtained by following

$$\langle \hat{n}_m \rangle = \int \frac{d\omega}{2\pi} \mathcal{S}_{bb}[\omega] \tag{5.19}$$

with the noise spectrum given in Eq. (5.16). To perform the integration of Eq. (5.16) via the *Residue theorem* [184], we have to first perform a stability analysis of the poles. Thus, we have the following four scenarios

$$\begin{aligned}
&1.\ \mathcal{Z}_+ > 0, \quad \mathcal{Z}_- > 0: \qquad p_1 = \mathcal{W}_R - i\,\mathcal{Z}_+, \quad p_2 = -\mathcal{W}_R - i\,\mathcal{Z}_-,\\
&2.\ \mathcal{Z}_+ < 0, \quad \mathcal{Z}_- < 0: \qquad p_1^* = \mathcal{W}_R + i\,\mathcal{Z}_+, \quad p_2^* = -\mathcal{W}_R + i\,\mathcal{Z}_-,\\
&3.\ \mathcal{Z}_+ > 0, \quad \mathcal{Z}_- < 0: \qquad p_1 = \mathcal{W}_R - i\,\mathcal{Z}_+, \quad p_2^* = -\mathcal{W}_R + i\,\mathcal{Z}_-,\\
&4.\ \mathcal{Z}_+ < 0, \quad \mathcal{Z}_- > 0: \qquad p_1^* = \mathcal{W}_R + i\,\mathcal{Z}_+, \quad p_2 = -\mathcal{W}_R - i\,\mathcal{Z}_-.
\end{aligned}$$

We can discard regime 4, since $\mathcal{Z}_+ > \mathcal{Z}_-$ for all parameters. Furthermore, note that regime 2 is unstable due to positive damping leading to a divergent evolution. Regime 3 is stable if $-\frac{\gamma}{2} < \mathcal{W}_I < \frac{\gamma}{2}$, namely for small optical damping. Here, the only possible stable solution arises when $\mathcal{Z}_\pm > 0$. Hence, based on this stability analysis and using the Residue theorem, we find the following integrals

$$\begin{aligned}
\mathcal{I}_1 &= \int_{-\infty}^{\infty} \frac{d\omega}{2\pi} \frac{1}{\left|(\omega-\Omega_+)(\omega-\Omega_-)\right|^2} = \frac{\mathcal{W}_I}{[\gamma^2 - 4\mathcal{W}_I^2]\,[\mathcal{W}_R^2 + \mathcal{W}_I^2]},\\
\mathcal{I}_2 &= \int_{-\infty}^{\infty} \frac{d\omega}{2\pi} \frac{\omega}{\left|(\omega-\Omega_+)(\omega-\Omega_-)\right|^2} = \frac{\frac{\gamma}{2}\mathcal{W}_R}{[\gamma^2 - 4\mathcal{W}_I^2]\,[\mathcal{W}_R^2 + \mathcal{W}_I^2]},\\
\mathcal{I}_3 &= \int_{-\infty}^{\infty} \frac{d\omega}{2\pi} \frac{\omega^2}{\left|(\omega-\Omega_+)(\omega-\Omega_-)\right|^2} = \frac{\mathcal{W}_I\left[\mathcal{W}_R^2 + \mathcal{W}_I^2 - \left(\frac{\gamma}{2}\right)^2\right]}{[\gamma^2 - 4\mathcal{W}_I^2]\,[\mathcal{W}_R^2 + \mathcal{W}_I^2]}.
\end{aligned} \tag{5.20}$$

These integrals can be further simplified using the same approximation yielding Eq. (5.18). As a consequence, using this approximation on the second equality in Eq. (5.17), results in $\mathcal{W}_R = \omega_m - \Re\{\Sigma_c[\omega_m]\}$ and $\mathcal{W}_I = \Im\{\Sigma_c[\omega_m]\}$. Hence, considering that $|\Sigma_c[\omega_m]/\omega_m|^2 \ll 1$ the integrals in Eq. (5.20) become

$$\mathcal{I}_1 \approx \frac{\mathcal{C}_{\text{eff}}}{2\omega_m^2\gamma_m\,[\mathcal{C}_{\text{eff}}^2 - 1]}, \qquad \mathcal{I}_2 \approx \frac{1}{2\omega_m\gamma_m\,[1 - \mathcal{C}_{\text{eff}}^2]}, \qquad \mathcal{I}_3 \approx \frac{\mathcal{C}_{\text{eff}}}{2\gamma_m\,[\mathcal{C}_{\text{eff}}^2 - 1]}\left[1 - \left(\frac{\gamma_m}{2\omega_m}\right)^2\right], \tag{5.21}$$

with the effective cooperativity defined as $\mathcal{C}_{\text{eff}} = -2\Im\{\Sigma_c[\omega_m]\}/\gamma_m$.

Following Eq. (3.138) with the mechanical spectra given by Eq. (5.16), we derive an expression in terms of the simplified integrals mentioned above, which reads:

$$\begin{aligned}
\langle \hat{n}_m \rangle \approx\ & \gamma_m\omega_m^2\left\{\left[\left(\frac{\gamma_m}{2\omega_m}\right)^2 + 1\right]\mathcal{I}_1 + \frac{2}{\omega_m}\mathcal{I}_2 + \left(\frac{1}{\omega_m}\right)^2\mathcal{I}_3\right\}\bar{n}_m^T + \gamma_m\left|\Sigma_c[\omega_m]\right|^2\left(\bar{n}_m^T + 1\right)\mathcal{I}_1\\
&+ \left(\omega_m^2\left[1 + \left(\frac{\gamma_m}{2\omega_m}\right)^2\right]\mathcal{I}_1 + 2\omega_m\mathcal{I}_2 + \mathcal{I}_3\right)\Gamma_{\text{S}}.
\end{aligned} \tag{5.22}$$

Finally, we find that the substitution of Eq. (5.21) into Eq. (5.22) coincides with the result obtained using (3.130) yielding

$$\langle \hat{n}_m \rangle \approx \frac{\bar{n}_m^T}{\mathcal{C}_{\text{eff}}+1} + \frac{\mathcal{C}_{\text{eff}}}{\mathcal{C}_{\text{eff}}+1}\frac{\left(\omega_m - \Delta_{\text{eff}}\right)^2 + \frac{\kappa^2}{4}}{4\omega_m \Delta_{\text{eff}}} \tag{5.23}$$

with the effective detuning $\Delta_{\text{eff}} \equiv |\Lambda| - \tilde{\Delta}$. In the last equation, as well as in Eq. (3.130), the first term corresponds to a modified thermal occupation, while the second term arises from unwanted cavity backaction heating, thereby imposing limits on cooling. Note that in the absence of optomechanical interaction, the mechanical occupation is, on average, its thermal occupation, denoted as $\bar{n}_m^T$. Note that, under the assumption that $\Sigma_c[\omega_m]/\omega_m \ll 1$, the term proportional to $\bar{n}_m^T + 1$ is negligible. The above implies that the off-diagonal elements in Eq. (5.12) are disregarded, along with the induced squeezing described by non-resonant processes.

From Eq. (5.23), we observe that at high effective cooperativity, the phonon number is primarily determined by the cavity backaction, which results in the following expression for the occupation number:

$$\bar{n}_{\text{BA}} \equiv \lim_{\mathcal{C}_{\text{eff}}\to\infty} \bar{n}_m = \frac{\left(\omega_m - \Delta_{\text{eff}}\right)^2 + \frac{\kappa^2}{4}}{4\omega_m \Delta_{\text{eff}}}, \tag{5.24}$$

This result, under the replacement $\Delta_{\text{eff}} \to -\Delta$, has an equivalent expression to the lowest achievable phonon number for a linear cavity, demonstrating that cavity backaction ultimately defines the cooling limits according to the standard framework of laser cooling [1].

However, we can still determine the *optimal detuning* for minimizing the backaction phonon number in Eq. (5.24). This optimal detuning is given by: $\Delta_{\text{eff}} \to \sqrt{\kappa^2/4 + \omega_m^2}$. Substituting this optimal detuning into the expression for the backaction phonon number results in the minimum achievable backaction phonon number as:

$$\bar{n}_{\text{BA}}^{\min} \equiv \bar{n}_{\text{BA}}\big|_{\Delta_{\text{eff}}\to\sqrt{\kappa^2/4+\omega_m^2}} = \frac{\sqrt{\frac{\kappa^2}{\omega_m^2}+4}-2}{4}. \tag{5.25}$$

Thus, ground state cooling, i.e. $\bar{n}_{\text{BA}}^{\min} < 1$, is only possible when

$$\frac{\omega_m}{\kappa} > \frac{1}{4\sqrt{2}} \approx 0.177, \tag{5.26}$$

which coincides with the case of a linear cavity.

The experimental work by Zoepfl *et al.* [3] used similar parameters as those provided in Table 5.1, and with $\omega_m/\kappa = 0.1$ places the system in the unresolved sideband regime. A high effective cooperativity, $\mathcal{C}_{\text{eff}}$, enables, in particular, the suppression of the thermal occupation as we see in the first term of Eq. (5.23). From our analysis, we thus find that the corresponding minimal value for the mechanical occupation is only reachable for high effective cooperativity and thus strong enough driving. Operating below the bifurcation point of the cavity, the driving strength is constrained, and with the given parameters, we can reach an effective cooperativity of $\mathcal{C}_{\text{eff}} \approx 264$, as we show in Fig. 5.5. In contrast, for equivalent parameters and driving strength, a linear cavity achieves an effective cooperativity of only $\mathcal{C}_{\text{eff}} \approx 22$. This demonstrates that, from the first term in Eq. (5.23), under the given conditions, the use of the nonlinearity in the cavity enables better cooling performance by one order of magnitude in the minimum phonon occupation. To reach a comparable cooling limit, a linear cavity would require nearly 12 times more input power. This is feasible because a linear system requires a notoriously stronger input power to become bistable. Hence, it is not limited by the drive power in the same way as a nonlinear cavity. Nevertheless, this highlights the superior cooling efficiency of a nonlinear cavity compared to a linear cavity at low input powers.

Based on the experimental realization in [3]. To avoid undesirable high thermal occupation of the cavity and ensure it operates in a superconducting state, the experiment is housed in a dilution refrigerator, allowing the samples to be cooled down to $T \approx 40$ mK. For the parameters given in Table 5.1 this implies the mechanical mode to be in a thermal occupation of $\bar{n}_m^T = k_{\text{B}}T/\omega_m \approx 2778$.

Using Eq. (5.23) with the parameters given in Table 5.1, it can be seen that the mechanical

occupation can be suppressed from 2778 thermal phonons down to $\bar{n}_m = 12.66$, which is about 220 times lower than the thermal occupation. This result agrees with the cooling performance demonstrated experimentally in [3] and is shown in Fig. 5.5. According to Eq. (5.23), this occupation arises from the modified thermal and the backaction contributions, with the latter accounting for ~ 3 phonons. The above also indicates that for the parameters given in Table 5.1 we are still not limited by the cavity backaction. On the other hand, with the same parameters and identical input power, a linear cavity achieves a cooling limit of ~ 123 phonons. This demonstrates that, under the given conditions, a nonlinear cavity improves cooling performance by nearly an order of magnitude as depicted in the inset of Fig. 5.5.

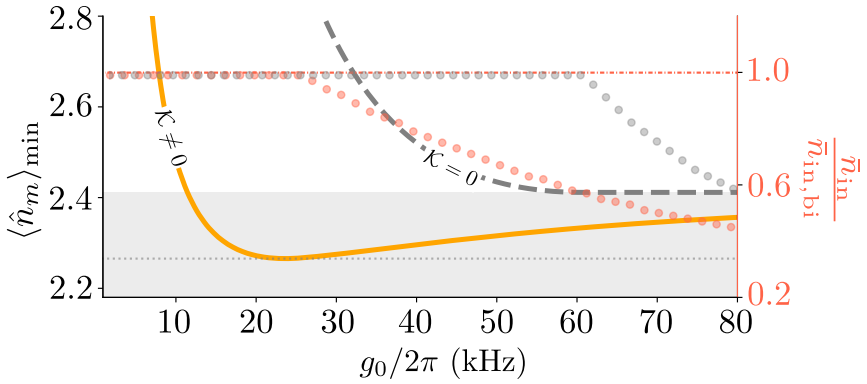

FIGURE 5.6: Lowest phonon number reached as a function of the optomechanical coupling strength always using the optimal input power (red dotted plot) up to bistability for the nonlinear setup (orange). The use of a nonlinear cavity outperforms an identical but linear (grey dashed) setup even for weaker coupling strengths. For each value of coupling strength, we have used the optimal input power below bifurcation (red/grey dotted line for $\mathcal{K} \neq 0/\mathcal{K} = 0$). The grey-shaded region shows the phonon occupation below the linear limit. Note, that the optimal input power decreases for larger coupling strengths to minimize the backaction contribution. The remaining parameters are given in Table 5.1.

To further illustrate the efficiency of a nonlinear cavity in the unresolved sideband regime, consider the cooling limit of $\bar{n}_m = 12.66$ phonons. Achieving this level of cooling with a nonlinear cavity requires only 9.26 intracavity photons. In contrast, a linear cavity, under equivalent conditions, would necessitate approximately 144 photons to reach the same cooling performance. This difference highlights the enhanced efficiency of a nonlinear cavity, which allows for more effective cooling with significantly fewer photons.

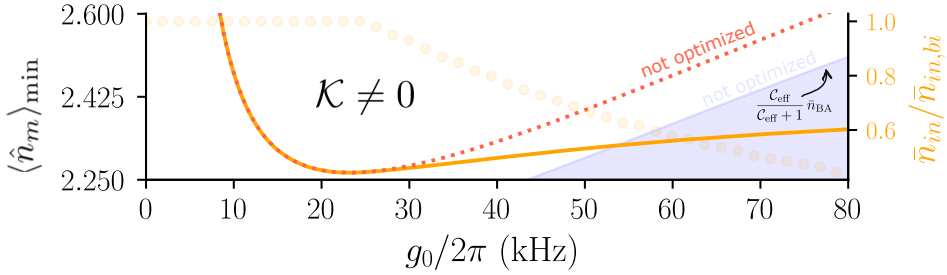

FIGURE 5.7: Lowest phonon number reached as a function of the optomechanical coupling strength obtained for a nonlinear cavity for optimized (orange) and not optimized (red-dotted) input power. For strong enough interaction strengths, the optimization of the driving strength results in a reduction of the detrimental backaction contribution (blue-shaded area with not optimized power), which for $g_0/2\pi = 23.28$ kHz set the cooling limits.

We now relax the constraints imposed by the parameters listed in Table 5.1 and investigate the lowest phonon occupation achievable as the optomechanical coupling strength increases as shown in Fig. 5.6. Here, the minimum phonon number is achieved by optimizing the

input power for each optomechanical coupling strength, under the condition that the system remains in the monostable regime. This means that we allow the *optimal input power* to only take values within the range set by the bifurcation threshold given by Eq. (5.8) i.e. $\bar{n}_{\rm in}/\bar{n}_{\rm in,bi} \in [0, 0.99]$. The optimal input power is then shown by the red dots for a nonlinear cavity in Fig. 5.6. The lowest phonon number obtained for a nonlinear cavity under these conditions is depicted by the solid-orange curve in Fig. 5.6. In contrast, the solid-grey curve represents the limits obtained with a linear cavity using equivalent parameters and with the optimized power also within the range $\bar{n}_{\rm in}/\bar{n}_{\rm in,bi} \in [0, 0.99]$. Here, we show that the nonlinear setup allows cooling down to $\bar{n}_m = 2.26$ for a coupling strength of $g_0/2\pi = 23.28$ kHz when driven at $\bar{n}_{\rm in} = 0.99\bar{n}_{\rm in,bi}$, where all other parameters are given in Table 5.1. This represents a 26% improvement compared to the linear setup, which under identical parameters yields $\bar{n}_m = 3.06$, since the power is not optimized. Moreover, linear cooling requires a larger optomechanical coupling strength or a stronger input power to achieve the best cooling of 2.41 phonons for $\omega_m/\kappa = 0.1$ as we see in Fig. 5.6. In contrast, the nonlinear setup provides at lower g_0 a more efficient cooling even surpassing this value.

In Fig. 5.7 we compare the optimal result discussed above with the lowest phonon number obtained when the system is not operated at optimized input power, but instead at $\bar{n}_{\rm in} = \bar{n}_{\rm in,crit}$ across all coupling strengths. Recalling Eq. (5.23), we observe that for sufficiently strong coupling strengths, the thermal contribution is almost completely suppressed (see Fig. 5.8), leaving the backaction contribution as the limiting factor for cooling. In the nonlinear system, with sufficiently strong interaction, the optimized input power effectively minimizes this backaction contribution. This is illustrated in Fig. 5.7, where the optimized result, represented by the orange-solid curve (see also Fig. 5.6), shows improved cooling for $g_0/2\pi >$ 26.1 kHz compared to the red-dotted curve, where the input power is kept at $\bar{n}_{\rm in} = \bar{n}_{\rm in,crit}$. Since a linear cavity demands either higher coupling strengths or increased input powers to reach the cooling limits of a nonlinear cavity, under equivalent conditions as the nonlinear system, the improvement achieved through optimized power becomes significant for $g_0/2\pi >$ 60 kHz.

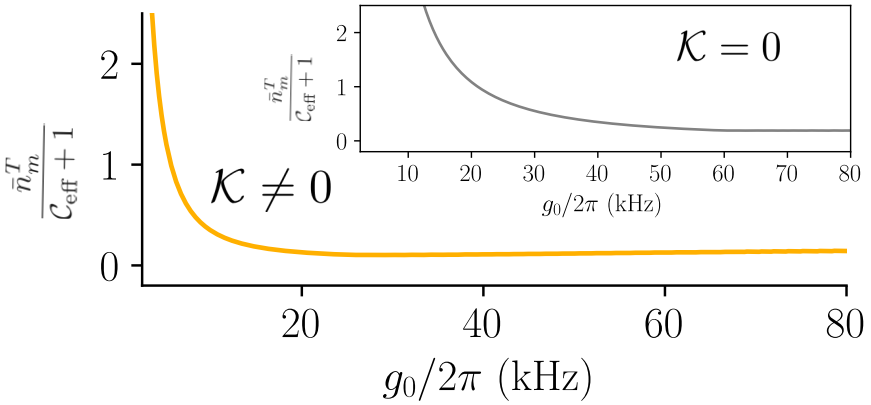

FIGURE 5.8: Modified thermal occupation as a function of the optomechanical coupling strength for optimized input power. For $\bar{n}_m^T = 2778$, the high effective cooperativity of the nonlinear cavity suppresses the thermal contribution at lower optomechanical coupling strength compared to a linear cavity (see inset) under similar conditions and optimized power. At large coupling strengths, the reduction of the input power (see Fig. 5.6) leads to the minimization of the unwanted backaction contribution, a the expense of a slight increase of the thermal contribution. This occurs since the backaction contribution sets the cooling limits at strong coupling strengths.

As shown in Fig. 5.5, the cavity's nonlinearity increases the effective cooperativity, resulting in a more efficient suppression of thermal occupation compared to a linear cavity. Recalling Eq. (5.23), increasing the optomechanical coupling strength raises the effective cooperativity, leading to $\bar{n}_m^T(\mathcal{C}_{\rm eff}+1)^{-1} \to 0$. This is illustrated in Fig. 5.8, where the cavity nonlinearity enables a suppression of the thermal contribution at weaker coupling strengths than in a linear cavity under similar conditions.

However, as the optomechanical coupling increases, the backaction contribution becomes the limiting factor for cooling, as it scales with $\mathcal{C}_{\rm eff}(\mathcal{C}_{\rm eff}+1)^{-1}$. Hence for such coupling

strengths, the optimization of the input power becomes critical since the effective cooperativity depends on the intracavity photon number: $\mathcal{C}_{\text{eff}} \sim g_0^2 \bar{n}_c$. Therefore, a weaker input power permits reducing the backaction contribution (see blue-shaded area in Fig. 5.7). This explains the decrease of the optimal input power shown in Figs. 5.6 and 5.7 for larger optomechanical coupling strength.

To further explore the advantages of the nonlinear setup, we analyzed the lowest mechanical occupation achieved as a function of the resolved parameter, ω_m/κ, as shown in Fig. 5.9. This comparison includes the cooling performance of the nonlinear system (orange) and the conventional linear system (dashed grey) for a fixed $g_0/2\pi = 15$ kHz, with both systems driven equally at $\bar{n}_{\text{in}} = \bar{n}_{\text{in,crit}}$. Notably, for a given optomechanical coupling strength, the lowest mechanical occupation achieved with the nonlinear cavity closely approaches the minimum phonon number imposed by the cavity backaction (blue-shaded area). Our findings reveal that the more unresolved the system is, the greater the improvement with the nonlinear cavity. Conversely, as we approach the resolved sideband regime, the advantage of the nonlinear setup diminishes, yielding results similar to the linear system. For $\omega_m/\kappa > 1$, we observe an increase in temperature since the driving power is not optimized. Unlike the nonlinear system, the linear system is not backaction limited for the given input power in this regime. Hence, for a linear optomechanical system to reach its backaction limit we would require a substantially higher input power.

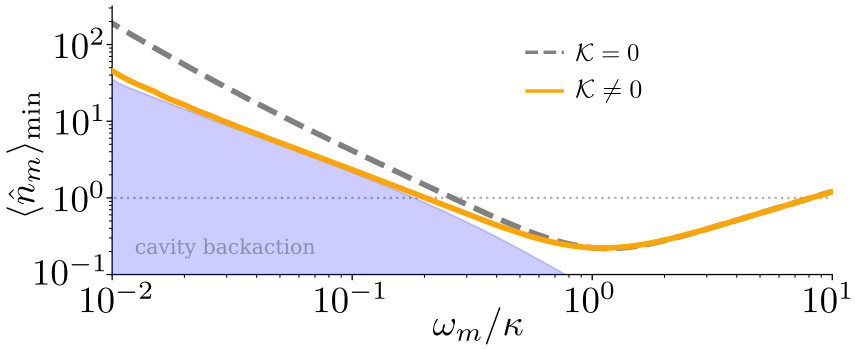

FIGURE 5.9: Lowest phonon occupation reached as a function of the resolved sideband parameter ω_m/κ. In the unresolved sideband regime, a nonlinear cavity (orange) outperforms an identical but linear cavity (dashed grey) at the same input power. For given parameters with an optomechanical coupling strength of $g_0/2\pi = 15$ kHz the mechanical occupation is limited by the cavity unwanted backaction heating (blue area). With increasing mechanical frequency, this improvement becomes smaller showing equivalent results to the linear setup. In the resolved sideband regime the thermal occupation of the bath overcomes the cooling capabilities in both setups at the given input power. For $\omega_m/\kappa > 1$ we observe a temperature increase since the driving power is not optimized in the linear regime, while for the nonlinear case it is always close to the critical input power, $\bar{n}_{\text{in}} = \bar{n}_{\text{crit}}$.

As illustrated in Fig. 5.9, the use of a nonlinear cavity allows for ground state cooling at a coupling strength of $g_0/2\pi = 15$ kHz for a resolved sideband parameter $\omega_m/\kappa = 0.21$. In contrast, achieving the same cooling limit with a linear cavity requires $\omega_m/\kappa = 0.27$. This observation demonstrates that, within the unresolved sideband regime, a nonlinear cavity driven close to its critical input power set by Eq. (5.8) is more efficient for cooling compared to a linear cavity.

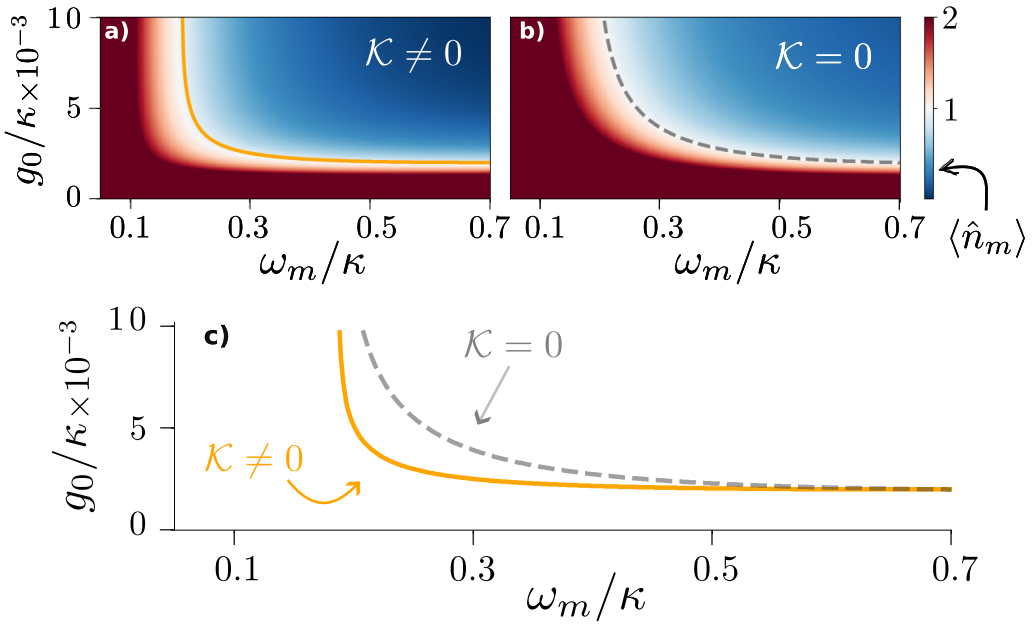

FIGURE 5.10: Average phonon number as a function of the optomechanical coupling strength g_0/κ and resolved sideband parameter ω_m/κ using a nonlinear a) and linear system b). The solid orange and dashed grey lines show the values for which the ground state is achieved in a nonlinear and linear setup, respectively. Ground state cooling can be obtained using a nonlinear cavity (orange) both at lower coupling strength and smaller mechanical frequency as for an equivalent linear system as shown in c). All other parameters are given in Table 5.1.

In Fig. 5.10, we illustrate the conditions under which ground state cooling is achieved as a function of the resolved sideband parameter ω_m/κ for a given optomechanical coupling strength g_0/κ. Specifically, at $g_0/\kappa = 0.85 \times 10^{-3}$, the nonlinear cavity (depicted in orange) is capable of reaching ground state cooling at $\omega_m/\kappa = 0.189$. In contrast, achieving the same level of cooling in a linear system requires a significantly higher coupling strength of $g_0/\kappa = 1.79 \times 10^{-3}$ and a slightly larger mechanical frequency of $\omega_m/\kappa = 0.192$. Furthermore, as the mechanical frequency increases, the advantages of employing a nonlinear cavity diminish, resulting in comparable cooling performance to that of the linear system. This observation confirms that, within the unresolved sideband regime, a nonlinear cavity enables ground state cooling at lower coupling strengths compared to a linear cavity.

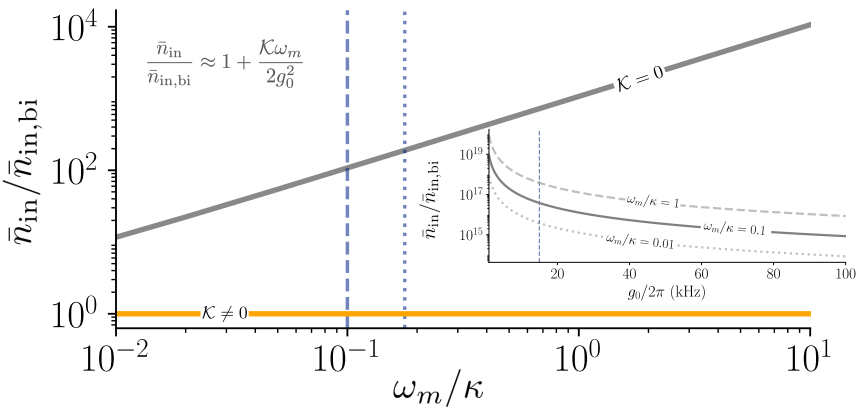

FIGURE 5.11: Required input power for optimal cooling as a function of the resolved sideband parameter, ω_m/κ. A linear cavity (grey) operating in the monostable requires substantially more input power to reach the backaction limit compared to a nonlinear system (orange). The dashed vertical line represents experimental parameters, while the dotted vertical line marks the resolved sideband parameter from which ground state cooling becomes feasible. For a high-Q mechanical oscillator, the input power exhibits a linear dependence. Inset shows the required input power for optimal cooling as a function of the optomechanical coupling strength for different resolved sideband parameters. For the parameters given in Table 5.1, with an optomechanical coupling strength of $g_0/2\pi = 15$ kHz.

Thus far, we have constrained the input power to the critical value given in Eq. (5.8). This threshold arises from the monostable condition we have implemented for the nonlinear cavity. In contrast, the critical input power for a linear optomechanical system is significantly higher, determined by the optomechanically induced Kerr as shown by Eq. (3.73). This suggests that driving the linear system harder would eventually cause it to approach the backaction limit, as illustrated in Fig. 5.9.

Restricting the linear cavity to the monostable regime, i.e., to powers below the bistable regime induced by the mechanical Kerr, we find that the optimal input power is at $\bar{n}_{\rm in} = 0.99\bar{n}_{\rm in,bi}^{\mathcal{K}=0}$ and with Eq. (3.73) we obtain

$$\frac{\bar{n}_{\rm in}}{\bar{n}_{\rm in,bi}} \approx \frac{\bar{n}_{\rm in,bi}^{\mathcal{K}=0}}{\bar{n}_{\rm in,bi}} = 1 + \frac{\mathcal{K}}{\mathcal{K}_m} \approx 1 + \frac{\mathcal{K}\omega_m}{2g_0^2}, \tag{5.27}$$

where we used the definition of the mechanical Kerr in Eq. (5.6) in the last step. In Fig. 5.11, we plot the last equation as a function of the resolved sideband parameter. For the nonlinear cavity, this corresponds to driving at $\bar{n}_{\rm in} = \bar{n}_{\rm in,crit}$, as shown by the orange line. In contrast, for a high-Q mechanical oscillator, a linear system requires substantially stronger driving —scaling linearly— to reach the backaction limit, particularly in the unresolved sideband regime. Using experimental parameters, at $\omega_m/\kappa = 0.1$ (dashed vertical line), a linear system requires approximately 107 times more input power than a nonlinear system. This highlights the improved cooling efficiency of our nonlinear setup in the unresolved sideband regime.

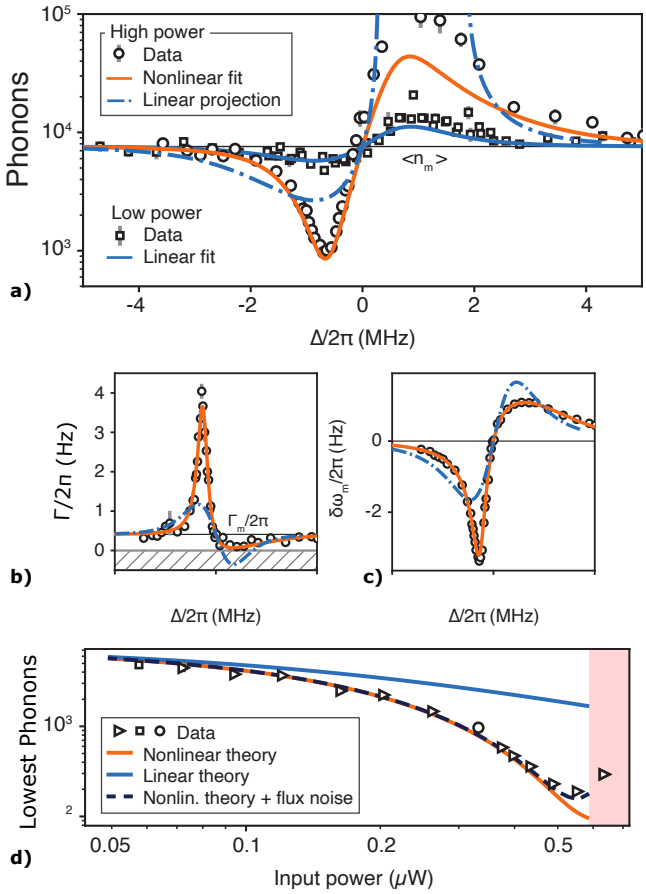

FIGURE 5.12: Experimental results obtained at $g_0/2\pi = 201 \pm 3$ Hz for $\mathcal{K}/2\pi = 12.2 \pm 0.1$ kHz/photon. a) Shows the mechanical occupation as a function of the cavity detuning for high and low powers. b) and c) present the modification of the mechanical linewidth and frequency, respectively, against detuning. d) presents the lowest phonon number for different input power. Before bistability (red-shaded region), the cooling is limited by flux noise. The errors shown are the standard errors. Plots taken with permission from D. Zoepfl [3].

Finally, in Fig. 5.12, we present the experimental results obtained at $g_0/2\pi = 201 \pm 3$ Hz, chosen to minimize limiting effects from flux noise, as reported by D. Zoepfl et al. [3]. At low power, the cavity behaves effectively as a linear system, as shown in Fig. 5.12a). However, at high power, near the onset of bistability, the cooling trace in Fig. 5.12a) exhibits excellent agreement with our nonlinear theory for $\mathcal{K}/2\pi = 12.2 \pm 0.1$ kHz/photon. Furthermore, at high power, a purely linear cavity model—assuming identical parameters—predicts both weaker cooling and greater heating than that observed experimentally. Fig. 5.12b) and c) show the measured changes in mechanical linewidth and frequency at high power, respectively, again demonstrating strong agreement with the nonlinear theory. Fig. 5.12d) presents the lowest phonon number measured for each cooling trace as a function of input power, where increasing drive power leads to a significant enhancement in cooling. Notably, our nonlinear model accurately predicts these cooling limits, revealing an improvement of one order of magnitude over a conventional linear system. To account for flux noise at high input power, a Gaussian distribution for the detuning is incorporated [3].

So far, we have limited our analysis to the regime just before the bifurcation threshold, ensuring $\bar{n}_c$ given by Eq. (5.5) is a single-valued function. Nevertheless, in the next section, we will loosen this constraint and study cooling above bistability as done in the work of L. Deeg *et al.* [35].

5.4.3 Backaction cooling in the bistable regime

Throughout this section, we have studied dynamical backaction cooling in an optomechanical system using a nonlinear cavity, slightly below the bifurcation threshold set by Eq.(5.8). Here, we will relax this condition and analyze cooling above bistability. We will show that the theory derived in the last section also describes backaction cooling beyond the bifurcation point as demonstrated in recent work [35].

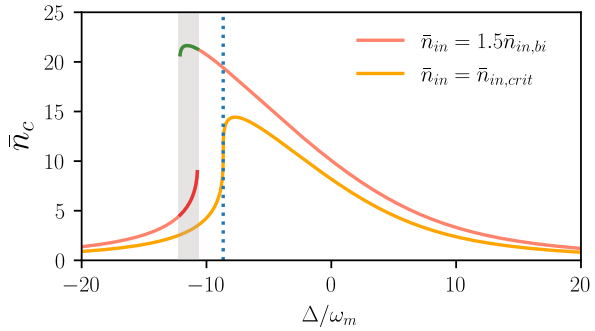

FIGURE 5.13: Intracavity photon number as a function of the optical detuning for different driving strengths. For driving powers above threshold ($\bar{n}_{\mathrm{in,bi}}$) as illustrated by the red line, $\bar{n}_c$ becomes a multivalued function for certain detunings. This gives rise to a high and low photon branch, depicted in green and red, respectively. Around those detunings for which $\bar{n}_c$ switches branches, the optical damping increases and the best cooling arises.

Recalling the cubic equation describing the intracavity photon number given in Eq. (5.5). If the drive strength exceeds the critical input power in Eq. (5.8), for certain driving frequencies the cavity photon number $\bar{n}_c$ splits into a high and a low photon number solution. This is depicted in Fig. 5.13, where the high and low photon branches are illustrated in green and red, respectively.

Similarly as in the case before bistability, at high driving strengths, the photon number spectrum deviates from a typical Lorentzian distribution and becomes highly asymmetric as a function of the detuning with a pronounced slope. As shown in Sec. 5.4.1, this occurs at the critical detuning given in Eq. (5.7) (see Fig. 4.7), but also for detunings where the photon number *jumps* from one branch to the other as illustrated in Fig. 5.13. Around these points, the asymmetry of the photon number spectrum rises resulting in an increased imbalance between the Stokes and anti-Stokes rates. As studied in Sec. 5.4.1, a larger imbalance enhances the cooling capabilities as illustrated in Fig. 5.14. This enhanced imbalance leads to improved cooling around these detunings as we can observe in the inset in Fig. 5.14, where the lowest phonon occupation is obtained for the low photon-number branch. Note, the lowest phonon number achieved for $\bar{n}_{\mathrm{in}} = 1.5\bar{n}_{\mathrm{in,bi}}$ is given by approximately 9 phonons, whereas for an input power below bifurcation, $\bar{n}_{\mathrm{in}} = \bar{n}_{\mathrm{in,crit}}$, is around 13 phonons.

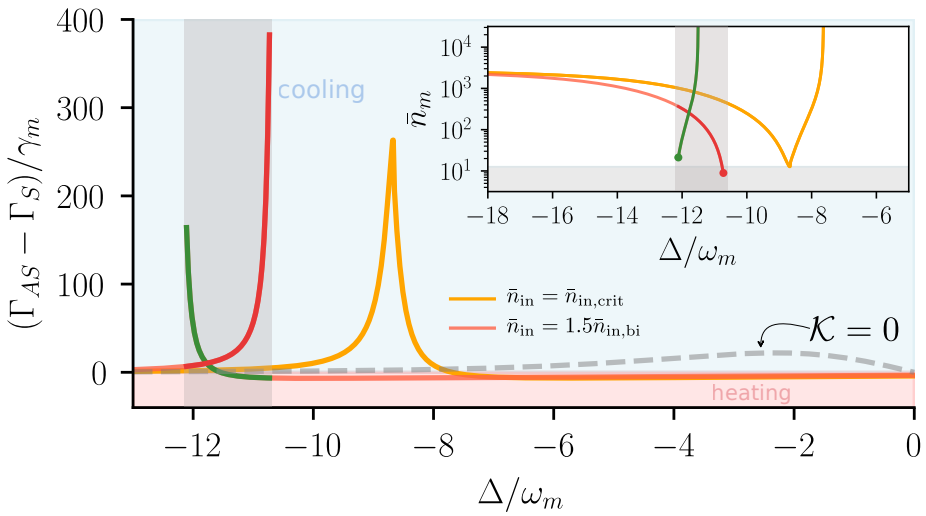

FIGURE 5.14: Effective cooperativity $\mathcal{C}_{\rm eff} = \Gamma_{\rm opt}/\gamma_m$ as a function of the cavity detuning for different driving strengths. The inset shows the corresponding average mechanical occupation as a function of the cavity detuning. The nonlinear cavity exhibits maximum cooperativity at the borders of the bistable interval (shaded-grey). At these points, the asymmetry of the photon number spectrum reaches its maximum, which happens where the branch switching occurs (see Fig. 5.13). The low-photon branch (red) shows the highest cooperativity and correspondingly best cooling limit (see inset).

Nevertheless, to observe backaction above bistability it is vital to be sufficiently close to these *switching* detunings. As we see in Fig. 5.13, a slight change in these detunings leads to an abrupt modification of the photon number spectrum and consequently of its asymmetry. Due to this high sensitivity, cooling above bistability becomes experimentally challenging, since it requires a well-isolated setup from external noise sources, like flux or vibrational noise.

To experimentally study the mechanics, we measure the homodyne noise spectrum of a probe tone applied to the cavity. As a result of the optomechanical interaction, this probe tone experiences an effective amplitude (phase) modulation at the mechanical frequency ω_m passing through the system [94]. To extract the phonon number, mechanical frequency and damping, we fit a model of a damped harmonic oscillator to the resulting sidebands. The calibration of the signal is performed following [182]. To select the high and low photon number branches, the drive resonance is slowly tuned in resonance from distinct directions.

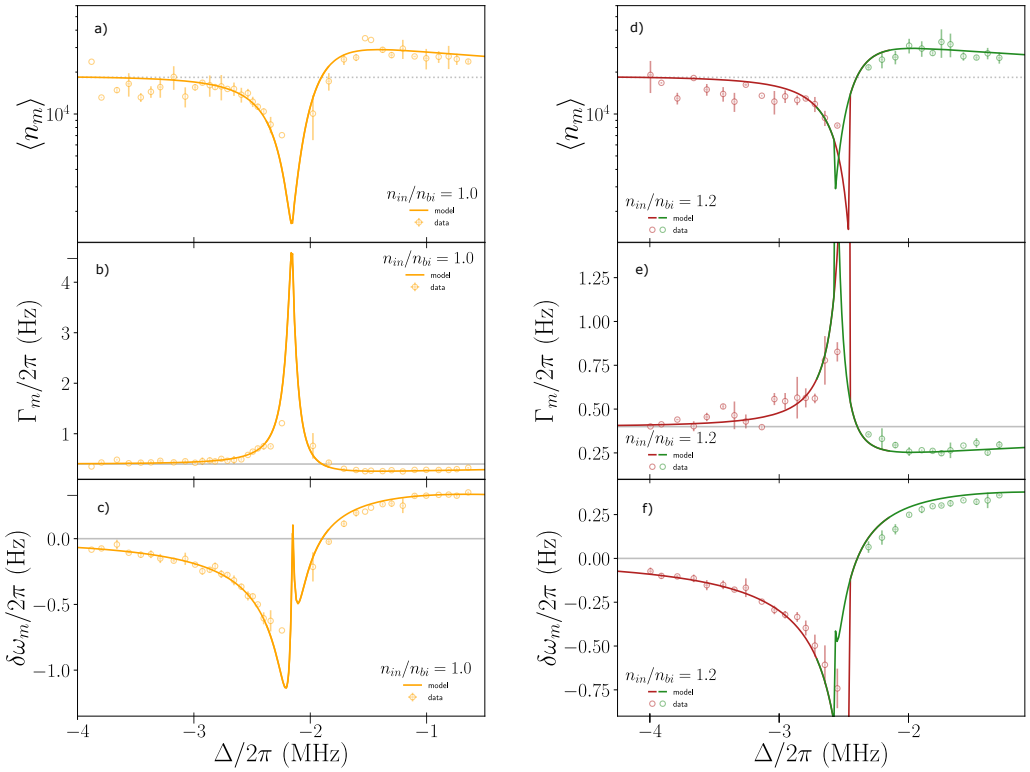

FIGURE 5.15: Phonon number $\langle \hat{n}_m \rangle$ (a and d), mechanical linewidth $\Gamma_m/2\pi$ (b and e) and frequency shift $\delta\omega_m/2\pi$ (c and f) as a function of the cavity detuning. In a) and d) the grey-dotted line depicts the bath temperature at $T = 267$ mK, whereas for b) and e) the grey line illustrates the uncoupled mechanical linewidth $\gamma_m/2\pi = 0.4$ Hz. In a-c we show the data and theoretical predictions obtained for $\bar{n}_{\rm in} = \bar{n}_{\rm in,bi}$ and for d-f $\bar{n}_{\rm in} = 1.2\bar{n}_{\rm in,bi}$. Green and red depict the high and low photon branches, respectively. Cooling traces at $g_0/2\pi = (99 \pm 1)$ Hz, $\mathcal{K}/2\pi = (14 \pm 1)$ Hz, $\omega_m/2\pi = 287.3$ kHz and $\kappa/2\pi = 2.8$ MHz.

The cooling traces obtained for $\bar{n}_{\rm in} = \bar{n}_{\rm in,bi}$ and $\bar{n}_{\rm in} = 1.2\bar{n}_{\rm in,bi}$ are shown in Fig. 5.15. Due to the driving power above the bifurcation threshold, for certain detuning these curves feature two distinct solutions as we see in Fig. 5.13. The solid lines in Fig. 5.15 correspond to the theoretical predictions, which show great agreement with the experimental data (circles). The agreement is also consistent with the selection of the photon branch, accurately showing the detuning for which a branch switching occurs. In Fig. 5.15 e), in a certain interval of detunings, the high photon branch (green) results in heating of the mechanics, before switching to the lower branch. This arises from the very narrow optical cooling feature from the higher photon branch, which is experimentally not accessible. The difficulty in accessing the cooling feature of the high-photon branch is also evident in the numerical analysis, where even a slight variation in the optical detuning causes a significant change in the phonon number as shown in Fig. 5.16.

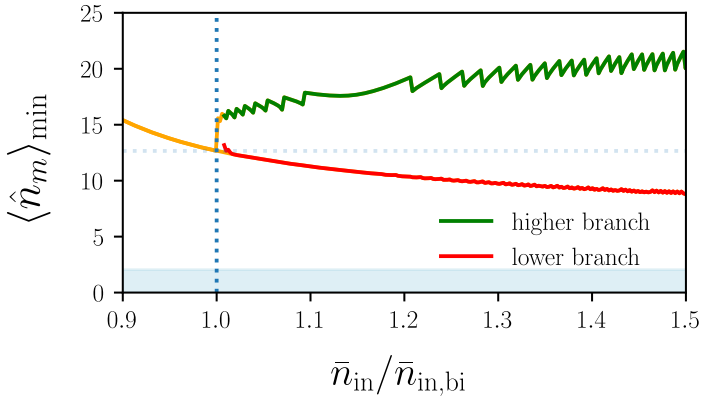

FIGURE 5.16: Lowest phonon number as a function of the input power. For input powers above the bifurcation threshold, the intracavity photon number exhibits a high (green) and low (red) photon number branch. Consistent with experimental observations, within the high-photon branch, a slight change in the cavity detuning leads to a large modification of the phonon number, due to the very narrow cooling feature of this solution. In contrast, for the parameters given in Table 5.1 the low-photon branch reaches the backaction limit. For this plot, we used the parameters provided in Table 5.1.

Throughout this chapter, we explored the benefits of using a nonlinear optomechanical setup for backaction cooling of a mechanical mode. As explained in Chapter 3, cooling arises from the imbalance between the Stokes and anti-Stokes scattering rates. Increasing the asymmetry between these rates can lead to higher optomechanical damping, $\Gamma_{\rm opt}$, and consequently to a more effective cooling of the mechanical mode. In Chapter 4, we demonstrated that the photon number spectrum $\mathcal{S}_{\rm nn}[\omega]$ of a nonlinear cavity, as described by Eq. (4.29), is asymmetric and exhibits non-Lorentzian behaviour. We also showed that the highest asymmetry, indicated by the maximum effective skewness (see Fig. 4.7), occurs where $d\bar{n}_c/d\Delta$ has the steepest slope, specifically at the critical detuning $\Delta_{\rm bi}$ for driving strengths just below the bifurcation threshold. The significant asymmetry in the photon number spectrum results in a nonlinear optomechanical setup exhibiting a higher optomechanical damping rate compared to an equivalent linear system. Before bifurcation, this is illustrated in Fig. 5.5, where the maximum effective cooperativity is located at the bifurcation detuning, $\Delta_{\rm bi}$, aligning with the position of the lowest phonon number. For the parameters provided in Table 5.1, this translates to an order of magnitude improvement in cooling capabilities over an identical linear system. Moreover, for driving strengths above the bifurcation threshold, this is shown in Fig. 5.14. The large sensitivity of the high-photon branch to driving frequencies leads to a very narrow cooling feature, which makes it experimentally inaccessible. This sensitivity of the high-photon branch can also be observed numerically in Fig. 5.16.

Furthermore, we showed that the nonlinear setup achieves more efficient cooling compared to a linear system at lower optomechanical coupling strengths, as illustrated in Fig. 5.6. Additionally, Fig. 5.9 demonstrates that the nonlinear cavity performs significantly better in the unresolved regime. In contrast, as we approach the resolved sideband regime, the cooling limits converge with those of the linear setup. Finally, Fig. 5.10 shows the average phonon number as a function of the resolved parameter and optomechanical coupling strength, highlighting the advantages of the nonlinear configuration over the conventional linear system in cooling performance.

Figure 5.10 illustrates that far in the unresolved sideband regime we can not overcome the cavity backaction. Hence, to surpass this limitation alternative protocols are required, which implement feedback techniques or employ squeezing. In the next chapter, we will explore a pathway to achieving the ground state by injecting a squeezed vacuum into our nonlinear setup, based on the protocol developed by Asjad *et al.* [185].

So far we have focused our study on understanding the influence of the nonlinearity for backaction cooling a low-frequency mechanical oscillator. In the next section, inspired by the work of C. Laflamme and A. A. Clerk [178], we will analyze the effect that the intrinsic nonlinearity has on position detection.

5.5 Effective cavity dynamics: behaviour near bifurcation

In the last section, we derived the effective dynamics of the mechanics yielding Eq. (5.12). Here, we will follow the same steps and transform Eq. (5.9) into the frequency domain and solve the system of equations for the cavity operators. This results into a reduced system

$$\begin{pmatrix} \mathcal{X}_{\mathrm{c,eff}}^{-1}[\omega] & -i\Lambda_{\mathrm{eff}} \\ i\Lambda_{\mathrm{eff}}^{*} & \mathcal{X}_{\mathrm{c,eff}}^{-1*}[-\omega] \end{pmatrix} \begin{bmatrix} \hat{d}[\omega] \\ \hat{d}^{\dagger}[\omega] \end{bmatrix} = -\sqrt{\kappa} \begin{bmatrix} \hat{D}_{\mathrm{in}}[\omega] \\ \hat{D}_{\mathrm{in}}^{\dagger}[\omega] \end{bmatrix}. \tag{5.28}$$

where we introduced the *effective cavity susceptibility* $\mathcal{X}_{\mathrm{c,eff}}^{-1}[\omega] = \mathcal{X}_{c}^{-1}[\omega] - i\Sigma_m[\omega]$ with the mechanical self-energy given in Eq. (3.157). Similarly, as for the mechanical case analyzed in Chapter 3, the induced dynamics are encoded in the effective susceptibility:

$$\mathcal{X}_{\mathrm{c,eff}}^{-1}[\omega] = -i\left(\omega + \Delta[\omega]\right) + \frac{\kappa[\omega]}{2}, \tag{5.29}$$

with the frequency-dependent detuning and damping

$$\Delta_{\mathrm{eff}}[\omega] \equiv \tilde{\Delta} + \Re\{\Sigma_m[\omega]\}, \quad \kappa_{\mathrm{eff}}[\omega] \equiv \kappa + 2\Im\{\Sigma_m[\omega]\}, \tag{5.30}$$

respectively. We will recall that $\Sigma_m[\omega] = \Sigma_m^{*}[-\omega]$ and to simplify notation we will omit the frequency dependency on $\Delta_{\mathrm{eff}}[\omega]$ and κ_{eff}. In the off-diagonal entries of the susceptibility matrix in Eq. (5.28) the presence of the optomechanical interaction also leads to a modified frequency dependent squeezing strength defined as $\Lambda_{\mathrm{eff}} = \left(|\Lambda| + \Sigma_m[\omega]\right) e^{+2i\phi_c}$.

The dynamics described by Eq. (5.28) resemble those associated with a degenerate parametric amplifier driven by a nonresonant pump [183] as we described in Chapter 4 with the particularity of having the modification due to the optomechanical interaction. This modification can also be observed in the cavity input noise, which now contains the mechanical noise contribution

$$\begin{bmatrix} \hat{D}_{\mathrm{in}}[\omega] \\ \hat{D}_{\mathrm{in}}^{\dagger}[\omega] \end{bmatrix} = \begin{bmatrix} \hat{d}_{\mathrm{in}}[\omega] \\ \hat{d}_{\mathrm{in}}^{\dagger}[\omega] \end{bmatrix} - i|G|\sqrt{\frac{2}{\kappa}}\hat{X}_m^{0}[\omega] \begin{pmatrix} e^{i\phi_c} \\ -e^{-i\phi_c} \end{pmatrix} \tag{5.31}$$

with the oscillator's position quadrature

$$\hat{X}_m^{0}[\omega] = -\sqrt{\frac{\gamma_m}{2}}\left(\mathcal{X}_m[\omega]\hat{b}_{\mathrm{in}}[\omega] + \mathcal{X}_m^{*}[-\omega]\hat{b}_{\mathrm{in}}^{\dagger}[\omega]\right). \tag{5.32}$$

It is now convenient to derive the equations of motion in the quadrature basis using the following transformation

$$\begin{bmatrix} \hat{U} \\ \hat{V} \end{bmatrix} = \mathbf{T} \begin{bmatrix} \hat{d} \\ \hat{d}^{\dagger} \end{bmatrix}, \qquad \boldsymbol{T} \equiv \frac{1}{\sqrt{2}} \begin{pmatrix} e^{-i\theta} & e^{i\theta} \\ -ie^{-i\theta} & ie^{i\theta} \end{pmatrix}. \tag{5.33}$$

Using this transformation, we find then that the effective input noise given in Eq. (5.31) in the quadrature basis becomes

$$\begin{bmatrix} \hat{U}_{\mathrm{eff,in}}[\omega] \\ \hat{V}_{\mathrm{eff,in}}[\omega] \end{bmatrix} = \begin{bmatrix} \hat{U}_{\mathrm{in}}[\omega] \\ \hat{V}_{\mathrm{in}}[\omega] \end{bmatrix} + \frac{2|G|}{\sqrt{\kappa}}\hat{X}_m^{0}[\omega] \begin{pmatrix} \sin(\vartheta) \\ -\cos(\vartheta) \end{pmatrix}, \tag{5.34}$$

with the relative phase $\vartheta \equiv \phi_c - \theta$ between the driving phase and the quadrature's angle. Note, for $\vartheta = 0$, the effective noises reduces to

$$\hat{U}_{\mathrm{eff,in}}[\omega] = \hat{U}_{\mathrm{in}}[\omega], \quad \hat{V}_{\mathrm{eff,in}}[\omega] = \hat{V}_{\mathrm{in}}[\omega] - \frac{2|G|}{\sqrt{\kappa}}\hat{X}_m^{0}[\omega], \tag{5.35}$$

with a vanishing mechanical noise contribution in one of the quadratures. This feature is particularly important in sensing applications, as we will see in the next section.

Hence, the dynamics described by Eq. (5.28) under the transformation given in Eq. (5.33) take the form

$$\begin{bmatrix} \hat{U}[\omega] \\ \hat{V}[\omega] \end{bmatrix} = -\sqrt{\kappa}\, \boldsymbol{\chi}_{\mathrm{eff}}[\omega] \begin{bmatrix} \hat{U}_{\mathrm{eff,in}}[\omega] \\ \hat{V}_{\mathrm{eff,in}}[\omega] \end{bmatrix}, \tag{5.36}$$

with the diagonal matrix

$$\boldsymbol{\chi}_{\mathrm{eff}}^{-1}[\omega] = \begin{bmatrix} \chi_1^{-1}[\omega] & 0 \\ 0 & \chi_2^{-1}[\omega] \end{bmatrix}, \quad \chi_{1,2}^{-1}[\omega] = -i\omega + \frac{\kappa_{\mathrm{eff}}}{2} \mp \sqrt{|\Lambda_{\mathrm{eff}}|^2 - \Delta_{\mathrm{eff}}^2}. \tag{5.37}$$

This equation indicates that the system has a parametric threshold when

$$|\Lambda_{\mathrm{eff}}| \to \sqrt{\frac{\kappa_{\mathrm{eff}}^2}{4} + \Delta_{\mathrm{eff}}^2}. \tag{5.38}$$

This results into

$$\begin{aligned} \hat{U}[\omega] &= -\chi_1[\omega] \left[\sqrt{\kappa} \hat{U}_{\mathrm{in}}[\omega] + 2|G| \sin(\vartheta) \hat{X}_m^0[\omega] \right], \\ \hat{V}[\omega] &= -\chi_2[\omega] \left[\sqrt{\kappa} \hat{V}_{\mathrm{in}}[\omega] - 2|G| \cos(\vartheta) \hat{X}_m^0[\omega] \right]. \end{aligned} \tag{5.39}$$

Note that in the absence of optomechanical interaction and for a resonant pump $\tilde{\Delta} = 0$, these equations describe the usual dynamics of a DPA: if $|\Lambda| \to \kappa/2$ then $\kappa\chi_1[0] \to \infty$, while $\kappa\chi_2[0] \to 1$, such that $\hat{U}$ becomes amplified, while $\hat{V}$ squeezed.

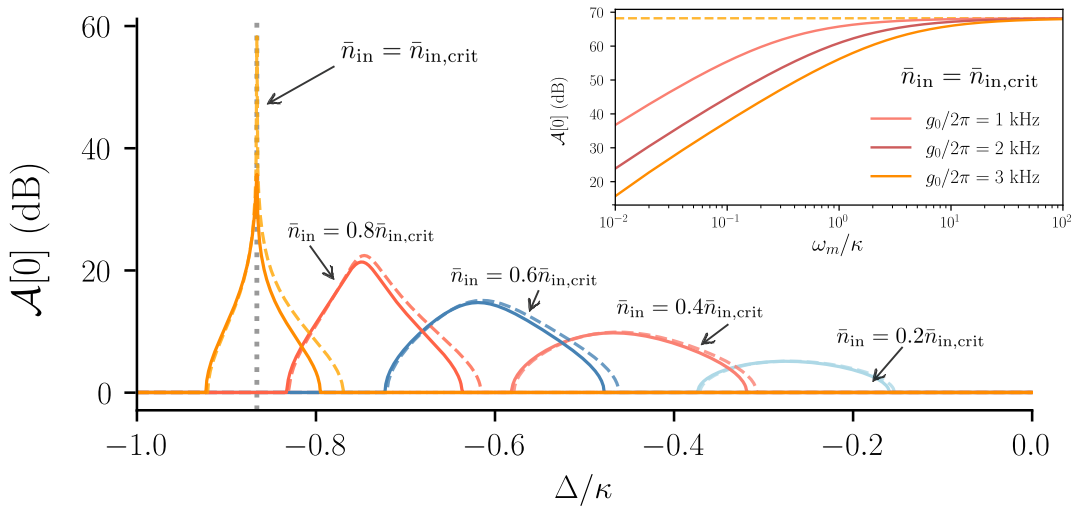

FIGURE 5.17: Parametric amplification coefficient at zero frequency as a function of the cavity detuning for different driving powers. Dashed lines illustrate the result of an uncoupled nonlinear cavity. Solid lines show the effective cavity dynamics of a nonlinear cavity coupled via radiation pressure to a mechanical mode. Operating slightly below the threshold power, the system exhibits maximum amplification near the bifurcation points. The interaction with the mechanics reduces the amplification efficiency and narrows the detuning range where amplification occurs. For this plot $g_0/2\pi = 30$ kHz and the parameters given in Table 5.1. For $\mathcal{A}[0] = 0$ there is no amplification. INSET shows the maximum gain obtained operating at the bifurcation threshold as a function of the resolved parameter for different optomechanical coupling strengths.

Using the input-output relation in Eq. (2.50), we can describe the output field leaving the cavity from Eq. (5.39). For the $\hat{U}$ quadrature it reads

$$\hat{U}_{\mathrm{out}}[\omega] = (1 - \kappa\chi_1[\omega])\, \hat{U}_{\mathrm{in}}[\omega] - 2|G|\sqrt{\kappa}\chi_1[\omega] \sin(\vartheta) \hat{X}_m^0[\omega]. \tag{5.40}$$

Using the last equation we can calculate the output noise spectrum using Eqs. (3.151) and (3.152) resulting in

$$\mathcal{S}_{uu}^{\text{out}}[\omega] = \frac{1}{2}\mathcal{A}[\omega] + 4|G|^2\kappa|\chi_1[\omega]|^2\sin^2(\vartheta)\mathcal{S}_{xx}^{0}[\omega] \tag{5.41}$$

where we introduced the quadrature's *parametric amplification coefficient*[3]

$$\mathcal{A}[\omega] = |1 - \kappa\chi_1[\omega]|^2 \tag{5.42}$$

and the oscillator's position spectrum is given in Eq. (3.155).

As pointed out by C. Laflamme and A. A. Clerk [178], the measurement capabilities of a bare nonlinear cavity are strongly tied to its amplification properties, especially near its bifurcation point. As we illustrate in Fig. 5.17, for zero frequency and near the bifurcation point, the amplification coefficient satisfies $\mathcal{A}[0] \gg 1$, which is associated with prominent amplification capabilities.

Here, we demonstrate that the optomechanical interaction of the nonlinear cavity with a mechanical oscillator reduces its amplification limits, particularly in the unresolved sideband regime. As depicted in the inset in Fig. 5.17, for a nonlinear cavity operating near bifurcation, the amplification coefficient, $\mathcal{A}[0]$, is strongly reduced when it is coupled to a low-frequency mechanical oscillator via radiation pressure. Conversely, in the resolved sideband regime, the amplification resembles that of an uncoupled nonlinear cavity.

Additionally, in Fig. 5.17, we show that the coupled system exhibits amplification over a narrow detuning range, making it more sensitive to small changes. However, as we approach the resolved sideband regime, these detrimental mechanical effects diminish. In Fig. 5.18, we compare the amplification coefficient as a function of frequency for a bare nonlinear cavity operating near bifurcation (dashed line) and a nonlinear cavity also near bifurcation but coupled to a low-frequency resonator via radiation pressure (solid line). As shown in Fig. 5.17, the maximum amplification occurs at zero frequency, where the interaction with the mechanics significantly reduces its efficiency. For non-zero frequencies, the uncoupled nonlinear cavity displays a symmetric amplification curve around the peak. However, when coupled to the oscillator, the amplification profile becomes asymmetrical around $\omega = 0$.

In the next section, we will extend this analysis and study the sensing properties of a nonlinear cavity coupled via radiation radiation-pressure force to a mechanical oscillator. Recalling our analysis in Chapter 3, we will explore how the nonlinearity in the cavity modifies both the imprecision and backaction noise contribution and show that under specific conditions the SQL in position detection can be reached.

[3] It is also frequently denoted as the *gain*.

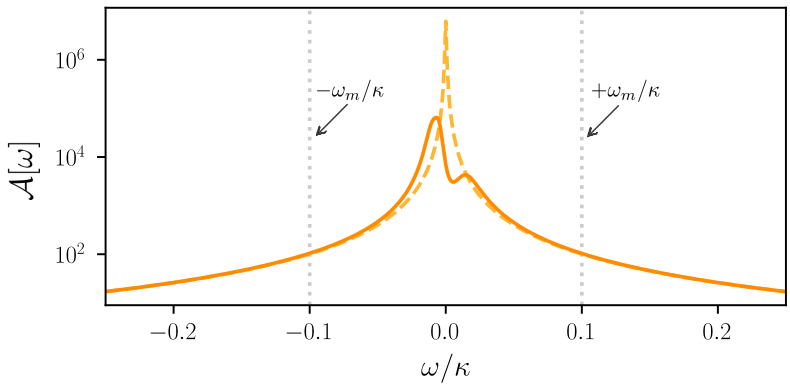

FIGURE 5.18: The parametric amplification coefficient is plotted as a function of the driving frequency while operating at the bifurcation threshold. The dashed line represents the outcome of an uncoupled degenerate parametric amplifier (DPA), whereas the solid line illustrates the effect when the DPA is optomechanically coupled to a mechanical oscillator. This comparison highlights the reduction in amplification efficiency around $\omega = 0$ due to the interaction with the mechanical mode, especially near the bifurcation point. For this plot, we used the parameters found in Table 5.1.

5.6 Sensing and standard quantum limit

In the last section, we analyzed the effective cavity dynamics and demonstrated that a nonlinear cavity near its bifurcation point can lead to significant amplification [178]. In Sec. 3.8, we briefly examined one of the most critical applications of an optomechanical system: sensing mechanical motion with quantum-limited precision. That analysis, based on the system's Hamiltonian from Eq. (3.76), focused on a linear cavity at zero detuning ($\Delta = 0$), resulting in dynamical backaction evasion.

In this section, we will investigate how the cavity nonlinearity affects the position detection of a mechanical oscillator via radiation pressure. We will show that the minimum added noise achieves similar limits to those of a linear cavity under optimal conditions.

Recalling the system's dynamics Eq. (5.9), we find that

$$\mathcal{X}_{\mathcal{K}}^{-1}[\omega]\hat{d}[\omega] = -i\sqrt{2}G_{\mathcal{K}}\hat{X}_m[\omega] - \sqrt{\kappa}\hat{\xi}_{\mathcal{K}}[\omega], \tag{5.43}$$

with $\sqrt{2}\hat{X}_m = \hat{b} + \hat{b}^\dagger$ the oscillator's position quadrature and the Kerr-cavity susceptibility defined in Eq. (4.28). In Eq. (5.43), due to the presence of the nonlinearity, the cavity couples to the mechanical mode with an effective coupling strength $G_{\mathcal{K}} = G\,(1 - i|\Lambda|\mathcal{X}_c^*[-\omega])$. In addition, the cavity's input noise becomes, due to the intrinsic nonlinearity, $\hat{\xi}_{\mathcal{K}}[\omega] \equiv \hat{d}_{\text{in}}[\omega] + i\Lambda\mathcal{X}_c^*[-\omega]\hat{d}_{\text{in}}^\dagger[\omega]$.

To analyze the total noise, we recall the input-output relation in Eq. (2.50) yielding the following expression for the cavity output operator

$$\hat{d}_{\text{out}}[\omega] = (1 - \kappa\mathcal{X}_{\mathcal{K}}[\omega])\,\hat{d}_{\text{in}}[\omega] - i\kappa\Lambda\mathcal{X}_{\mathcal{K}}[\omega]\mathcal{X}_c^*[-\omega]\hat{d}_{\text{in}}^\dagger[\omega] - i\sqrt{2\kappa}G_{\mathcal{K}}\mathcal{X}_{\mathcal{K}}[\omega]\hat{X}_m[\omega]. \tag{5.44}$$

We will now express the last equation in the quadrature basis using Eq. (3.149). Hence, we find

$$\hat{U}_{\text{out}}[\omega] = \mathbb{A}_{c,\vartheta}[\omega]\hat{d}_{\text{in}}[\omega] + \mathbb{A}_{c,\vartheta}^*[-\omega]\hat{d}_{\text{in}}^\dagger[\omega] + \mathbb{A}_{m,\vartheta}[\omega]\hat{X}_m[\omega] \tag{5.45}$$

with the coefficients

$$\mathbb{A}_{c,\vartheta}[\omega] = \frac{e^{-i\phi_c}}{\sqrt{2}}\left[(1-\kappa\mathcal{X}_{\mathcal{K}}[\omega])\,e^{+i\vartheta} + \frac{i\kappa|\Lambda|e^{-i\vartheta}}{\tilde{\Delta}^2-|\Lambda|^2+\left[\frac{\kappa}{2}-i\omega\right]^2}\right], \tag{5.46}$$

$$\mathbb{A}_{m,\vartheta}[\omega] = 2\sqrt{\kappa}|G|\,\frac{\left[\tilde{\Delta}-|\Lambda|\right]\cos(\vartheta)+\left[\frac{\kappa}{2}-i\omega\right]\sin(\vartheta)}{\tilde{\Delta}^2-|\Lambda|^2+\left[\frac{\kappa}{2}-i\omega\right]^2}. \tag{5.47}$$

Note that these coefficients depend on the relative phase $\vartheta = \phi_c - \theta$ between the driving phase and the measurement quadrature angle. The first two terms in Eq. (5.45) only involve the input noises of the cavity, whereas the last term results from the optomechanical interaction. Later, we will show that this term includes a noise contribution of both mechanical and cavity modes, whereas the latter will give rise to the backaction noise.

The spectral density of the output operator in Eq. (5.45) is given by

$$\mathcal{S}^{\text{out}}_{uu}[\omega] = |\mathbb{A}_{c,\vartheta}[\omega]|^2 + |\mathbb{A}_{m,\vartheta}[\omega]|^2\mathcal{S}_{xx}[\omega], \tag{5.48}$$

with the oscillator's position spectral density given by Eq. (3.154). This mechanical noise spectral density gives the position spectrum of the mechanical vibration via $x_{\text{zpf}}\mathcal{S}_{xx}[\omega]$. Such measure quantifies the ability of the mechanical mode to absorb or emit phonons to the environment as explained in Chapter 3.

Recalling the dynamics given in Eq. (5.9), we find that the dynamics of the position quadrature read

$$\hat{X}_m[\omega] = \hat{X}^0_m[\omega] - \frac{\Sigma_m[\omega]}{\sqrt{2}|G|^2}\hat{F}_{\mathcal{K}}[\omega], \tag{5.49}$$

where the first term represents the uncoupled oscillator's dynamics given in Eq. (5.32). Here, the last term arises due to the radiation pressure interaction, where the linearized force operator reads

$$\hat{F}_{\mathcal{K}}[\omega] = |G|\left(e^{-i\phi_c}\hat{d}[\omega] + e^{+i\phi_c}\hat{d}^\dagger[\omega]\right) \tag{5.50}$$

and the mechanical self energy given in Eq. (3.157). Using Eq. (5.43) it can be shown that the linearized force operator can be written as

$$\hat{F}_{\mathcal{K}}[\omega] = \hat{F}_{\text{in}}[\omega] + \sqrt{2}\Sigma^{\mathcal{K}}_c[\omega]\hat{X}_m[\omega] \tag{5.51}$$

with $\hat{F}_{\text{in}}[\omega]$ introduced in Eq. (5.15). The last term in Eq. (5.51) represents the dynamical backaction on the oscillator's dynamics which is proportional to the nonlinear cavity self-energy defined in Eq. (5.13). From the last equation, it can be seen that dynamical backaction can be evaded when the cavity is located at the EP ($\tilde{\Delta} = |\Lambda|$). Equivalently, dynamical backaction evasion (DBAE) can be achieved for a linear cavity on resonance. This implies that the second term in Eq. (5.51) vanishes and the force operator is solely characterized by intrinsic cavity input noise.

Eq. (5.51) can now be substituted into the equations of motion for the mechanical position quadrature given in Eq. (5.49) yielding

$$\mathcal{X}^{-1}_{xx}[\omega]\hat{X}_m[\omega] = \hat{X}^0_m[\omega] - \frac{\Sigma_m[\omega]}{\sqrt{2}|G|^2}\hat{F}^0_{\mathcal{K}}[\omega], \tag{5.52}$$

where we introduced the susceptibility

$$\mathcal{X}^{-1}_{xx}[\omega] \equiv 1 + \frac{\Sigma_m[\omega]\Sigma^{\mathcal{K}}_c[\omega]}{|G|^2}, \tag{5.53}$$

which under a DBAE scheme becomes unity. We are now able to obtain an expression of the mechanical oscillator's position spectral density given in Eq. (5.52), which reads

$$\mathcal{S}_{xx}[\omega] = \frac{1}{2}|\mathcal{X}_{xx}[\omega]|^2 \left(\mathcal{S}^0_{xx}[\omega] + \left| \frac{\Sigma_m[\omega]}{G^2} \right|^2 \mathcal{S}^{\mathcal{K}}_{FF}[\omega] \right) \tag{5.54}$$

with $\mathcal{S}^0_{xx}[\omega]$ given in Eq. (3.155).

The last term in Eq. (5.54) corresponds to the backaction in the form of the radiation pressure force spectrum

$$\mathcal{S}^{\mathcal{K}}_{FF}[\omega] = g_0^2 \mathcal{S}^{\mathcal{K}}_{nn}[\omega] \tag{5.55}$$

with the photon number spectrum given in Eq. (4.29), which we analyzed in detail in Chapter 4.

Finally, combining Eqs. (5.48) and (5.54) yields the total noise measured at the detector:

$$\bar{\mathcal{S}}^{\text{out}}_{uu}[\omega] = \bar{\mathcal{S}}^{\mathcal{K}}_{uu}[\omega] + |\mathcal{G}[\omega]|^2 \left(\bar{\mathcal{S}}^0_{xx}[\omega] + \left| \frac{\Sigma_m[\omega]}{G^2} \right|^2 \bar{\mathcal{S}}^{\mathcal{K}}_{FF}[\omega] \right), \tag{5.56}$$

with

$$\bar{\mathcal{S}}^{\mathcal{K}}_{uu}[\omega] = \frac{1}{2} \left\{ |\mathbb{A}_{c,\vartheta}[\omega]|^2 + |\mathbb{A}_{c,\vartheta}[-\omega]|^2 \right\}, \tag{5.57}$$

and where the gain is defined as

$$\sqrt{2}\mathcal{G}[\omega] = \mathbb{A}_{m,\vartheta}[\omega]\, \mathcal{X}_{xx}[\omega]. \tag{5.58}$$

For further insight, the expression for the total noise derived above can be recast into the form presented in Eq. (3.143), where the imprecision and backaction noises of the nonlinear cavity are given by:

$$\bar{\mathcal{S}}^{\text{imp}}_{uu}[\omega] = \frac{\bar{\mathcal{S}}^{\mathcal{K}}_{uu}[\omega]}{|\mathcal{G}[\omega]|^2} \tag{5.59}$$

and

$$\bar{\mathcal{S}}_{\text{BA}}[\omega] = \left| \frac{\Sigma_m[\omega]}{G^2} \right|^2 \bar{\mathcal{S}}^{\mathcal{K}}_{FF}[\omega], \tag{5.60}$$

respectively, whose sum yields the total added noise as in Eq. (3.144).

So far we have shown that the total output noise of a nonlinear optomechanical system yields Eq. (5.56), where both gain and added noise are modified due to the nonlinearity in the cavity. As a consequence of the Kerr nonlinearity, the additional input noise in Eq. (5.43) increases the imprecision noise compared to an equivalent linear system.

5.6.1 Dynamical backaction evasion scheme

An increase in our system's sensing capabilities is directly related to the gain strength in Eq. (5.58), which becomes larger when the DBAE condition is satisfied. For a nonlinear setup, this implies the cavity to be located at the EP, $\tilde{\Delta} = |\Lambda|$. In contrast, for a linear cavity, this is satisfied on resonance $\Delta = 0$, leading to an equivalent expression for the gain:

$$\mathcal{G}[\omega]|_{\tilde{\Delta}=|\Lambda|} = \frac{\sqrt{2\kappa}|G|\sin(\vartheta)}{\frac{\kappa}{2} - i\omega}. \tag{5.61}$$

The only distinction of a linear or nonlinear cavity is imprinted in the multiphoton coupling strength $G = g_0\sqrt{\bar{n}_c}$ since the latter would be described by Eq. (5.5). The last expression reveals that the maximum gain occurs when $\vartheta = \pi/2$. For the case where $\phi_c = 0$, this implies that to optimally measure the mechanical oscillator's position, we should focus on measuring

the $\hat{V}$ quadrature of the output field, in which the resonator's position is encoded, which agrees with the result obtained in Eq. (5.31). Notably, the enhancement in measurement sensitivity compared to a linear cavity is primarily determined by the intracavity photon number. In Fig. 5.19 we compare the intracavity photon number corresponding to a nonlinear and linear cavity as a function of the optical detuning. Due to the nonlinearity, as we approach the bifurcation point $\Delta_{\rm bi}$ from the right (blue vertical line), the number of circulating photons in the nonlinear cavity becomes significantly larger than in a linear cavity. As we approach the resonance condition $\Delta = 0$, this effect is reversed, although the nonlinear cavity becomes unstable. Hence, the most significant enhancement in measurement gain compared to a linear cavity can be achieved by operating near the critical detuning of the nonlinear optomechanical system.

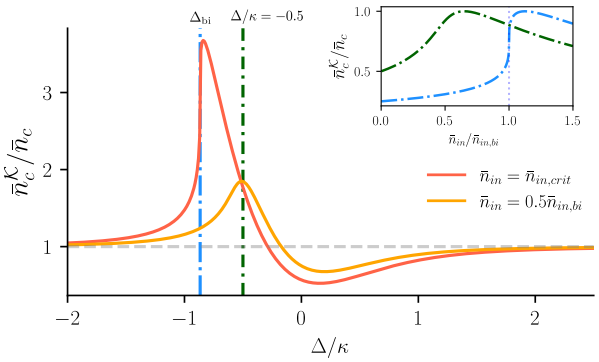

FIGURE 5.19: Photon number comparison as a function of the cavity detuning for different driving strengths. Here, we calculate the ratio between the circulating photon number of a nonlinear and linear cavity at the same input power as we vary the cavity detuning. As we also see in Fig. 5.3, as we approach the critical detuning $\Delta_{\rm bi}$ this difference becomes significantly larger. Since this occurs due to the Kerr nonlinearity positively skewing the photon number distribution, the strongest effect is found when the system is driven slightly below the critical input power. Inset shows this comparison as a function of the input power for $\Delta = \Delta_{\rm bi}$ (dashed-dotted blue) and $\Delta/\kappa = -0.5$ (dashed-dotted green).

As indicated by the final expression, an increased optomechanical coupling strength results in higher gain and to a reduction in imprecision noise, as shown in Eq. (5.57). However, as discussed in Chapter 3, a stronger optomechanical interaction simultaneously leads to a significant increase in backaction noise.

The DBAE condition has also an impact on the backaction noise contribution, since at the EP the backaction noise spectrum given in Eq. (5.60) becomes

$$\bar{\mathcal{S}}_{\rm BA}[\omega]|_{\tilde{\Delta}=|\Lambda|} = \left|\frac{\Sigma_m[\omega]}{G^2}\right|^2 \mathcal{S}^0_{FF}[\omega] \tag{5.62}$$

with the force spectral density of a linear cavity on resonance given by

$$\mathcal{S}^0_{FF}[\omega] = \frac{G^2\,\kappa}{\omega^2 + \frac{\kappa^2}{4}}. \tag{5.63}$$

As demonstrated in Eq. (5.62), under the DBAE condition, both the gain and the backaction noise spectrum of a nonlinear cavity resemble those of a linear cavity on resonance. The primary difference then lies in the distinct descriptions of the average cavity photon number.

Recalling that, for a high-quality factor mechanical oscillator $\omega_m \gg \gamma_m$ the symmetrized noise spectral density of the mechanical mode at zero temperature given in Eq. (3.155) becomes $\bar{\mathcal{S}}^0_{xx}[\omega_m] \approx 2/\gamma_m$. Similarly the mechanical susceptibility can be then written as $\Sigma_m[\omega_m]/G^2 \approx i\bar{\mathcal{S}}^0_{xx}[\omega_m]$. Therefore, assuming a high-Q mechanical oscillator, we find that the total added noise given in Eq. (5.56) under the DBAE condition at $\omega = \omega_m$ reads

$$\bar{\mathcal{S}}^{\rm out}_{uu}[\omega_m]_{\tilde{\Delta}=|\Lambda|} \approx \bar{\mathcal{S}}^{\mathcal{K}}_{uu}[\omega_m]|_{\tilde{\Delta}=|\Lambda|} + \frac{4}{\gamma_m}\mathcal{S}^0_{FF}[\omega_m]\sin^2(\vartheta)\left(1 + \frac{2}{\gamma_m}\mathcal{S}^0_{FF}[\omega_m]\right) \tag{5.64}$$

with the symmetrized spectral density of the nonlinear cavity located at the EP

$$\bar{\mathcal{S}}^{\mathcal{K}}_{uu}[\omega_m]|_{\bar{\Delta}=|\Lambda|} = \frac{1}{2} - \frac{\kappa|\Lambda|\sin(2\vartheta)}{\omega_m^2 + \frac{\kappa^2}{4}} + \left(\frac{\sqrt{2}\kappa|\Lambda|\sin(\vartheta)}{\omega_m^2 + \frac{\kappa^2}{4}}\right)^2, \tag{5.65}$$

which becomes $\bar{\mathcal{S}}_{uu}[\omega_m]|_{\Delta=0} = 1/2$ for a linear cavity on resonance. As the last equation shows, even when operating at the EP, the noise spectrum of the nonlinear cavity exhibits additional noise contributions compared to a linear system on resonance. In contrast to Eq. (3.144), the added noise associated with the nonlinear optomechanical system reads

$$\bar{\mathcal{S}}^{\text{add}}_{uu}[\omega_m] = \bar{\mathcal{S}}_{\text{BA}}[\omega_m] + \frac{\bar{\mathcal{S}}^{\mathcal{K}}_{uu}[\omega_m]|_{\bar{\Delta}=|\Lambda|}}{|\mathcal{G}[\omega_m]|^2}. \tag{5.66}$$

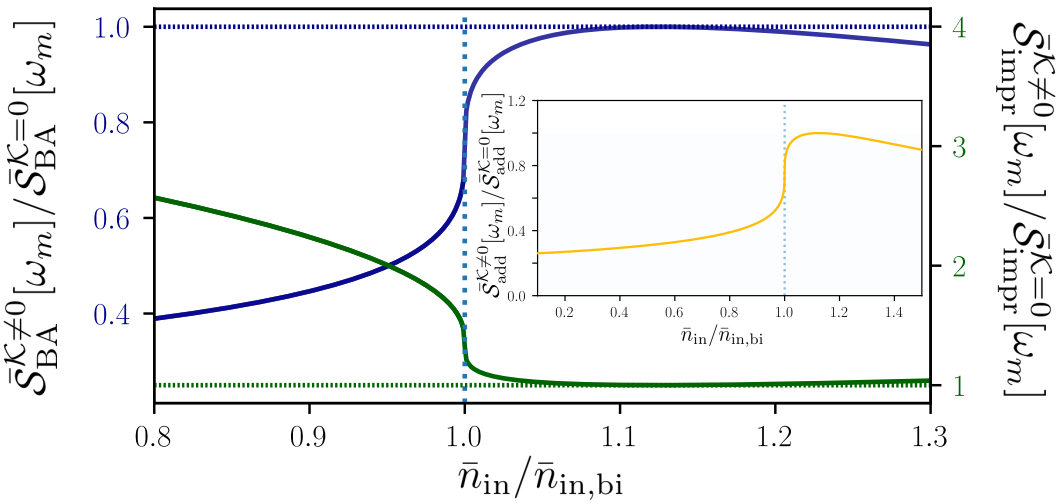

FIGURE 5.20: Backaction (blue) and imprecision (green) spectral noise densities evaluated at the mechanical resonance frequency as a function of the cavity's driving power. We compare the results obtained using a nonlinear at $\Delta = \Delta_{\text{bi}}$ against a linear cavity at $\Delta = 0$ optomechanical system under DBAE conditions by dividing the former over the latter. For $\bar{n}_{\text{in}} < \bar{n}_{\text{in,bi}}$ and operating at the critical detuning, the imprecision noise corresponding to the nonlinear cavity even doubles that of a linear cavity at zero detuning. For increasing driving strength the imprecision noise becomes similar. This behaviour is reversed for the backaction noise contribution. For this plot the parameters given in Table 5.1 were used.

However, an optimal phase ϑ can be determined to minimize the added noise. Hence, by performing an extrema analysis of the added noise expression in Eq. (5.66) under DBAE conditions, we can identify the following optimal value

$$\tan(\vartheta) = \frac{\frac{\kappa^2}{4} + \omega_m^2}{2\kappa|\Lambda|}. \tag{5.67}$$

In contrast, a similar analysis for a linear cavity leads to the value $\vartheta = \pi/2$, which is also associated with maximum gain as we can see in Eq. (5.58). Since the RHS of Eq. (5.67) is non-zero, by choosing this optimal value, the quadratures might become non-orthogonal, leading to possible measurement complications and to a substantial influence on the noise properties [178]. The optimal phase above is chosen to minimize the added noise in the measurement process. However, this optimization can lead to a reduction in gain, which is disadvantageous for measurement sensitivity.

For the optimal value given in Eq. (5.67), the imprecision associated with a nonlinear cavity mimics the noise contribution of an empty cavity on resonance, which reads

$$\mathcal{S}_{uu}^{\mathrm{imp}}[\omega_m] = \frac{\frac{\kappa^2}{4}+\omega_m^2}{4|G|^2\kappa}. \tag{5.68}$$

If, on the other hand, we choose the phase that maximizes the measurement gain ($\vartheta = \pi/2$), the imprecision noise of a nonlinear cavity will have additional noise contributions, as we can see in the expression below

$$\mathcal{S}_{uu}^{\mathrm{imp}}[\omega_m] = \frac{\frac{\kappa^2}{4}+\omega_m^2}{4|G|^2\kappa} + \frac{\kappa|\Lambda|^2}{G^2\left[\frac{\kappa^2}{4}+\omega_m^2\right]}. \tag{5.69}$$

This again shows the trade-off between maximizing measurement sensitivity at the expense of increased imprecision noise even under DBAE conditions for a nonlinear cavity.

Thus, for a high-Q oscillator, $\omega_m \gg \gamma$, optimizing the relative phase as in Eq. (5.67) leads to the minimum added noise given by

$$\mathcal{S}_{uu}^{\mathrm{add}}[\omega_m]|_{\tilde{\Delta}=|\Lambda|} = \frac{\frac{\kappa^2}{4}+\omega_m^2}{4|G|^2\kappa} + \frac{4|G|^2\kappa}{\gamma^2\left(\frac{\kappa^2}{4}+\omega_m^2\right)}, \tag{5.70}$$

where the second term corresponds to the backaction contribution within the DBAE scheme. The equation above is equivalent to the expression for the added noise of an empty cavity at resonance when $\vartheta = \pi/2$. Additionally, if we parameterize this expression in terms of the cooperativity, $\mathcal{C} = 4G^2/\kappa\gamma_m$, and assume $\omega_m \ll \kappa$ we find that the optimal coupling required to reach the quantum limit on resonance becomes $\mathcal{C} = 1/4$, which results into $\mathcal{S}_{uu}^{\mathrm{add}}[\omega_m]|_{\tilde{\Delta}=|\Lambda|} = \bar{\mathcal{S}}_{xx}^{0}[\omega_m] = 2/\gamma_m$.

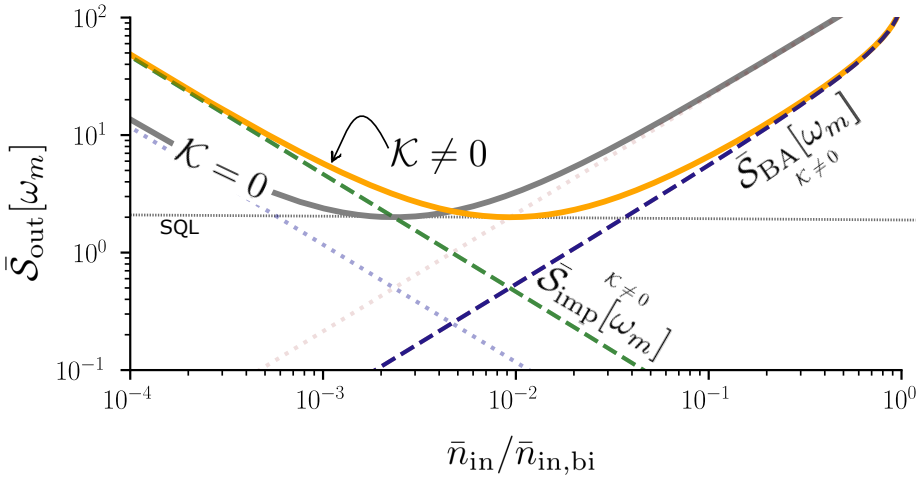

FIGURE 5.21: Comparison of the measured noise spectral density at the detector, evaluated at the mechanical resonance frequency, as a function of the cavity's input power using a nonlinear (orange) and linear (grey) optomechanical system. These spectral densities include the cavity's intrinsic noise contribution and the added noise due to measurement imprecision and backaction of the oscillator. As in Fig. 3.16, we illustrate the trade-off between imprecision and backaction noise as the driving power increases. Within the DBAE scheme, a nonlinear cavity (orange) reaches equivalent results as a linear cavity at zero detuning but requires stronger driving. For a nonlinear cavity, the imprecision and backaction contributions are depicted by the green and blue dashed lines, respectively. Notably, the backaction contribution is reduced allowing for stronger driving powers. For this plot we used $\bar{n}_m^T = 0$ and the parameters given in Table 5.1.

As in the work of C. Laflamme and A. A. Clerk [32], in Sec. 5.5 we observed that a nonlinear cavity near bifurcation enables strong amplification, particularly at zero frequency ($\mathcal{A}[0] \gg 1$), as shown in Fig. 5.18. However, when the cavity interacts with a low-frequency mechanical

oscillator via radiation pressure, the amplification limit is reduced at zero frequency and becomes more sensitive to detuning variations, as depicted in Fig. 5.17.

In this section, we analyzed the sensing capabilities of a nonlinear cavity in position detection via the radiation pressure of a low-frequency mechanical oscillator. We showed that, due to the intrinsic nonlinearity, the cavity possesses larger imprecision noise compared to a linear system. Optimal sensitivity is achieved under a DBAE scheme, similar to the result analyzed in Sec. 3.8 for a linear cavity at zero detuning. For a nonlinear cavity setup, DBAE implies operating at one of the system's EPs, ensuring zero cavity self-energy, introduced in Eq. (5.13).

In Fig. 5.21 we show that SQL in position detection can be realized with a nonlinear cavity within a DBAE at the expense of higher input powers even beyond the high amplification regime. While being constraint by the SQL, the nonlinear setup exhibits increased imprecision noise compared to a linear cavity. Notably, we demonstrate that a nonlinear system, leads to lower backaction noise, enabling stronger driving. As indicated in [32], the use of the correlations between backaction and imprecision noise could be beneficial, which will be explored in future work.

In Sec. 5.4, we demonstrated that backaction cooling in optomechanics using a nonlinear cavity enables more efficient cooling, particularly in the unresolved sideband regime, compared to conventional linear systems. However, in the unresolved sideband regime, cooling to the ground state is still hindered by cavity backaction. In the next chapter, we will explore the cooling performance of a nonlinear optomechanical system when a squeezed vacuum is injected into the cavity. We will show that this method can suppress the unwanted Stokes process, thus overcoming the backaction limit.

Chapter 6

Kerr-enhanced optomechanical cooling: towards the ground state

In Chapter 5, we showed that in the unresolved sideband regime a nonlinear cavity outperforms a linear system. However, despite this improvement, cooling to the ground state is still constrained by the cavity backaction as shown in Fig. 5.9. To surpass the cavity backaction many approaches have been considered, including the use of optomechanical induced transparency [171], pulsed cooling schemes [186], quantum control schemes [187] and cavity sideband-cooling [188] among others.

Alternatively, the application of squeezed light, whether generated within or external to the cavity, has been investigated as a means to enhance cooling performance in optomechanical systems [172, 185, 189–191]. In Chapter 3, we saw that the average mechanical occupation is composed by the modified thermal occupation and the cavity backaction, where the latter can be conveniently written in terms of the scattering rates as

$$\bar{n}_{\mathrm{BA}} = \frac{\Gamma_{\mathrm{S}}}{\Gamma_{\mathrm{AS}} - \Gamma_{\mathrm{S}}}. \tag{6.1}$$

The denominator of the last equation already indicates that the imbalance between the Stokes and anti-Stokes processes originates the cooling when $\Gamma_{\mathrm{opt}} = \Gamma_{\mathrm{AS}} - \Gamma_{\mathrm{S}} > 0$. In Chapter 5 we showed that a nonlinear cavity increases the asymmetry between these processes ultimately improving the cooling performance over a linear setup. However, from Eq. (6.1), the unwanted heating process, Γ_{S}, sets the limits to cooling as we saw in Fig. 5.9. In laser cooling the Stokes scattering is reduced using a smaller cavity linewidth, much smaller than the mechanical resonant frequency, and consequently entering the resolved sideband regime, where the minimum average occupation is given by Eq. (3.133).

In this Chapter, we will first study the intracavity squeezing in an uncoupled driven Kerr-cavity described by the Hamiltonian in Eq. (4.23). Next, following M. Asjad *et al.* [31], we will explore a method that completely suppresses the Stokes process, providing significant advantages, especially in the unresolved sideband regime. Since an introduction to squeezing is beyond the scope of this work, we refer the reader to comprehensive reviews that provide valuable insights into the topic [127, 169, 192].

6.1 Intracavity squeezing

Squeezed states of light have a wide range of applications, including their use in optical communication due to an improved signal-to-noise ratio [193] and in laser interferometry for gravitational wave detection [49]. Additionally, squeezed light has been shown to enhance optomechanical cooling [31, 32, 173, 176], with the squeezing generated either externally or within the cavity. Given these and many other applications, the generation of squeezed light has been a prolific field of research [194]. The Hamiltonian of our nonlinear cavity, presented in Eq. (4.23), is equivalent to that of a detuned DPA, which has been shown to produce squeezed states [183, 195]. In this section, we will focus on the intracavity squeezing generated by our nonlinear cavity, particularly when the cavity operates near the bifurcation point.

To analyze the internal squeezing of the bare cavity, we use the dynamics of cavity fluctuations described by the quantum Langevin equations in Eq. (4.24). These dynamics are

governed by the quadratic Hamiltonian in Eq. (4.23) and can also be explored through the master equation formalism (see Chapter 2). Additionally, given Gaussian initial conditions, the time evolution remains confined to Gaussian states [196, 197]. One way to characterize a Gaussian state is by calculating its *covariance matrix*, $\boldsymbol{\sigma}$, which provides insight into the internal correlations within the mode[1]. The maximal observable squeezing, namely the minimal quadrature variance, is measured by the smallest eigenvalue of the covariance matrix, which we denote $\lambda = \min[\mathrm{eig}(\boldsymbol{\sigma})]$ [199].

Given the system's dynamics in Eq. (4.24), the system's state is fully characterized by the first and second moments, $\langle\hat{\mathcal{O}}_i\rangle$ and $\langle\hat{\mathcal{O}}_i\hat{\mathcal{O}}_j\rangle$, of the quadrature operators defined in Eq. (5.33). To quantify the correlations between the quadratures, these moments are typically arranged into a covariance matrix, defined as follows:

$$\boldsymbol{\sigma} = \begin{bmatrix} \langle\delta\hat{U}^2\rangle & \frac{1}{2}\langle\{\delta\hat{U},\delta\hat{V}\}\rangle \\ \frac{1}{2}\langle\{\delta\hat{U},\delta\hat{V}\}\rangle & \langle\delta\hat{V}^2\rangle \end{bmatrix}, \tag{6.2}$$

with $\delta\hat{o} = \hat{o} - \langle\hat{o}\rangle$.

In the absence of optomechanical interaction ($g_0 = 0$), it can be shown that the dynamics of the covariance matrix given in Eq. (6.2) obey the Lyapunov equation [168, 200]

$$\frac{d}{dt}\boldsymbol{\sigma} = \boldsymbol{A}\boldsymbol{\sigma} + \boldsymbol{\sigma}\boldsymbol{A}^\dagger + 2\boldsymbol{\mathcal{D}}, \tag{6.3}$$

where $\boldsymbol{A} = \mathbf{T}\boldsymbol{\mathcal{A}}\mathbf{T}^{-1}$ is the so-called *drift matrix* of the quadratures with $\boldsymbol{\mathcal{A}}$ the dynamical matrix given in Eq. (4.25) and $\boldsymbol{T}$ is the transformation matrix from Eq. (5.33). Furthermore, the last term in Eq. (6.3) is the *diffusion matrix*

$$\boldsymbol{\mathcal{D}} = \kappa\begin{pmatrix} 1 & 0 \\ 0 & 1 \end{pmatrix} \tag{6.4}$$

which corresponds to the noise correlations.

If the dynamics described by Eq. (4.24) are stable, then the covariance matrix reaches a unique steady state $\dot{\boldsymbol{\sigma}} = 0$, which leads us to the following equation

$$\boldsymbol{A}\boldsymbol{\sigma} + \boldsymbol{\sigma}\boldsymbol{A}^\dagger + 2\boldsymbol{\mathcal{D}} = 0, \tag{6.5}$$

whose solution reads

$$\boldsymbol{\sigma} = \frac{1/2}{\tilde{\Delta}^2 + \frac{\kappa^2}{4} - |\Lambda|^2}\begin{pmatrix} \tilde{\Delta}^2 + \frac{\kappa^2}{4} - |\Lambda|\left(\tilde{\Delta}\cos(\varsigma) - \frac{\kappa}{2}\sin(\varsigma)\right) & |\Lambda|\left(\frac{\kappa}{2}\cos(\varsigma) + \tilde{\Delta}\sin(\varsigma)\right) \\ |\Lambda|\left(\frac{\kappa}{2}\cos(\varsigma) - \tilde{\Delta}\sin(\varsigma)\right) & \tilde{\Delta}^2 + \frac{\kappa^2}{4} + |\Lambda|\left(\tilde{\Delta}\cos(\varsigma) - \frac{\kappa}{2}\sin(\varsigma)\right) \end{pmatrix} \tag{6.6}$$

with the short notation $\varsigma \equiv 2\theta - \phi_c$ and where we used $\Lambda = |\Lambda|e^{i\phi_c}$ with ϕ_c the drive amplitude's phase. From the last expression, we find that in the absence of the nonlinearity, the covariance matrix becomes

$$\boldsymbol{\sigma} = \frac{1}{2}\begin{pmatrix} 1 & 0 \\ 0 & 1 \end{pmatrix}, \tag{6.7}$$

as expected for a vacuum state.

[1] Two-mode entanglement for two-mode Gaussian states can also be calculated using the covariance matrix. By diagonalizing the covariance matrix, one obtains a pair of symplectic eigenvalues, $\mu_\pm$. A sufficient condition for two-mode entanglement is met if the smaller eigenvalue, μ_-, satisfies $\mu_- < 1/2$ [80, 198].

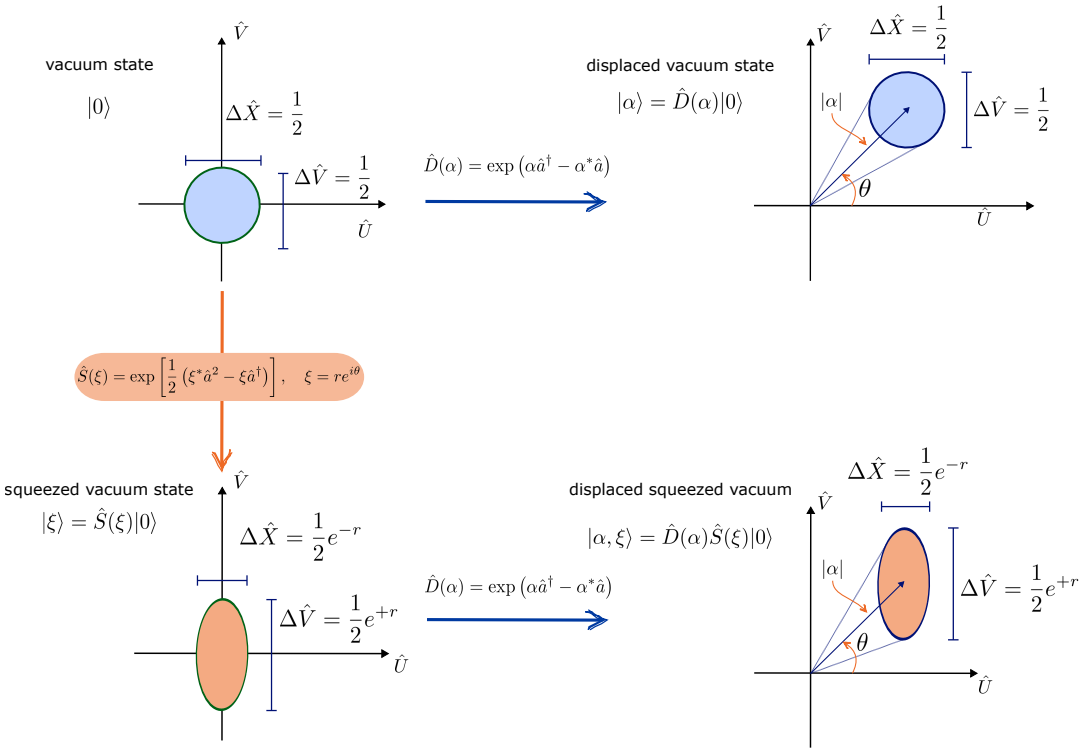

FIGURE 6.1: (clockwise from top left) Error ellipses for a vacuum, displaced vacuum, displaced squeezed and squeezed vacuum states. In the ellipses below, squeezing is in the $\hat{X}$ quadrature. In this example, $\lambda_\pm = e^{\mp r}/2$ are the eigenvalues that define the amount of squeezing and amplification, while θ is the squeezing angle.

A state $\hat{\rho}$ is said to be squeezed if the minimal eigenvalue, $\lambda_{\min}$, of its covariance matrix satisfies the condition $\lambda_{\min} < 1/2$. Hence, from the covariance matrix in Eq. (6.6) we can determine the maximal observable squeezingby computing its eigenvalues, which read

$$\lambda_\pm = \frac{1}{2\,(1 \pm \mathcal{R})}, \quad \mathcal{R} = \frac{|\Lambda|}{\sqrt{\tilde{\Delta}^2 + \frac{\kappa^2}{4}}}, \tag{6.8}$$

where the parameter $\mathcal{R} \in [0, 1]$ characterizes the amount of squeezing produced by the Kerr-cavity. It follows that if $\lambda_{\min} = \lambda_+ < 1/2$ one of the quadratures has a variance smaller than that of the ground state of a harmonic oscillator, hence it is squeezed. From Eq. (6.8), the amount of internal squeezing is photon-dependant since the single-mode squeezing strength is enhanced by the number of photons circulating in the cavity.

As discussed in Chapter 5, at low input powers, the average photon number described by Eq. (5.5) exhibits Lorentzian behaviour. This results in a low photon number away from resonance ($\Delta = 0$) and consequently a smaller value of $\mathcal{R}$ due to its photon dependence. Fig. 6.2a) illustrates this, showing the parameter $\mathcal{R}$ from Eq. (6.8) as a function of the optical detuning and input power. However, due to the nonlinear shape of the intracavity photon number distribution, increasing the input power leads to larger values of $\mathcal{R}$ away from resonance. The maximum value of $\mathcal{R}$ occurs at the bifurcation point, where the slope $d\bar{n}_c/d\Delta$ is maximal.

Moreover, the intracavity squeezing strength obtained from Eq. (6.8) is illustrated in Fig. 6.2b) as a function of optical detuning and input power. Characterized by the parameter $\mathcal{R}$, the squeezing strength exhibits behaviour similar to that shown in Fig. 6.2a). Maximum squeezing occurs precisely at the parametric threshold condition given by Eq. (5.38), which coincides with the bifurcation condition. Near this point, the nonlinear cavity fluctuations increase, resulting in a maximum squeezing strength of approximately 3 dB, as shown in Fig. 6.2b). This result aligns with the limit of quadrature squeezing under resonant parametric driving [201, 202]. This also agrees with the analysis of Chapter 5, where we show that the cavity features maximum parametric amplification near the bifurcation point as shown in

Fig. 5.17. All this suggests that operating near this point could be particularly advantageous for sensing applications, as small perturbations can result in significant changes in the cavity state as indicated in the work of C. Laflamme and A. A. Clerk [178].

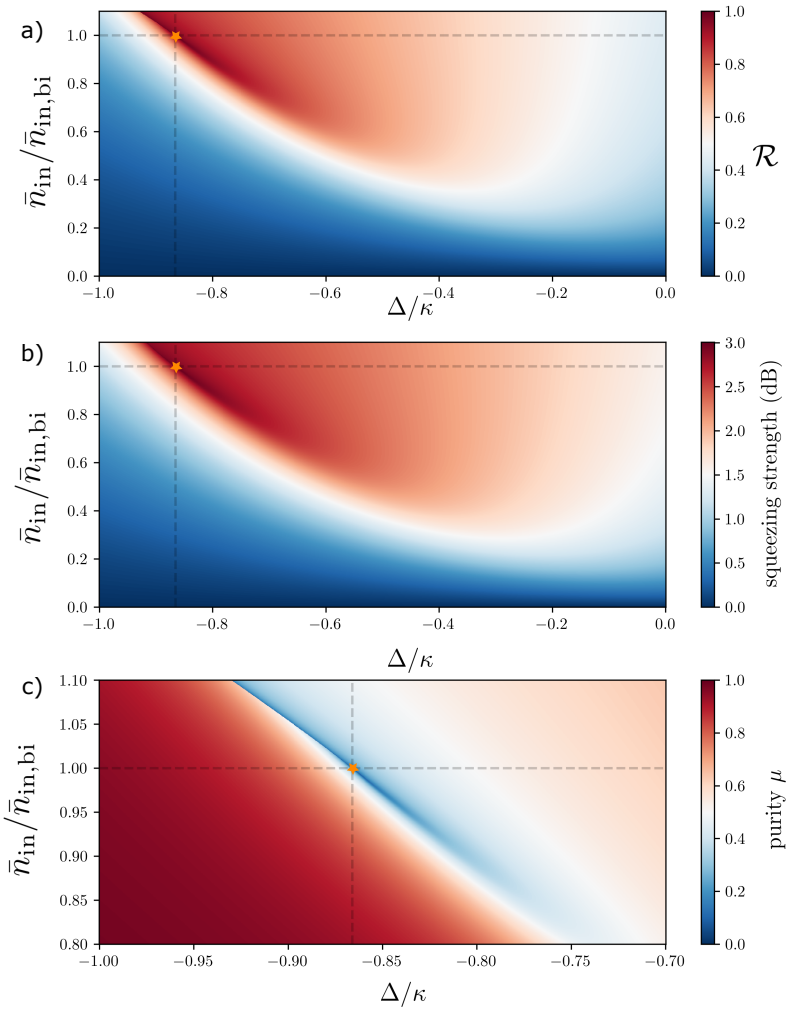

FIGURE 6.2: a) Parameter $\mathcal{R}$, b) squeezing strength (in dB), and c) purity, as functions of input power and cavity detuning. In a), as the system approaches the parametric threshold (marked by a star in all plots), $\mathcal{R} \to 1$, indicating maximum squeezing strength in b) and correspondingly the lowest purity in c). These phenomena coincide with the bifurcation condition, where the cavity operates near the critical input power, $\bar{n}$in,bi, and at the bifurcation point, Δbi.

One of the main objectives of a quantum measurement is to enhance resolution without introducing additional noise to the system being measured. Therefore, aside from the degree of squeezing, the *purity* of the state is an essential figure of merit. For single-mode Gaussian states, the purity is defined as $\mathcal{P} = [2\sqrt{\det(\boldsymbol{\sigma})}]^{-1}$, where $\mathcal{P} \in [0, 1]$. In Gaussian states, purity is related to the average thermal excitation number via $\mathcal{P} = [2\bar{n} + 1]^{-1}$ [203]. As a result, the purity reflects the degree of *mixedness* of the quantum state. A higher purity corresponds to a lower thermal occupation number, which is essential for achieving quantum-limited amplification and minimizing the influence of unwanted thermal effects. From the covariance matrix in Eq. (6.6), we derive the purity of the nonlinear cavity which reads

$$\mathcal{P} = \sqrt{1 - \mathcal{R}^2} \tag{6.9}$$

with the parameter $\mathcal{R}$ defined in Eq. (6.8). This equation suggests that as $\mathcal{R} \to 1$, the purity of the nonlinear cavity approaches zero. This is illustrated in Fig. 6.2c), where we show the

purity as a function of the optical detuning and input power. Thus, near the bifurcation point, the purity tends to zero, which is related to a perfect single mode squeezer.

As discussed in Sec. 5.4, the best cooling in the unresolved sideband regime occurs near the cavity's bifurcation point, where the asymmetry between the Stokes and anti-Stokes rates is maximized, leading to increased optomechanical damping. In Sec. 5.5, we examined the cavity's amplification properties, which also demonstrated a maximal amplification near the bifurcation point. This happens as the cavity approaches the parametric threshold described by Eq. (5.38). For a bare nonlinear cavity, nearing this threshold corresponds to the condition $\mathcal{R} \to 1$.

In the following section, we will use the parameters from Sec. 5.4 and extend our analysis by exploring a different cooling protocol. Specifically, we will analyze sideband cooling in the unresolved sideband regime with a nonlinear cavity and injected squeezed vacuum. This approach leverages the cooling advantages of a nonlinear cavity, as discussed in Chapter 5, while significantly reducing the unwanted cavity backaction, as highlighted in [31].

6.2 Driving with squeezed light

Advances in the generation of squeezed light have been driven by its wide range of applications in quantum information and metrology [204–207], and it has been proposed for the creation of non-classical mechanical states [208].

Formally, pure squeezed states arise through the action of the *squeezing operator* $\hat{S}(r) = \exp\left[re^{i\theta}\hat{a}^2/2 + \text{h.c}\right]$ onto the vacuum state of a bosonic mode $\hat{a}$, where $r \in [0, \infty)$ and $\theta \in [0, 2\pi]$ denote the squeezing strength and angle, respectively. Experimentally, as discussed in Sec. 6.1, squeezing can be produced using a DPA [183], whose output field can then be injected into another system's input port, as illustrated in Fig. 6.3. This process is mathematically described using the framework of *cascaded open quantum systems* [209]. Here, we will employ the input-output formalism introduced in Sec. 2.3, and follow the work of J. Monsel *et al.* [191].

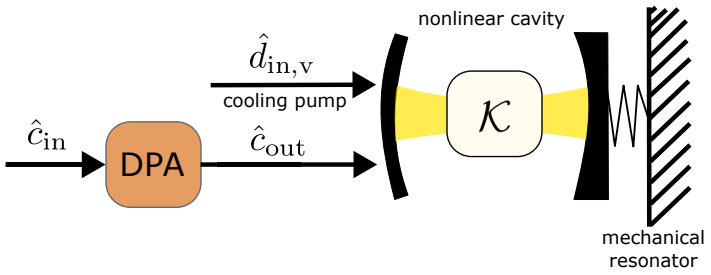

FIGURE 6.3: Graphic description of the optomechanical system with a driven nonlinear cavity. Via the output port of a degenerate parametric amplifier (DPA), squeezed vacuum is injected into the system.

Within the input-output formalism, the dynamics of the DPA are given by the quantum Langevin equations given below

$$\frac{d}{dt}\begin{bmatrix}\hat{c}\\ \hat{c}^\dagger\end{bmatrix} = \mathbf{M}_{\text{DPA}}\begin{bmatrix}\hat{c}\\ \hat{c}^\dagger\end{bmatrix} - \sqrt{\zeta}\begin{bmatrix}\hat{c}_{\text{in}}\\ \hat{c}_{\text{in}}^\dagger\end{bmatrix}, \quad \mathbf{M}_{\text{DPA}} = \begin{bmatrix}-\frac{\zeta}{2} & \chi\\ \chi^* & -\frac{\zeta}{2}\end{bmatrix}, \tag{6.10}$$

where $\hat{c}$ ($\hat{c}^\dagger$) are the creation (annihilation) operator, and where we assumed that the DPA is resonant with the cavity's pump frequency, such that it is set at $\omega_{\text{DPA}} = 2\omega_p$. Here, the input field is given by $\sqrt{\zeta}\hat{c}_{\text{in}} = \sqrt{\zeta_{\text{s}}}\hat{c}_{\text{in,s}} + \sqrt{\zeta_{\text{v}}}\hat{c}_{\text{in,v}}$, where $\zeta = \zeta_{\text{s}} + \zeta_{\text{v}}$ is the total decay rate. In the off-diagonal entries of the dynamical matrix $\mathbf{M}_{\text{DPA}}$ we find the squeezing parameter $\chi = |\chi|e^{-2i\varphi}$ with φ the squeezing angle. Here, the input vacuum noise, $\hat{c}_{\text{in,v}}$, corresponds to the inherent losses of the DPA, whose corresponding coupling is given by ζ_{v}. On the other hand, $\hat{c}_{\text{in,s}}$ is related to the external modes of the electromagnetic field, that are controlled and used to drive the optomechanical system.

Here, we are using the DPA as an auxiliary system that generates squeezing. The generated squeezing leaves the DPA from the output port, which subsequently can be used as the input field of a secondary system. For convenience, we will assume that the *secondary system* is a cavity represented by the mode d. This implies that the input field of the cavity will be composed of the output field of the DPA and its intrinsic uncontrolled losses, which is described by the following equation:

$$\sqrt{\kappa}\hat{d}_{\rm in} = \sqrt{\kappa_{\rm s}}\hat{c}_{\rm out} + \sqrt{\kappa_{\rm v}}\hat{d}_{\rm in,v}. \tag{6.11}$$

Here, $\kappa = \kappa_{\rm s} + \kappa_{\rm v}$ is the cavity's total loss rate, where $\kappa_{\rm s}$ describes the photon exchange rate with the squeezed bath, $\hat{d}_{\rm in,v}$ is related to the uncontrolled losses of the cavity at rate $\kappa_{\rm v}$, and $\hat{c}_{\rm out} = \sqrt{\zeta_{\rm s}}\hat{c} + \hat{c}_{\rm in,s}$ describes the output operator of the DPA.

The Fourier transform of Eq. (6.10) and Eq. (6.11) yield the equation of motion of the output field in frequency space

$$\begin{bmatrix} \hat{c}_{\rm out}[\omega] \\ \hat{c}^{\dagger}_{\rm out}[\omega] \end{bmatrix} = \mathbf{S}_{\rm DPA}[\omega] \begin{bmatrix} \hat{c}_{\rm in}[\omega] \\ \hat{c}^{\dagger}_{\rm in}[\omega] \end{bmatrix} \tag{6.12}$$

with the scattering matrix given by

$$\mathbf{S}_{\rm DPA}[\omega] = \mathbf{1} - \frac{\zeta}{\left(\frac{\zeta}{2} - i\omega\right)^2 - |\chi|^2} \begin{bmatrix} \frac{\zeta}{2} - i\omega & \chi \\ \chi^* & \frac{\zeta}{2} - i\omega \end{bmatrix}. \tag{6.13}$$

With the last equation, we can now write the explicit expression of the output field operator

$$\hat{c}_{\rm out}[\omega] = \mathcal{X}_{\rm DPA}[\omega]\left[\left(\frac{\zeta^2}{4} + |\chi|^2 + \omega^2\right)\hat{c}_{\rm in}[\omega] - \zeta\chi\,\hat{c}^{\dagger}_{\rm in}[\omega]\right], \quad \mathcal{X}^{-1}_{\rm DPA}[\omega] = \left(\frac{\zeta}{2} - i\omega\right)^2 - |\chi|^2. \tag{6.14}$$

Furthermore, assuming that the DPA's bath only non-zero noise correlator is $\langle \hat{c}_{\rm in}[\omega]\hat{c}^{\dagger}_{\rm in}[\omega']\rangle = 2\pi\delta[\omega + \omega']$, then from Eq. (6.14) it yields

$$\begin{aligned} \langle \hat{c}^{\dagger}_{\rm out}[\omega]\hat{c}_{\rm out}[\omega']\rangle =& \frac{\zeta|\chi|}{2}\left[\frac{1}{\left(\frac{\zeta}{2} - |\chi|\right)^2 + \omega^2} - \frac{1}{\left(\frac{\zeta}{2} + |\chi|\right)^2 + \omega^2}\right] 2\pi\delta[\omega + \omega'] \\ \langle \hat{c}_{\rm out}[\omega]\hat{c}_{\rm out}[\omega']\rangle, =& \frac{\zeta|\chi|e^{-2i\varphi}}{2}\left[\frac{1}{\left(\frac{\zeta}{2} - |\chi|\right)^2 + \omega^2} + \frac{1}{\left(\frac{\zeta}{2} + |\chi|\right)^2 + \omega^2}\right] 2\pi\delta[\omega + \omega']. \end{aligned} \tag{6.15}$$

To proceed with the analysis, we will treat the noise correlators given above within the *white noise approximation* [39]. For this, we will transform Eq. (6.15) into the time domain, by applying an inverse Fourier transform. Recall the *characteristic function* of a Cauchy distribution

$$\int_{-\infty}^{\infty} dx\, \frac{e^{itx}}{(x-\alpha)^2 + \beta^2} = \frac{\pi}{\beta} e^{i\alpha t} e^{-\beta|t|}, \quad t, \alpha, \beta \in \mathbb{R}, \tag{6.16}$$

allows us to write the noise correlators given in Eq. (6.15) as

$$\begin{aligned} \langle \hat{c}^{\dagger}_{\rm out}(t)\hat{c}_{\rm out}(t')\rangle &= \frac{\zeta\,|\chi|}{2}\left[\frac{e^{-\kappa_-(t-t')}}{\kappa_-} - \frac{e^{-\kappa_+(t-t')}}{\kappa_+}\right], \\ \langle \hat{c}_{\rm out}(t)\hat{c}_{\rm out}(t')\rangle &= \frac{\zeta\,|\chi|e^{-2i\varphi}}{2}\left[\frac{e^{-\kappa_-(t-t')}}{\kappa_-} + \frac{e^{-\kappa_+(t-t')}}{\kappa_+}\right], \end{aligned} \tag{6.17}$$

where we introduced $\kappa_\pm = \zeta/2 \pm |\chi|$ and assumed that $\zeta/2 > |\chi|$. Here, κ_+ and κ_- correspond to the decay rates of the squeezed and anti-squeezed quadratures of the output field. Furthermore, within the white noise approximation the correlation functions in Eq. (6.17) can be further simplified. For this we take the limit $\kappa_\pm \to \infty$ in Eq. 6.17 and obtain

$$\langle \hat{c}^\dagger_{\mathrm{out}}(t)\hat{c}_{\mathrm{out}}(t')\rangle = \xi N_s \delta(t-t'), \quad \langle \hat{c}_{\mathrm{out}}(t)\hat{c}_{\mathrm{out}}(t')\rangle = \xi M_s e^{-2i\varphi}\delta(t-t') \tag{6.18}$$

with

$$N_s = \frac{\left(\kappa_+^2 - \kappa_-^2\right)^2}{4\kappa_+^2\kappa_-^2}, \quad M_s = \frac{\kappa_+^4 - \kappa_-^4}{4\kappa_+^2\kappa_-^2}, \quad M_s^2 = N_s(N_s+1). \tag{6.19}$$

Here, we introduced a scaling parameter $\xi = \kappa_{\mathrm{s}}\zeta_{\mathrm{s}}/\kappa\zeta \in [0,1]$ which accounts for intrinsic losses in the system, this parameter quantifies how effectively the squeezed vacuum is produced and routed towards the nonlinear cavity. We refer to this parameter as the *purity* of the squeezing. For $\xi = 1$ we have pure squeezing and $\xi = 0$ implies having vacuum noise only. From the last result and recalling Eq. (6.11), we find that the squeezed input noise operators of the cavity satisfy

$$\langle \hat{d}_{\mathrm{in}}(t)\hat{d}^\dagger_{\mathrm{in}}(t')\rangle = (\xi N_s + 1)\delta(t-t'), \quad \langle \hat{d}_{\mathrm{in}}(t)\hat{d}_{\mathrm{in}}(t')\rangle = \xi M_s \delta(t-t'). \tag{6.20}$$

In addition, we can quantify the amount of squeezing using the *squeezing factor* r, which is related to the noise correlators in Eq. (6.20) through the following relation [39]

$$N_s = \frac{1}{\xi}\sinh^2(r), \quad M_s = \frac{1}{\xi}\sinh(r)\cosh(r). \tag{6.21}$$

So far in this section, we have demonstrated how a DPA provides squeezing through its output field, with its noise characterized by the correlators in Eq. (6.18). In the next section, we will use the output field of the DPA as the input field for the nonlinear cavity. We will show that injecting a squeezed vacuum into the nonlinear cavity offers a way to mitigate unwanted cavity backaction, thereby improving the cooling performance.

6.3 Scattering behaviour: radiation pressure force spectrum

In Chapter 3, we demonstrated that the Stokes and anti-Stokes processes are described by Eq. (3.125), which are governed by the radiation pressure force spectrum given in Eq. (3.38). Up to this point, we derived the force spectrum assuming only vacuum noise entering the nonlinear cavity, with its noise correlators defined in Eq. (3.60).

In this chapter, however, we will inject a squeezed vacuum generated externally from a DPA. As a result, the input noise correlators are now described by Eq. (6.20). Referring back to the expression for the linearized force spectrum in Eq. (5.15), we obtain the following correlator:

$$\begin{aligned}\left\langle \hat{F}[\omega]\hat{F}[\omega']\right\rangle = {} & 2\pi\Big(\eta^*[-\omega]\eta[\omega']\left(\xi N_s + 1\right) + \eta[\omega]\eta^*[-\omega']\xi N_S\Big)\delta[\omega+\omega'] \\ & + 2\pi\Big(\eta[\omega]\eta[\omega']\xi M_S e^{-2i\varphi} + \eta^*[-\omega]\eta^*[-\omega']\xi M_S e^{+2i\varphi}\Big)\delta[\omega+\omega'],\end{aligned} \tag{6.22}$$

where we have Fourier transformed the noise correlators given in Eq. (6.20). This result can then be substituted into Eq. (3.38) yielding the radiation pressure force spectrum given below

$$\begin{aligned}\mathcal{S}^{\mathrm{s}}_{FF}[\omega] = \mathcal{S}_{FF}[\omega]\left\{1+\left[1+\frac{\left[\omega-\Delta_{\mathrm{eff}}\right]^2+\frac{\kappa^2}{4}}{\left[\omega+\Delta_{\mathrm{eff}}\right]^2+\frac{\kappa^2}{4}}\right]\xi N_s\right\}\\ -\frac{2\xi M_s\left\{\left(\Delta^2_{\mathrm{eff}}-\omega^2-\frac{\kappa^2}{4}\right)\cos(2\varphi)-\Delta_{\mathrm{eff}}\kappa\sin(2\varphi)\right\}}{\left[\tilde{\Delta}^2-\omega^2+\frac{\kappa^2}{4}-|\Lambda|^2\right]^2+\kappa^2\omega^2}\end{aligned} \tag{6.23}$$

with the effective detuning $\Delta_{\mathrm{eff}} = |\Lambda| - \tilde{\Delta}$. Note that, in the absence of squeezing, namely setting $\xi = 0$ in the expression given above, we recover $\mathcal{S}_{FF}[\omega] = g_0^2\mathcal{S}_{nn}[\omega]$ with the photon number spectrum given by Eq. (4.29). Thus, the squeezed input noise, through the new noise correlators from Eq. (6.20), modifies the radiation pressure force spectrum, as can be observed in Eq. (6.23). Furthermore, it can be shown that, for a linear cavity ($\mathcal{K} = 0$) the last expression agrees with the result derived in [185].

In Chapter 5, we demonstrated that the asymmetry caused by the cavity's nonlinearity enhances cooling efficiency in the unresolved sideband regime. At this point, it is natural to ask whether injecting squeezed light could further improve optomechanical damping. However, the total damping remains unchanged when coherent light is replaced with a squeezed vacuum, i.e. it yields Eq. (5.11). Thus, squeezed light cannot directly enhance the optomechanical damping. Still, as we will show below, it can minimize the Stokes process, effectively reducing unwanted cavity backaction.

First, to minimize the Stokes process, an extrema analysis was conducted to determine the optimal squeezing phase, which is expressed as follows

$$\frac{d}{d\varphi}\mathcal{S}^{\mathrm{s}}_{\mathrm{FF}}[-\omega_m] = 0 \quad \Rightarrow \quad \varphi = \frac{1}{2}\arctan\left(\frac{\kappa\Delta_{\mathrm{eff}}}{\omega_m^2-\Delta^2_{\mathrm{eff}}+\frac{\kappa^2}{4}}\right)+k\pi \tag{6.24}$$

with $k \in \mathbb{Z}$. We can now use this condition in Eq. (6.23) and find an expression for the minimized Stokes rate

$$\begin{aligned}\frac{\Gamma_{\mathrm{S}}}{g_0^2\bar{n}_c\kappa} = \frac{\left[\Delta_{\mathrm{eff}}-\omega_m\right]^2+\frac{\kappa^2}{4}}{P[\omega_m]}\Bigg\{1+\left[1+\frac{\left[\Delta_{\mathrm{eff}}+\omega_m\right]^2+\frac{\kappa^2}{4}}{\left[\Delta_{\mathrm{eff}}-\omega_m\right]^2+\frac{\kappa^2}{4}}\right]\xi N_s\\ -2\xi M_s\sqrt{\frac{\left[\Delta_{\mathrm{eff}}+\omega_m\right]^2+\frac{\kappa^2}{4}}{\left[\Delta_{\mathrm{eff}}-\omega_m\right]^2+\frac{\kappa^2}{4}}}\Bigg\},\end{aligned} \tag{6.25}$$

where we defined the pole

$$P[\omega] = \left[\tilde{\Delta}^2-\omega^2+\frac{\kappa^2}{4}-|\Lambda|^2\right]^2+\kappa^2\omega^2. \tag{6.26}$$

Similarly, the anti-Stokes process can be derived by noticing that the optimal squeezing phase is symmetrical in ω_m, such that we arrived at

$$\begin{aligned}\frac{\Gamma_{\mathrm{AS}}}{g_0^2\bar{n}_c\kappa} = \frac{\left[\Delta_{\mathrm{eff}}+\omega_m\right]^2+\frac{\kappa^2}{4}}{P[\omega_m]}\Bigg\{1+\left[1+\frac{\left[\Delta_{\mathrm{eff}}-\omega_m\right]^2+\frac{\kappa^2}{4}}{\left[\Delta_{\mathrm{eff}}+\omega_m\right]^2+\frac{\kappa^2}{4}}\right]\xi N_s\\ -2\xi M_s\sqrt{\frac{\left[\Delta_{\mathrm{eff}}-\omega_m\right]^2+\frac{\kappa^2}{4}}{\left[\Delta_{\mathrm{eff}}+\omega_m\right]^2+\frac{\kappa^2}{4}}}\Bigg\}.\end{aligned} \tag{6.27}$$

Thus far, we have minimized the unwanted Stokes scattering process by finding an optimal squeezing phase. This led to the condition outlined in Eq. (6.24) and ultimately to the minimized Stokes rates given in Eq. (6.25). Below, we will utilize these results to overcome the cavity backaction limit defined by Eq. (5.24).

6.4 Surpassing the backaction limit

We are now in the position to use Eqs. (6.25) and (6.27) associated to the minimized Stokes and anti-Stokes rates, respectively. Using these results in Eq. (6.1), we find that the cavity backaction limit becomes

$$\bar{n}_{\mathrm{BA}}^{\mathrm{s}} = \bar{n}_{\mathrm{BA}} \left\{ 1 + \left[1 + \frac{1}{\wp^2} \right] \xi N_s - \frac{2\xi M_s}{\wp} \right\}, \tag{6.28}$$

with $\bar{n}_{\mathrm{BA}}$ given by Eq. (5.24) and where we defined

$$\wp^2 = \frac{\left[\Delta_{\mathrm{eff}} - \omega_m\right]^2 + \frac{\kappa^2}{4}}{\left[\Delta_{\mathrm{eff}} + \omega_m\right]^2 + \frac{\kappa^2}{4}}. \tag{6.29}$$

For $\xi = 0$ in Eq. (6.28) we recover $\bar{n}_{\mathrm{BA}}$, which is the backaction corresponding to a cavity driven with solely input vacuum noise. We can further minimize the backaction limit given in Eq. (6.28) over the properties of the squeezed input light and find that it has to fulfill

$$\wp = \frac{N_s}{M_s} = \sqrt{\frac{N_s}{N_s + 1}}, \tag{6.30}$$

where in the second equality we used that $M_s^2 = N_s(N_s + 1)$. For this condition to hold we solve the last equation for N_s and find it has to satisfy

$$N_s = \frac{\wp^2}{1 - \wp^2} \geq 0 \quad \Rightarrow \quad \wp < 1. \tag{6.31}$$

Finally, plugging these conditions into Eq. (6.28) we find

$$\bar{n}_{\mathrm{BA}}^{\mathrm{s}} = \bar{n}_{\mathrm{BA}} \left(1 - \xi\right). \tag{6.32}$$

As expected, in the absence of squeezing we recover Eq. (5.24), but for $\xi = 1$ we can fully suppress the quantum backaction limit. Additionally, using Eq. (6.21) together with Eq. (6.30), we find that the squeezing factor can be expressed in the following way[2]

$$\sinh^2(r) = \frac{\xi \wp^2}{1 - \wp^2} \geq 0 \tag{6.34}$$

with $\wp$ given in Eq. (6.29).

In Chapter 5, we concluded that the lowest mechanical occupation was constrained by the cavity backaction limit, as shown in Fig. 5.10. However, with Eq. (6.32), we have demonstrated that the cavity backaction can be fully suppressed when only squeezed vacuum ($\xi = 1$) is introduced into the nonlinear system from the DPA. This approach allows for improved cooling and effectively overcomes the detrimental effects of cavity backaction.

[2]To express the squeezing strength in units of dB we use the following formula

$$\varrho = -10 \log_{10}\left(e^{-2r}\right). \tag{6.33}$$

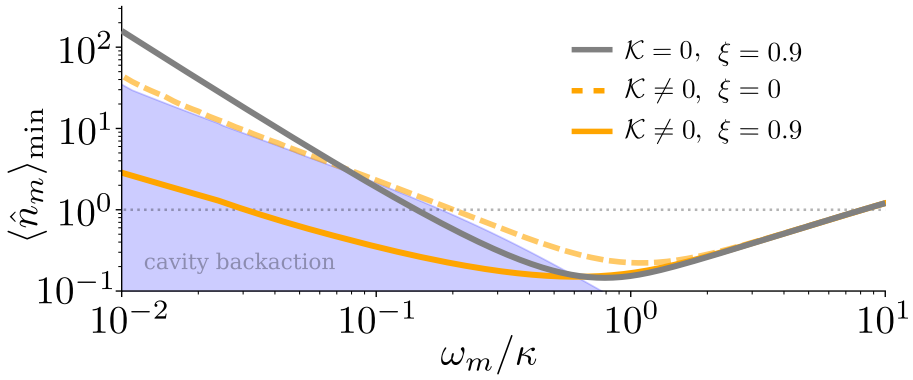

FIGURE 6.4: Lowest phonon occupation as a function of the resolved sideband parameter ω_m/κ at $g_0/2\pi = 15$ kHz. A nonlinear cavity driven with only vacuum noise (dashed-orange) is limited by the unwanted cavity backaction, which can be suppressed when squeezed input light enters the cavity (solid-orange) yielding lower cooling limits. The suppression of the cavity backaction using squeezed light also improves the cooling limits achieved using an equivalent linear cavity (solid-grey). In the unresolved sideband regime a nonlinear cavity outperforms an equivalent linear system, but this improvement decreases as ω_m increases.

Fig. 6.4 shows the optimal cooling achieved as a function of the resolved sideband parameter (ω_m/κ) for both a linear (grey) and a nonlinear (orange) cavity when driven by squeezed vacuum, which enables the suppression of cavity backaction as shown in Eq. (6.32). The nonlinear cavity again exhibits superior cooling performance, particularly in the deep unresolved sideband regime, compared to an equivalent linear system under the same conditions. Moreover, the nonlinear cavity with injected squeezed vacuum substantially outperforms the cooling limits achieved without it. Using the squeezing protocol and an optomechanical coupling strength of $g_0/2\pi = 15$kHz, a nonlinear cavity enables ground state cooling at $\omega_m/\kappa = 0.03$, whereas a linear cavity requires $\omega_m/\kappa = 0.144$ to achieve the same result. This further highlights the advantages of a nonlinear cavity in the unresolved sideband regime.

For the parameters given in Table 5.1, the cooling limits of the linear cavity are not constrained by backaction effects. Consequently, even with high-purity squeezing ($\xi = 0.99$), which almost entirely suppresses unwanted cavity backaction, the linear cavity can only achieve ground state cooling at $\omega_m/\kappa = 0.13$. In contrast, at such a value, a nonlinear cavity reaches the ground state with a lower purity of $\xi = 0.44$. This indicates that the nonlinear cavity requires a smaller squeezing strength of $\varrho = 6.48$ dB compared to $\varrho = 10.15$ dB for the linear cavity, as shown in Fig. 6.5.

As discussed in Chapter 5, the cooling advantages of the nonlinear cavity diminish as we approach the resolved sideband regime. Additionally, for $\omega_m/\kappa > 1$, the driving power is no longer optimized (see Fig. 5.6), resulting in increased phonon occupation as the thermal bath's contribution surpasses the system's cooling capability at the given input power. In the resolved sideband regime, optimal cooling occurs when the cavity is driven at $\Delta = -\omega_m$. From Eq. (6.29), we observe that for $\omega_m/\kappa > 1$, optimal cooling corresponds to $\wp^2 \to 0$ (as $\Delta_{\text{eff}} \to \omega_m$), which leads to a squeezing strength that approaches zero, as shown in Fig. 6.5.

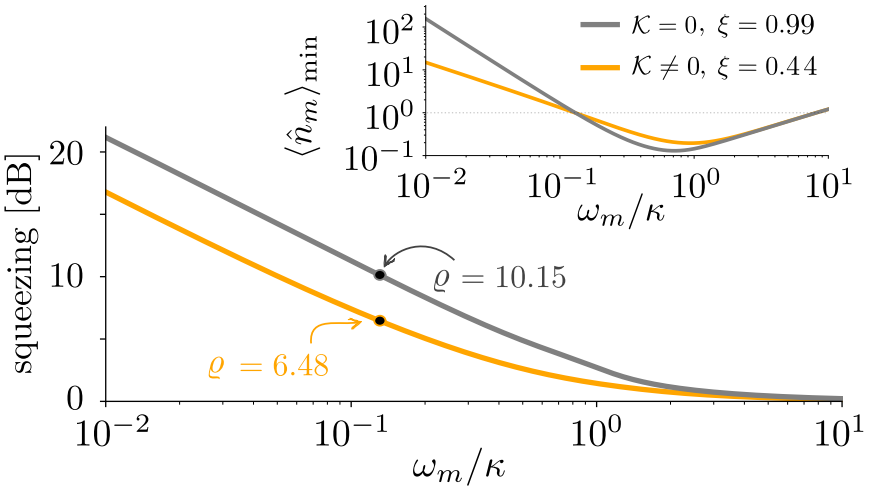

FIGURE 6.5: Squeezing for optimal cooling as a function of the resolved sideband parameter. The orange line depicts the associated squeezing strength of a nonlinear cavity with a purity of $\xi = 0.44$, which reaches ground state cooling at $\omega_m/\kappa = 0.13$ for $\varrho = 6.48$ dB. Conversely, a linear cavity (grey) needs higher purity ($\xi = 0.99$), which consequently translates into more squeezing strength ($\varrho = 10.15$ dB), to achieve ground state cooling for a similar resolved sideband parameter. Inset shows the minimum phonon number as a function of the resolved parameter for a linear (grey) and nonlinear (orange) cavity using a purity of $\xi = 0.99$ and $\xi = 0.44$, respectively. Here, ground state cooling is obtained at $\omega_m/\kappa = 0.13$, where both lines intersect. For this plot we used $g_0/2\pi = 15$ kHz and all other parameters given by Table 5.1.

Throughout this chapter, we demonstrated that maximum intracavity squeezing occurs near the bifurcation point as illustrated in Fig. 6.2b). However, as shown in Fig. 6.2c), as we approach this point, the system's low purity ($\mathcal{P}$) indicates a high level of thermal occupation. In addition, we investigated the cooling improvements achieved when the cavity is driven with a squeezed vacuum, as outlined by M. Asjad *et al.* [185]. Injecting a squeezed vacuum allows for the suppression of the Stokes process, eliminating unwanted cavity backaction and ultimately enhancing the cooling performance. Fig. 6.4 shows that with squeezed vacuum, a nonlinear cavity achieves ground state cooling of the mechanical oscillator deep in the unresolved sideband regime, surpassing the limit given by Eq. (5.26) when driven by vacuum noise. Moreover, as depicted in Fig. 6.5, the nonlinear cavity not only requires less purity (ξ) but also lower squeezing strength to reach the ground state compared to a linear cavity under equivalent conditions.

In the last two chapters, we demonstrated that the nonlinear nature of the cavity plays a key role in describing optomechanical backaction. Understanding the classical dynamics is essential, as the strongest cooling occurs at the bifurcation point of the classical cavity dynamics. We demonstrated, that this enhanced cooling performance arises from the distinctive asymmetric photon number spectral density of the nonlinear cavity. Additionally, we showed that the bifurcation point aligns with both the parametric threshold condition and the point of maximum intracavity squeezing.

We further found that the limits for dynamical backaction cooling are the same for both linear and nonlinear systems. However, when driven with squeezed vacuum to counteract unwanted backaction heating, the nonlinear cavity again shows superior cooling efficiency. Under identical parameters, ground state cooling with a nonlinear cavity requires significantly less squeezing strength than with a linear system.

Although typically viewed individually as unwanted features, combining an optomechanical system in the unresolved sideband regime with an intrinsically nonlinear cavity significantly improves the cooling performance. This makes the nonlinear cavity an appealing candidate for applications involving large, low-frequency mechanical systems.

Chapter 7

Quadratic optomechanics via photon pressure interaction

Throughout this work, we first explored the fundamentals of optomechanics and, in Chapter 5, specifically analyzed a novel nonlinear optomechanical setup in which a SQUID cavity is inductively coupled to a cantilever with a magnetic tip [3]. We demonstrated that the intrinsic nonlinearity of the cavity enhances backaction cooling, particularly in the unresolved sideband regime. In this chapter, we will investigate how such cavity nonlinearities also impact optomechanical effects, specifically OMIT (see Sec. 3.9). However, we will examine these effects in an *artificial optomechanical system*, where the interaction occurs solely between photons, in the absence of a mechanical element.

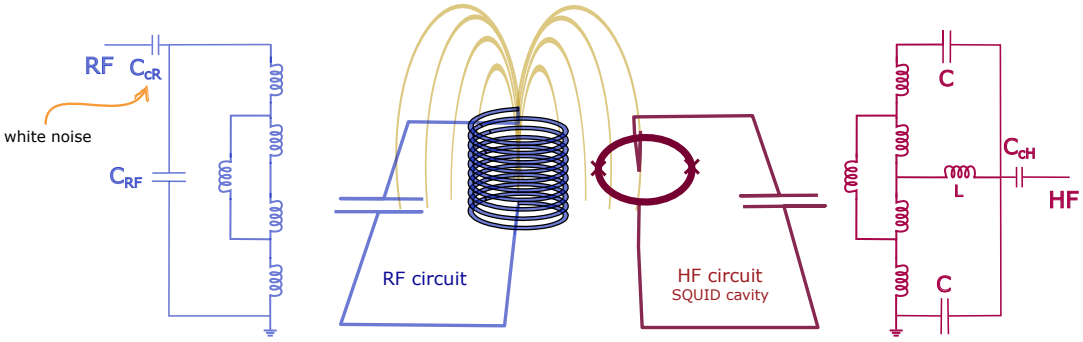

FIGURE 7.1: Illustration of the two-mode superconducting LC circuit with tunable photon-pressure coupling. Depicted in blue and red are the RF and HF circuits, respectively, both composed by inductors and capacitors. The RF contains an inductor wire that forms the loop of the SQUID, which is embedded in the HF circuit. As shown in the middle schematic, the circulating current in the RF's inductor introduces additional flux to the SQUID loop, thereby modulating the frequency of HF mode.

Recently, the radiation-pressure interaction between off-resonant photons, also known as *photon pressure coupling*, has gained significant attention due to its potential for achieving quantum control in the radio-frequency (RF) regime [96, 210–212]. This interaction can be realized using two superconducting LC circuits, a promising platform for exploring commonly inaccessible parameter regimes.

Photon pressure devices have been realized in the classical regime, at the expense of large thermal occupation, showing strong interaction strengths, thereby providing a pathway to explore optomechanical effects in a different platform [211, 212]. However, as in optomechanics, photon-pressure-based devices equally suffer from the presence of high thermal occupations, limiting the possibility of testing fundamental effects in the quantum regime. Recently, sideband cooling using photon pressure has been realized demonstrating the reduction of the thermal occupation by 75% [96].

The device sketched in Fig. 7.1 integrates a superconducting RF mode coupled via photon pressure to a superconducting high-frequency (HF) cavity mode within a galvanic coupling architecture, similar to the work by Rodrigues *et al.* [96, 140]. The RF superconducting LC circuit, in addition to its large parallel-plate capacitor, includes a short inductor wire forming the loop of the SQUID, as shown in blue in Fig. 7.1. The SQUID facilitates the interaction,

via the inductor wire, of the RF mode and the HF circuit. The HF mode, depicted in red in Fig. 7.1, consists of two integrated capacitors, C, and a linear inductor, L. These modes are then coupled individually to coplanar waveguide feedlines for driving and readout. The chip is mounted onto a circuit board with connected microwave input and output ports, and placed inside a copper housing. Additionally, a superconducting magnet is attached to this housing to apply an external out-of-plane magnetic field. Finally, the device is placed inside a cryoperm magnetic shielding and mounted to the mixing chamber of a dilution refrigerator with a base temperature of $T \sim 15$mK.

Moreover, this setup allows the introduction of noise into the RF mode. The signal from the *vector network analyzer* (VNA) is attenuated and combined with a noise signal via a directional coupler. The noise is generated by mixing a coherent signal with white noise from a DC source. The resulting combined signal, containing both the VNA's controlled input and the generated noise, is filtered and fed into the RF circuit. This configuration enables testing of the RF mode under controlled conditions, with the ability to independently adjust both the VNA signal and the noise, facilitating various test scenarios for analyzing the RF mode's response in noisy environments.

In this chapter, we will first present the Hamiltonian formulation of the setup, which reveals a quadratic optomechanical-like interaction. Next, we will examine the dynamics of the fluctuations, demonstrating how this interaction enables cooling of the RF mode through a two-photon process. Finally, we will show that the resulting quadratic interaction leads to OMIT and investigate the effects of noise injection into the RF mode on this phenomenon.

7.1 Hamiltonian formulation

In Chapter 3 we showed that a superconducting LC circuit can be described by the Hamiltonian of a quantum harmonic oscillator with frequency given by Eq. (3.10). Hence, the uncoupled Hamiltonian describing the HF and RF modes can be written as

$$\hat{\mathcal{H}}_0 = \omega_0 \hat{a}^\dagger \hat{a} + \Omega_0 \hat{b}^\dagger \hat{b}, \tag{7.1}$$

with $\hat{a}^\dagger$ ($\hat{a}$) and $\hat{b}^\dagger$ ($\hat{b}$) the creation (annihilation) operators of the HF and RF modes, respectively. Here, ω_0 is the resonant frequency of the HF modes, while Ω_0 denotes the resonant frequencies of the low-frequency oscillator.

In Chapter 4, we explained that when magnetic flux, Φ, is applied through the SQUID (see Fig. 7.2), for instance, by the external coil as illustrated in Fig. 7.1, the resulting circulating current modifies the inductance of the Josephson junctions and consequently modifies the resonance frequency of the HF mode. Therefore, any circulating current in the RF's inductor introduces additional flux to the SQUID loop leading to a parametric interaction between the modes. Due to the photon pressure interaction between these modes, the HF resonant frequency is modulated through variations in the magnetic flux resulting in

$$\omega_0(\Phi) \approx \omega_0 + \Phi_{\text{zpf}} \frac{\partial \omega_0}{\partial \Phi} \hat{x} + \frac{\Phi_{\text{zpf}}^2}{2} \frac{\partial^2 \omega_0}{\partial^2 \Phi} \hat{x}^2 + \dots. \tag{7.2}$$

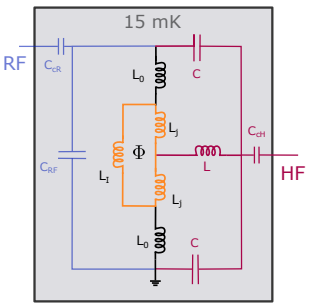

FIGURE 7.2: Schematic of the whole circuit.

Here, $\partial\omega_0/\partial\Phi$ is the flux responsivity of the HF mode resonance frequency with Φ_{zpf} the zero-point flux $\Phi_{\text{zpf}} \approx 635\mu\Phi_0$, and $\hat{x} = \hat{\Phi}/\Phi_{\text{zpf}}$ is the RF-induced flux threading the SQUID. Using Eq. (7.2) into Eq. (7.1), we find that the Hamiltonian describing the photon pressure interaction between the HF and RF modes is given by

$$\hat{\mathcal{H}} = \hat{\mathcal{H}}_0 + g_0 \hat{a}^\dagger \hat{a} \left(\hat{b} + \hat{b}^\dagger\right) + g_2 \hat{a}^\dagger \hat{a} \left(\hat{b} + \hat{b}^\dagger\right)^2 + \hat{\mathcal{H}}_{\text{d}}(t), \tag{7.3}$$

where $\hat{\mathcal{H}}_{\text{d}} = \alpha_p e^{-i\omega_p t} \hat{a}^\dagger + \text{h.c}$ corresponds to the time-dependent driving. Here, we also introduced the first and second-order photon pressure single-photon coupling strength given

by

$$g_0 \equiv \frac{\partial \omega_0}{\partial \Phi}\Phi_{\mathrm{zpf}}, \qquad g_2 \equiv \frac{1}{2}\frac{\partial^2 \omega_0}{\partial^2 \Phi}\Phi_{\mathrm{zpf}}^2. \tag{7.4}$$

The resemblance of the Hamiltonian in Eq. (7.3) to the radiation pressure interaction in optomechanics justifies referring to this setup as an *artificial optomechanical* system. In this case, the RF circuit replaces the *mechanical mode*, with its *displacement* modulating the resonant frequency of the HF mode. Due to the strong single-photon coupling achievable via photon pressure interaction, the interaction is accurately described up to second order. As a result, the flux-mediated coupling through the SQUID leads to a $\hat{x}^2$ coupling.

In Chapter 4, we demonstrated that the Hamiltonian describing a superconducting LC circuit with a Josephson junction resembles that of a Duffing oscillator. However, since the experiments conducted with this setup operate in the low-power regime, both circuits behave as harmonic oscillators, allowing us to neglect their nonlinearities [96].

As discussed in Chapter 3, the radiation pressure interaction in optomechanics is inherently nonlinear. Considering position-squared coupling in optomechanics has been proposed for applications such as QND measurements of phonon number [64], detecting phonon shot noise [130], and for cooling and squeezing mechanical motion [213, 214]. Quadratic interactions can be realized in systems like the *membrane-in-the-middle* architecture, where the membrane is positioned at a node or antinode of the cavity mode [64, 215]. However, despite efforts to enhance this interaction [216], the $\hat{x}^2$ coupling remains typically too weak to observe as it scales with $\sim x_{\mathrm{zpf}}^2$.

Due to their high tunability and large coupling strength, photon pressure devices allow for testing optomechanical effects in a different platform, enabling the exploration of otherwise inaccessible parameter regimes.

7.1.1 Displacement transformation

Similar to the approach in Chapter 3, we will analyze the system's dynamics described by Eq. (7.3) within the linearized approximation. This requires the introduction of a displacement operator for each mode. For the HF mode, we apply $\hat{\mathcal{D}}^\dagger(\alpha)\hat{a}\hat{\mathcal{D}}(\alpha) = \alpha + \hat{d}$, where $\alpha = \langle \hat{a} \rangle$ represents the average amplitude and $\hat{d}$ the fluctuations. Similarly, for the RF mode, we use $\hat{\mathcal{D}}^\dagger(\beta)\hat{b}\hat{\mathcal{D}}(\beta) = \beta + \hat{b}$, with $\beta = \langle \hat{b} \rangle$, keeping $\hat{b}$ to describe the RF mode fluctuations for convenience. Following the approach outlined in Sec. 3.4.3, we find that the linearized Hamiltonian is given by

$$\hat{\mathcal{H}}_{\mathrm{lin}} = \hat{\mathcal{H}}_0' + \hat{\mathcal{H}}_{\mathrm{lin}}^{(1)} + \hat{\mathcal{H}}_{\mathrm{lin}}^{(2)} \tag{7.5}$$

where $\hat{\mathcal{H}}_0' = -\Delta \hat{d}^\dagger \hat{d} + \Omega_0 \hat{b}^\dagger \hat{b}$ is the free Hamiltonian with $\Delta = \omega_p - \omega_0$. In Eq. (7.5), the last two terms emerge from the first and second-order interactions, respectively. Similarly, as in the usual linearized optomechanical interaction given in Eq. (3.75), the following Hamiltonian results from the first-order coupling

$$\hat{H}_{\mathrm{lin}}^{(1)} = \underbrace{g_0\langle \hat{x} \rangle \hat{d}^\dagger \hat{d}}_{\text{induced frequency shift}} + \underbrace{g_0\left[\alpha^* \hat{d} + \alpha \hat{d}^\dagger\right]\left[\hat{b} + \hat{b}^\dagger\right]}_{\text{quadrature-to-quadrature coupling}} + \underbrace{g_0 \hat{d}^\dagger \hat{d}\left[\hat{b} + \hat{b}^\dagger\right]}_{\text{smaller by a factor of } \alpha}. \tag{7.6}$$

On the other hand, the second-order interaction, which originates from the quadratic coupling, leads to the following Hamiltonian

$$\begin{aligned}
\hat{\mathcal{H}}_{\mathrm{lin}}^{(2)} &= g_2\left[1 + \langle \hat{x} \rangle^2\right]\hat{d}^\dagger \hat{d} + 2g_2|\alpha|^2 \hat{b}^\dagger \hat{b} \\
&+ 2g_2\langle \hat{x} \rangle\left(\alpha^* \hat{d} + \alpha \hat{d}^\dagger\right)\left(\hat{b} + \hat{b}^\dagger\right) + 2g_2\langle \hat{x} \rangle \hat{d}^\dagger \hat{d}\left(\hat{b} + \hat{b}^\dagger\right) \\
&+ g_2|\alpha|^2\left(\hat{b}^2 + \hat{b}^{\dagger 2}\right) + g_2\left(\alpha^* \hat{d} + \alpha \hat{d}^\dagger\right)\left(\hat{b}^2 + \hat{b}^{\dagger 2}\right) + g_2 \hat{d}^\dagger \hat{d}\left(\hat{b}^2 + \hat{b}^{\dagger 2}\right) \\
&+ 2g_2 \hat{b}^\dagger \hat{b}\left(\alpha^* \hat{d} + \alpha \hat{d}^\dagger\right) + 2g_2 \hat{d}^\dagger \hat{d}\hat{b}^\dagger \hat{b} + g_2\left(\alpha^* \hat{d} + \alpha \hat{d}^\dagger\right)
\end{aligned} \tag{7.7}$$

The first line corresponds to the induced frequency shifts of both modes. The second line represents a quadrature-to-quadrature interaction along with a nonlinear term in the fluctuations, which is typically neglected due to its smallness. The third line describes two-photon processes: the first term is linked to single-mode squeezing of the RF mode, the second involves interaction with the HF quadrature, and the last term represents a nonlinear fluctuation term. The final line includes a nonlinear fluctuation term, a cross-Kerr interaction, and a constant term.

In Sec. 3.5, we demonstrated that the drive frequency determines the dominant resonant processes. Next, we will analyze the effective dynamics that emerge when the HF mode is driven on the second lower red sideband.

7.1.2 Resonant dynamics

To analyze the resonant interactions, we move to a rotating frame with respect to the free Hamiltonian given in Eq. (7.1), namely we do

$$\hat{\mathcal{H}}'_{\rm lin} = \hat{U}^\dagger \hat{\mathcal{H}}_{\rm lin} \hat{U} - \hat{\mathcal{H}}'_0 \tag{7.8}$$

where the unitary is given by $\hat{U} = e^{-i\hat{\mathcal{H}}'_0 t}$ and with $\hat{\mathcal{H}}_{\rm lin}$ is the Hamiltonian derived above in Eq. (7.5).

The device operates in the resolved sideband and is operated with the pump tone set to the second lower sideband, i.e., $\Delta = -2\Omega_0$. Under these specific conditions, we can apply the RWA to the Hamiltonian in Eq. (7.8), yielding the effective Hamiltonian that describes the resonant processes (in the original frame)

$$\hat{\mathcal{H}}_{\rm lin} = -\tilde{\Delta}\hat{d}^\dagger\hat{d} + \tilde{\Omega}\hat{b}^\dagger\hat{b} + G_2\left(\hat{d}\hat{b}^{\dagger 2} + \hat{d}^\dagger\hat{b}^2\right) + 2g_2\hat{d}^\dagger\hat{d}\hat{b}^\dagger\hat{b}. \tag{7.9}$$

Here, we define the multiphoton coupling strength as $G_2 = g_2\alpha$, the modified detuning as $\tilde{\Delta} = \Delta - g_0\langle\hat{x}\rangle - g_2\left[1 + \langle\hat{x}\rangle^2\right]$ and RF frequency as $\tilde{\Omega}_0 = \Omega_0 + 2g_2|\alpha|^2$. Assuming these frequency shifts are small, i.e. $\tilde{\Delta} \approx \Delta$ and $\tilde{\Omega} \approx \Omega_0$, and that the cross-term is negligible by a factor of α, the effective system Hamiltonian becomes

$$\hat{\mathcal{H}}_{\rm eff} = -\Delta\hat{d}^\dagger\hat{d} + \Omega_0\hat{b}^\dagger\hat{b} + G_2\left(\hat{d}\hat{b}^{\dagger 2} + \hat{d}^\dagger\hat{b}^2\right). \tag{7.10}$$

This Hamiltonian describes a pump-tunable beam-splitter-like interaction between two low-frequency photons and a single excitation of the HF mode. In the following section, we will explore the dynamics that result from this effective Hamiltonian.

7.2 Dynamics

We will examine the dynamics of the fluctuations using the input-output formalism introduced in Chapter 2. This approach provides a clear framework for analyzing the fields entering and exiting the system, which will be particularly useful in the forthcoming analysis. The quantum Langevin equations for the HF mode read

$$\frac{d}{dt}\hat{d} = \left(i\Delta - \frac{\kappa}{2}\right)\hat{d} - iG_2\hat{b}^2 - \sqrt{\kappa}\hat{d}_{\rm in}, \tag{7.11}$$

$$\frac{d}{dt}\hat{n}_{\rm HF} = -iG_2\left(\hat{d}^\dagger\hat{b}^2 - \hat{d}\hat{b}^{\dagger 2}\right) - \kappa\hat{n}_{\rm HF} - \sqrt{\kappa}\left(\hat{d}^\dagger_{\rm in}\hat{d} + \hat{d}^\dagger\hat{d}_{\rm in}\right) \tag{7.12}$$

with $\hat{n}_{\rm HF} = \hat{d}^\dagger\hat{d}$ as the photon number operator of the HF mode, and κ representing the cavity loss rate. The last terms correspond to the cavity input noise operators. Since the HF mode has zero thermal occupation, $\bar{n}^T_{\rm HF} \approx 0$, these operators follow the noise correlators outlined in Eq. (3.60).

On the other hand, the equations of motion of the RF mode are given by

$$\frac{d}{dt}\hat{b} = -\left(i\Omega_0 + \frac{\Gamma}{2}\right)\hat{b} - 2iG_2\hat{d}\hat{b}^\dagger - \sqrt{\Gamma}\hat{b}_{\rm in}, \tag{7.13}$$

$$\frac{d}{dt}\hat{b}^2 = -2\left(i\Omega_0 + \frac{\Gamma}{2}\right)\hat{b}^2 - 4iG_2\hat{d}\left(\hat{n}_{\rm RF} + \frac{1}{2}\right) - 2\sqrt{\Gamma}\hat{b}\hat{b}_{\rm in}, \tag{7.14}$$

$$\frac{d}{dt}\hat{n}_{\rm RF} = -2iG_2\left(\hat{d}\hat{b}^{2\dagger} - \hat{d}^\dagger\hat{b}^2\right) - \Gamma\hat{n}_{\rm RF} - \sqrt{\Gamma}\left(\hat{b}^\dagger\hat{b}_{\rm in} + \hat{b}_{\rm in}^\dagger\hat{b}\right). \tag{7.15}$$

with the associated photon number operator $\hat{n}_{\rm RF} = \hat{b}^\dagger\hat{b}$ and where Γ denotes the decay rate of the mode. The noise operators of the RF mode satisfy Eq. (3.61) with the average thermal occupation given by $\bar{n}_{\rm RF}^T$.

Using the equations of motion derived in this section, we will now demonstrate sideband cooling of the RF mode through a two-photon mechanism.

7.3 Two-photon cooling

One of the main achievements in optomechanics is the ground state cooling of a mechanical mode. Similarly, in photon pressure-based systems, thermal decoherence poses a significant challenge to accessing the full quantum behaviour of photons with sub-gigahertz frequencies. Nonetheless, sideband cooling of a thermally excited RF circuit has been successfully demonstrated using a microwave cavity [96].

Assuming a drive detuning set to the second lower sideband, we derived the Hamiltonian in Eq. (7.10), which captures the resonant interaction governing the dynamics of the fluctuations. This interaction describes how photons from the pump upward-scatter to the resonance frequency of the HF circuit, ω_0, while removing two photons from the RF circuit. This energy extraction results in backaction cooling of the low-frequency mode through a two-photon mechanism such as described for an optomechanical system in the work by A. Nunnenkamp *et al.* [213].

Finding the average occupation of the RF requires solving terms involving two operators, such as $\hat{d}\hat{b}^\dagger$, as we see in Eq. (7.15). Due to the non-quadratic Hamiltonian and therefore nonlinear dynamics as shown in the last section, the treatment of the equations of motion of terms involving two or more operators requires special attention. The above is because the commutativity of the operators does not ensure equivalent equations of motion of their product in systems with nonlinear interactions[1]. This arises from the interaction Hamiltonian, which despite the commutation relation of the operators in question, can lead to distinct evolution. Hence, to guarantee a correct treatment of their dynamics, it is fundamental to respect the right ordering of the operators in the Langevin equation.

To derive the average occupation of the RF mode, we use the equation of motion given by Eqs. (7.11)-(7.15). We will first calculate the dynamics of the induced processes in Eq. (7.15). Hence, using the product rule, we find

$$\begin{aligned}\frac{d}{dt}\hat{d}\hat{b}^{2\dagger} = &\left[i\left(\Delta + 2\omega_m\right) - \frac{1}{2}\left(\kappa + 2\gamma\right)\right]\hat{d}\hat{b}^{2\dagger} - iG_2\hat{b}^\dagger\hat{b}^\dagger\hat{b}\hat{b} \\ &+ 4iG_2\hat{n}_{\rm HF}\left[\hat{n}_{\rm RF} + \frac{1}{2}\right] - \sqrt{\kappa}\hat{d}_{\rm in}\hat{b}^\dagger\hat{b}^\dagger - 2\sqrt{\gamma}\hat{d}\hat{b}_{\rm in}^\dagger\hat{b}^\dagger.\end{aligned} \tag{7.17}$$

Given the high decay rate of the HF mode, we can approximate Eq. (7.12) by its steady state solution, which is expressed as follows:

$$\hat{n}_{\rm HF} = -\frac{iG_2}{\kappa}\left(\hat{d}^\dagger\hat{b}^2 - \hat{d}\hat{b}^{\dagger 2}\right) - \frac{\sqrt{\kappa}}{\kappa}\left(\hat{d}_{\rm in}^\dagger\hat{d} + \hat{d}^\dagger\hat{d}_{\rm in}\right), \tag{7.18}$$

[1] Mathematically this can be summarized as given two arbitrary bosonic operators $\hat{u}$ and $\hat{v}$

$$[\hat{u},\hat{v}] = 0 \implies \frac{d}{dt}\hat{u}\hat{v} = \frac{d}{dt}\hat{v}\hat{u} \wedge \left[\hat{u}\hat{v},\hat{\mathcal{H}}\right] = \left[\hat{v}\hat{u},\hat{\mathcal{H}}\right] \tag{7.16}$$

for a nonlinear Hamiltonian $\hat{\mathcal{H}}$.

and similarly for the RF mode

$$\hat{n}_{\mathrm{RF}} = \frac{2iG_2}{\Gamma}\left(\hat{d}^\dagger\hat{b}^2 - \hat{d}\hat{b}^{\dagger 2}\right) - \frac{\sqrt{\Gamma}}{\Gamma}\left(\hat{b}_{\mathrm{in}}^\dagger\hat{b} + \hat{b}^\dagger\hat{b}_{\mathrm{in}}\right). \tag{7.19}$$

These equations can be combined, allowing us to express Eq. (7.18) in terms of $\hat{n}_{\mathrm{RF}}$, namely

$$\hat{n}_{\mathrm{HF}} = -\frac{1}{2\kappa}\left(\Gamma\hat{n}_{\mathrm{RF}} + \sqrt{\Gamma}\left[\hat{b}_{\mathrm{in}}^\dagger\hat{b} + \hat{b}^\dagger\hat{b}_{\mathrm{in}}\right]\right) - \frac{1}{\sqrt{\kappa}}\left(\hat{d}_{\mathrm{in}}^\dagger\hat{d} + \hat{d}^\dagger\hat{d}_{\mathrm{in}}\right). \tag{7.20}$$

Our goal is to find the average occupation of the RF mode, which we will onwards denote as $\langle\hat{n}_{\mathrm{RF}}\rangle \equiv n_{\mathrm{RF}}^{\mathrm{cool}}$. For this, we must calculate the expectation value of Eq. (7.17). However, due to the nonlinearity of the system dynamics, the analysis of the evolution of terms like $\langle\hat{d}\hat{b}^{2\dagger}\rangle$ demands knowledge of higher order moments such as $\langle\hat{b}^{2\dagger}\hat{b}^2\rangle$ as we see in Eq. (7.17), leading to an infinite hierarchy of equations. Therefore, to enable a manageable analytical study, we truncate these equations in an appropriate order. For this we assume the state remains Gaussian at all times and apply the *Gaussian state approximation* (GSA), allowing all higher-order moments to factorize into products of first- and second-order moments [217–219]. Given an initial Gaussian state, this approximation holds since $g_2 \ll \kappa$ and $\bar{n}_{\mathrm{HF}}^T \approx 0$, ensuring the Gaussianity of the state even though the Hamiltonian in Eq. (7.3) governing the dynamics is non-quadratic. Hence, within the GSA and using Wick's theorem [220] we find that higher moments factorize accordingly to, for instance

$$\langle\hat{b}^{2\dagger}\hat{b}^2\rangle \approx \langle\hat{b}^{2\dagger}\rangle\langle\hat{b}^2\rangle + 2(n_{\mathrm{RF}}^{\mathrm{cool}})^2, \qquad \langle\hat{n}_{\mathrm{RF}}^2\rangle \approx 2(n_{\mathrm{RF}}^{\mathrm{cool}})^2 + n_{\mathrm{RF}}^{\mathrm{cool}} + \langle\hat{b}^{2\dagger}\rangle\langle\hat{b}^2\rangle. \tag{7.21}$$

Notably, the expectation value $\langle\hat{b}^{2\dagger}\hat{b}^2\rangle$ is proportional to the *second-order correlation function* $g^{(2)}(0) = \langle\hat{b}^{2\dagger}\hat{b}^2\rangle/\langle\hat{b}^\dagger\hat{b}\rangle^2$, which is fundamental for the characterization of the system's state [192]. It allows therefore to distinguish between classical and quantum states in the following way: $g^{(2)}(0) = 1$, $g^{(2)}(0) > 1$ or $g^{(2)}(0) < 1$ are associated to coherent, thermal or non-classical states, respectively.

The multiplication of Eq. (7.20) from the right by $\hat{n}_{\mathrm{RF}}$ gives us precisely the third term in Eq. (7.17), which reads

$$\langle\hat{n}_{\mathrm{HF}}\hat{n}_{\mathrm{RF}}\rangle = -\frac{1}{2\kappa}\left(\Gamma\langle\hat{n}_{\mathrm{RF}}^2\rangle + \sqrt{\Gamma}\left\langle\left(\hat{b}_{\mathrm{in}}^\dagger\hat{b} + \hat{b}^\dagger\hat{b}_{\mathrm{in}}\right)\hat{n}_{\mathrm{RF}}\right\rangle\right) - \frac{1}{\sqrt{\kappa}}\left\langle\left(\hat{d}_{\mathrm{in}}^\dagger\hat{d} + \hat{d}^\dagger\hat{d}_{\mathrm{in}}\right)\hat{n}_{\mathrm{RF}}\right\rangle. \tag{7.22}$$

To proceed we need to find an expression for $\langle\hat{n}_{\mathrm{RF}}^2\rangle$, which appears on the last equation. Using the relations obtained in Eq. (7.21) and recalling that the variance of a thermal state satisfies

$$\langle\hat{n}_{\mathrm{RF}}^2\rangle - \langle\hat{n}_{\mathrm{RF}}\rangle^2 = n_{\mathrm{RF}}^{\mathrm{cool}} + \left(n_{\mathrm{RF}}^{\mathrm{cool}}\right)^2, \tag{7.23}$$

this term can be expressed as follows

$$\langle\hat{n}_{\mathrm{RF}}^2\rangle = 2\left(n_{\mathrm{RF}}^{\mathrm{cool}}\right)^2 + n_{\mathrm{RF}}^{\mathrm{cool}}. \tag{7.24}$$

In addition, the expectation value of the last terms in Eq. (7.22) can be calculated within the input-output formalism [39, 44]. Noticing that the last term is zero, since we are assuming zero thermal occupation for the HF mode, $\bar{n}_{\mathrm{HF}}^T \approx 0$, then the only terms remaining are those involving the RF mode noise operators:

$$\sqrt{\Gamma}\langle\left[\hat{b}_{\mathrm{in}}^\dagger\hat{b} + \hat{b}^\dagger\hat{b}_{\mathrm{in}}\right]\hat{n}_{\mathrm{RF}}\rangle = -2\Gamma\left[n_{\mathrm{RF}}^{\mathrm{cool}}\bar{n}_{\mathrm{RF}}^T + \frac{1}{4}\left(n_{\mathrm{RF}}^{\mathrm{cool}} + \bar{n}_{\mathrm{RF}}^T\right)\right]. \tag{7.25}$$

Using these results into Eq. (7.22), we find

$$\langle\hat{n}_{\mathrm{HF}}\hat{n}_{\mathrm{RF}}\rangle = \frac{\Gamma}{2\kappa}\left(2\left[n_{\mathrm{RF}}^{\mathrm{cool}}\bar{n}_{\mathrm{RF}}^T + \frac{1}{4}\left(n_{\mathrm{RF}}^{\mathrm{cool}} + \bar{n}_{\mathrm{RF}}^T\right)\right] - \left[2\left(n_{\mathrm{RF}}^{\mathrm{cool}}\right)^2 + n_{\mathrm{RF}}^{\mathrm{cool}}\right]\right), \tag{7.26}$$

which combined with Eq. (7.20) leads to

$$\langle \hat{n}_{\mathrm{HF}} \hat{n}_{\mathrm{RF}} \rangle + \frac{1}{2} \langle \hat{n}_{\mathrm{HF}} \rangle = -\frac{\Gamma}{2\kappa} \left[n_{\mathrm{RF}}^{\mathrm{cool}} - \bar{n}_{\mathrm{RF}}^{T} \right] \left[2 n_{\mathrm{RF}}^{\mathrm{cool}} + 1 \right]. \tag{7.27}$$

From Eq. (7.15), we observe that in the absence of the photon pressure interaction ($G_2 = 0$), the average occupation of the RF mode would simply correspond to its thermal occupation, $n_{\mathrm{RF}}^{\mathrm{cool}} \approx \bar{n}_{\mathrm{RF}}^{T}$. Up to this point, the GSA has allowed us to obtain a closed system of equations, enabling us to study the dynamics of Eq. (7.17), which are crucial for understanding the cooling of the RF mode as we will see below.

The substitution of Eq. (7.27) let us find the the steady state solution of Eq. (7.17), namely

$$\langle \hat{d}\hat{b}^{2\dagger} \rangle = -\frac{2iG_2\Gamma}{\kappa} \mathcal{X}_q[0] \left\{ 2 \left[1 + \frac{\kappa}{2\Gamma} \right] (n_{\mathrm{RF}}^{\mathrm{cool}})^2 + \left[1 - 2\bar{n}_{\mathrm{RF}}^{T} \right] n_{\mathrm{RF}}^{\mathrm{cool}} - n_{\mathrm{RF}}^{T} \right\}, \tag{7.28}$$

where we used Eq. (7.21) and introduced the susceptibility $\mathcal{X}_q^{-1}[0] = -i\left(\Delta + 2\Omega_0\right) + \left(\kappa + 2\Gamma\right)/2$. Finally, this result can be plugged into the steady-state solution of Eq. (7.15), which reads

$$-2iG_2 \left(\langle \hat{d}^\dagger \hat{b}^2 \rangle - \langle \hat{d}\hat{b}^{2\dagger} \rangle \right) + \Gamma n_{\mathrm{RF}}^{\mathrm{cool}} - \Gamma \bar{n}_{\mathrm{RF}}^{T} = 0, \tag{7.29}$$

allowing us to find the following quadratic equation for the average occupation of the RF mode

$$\Gamma_q \left\{ 2 \left[1 + \frac{\kappa}{2\Gamma} \right] (n_{\mathrm{RF}}^{\mathrm{cool}})^2 + \left[1 - 2\bar{n}_{\mathrm{RF}}^{T} \right] n_{\mathrm{RF}}^{\mathrm{cool}} - n_{\mathrm{RF}}^{T} \right\} + \kappa n_{\mathrm{RF}}^{\mathrm{cool}} - \kappa \bar{n}_{\mathrm{RF}}^{T} = 0. \tag{7.30}$$

with the induced damping rate given by $\Gamma_q \equiv 4G_2^2 \left(\mathcal{X}_q[0] + \mathcal{X}_q^*[0] \right)$.

In this section, we have used the equation of motion derived in Sec. 7.2 to obtain an analytical expression describing the average occupation of the low-frequency circuit. To accomplish this we employed the GSA which allowed us to truncate the nonlinear equations of motion, resulting in a closed system described by second-order moments. Finally, solving the system of equations led us to the steady state solution given in Eq. (7.30), where the photon-pressure-induced damping for $\Delta = -2\Omega_0$ reads $\Gamma_q = 4G_2^2(\kappa + 2\Gamma)^{-1}$. Fig. 7.3 shows a great agreement of the analytical results with the numerical simulation using Qutip [221] for the low-frequency mode initially at $\bar{n}_{\mathrm{RF}}^{T} = 5$.

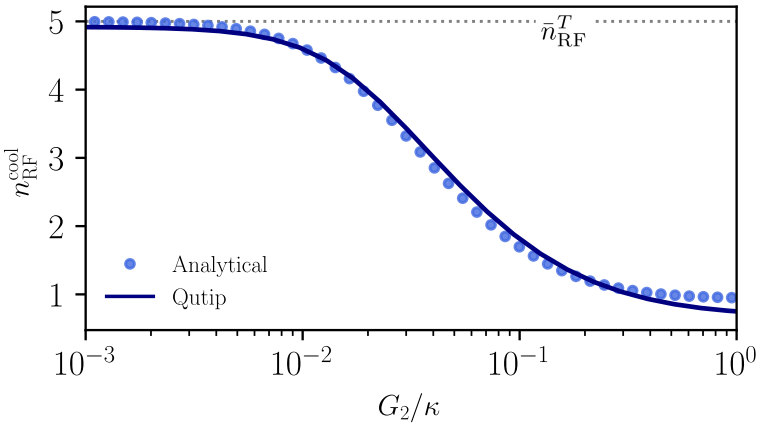

FIGURE 7.3: Two-photon cooling of the RF mode as a function of the multiphoton coupling strength. The solid line depicts the numerical simulation using Qutip [221]. The circles show the analytical solution obtained within the GSA using Eq. (7.30). For this plot $\Omega_0/2\pi = 450.6$ MHz, $\Gamma/2\pi = 30$ kHz, $\kappa/2\pi = 400$ kHz, $g_2/2\pi = 3.6$ kHz and $\bar{n}_{\mathrm{RF}}^{T} = 5$.

In the next section, we will demonstrate that the system described by the Hamiltonian in Eq. (7.10) leads to OMIT through a two-photon process.

7.4 Optomechanically induced transparency

In Sec. 3.9, we introduced OMIT, an effect analogous to EIT, observed in optomechanical systems. OMIT describes the emergence of a transparency window in the probe field resulting from the interaction between the optical and mechanical modes via radiation pressure in the presence of a strong control field. This phenomenon occurs when a control optical beam, tuned to a sideband transition of the optomechanical system, interferes destructively with the intracavity probe field, reducing or canceling the intensity of the probe, as shown in Fig. 7.4.

OMIT has also been shown to arise through a two-photon process in quadratically coupled systems [222], such as in membrane-in-the-middle configurations. In such systems, the anti-Stokes process describes the upward scattering of two phonons, whereas the mean displacement and momentum of the mechanical mode are both zero due to the symmetry of the intracavity field. Thus, the modulation of the cavity field arises from $\langle \hat{x}^2 \rangle$.

Recently, OMIT experiments have been conducted in photon pressure-based optomechanical systems to extract the single-photon coupling rate [140]. In this section, we will demonstrate the appearance of a transparency window resulting from the photon pressure interaction described by the Hamiltonian in Eq. (7.10). This setup provides a fully superconducting and highly tunable platform to study OMIT through two-photon processes. Furthermore, it enables the analysis of the RF mode's response to injected noise while performing the OMIT measurement.

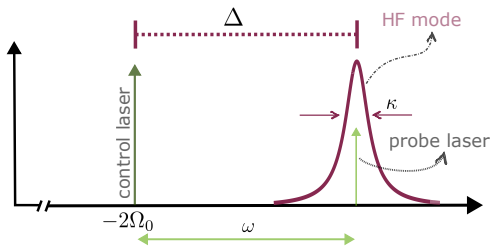

FIGURE 7.4: Schematic of the two-photon OMIT-like experiment via a photon-pressure-based interaction. A strong control field drives the HF mode at the second lower sideband. A second weak probe tone scans around the cavity's resonant frequency. The resulting destructive interference of the second sideband with the probe field leads to the emergence of the transparency window.

As shown in Fig. 7.4, the HF mode is driven by the probe tone, whose Hamiltonian reads

$$\hat{\mathcal{H}}_{\text{probe}} = -i\sqrt{\eta\kappa}\left(\alpha_p \hat{a}^\dagger e^{-i\omega_p t} - \alpha_p^* \hat{a} e^{+i\omega_p t}\right), \tag{7.31}$$

where $\alpha_p = e^{i\phi_p}\sqrt{P_{\text{probe}}/\omega_p}$ is the normalized amplitude with P_{probe}, ω_p and ϕ_p the probe's power, frequency and phase, respectively. Here, the total loss rate consist of $\kappa = \kappa_{\text{int}} + \kappa_{\text{ext}}$, where κ_{int} is related to the internal losses, whereas κ_{ext} determines the coupling to the external port. Ultimately, $\eta = \kappa_{\text{ext}}/\kappa$ is a dimensionless coupling parameter which can be experimentally tuned. Similarly, the strong control field will be characterized by

$$\hat{\mathcal{H}}_{\text{control}} = -i\sqrt{\eta\kappa}\left(\alpha_c \hat{a}^\dagger e^{-i\omega_c t} - \alpha_c^* \hat{a} e^{+i\omega_c t}\right) \tag{7.32}$$

with $\alpha_p = e^{i\phi_c}\sqrt{P_{\text{control}}/\omega_c}$. Considering these two tones, the total drive in Eq. (7.3) will be described by the sum of the probe and control fields, i.e. $\hat{\mathcal{H}}_d = \hat{\mathcal{H}}_{\text{probe}} + \hat{\mathcal{H}}_{\text{control}}$.

Since the probe field is much weaker than the control, it is the control field that provides the steady state solution $\langle \hat{a} \rangle$ of the system. In contrast, the probe field can be treated as the perturbation around the steady state solution. Thus, in the presence of both control and probe fields, the dynamics of the HF mode in Eq. (7.11) become

$$\frac{d}{dt}\hat{d} = \left(i\Delta - \frac{\kappa}{2}\right)\hat{d} - iG_2\hat{b}^2 - \sqrt{\eta\kappa}\alpha_p e^{-i\delta t}, \tag{7.33}$$

with the detuning $\Delta = \omega_c - \omega_0$ and $\delta = \omega_p - \omega_c$.

The solution of Eq. (7.33) and therefore the analysis of the HF circuit's response, requires the knowledge of the dynamics of $\hat{b}^2$, given in Eq. (7.14). This consists of a nonlinear system of equations, such that its analytical solution demands an approximation.

As mentioned above, the probe field can be thought of as a perturbation around the steady state related to the strong control field. Therefore, the presence of the probe field leads to non-zero average fluctuations, i.e. $\langle \hat{d} \rangle \neq 0$. Therefore, we find

$$\frac{d}{dt}\langle \hat{d} \rangle = \left(i\Delta - \frac{\kappa}{2} \right) \langle \hat{d} \rangle - iG_2 \langle \hat{b}^2 \rangle - \sqrt{\eta\kappa}\alpha_p e^{-i\delta t}, \tag{7.34}$$

which is coupled to the equation of motion of the expectation value of Eq. (7.14):

$$\frac{d}{dt}\langle \hat{b}^2 \rangle = -2 \left(i\Omega_0 + \frac{\Gamma}{2} \right) \langle \hat{b}^2 \rangle - 4iG_2 \langle \hat{d} \left(\hat{n}_{\mathrm{RF}} + \frac{1}{2} \right) \rangle, \tag{7.35}$$

where we used that $\langle \hat{b}\hat{b}_{\mathrm{in}} \rangle \approx 0$ for a weak enough coupling. This is true for the parameter regime in which the experiment is conducted with $g_2/\kappa \approx 0.008$. The last term of Eq. (7.35) leads to an infinite number of coupled equations. Below, we will take two different approaches to derive an analytical expression of the transmission of the probe, that are linked to the assumption of the system's correlations.

7.4.1 Semiclassical approach: mean field approximation

The *semiclassical*, also known as the *mean-field approximation*, is a widely used technique in quantum optics and many-body physics. It involves decoupling correlations between observables, approximating the expectation value of a product of operators as the product of their individual expectation values, i.e. $\langle \hat{\mathcal{A}}\hat{\mathcal{B}} \rangle \approx \langle \hat{\mathcal{A}} \rangle \langle \hat{\mathcal{B}} \rangle$. To illustrate this, we assume that these operators can be expressed as $\hat{\mathcal{O}} = \langle \hat{\mathcal{O}} \rangle + \delta\hat{\mathcal{O}}$ for $\hat{\mathcal{O}} = \hat{\mathcal{A}}, \hat{\mathcal{B}}$, where the first term is a classical component and the second represents the fluctuations around it. Hence, we can write

$$\langle \hat{\mathcal{A}}\hat{\mathcal{B}} \rangle = \langle \left[\langle \hat{\mathcal{A}} \rangle + \delta\hat{\mathcal{A}} \right] \left[\langle \hat{\mathcal{B}} \rangle + \delta\hat{\mathcal{B}} \right] \rangle = \left\langle \langle \hat{\mathcal{A}} \rangle \langle \hat{\mathcal{B}} \rangle + \underbrace{\langle \hat{\mathcal{A}} \rangle \, \delta\hat{\mathcal{B}} + \delta\hat{\mathcal{A}} \langle \hat{\mathcal{B}} \rangle + \delta\hat{\mathcal{A}}\delta\hat{\mathcal{B}}}_{\text{fluctuations}} \right\rangle \approx \langle \hat{\mathcal{A}} \rangle \langle \hat{\mathcal{B}} \rangle, \tag{7.36}$$

where the approximation results from assuming the fluctuations to be small compared to the classical components. In optomechanics, this assumption is generally valid for strongly driven systems operating far from instability, where fluctuations can be enhanced [80].

Using the approximation given in Eq. (7.36) we write $\langle \hat{d}\hat{n}_{\mathrm{RF}} \rangle \approx \langle \hat{d} \rangle n_{\mathrm{RF}}^{\mathrm{cool}}$, with $n_{\mathrm{RF}}^{\mathrm{cool}}$ given by the analytical solution in Eq. (7.30). This allows us to express Eq. (7.35) as

$$\frac{d}{dt}\langle \hat{b}^2 \rangle \approx -2 \left(i\Omega_0 + \frac{\Gamma}{2} \right) \langle \hat{b}^2 \rangle - 2iG_2 \langle \hat{d} \rangle \left(2\bar{n}_{\mathrm{RF}}^{\mathrm{cool}} + 1 \right), \tag{7.37}$$

where we neglected higher-order processes based on the weak coupling assumption. This equation can be transformed into frequency space using the Fourier transform defined in Eq. (3.106) resulting in

$$\langle \hat{b}^2[\omega] \rangle = -4iG_2 \mathcal{X}_{\mathrm{bb}}[\omega] \left(\bar{n}_{\mathrm{RF}}^{T} + \frac{1}{2} \right) \langle \hat{d}[\omega] \rangle \tag{7.38}$$

where we introduced the susceptibility $\mathcal{X}_{\mathrm{bb}}^{-1}[\omega] = -i\left(\omega - 2\Omega_0\right) + \Gamma$.

With the solution given in Eq. (7.38) we are finally in a position to find an expression for the effective dynamics of $\langle \hat{d} \rangle$. Taking the expectation value of Eq. (7.11) and moving to the Fourier space we find $\langle \hat{d}[\omega] \rangle = -\sqrt{\eta\kappa}\mathcal{X}_{\mathrm{c}}^{\mathrm{sc}}[\omega]\alpha_p e^{-i\delta t}$, where the modified cavity susceptibility is given by

$$\mathcal{X}_{\mathrm{c}}^{\mathrm{sc}}[\omega] = \frac{1}{-i\left(\omega + \Delta\right) + \frac{\kappa}{2} + 4G_2^2 \mathcal{X}_{bb}[\omega] \left(\bar{n}_{\mathrm{RF}}^{T} + \frac{1}{2} \right)} \tag{7.39}$$

with the susceptibility introduced for Eq. (7.38). Due to the dependence on the thermal

occupation of the RF mode, this equation indicates the ability to introduce noise to the low-frequency circuit, which will lead to a modification of the HF circuit response to the probe field.

So far, the derivation of the last equation is based on the semiclassical approximation Eq. (7.36), which discards possible correlations between the modes by assuming small fluctuations.

Next, we will take a different approach starting with Eq. (7.14), in which we do consider possible correlations, which might be encoded in the effective dynamics of $\langle \hat{d}\hat{n}_{\mathrm{RF}} \rangle$.

7.4.2 Beyond the semiclassical approximation

To arrive at the result given in Eq. (7.39) we assumed small fluctuations under the so-called mean-field approximation in Eq. (7.36). Additionally, within the weak coupling assumption, we also neglected higher-order terms resulting in Eq. (7.37).

Solving Eq. (7.35) is fundamental to understanding the cavity response. In contrast to the analysis done in Sec. 7.4.1, in this section, we will not employ the semiclassical approximation given in Eq. (7.36), but consider the dynamics of the product $\langle \hat{d}\hat{n}_{\mathrm{RF}} \rangle$. This translates into the consideration of possible correlations within the system. The quantum Langevin equation describing the dynamics of the product of these operators read

$$\begin{aligned} \frac{d}{dt}\langle \hat{d}\hat{n}_{\mathrm{RF}} \rangle = \left(i\Delta - \frac{\kappa + 2\Gamma}{2} \right) \langle \hat{d}\hat{n}_{\mathrm{RF}} \rangle - iG_2 \underbrace{\left\langle \hat{b}^\dagger \hat{b}^3 + 2\hat{d}^2 \hat{b}^{2\dagger} - 2\hat{d}^\dagger \hat{d}\hat{b}^2 \right\rangle}_{\text{higher-order moments}} \\ - \sqrt{\kappa_{\mathrm{ext}}} \langle \hat{d}_{\mathrm{in}} \rangle n_{\mathrm{RF}}^{\mathrm{cool}} + \Gamma \bar{n}_{\mathrm{RF}}^{T} \langle \hat{d} \rangle. \end{aligned} \tag{7.40}$$

In Sec. 7.3, we used the GSA to truncate the equations of motion, assuming the system's state remains Gaussian throughout its evolution. However, in this case, the introduction of the probe field could result in non-Gaussian dynamics and correlations between the modes due to the nonlinear interaction. Nevertheless, the higher-order terms in the final equation, being proportional to G_2, will scale as G_2^3 in the dynamics of $\langle \hat{d} \rangle$. Therefore, under the weak coupling assumption, these terms can be neglected, leading to the following equation:

$$\frac{d}{dt}\langle \hat{d}\hat{n}_{\mathrm{RF}} \rangle \approx \left(i\Delta - \frac{\kappa + 2\Gamma}{2} \right) \langle \hat{d}\hat{n}_{\mathrm{RF}} \rangle - \sqrt{\kappa_{\mathrm{ext}}} \langle \hat{d}_{\mathrm{in}} \rangle n_{\mathrm{RF}}^{\mathrm{cool}} + \Gamma \bar{n}_{\mathrm{RF}}^{T} \langle \hat{d} \rangle. \tag{7.41}$$

The last result allows us to solve the system of Eqs. (7.34), (7.35) and (7.41) in the frequency domain, yielding $\langle \hat{d}[\omega] \rangle = -\sqrt{\eta\kappa}\mathcal{X}_{\mathrm{c}}^{\mathrm{cr}}[\omega]\alpha_p e^{-i\delta t}$ with the effective susceptibility

$$\mathcal{X}_{\mathrm{c}}^{\mathrm{cr}}[\omega] = \frac{1 - 4G_2^2 \mathcal{X}_{\mathrm{bb}}[\omega]\mathcal{X}_{\mathrm{d,rf}}[\omega] n_{\mathrm{RF}}^{\mathrm{cool}}}{-i(\omega + \Delta) + \frac{\kappa}{2} + 4G_2^2 \mathcal{X}_{\mathrm{bb}}[\omega] \left(\mathcal{X}_{\mathrm{d,rf}}[\omega]\, \Gamma \bar{n}_{\mathrm{RF}}^{T} + \frac{1}{2} \right)}, \tag{7.42}$$

with $\mathcal{X}_{\mathrm{d,rf}}^{-1}[\omega] = -i(\omega + \Delta) + (\kappa + 2\Gamma)/2$.

Finally, in the next section, we will compare these two approaches and study the cavity response under certain parameters.

7.4.3 Cavity response

Up to this point, we have used two approaches to analyze the cavity's response. First, we employed the semiclassical approximation given in Eq. (7.36), neglecting possible system correlations. This initial method led us to the effective susceptibility given in Eq. (7.39). Contrary, our second approach did indeed consider possible correlations, thereby analyzing the equations of motion of the average of two operators, yielding the effective susceptibility given in Eq. (7.42).

To analyze the response of the cavity to the probe tone we use the input-output relation given in Eq. (2.50), which results in an expression that describes the linearized cavity response given below

$$\mathcal{S}_{11}[\omega] = 1 - \kappa_{\mathrm{ext}} \widetilde{\mathcal{X}}_{\mathrm{c}}[\omega], \tag{7.43}$$

with the modified susceptibility $\widetilde{\mathcal{X}}_c[\omega]$, which could be either $\mathcal{X}_c^{sc}[\omega]$ or $\mathcal{X}_c^{cr}[\omega]$ given by Eq. (7.39) or Eq. (7.42), respectively.

Two-photon induced OMIT has been already demonstrated within experimentally feasible coupling strengths in the standard optomechanical Hamiltonian given in Eq. (3.52) [223]. Here, we show, in a superconducting-based platform, that the two-photon resonance processes arise from the quadratic interaction when the system is strongly driven at the second lower sideband. Fig. 7.5 illustrates the cavity response as a function of probe detuning for different coupling strengths. Based on similar parameters as those used in [223], our semiclassical result, characterized by the cavity susceptibility in Eq. (7.39), shows great agreement with numerical simulations. Notably, even at a strong coupling strength of $g_2/\kappa = 0.5$, the semiclassical approach accurately captures the system's behaviour. In contrast, for $g_2/\kappa > 0.24$, we show that the first-order optomechanical interaction (see [223]) fails to match the numerical results, particularly when the probe is at the cavity frequency ($\Delta_{\text{probe}} = 0$). This illustrates that for $\Delta = -2\Omega_0$ and at high coupling strengths, nonlinear effects arise predominantly from the second-order interaction terms and not solely from the usually neglected nonlinear term given by the last term in Eq. (3.75).

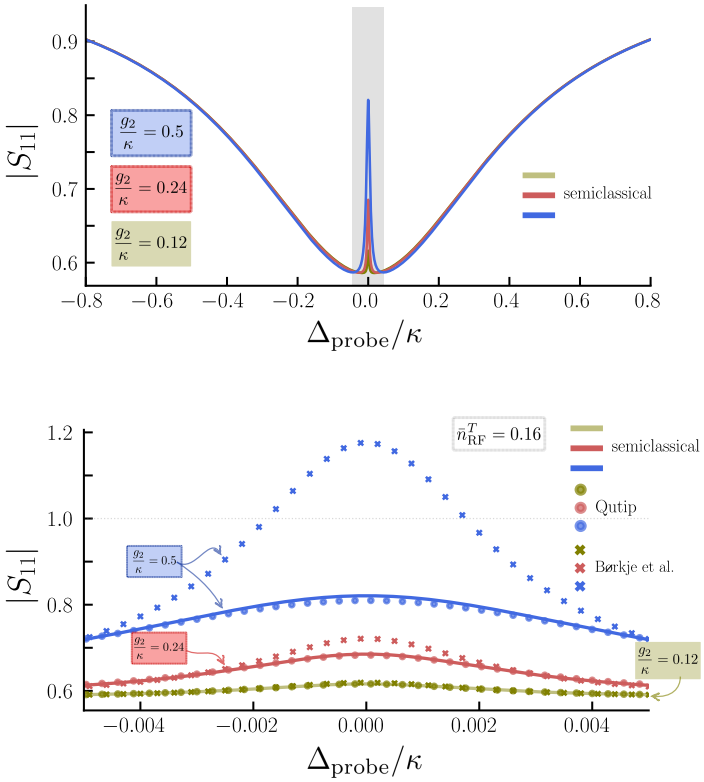

FIGURE 7.5: HF cavity response as a function of the probe detuning for different photon-pressure coupling strengths. The transparency window is marked by the grey-shaded area in the upper plot and shown in the lower plot for probe frequencies close to resonance. The circles in the lower plot show the numerical simulation using Qutip, solid lines show the result using the semiclassical approximation and the crosses the theory derived in K. Børkje *et al.* [223]. Contrary to the model used in [223], our semiclassical solution agrees well even for larger coupling strength with the numerical simulation. For this result we use $\bar{n}_{\text{RF}}^T = 0.16$, $\omega_m/2\pi = 1$ MHz, $\kappa = 0.1\omega_m$ and $\Gamma = 0.66$ Hz.

As shown in Fig. 7.5, the discrepancy between the results obtained using the Hamiltonian in Eq. (3.48) and the simulation becomes more pronounced near the resonant condition. This suggests an enhancement of nonlinear effects when the probe is resonant with the cavity. Therefore, in Fig. 7.6, we analyze the influence of these effects by comparing two approaches: the semiclassical result from Eq. (7.39) and the correlation-based result described by Eq. (7.42). We show that the amplitude of the transparency window is better captured by the correlation-inclusive result. This demonstrates that under resonant conditions, nonlinear effects are amplified, leading to larger fluctuations, which are better described by the

correlation-based approach in Eq. (7.42).

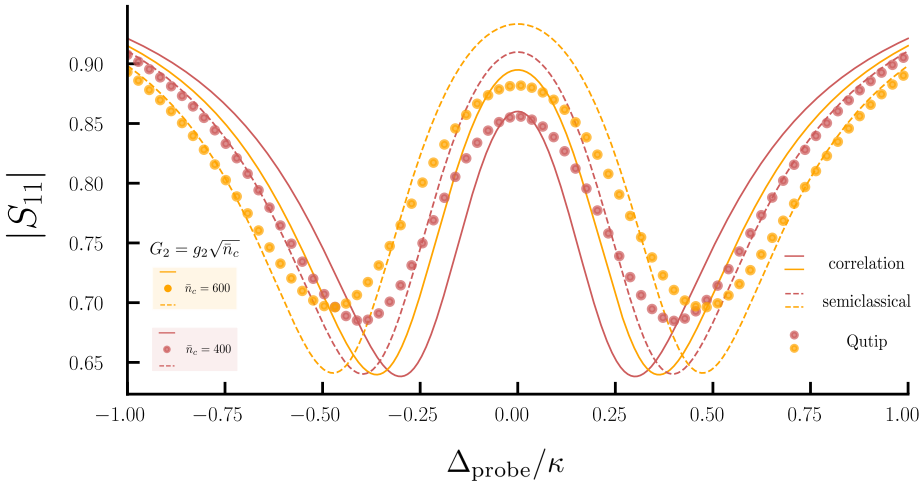

FIGURE 7.6: HF cavity response as a function of the probe detuning for different multiphoton coupling strengths $G_2 = g_2\sqrt{\bar{n}_c}$. The dashed lines show the result obtained using the semiclassical approximation, while solid lines describe the solution that considers possible correlations. These results are compared with the numerical simulation shown in circles. When the cavity is on resonance with the cavity ($\Delta = 0$) nonlinear effects are more pronounced, which are better captured beyond the semiclassical approximation. This effect is more significant as the effective coupling strength increases. Further away from the resonance condition, the semiclassical accurately describes the numerical results. For this plot $\Omega_0/2\pi = 450.6$ MHz, $\Gamma/2\pi = 30$ kHz, $\kappa/2\pi = 400$ kHz, $g_2/2\pi = 0.01$ kHz and $\bar{n}^T_{\text{RF}} = 1$.

Moreover, in Fig. 7.7, we present the effect of noise injection, i.e. larger $\bar{n}^T_{\text{RF}}$, through the RF circuit on the HF cavity's response as a function of probe detuning. For a fixed photon-pressure coupling strength of $G_2/\kappa = 0.09$, the semiclassical solution shows better agreement with the results than Eq. (7.42), particularly as more noise is introduced into the system. This holds even at zero detuning, where one would typically expect enhanced nonlinear effects due to the resonance condition. This suggests that at the given coupling strength, increased thermal noise diminishes quantum fluctuations.

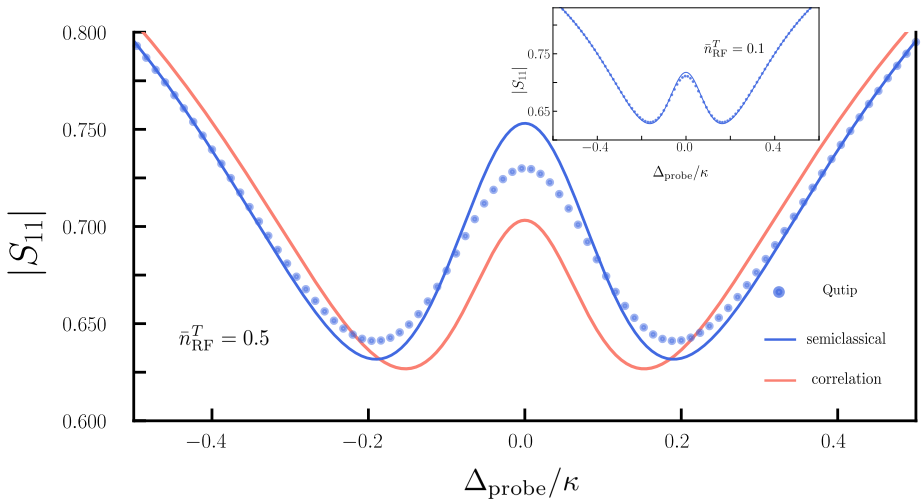

(A) For $\bar{n}^T_{\mathrm{RF}} = 0.5$, the correlation-based solution (solid red) does not match the numerical results. The inset highlights the great agreement of the semiclassical solution for lower noise injection $\bar{n}^T_{\mathrm{RF}} = 0.1$.

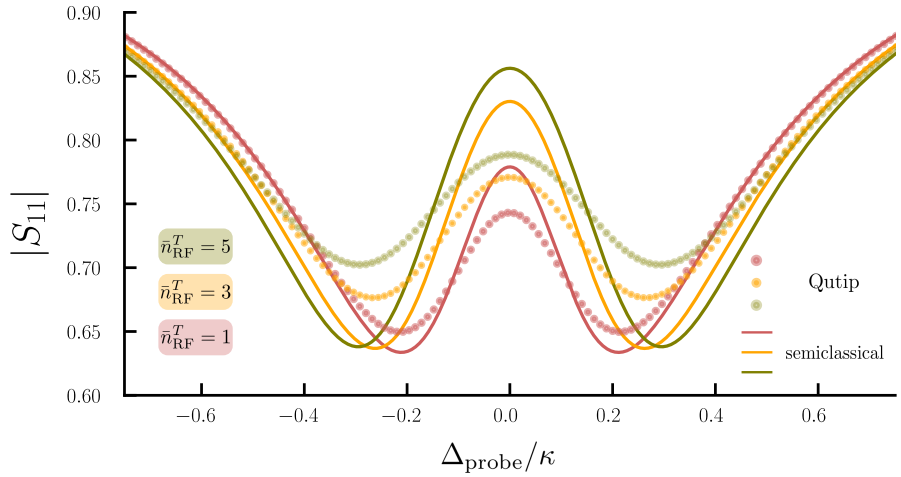

(B) Increased noise injection leads to a worsening of the analytical results, especially around the cavity resonance.

FIGURE 7.7: Effect of noise injection on the HF cavity response as a function of probe detuning for fixed coupling strength $G_2/\kappa = 0.09$. Circles represent the numerical simulation, while the solid lines correspond to the semiclassical approximation. Under noisy conditions and at this weak coupling strength, the semiclassical solution provides a more accurate approach. For this plot $\Omega_0/2\pi = 450.6$ MHz, $\Gamma/2\pi = 30$ kHz, $\kappa/2\pi = 400$ kHz.

In this chapter, we studied the quadratic coupling in an artificial optomechanical system that consists of a fully superconducting-based platform, describing the photon-pressure interaction between high- and low-frequency LC circuits. When the HF circuit is driven on the second lower sideband ($\Delta = -2\Omega_0$), we demonstrated that this interaction leads to a resonant two-photon cooling process, as described by the effective Hamiltonian in Eq. (7.10). By assuming that the system's state remains Gaussian at all times for weak coupling strengths, we derived an analytical expression for the average occupation of the RF mode. Within the resolved sideband regime, our result shows strong agreement with numerical simulations, even for multiphoton coupling $G_2 \sim \kappa$, as shown in Fig. 7.3.

Next, we demonstrated that the system leads to two-photon OMIT when a strong control field is applied at $\Delta = -2\Omega_0$ and a weak probe tone scans around the cavity's frequency. In Sec. 7.4, we analyzed the HF cavity's response to the weak probe tone using both semiclassical and correlation-based approaches. For weak coupling, the semiclassical solution showed strong agreement with numerical simulations, as depicted in Fig. 7.5. However, we noted that when the probe is resonant with the cavity frequency, nonlinear effects are enhanced, leading to increased fluctuations that the semiclassical description does not capture. In Fig.

7.6, we showed that the correlation-based result accurately describes the amplitude of the transparency window, even with increased thermal occupation and coupling strength. Lastly, in Fig. 7.7, we explored the impact of noise injection into the RF mode. The correlation-based solution failed to match the numerical simulations for higher noise and weak coupling, while the semiclassical solution correctly captured the system's behaviour, even under increased thermal occupation.

Chapter 8

Conclusions and outlook

In this work, we demonstrated that a nonlinear cavity dispersively coupled to a low-frequency mechanical oscillator leads to more efficient and enhanced dynamical backaction cooling compared to an equivalent linear system. Our results show that such an optomechanical system leverages its intrinsic cavity nonlinearity to significantly boost the optomechanical coupling, without requiring strong coupling strength or high driving power. This theoretical analysis builds on the novel experimental platform developed by D. Zoepfl *et al.* [3], which inductively couples a mechanical cantilever with a magnetic tip to a SQUID cavity. With recent advancements in magnetically coupled mechanical oscillators and superconducting circuits [22, 35, 115, 140, 179], this platform shows great promise for advancing quantum control of mechanical systems. Along with the ability to cool in the unresolved sideband regime, these systems are particularly relevant for applications involving large-scale mechanical systems, where achieving efficient cooling and precise control is critical for exploring quantum effects at macroscopic scales.

In Chapter 4, we demonstrated that embedding a SQUID into a microwave cavity makes the system sensitive to magnetic fields, which is essential for inductive coupling to a mechanical mode. Additionally, we showed that the Hamiltonian describing a superconducting circuit with a Josephson junction is equivalent to that of a Duffing oscillator. This Hamiltonian served as the foundation for analyzing a key feature of Kerr cavities: bistability. We emphasized the impact of the intracavity photon number on the dynamics of cavity fluctuations when operating near the bifurcation point. At this point, the nonlinearity induces both a slowing down of the cavity response and an enhanced asymmetry in the photon number spectrum. Finally, we highlighted how these properties make such a nonlinear cavity an ideal candidate for optomechanical cooling.

In Chapter 5, we examined the experimental setup developed by Zoepfl *et al.* [3], focusing on the enhanced backaction cooling capabilities of a SQUID cavity inductively coupled to a cantilever with a magnet on its tip. We demonstrated that this improved cooling performance stems from the asymmetric photon number spectrum characteristic of the nonlinear cavity. Consequently, the system profits from the intrinsic cavity nonlinearity to cool the low-frequency mechanical oscillator via sideband cooling, achieving more than an order of magnitude improvement over an equivalent linear system.

Furthermore, we showed that optimal cooling occurs when the cavity operates near the bifurcation point, where not only is cooling more effective, but it also requires approximately 12 times less input power than a linear setup. Additionally, in the unresolved sideband regime, the nonlinear system requires less optomechanical coupling strength to surpass the best cooling achieved by a linear cavity under the same input power conditions. Moreover, the nonlinear system outperforms the linear one in both cooling efficiency and capability, especially deeper into the unresolved sideband regime. Finally, we found that while the fundamental limits for dynamical backaction cooling are the same for both systems, the nonlinear setup reaches these limits with a drive amplitude two orders of magnitude weaker.

Loosening the experimental parameter constraints, we explored a squeezed-based protocol aimed at surpassing the cavity backaction limit, following the approach of [214]. In Chapter 6, we demonstrated that driving the nonlinear cavity with a squeezed vacuum can effectively mitigate unwanted backaction heating, allowing us to surpass the cavity backaction limit. We showed that the advantages of the nonlinear cavity lead to improved cooling performance. For the same parameters, achieving ground state cooling with a nonlinear cavity requires significantly less squeezing strength compared to a linear system, which is particularly promising

from an experimental standpoint.

Although traditionally viewed as separate challenges, we demonstrated that combining an optomechanical system in the unresolved sideband regime with an intrinsically nonlinear cavity results in superior cooling performance. This makes the nonlinear cavity an attractive platform for applications involving large, low-frequency mechanical systems.

Finally, in Chapter 7 we explored optomechanical effects in an entirely superconducting-based platform, where the absence of a mechanical element makes us refer to it as an artificial optomechanical system. Throughout this chapter, we studied the photon pressure interaction between high- and low-frequency circuits, effectively modelled by a quadratic optomechanical-like Hamiltonian. We demonstrated that, when the system is driven at the second lower sideband, this interaction enables a two-photon cooling process of the low-frequency circuit. Likewise, we derived an analytical expression that closely aligns with numerical simulations, even approaching the strong multiphoton coupling regime.

We further showed that this platform exhibits OMIT via a two-photon mechanism. Our study also revealed increased fluctuations when the probe is resonant with the cavity, a phenomenon well described by our correlation-based model. Additionally, we noted that for weak coupling and low noise injection into the low-frequency mode, the semiclassical approximation closely matches the numerical simulations. These results are significant since such platforms allow the exploration of optomechanical effects in otherwise incompatible parameter regimes.

Throughout this work, we primarily studied optomechanical systems based on superconducting quantum circuits, which due to their versatility and tunability offer great promise for quantum control of mechanical systems. Such a goal demands larger coupling strengths, which can be realized using inductively-based interactions. While we demonstrated cooling to about 200 times below the thermal occupation with our nonlinear system, the ultimate aim remains ground state cooling. Due to the limitations imposed by cavity backaction, our recent efforts explore the use of an auxiliary red-driven cavity coupled to the nonlinear optomechanical system. Alternatively, driving the nonlinear optomechanical setup with an additional second pump tone could disentangle the squeezing and cooling processes. Recent advances in coherent feedback protocols [75, 76], make it a possible alternative to boost our cooling limits and eventually reach the ground state.

Appendix A

Kerr-cavity in a squeezed basis

As explained in Chapter 6, if the cavity nonlinearity is not too strong $\Lambda < |\Delta|$ the dynamics of the nonlinear cavity given in Eq. (4.24) are equivalent to a those of linear cavity driven by a squeezed reservoir. Below, we use the *Bogoliubov transformation* to diagonalize the system and derive the spectral density of the force.

The drift matrix given in Eq. (4.25) can be diagonalized using the so-called Bogoliubov transformation. To diagonalize the system's Hamiltonian given in Eq. (4.1) we first introduce the *squeeze operator* [127, 224]

$$\hat{S}(\eta) \equiv \exp\left(\frac{1}{2}\eta^* \hat{d}^2 - \frac{1}{2}\eta \hat{d}^{2\dagger}\right), \quad \eta = re^{i\zeta}, \quad \tanh(2r) = \frac{|\Lambda|}{\tilde{\Delta}} \tag{A.1}$$

and transform the bosonic operators of the optical mode into a squeezed frame using the Baker-Hausdorff formula in Eq. (3.53). It then follows

$$\hat{d}_{\rm s} = \hat{S}^\dagger(r)\,\hat{d}\,\hat{S}(r) = \sum_{n=0}^{\infty} \frac{r^{2n}}{(2n)!}\,\hat{d} - \sum_{n=0}^{\infty} \frac{r^{(2n+1)}}{(2n+1)!}\,\hat{d}^\dagger = \cosh(r)\,\hat{d} - e^{i\zeta}\sinh(r)\,\hat{d}^\dagger, \tag{A.2}$$

where $\hat{d}_{\rm s}$ is now an operator in the squeezed frame. The last relation leads to the following transformation

$$\begin{bmatrix} \hat{d}_{\rm s} \\ \hat{d}_{\rm s}^\dagger \end{bmatrix} = \mathbf{S}(r) \begin{bmatrix} \hat{d} \\ \hat{d}^\dagger \end{bmatrix}, \quad \mathbf{S}(r) = \begin{bmatrix} \cosh(r) & -e^{i\zeta}\sinh(r) \\ -e^{-i\zeta}\sinh(r) & \cosh(r) \end{bmatrix} \tag{A.3}$$

Using the last expression we find the Hamiltonian of a driven Kerr-cavity in a squeezed frame

$$\hat{\mathcal{H}}_{\rm s} = \hat{S}^\dagger \hat{\mathcal{H}} \hat{S} = -\Delta_{\rm s} \hat{d}_{\rm s}^\dagger \hat{d}_{\rm s} \tag{A.4}$$

with the modified cavity frequency $\Delta_{\rm s} = \sqrt{\tilde{\Delta}^2 - |\Lambda|^2}$.

As shown in the work of Asjad *et al.* [176], if the nonlinearity is not too strong $|\Lambda| < |\Delta|$, the system described by Eq. (4.1) is equivalent to that of linear cavity driven by a squeezed reservoir as in the work of H. Lau and A. A. Clerk [32]. This indicates that, in the squeezed basis, the cavity noise correlators given in Eq. (3.60) become

$$\langle \hat{d}_{\rm in}^{\rm s\dagger}(t)\hat{d}_{\rm in}^{\rm s}(t')\rangle = n_{\rm s}\delta(t-t'), \quad \langle \hat{d}_{\rm in}^{\rm s}(t)\hat{d}_{\rm in}^{\rm s}(t')\rangle = m_{\rm s}e^{-i\zeta}\delta(t-t') \tag{A.5}$$

with $n_{\rm s} = \sinh^2(r)$ and $m_{\rm s} = \cosh(r)\sinh(r) = \sqrt{n_{\rm s}(n_{\rm s}+1)}$. In this new frame, the dynamics are characterized by the squeezed fluctuations, whose noise correlators are defined by the coefficients $n_{\rm s}$ and $m_{\rm s}$, which determine the number of excitations and the strength of the correlations of the input squeezed fields. Furthermore, from the definition in Eq. (A.1) and the explicit expression of the coefficients given in Eq. (A.5) we find that $\cosh(2r) = 2n_{\rm s} + 1$, which allow us to obtain the following relation

$$\tilde{\Delta} = \Delta_{\rm s}\,(2n_{\rm s}+1)\,. \tag{A.6}$$

Since we aim to obtain the Stokes and anti-Stokes rates via the force spectrum given in Eq. (3.125), we need to analyze how the radiation-pressure coupling is modified in the

squeezed frame. For this, we notice that under the Bogoliubov transformation (A.3) and a strong enough squeezing parameter, the linearized radiation pressure operator becomes

$$\hat{F}_{\rm s} \approx |G|e^{+r}\left(e^{-i\frac{\zeta}{2}}\hat{d}_{\rm s}+e^{+i\frac{\zeta}{2}}\hat{d}_{\rm s}^{\dagger}\right)\cos\left(\frac{\zeta-2\phi_{\rm c}}{2}\right). \tag{A.7}$$

From Eq. (A.5) we can rewrite the exponential as $e^{r}=\sqrt{n_{\rm s}}+\sqrt{n_{\rm s}+1}$, such that in the last equation we can identify the following relation

$$G_{\rm s}=|G|e^{i\frac{\zeta}{2}}\left(\sqrt{n_{\rm s}}+\sqrt{n_{\rm s}+1}\right). \tag{A.8}$$

Using the last equation and taking $\zeta=2\phi_{\rm c}$ then Eq. (A.7) becomes

$$\hat{F}_{\rm s} \approx \left(G_{\rm s}^{*}\hat{d}_{\rm s}+G_{\rm s}\hat{d}_{\rm s}^{\dagger}\right), \quad G_{\rm s}=G\left(\sqrt{n_{\rm s}}+\sqrt{n_{\rm s}+1}\right), \tag{A.9}$$

which has the same structure as Eq. (5.50).

From Eq. (A.4), we can deduce that the dynamics of the cavity in the squeezed frame resemble those of an empty cavity, namely

$$\hat{d}_{\rm s}[\omega]=-\sqrt{\kappa}\mathcal{X}_{\rm s}[\omega]\hat{d}_{\rm in}^{\rm s}[\omega], \tag{A.10}$$

with the susceptibility $\mathcal{X}_{\rm s}^{-1}[\omega]=-i(\omega+\Delta_{\rm s})+\kappa/2$ and the noise correlators given in Eq. (A.5). Similarly as in Eq. (6.22), with the results given above, we can compute the spectral density of the force

$$\mathcal{S}_{FF}^{\rm s}[\omega]=\frac{n_{\rm s}}{(\omega-\Delta_{\rm s})+\frac{\kappa^2}{4}}+\frac{n_{\rm s}+1}{(\omega+\Delta_{\rm s})+\frac{\kappa^2}{4}}-2m_{\rm s}\frac{\left[\Delta_{\rm s}^2-\frac{\kappa^2}{4}-\omega^2\right]\cos(4\phi_{\rm c})-\Delta_{\rm s}\kappa\sin(4\phi_c)}{\left[\frac{\kappa^2}{4}+(\omega-\Delta_{\rm s})^2\right]\left[\frac{\kappa^2}{4}+(\omega+\Delta_{\rm s})^2\right]}. \tag{A.11}$$

Recalling the Stokes and anti-Stokes rates given in Eq. (3.125), we can use the force spectrum derived in the last equation and suppress the Stokes heating process, i.e. $\mathcal{S}_{FF}^{\rm s}[-\omega_m]=0$ for a given optimal squeezing phase [31, 176]. This is done in Chapter 6 when squeezing is externally generated and injected into the cavity.

Bibliography

[1] M. Aspelmeyer, T. J. Kippenberg, and F. Marquardt, "Cavity optomechanics," *Rev. Mod. Phys.*, 4 Dec. 2014. DOI: 10.1103/RevModPhys.86.1391.

[2] G. Via, G. Kirchmair, and O. Romero-Isart, "Strong single-photon coupling in superconducting quantum magnetomechanics," *Phys. Rev. Lett.*, 14 Apr. 2015. DOI: 10.1103/PhysRevLett.114.143602.

[3] D. Zoepfl *et al.*, "Kerr enhanced backaction cooling in magnetomechanics," *Phys. Rev. Lett.*, 3 Jan. 2023. DOI: 10.1103/PhysRevLett.130.033601.

[4] R. B. Griffiths, *Consistent Quantum Theory*. Cambridge University Press, Nov. 2001. DOI: 10.1017/cbo9780511606052.

[5] D. J. Griffiths and D. F. Schroeter, *Introduction to Quantum Mechanics*. Cambridge University Press, Aug. 2018. DOI: 10.1017/9781316995433.

[6] H. M. Wiseman and G. J. Milburn, *Quantum Measurement and Control*. Cambridge University Press, Nov. 2009. DOI: 10.1017/cbo9780511813948.

[7] A. Einstein, B. Podolsky, and N. Rosen, "Can quantum-mechanical description of physical reality be considered complete?" *Physical Review*, May 1935. DOI: 10.1103/physrev.47.777.

[8] M. Planck, "Ueber das gesetz der energieverteilung im normalspectrum," *Annalen der Physik*, Jan. 1901. DOI: 10.1002/andp.19013090310.

[9] F. Fröwis, P. Sekatski, W. Dür, N. Gisin, and N. Sangouard, "Macroscopic quantum states: Measures, fragility, and implementations," *Reviews of Modern Physics*, May 2018. DOI: 10.1103/revmodphys.90.025004.

[10] A. J. Leggett, "Testing the limits of quantum mechanics: Motivation, state of play, prospects," *Journal of Physics: Condensed Matter*, Apr. 2002. DOI: 10.1088/0953-8984/14/15/201.

[11] I. Pikovski, M. R. Vanner, M. Aspelmeyer, M. S. Kim, and Č. Brukner, "Probing planck-scale physics with quantum optics," *Nature Physics*, Mar. 2012. DOI: 10.1038/nphys2262.

[12] C. L. Degen, F. Reinhard, and P. Cappellaro, "Quantum sensing," *Reviews of Modern Physics*, Jul. 2017. DOI: 10.1103/revmodphys.89.035002.

[13] D. Vitali *et al.*, "Optomechanical entanglement between a movable mirror and a cavity field," *Physical Review Letters*, Jan. 2007. DOI: 10.1103/physrevlett.98.030405.

[14] B. Pepper, R. Ghobadi, E. Jeffrey, C. Simon, and D. Bouwmeester, "Optomechanical superpositions via nested interferometry," *Physical Review Letters*, Jul. 2012. DOI: 10.1103/physrevlett.109.023601.

[15] U. Akram, W. P. Bowen, and G. J. Milburn, "Entangled mechanical cat states via conditional single photon optomechanics," *New Journal of Physics*, Sep. 2013. DOI: 10.1088/1367-2630/15/9/093007.

[16] K. E. Khosla, M. R. Vanner, W. P. Bowen, and G. J. Milburn, "Quantum state preparation of a mechanical resonator using an optomechanical geometric phase," *New Journal of Physics*, Apr. 2013. DOI: 10.1088/1367-2630/15/4/043025.

[17] C. Whittle, E. D. Hall, S. Dwyer, N. Mavalvala, V. Sudhir, and e. a. Abbott, "Approaching the motional ground state of a 10-kg object," *Science*, Jun. 2021. DOI: 10.1126/science.abh2634.

[18] A. F. Pace, M. J. Collett, and D. F. Walls, "Quantum limits in interferometric detection of gravitational radiation," *Physical Review A*, Apr. 1993. DOI: 10.1103/physreva.47.3173.

[19] S. Gröblacher *et al.*, "Demonstration of an ultracold micro-optomechanical oscillator in a cryogenic cavity," *Nature Physics*, Jun. 2009. DOI: 10.1038/nphys1301.

[20] A. A. Clerk, K. W. Lehnert, P. Bertet, J. R. Petta, and Y. Nakamura, "Hybrid quantum systems with circuit quantum electrodynamics," *Nature Physics*, Mar. 2020. DOI: 10.1038/s41567-020-0797-9.

[21] J. D. Teufel *et al.*, "Sideband cooling of micromechanical motion to the quantum ground state," *Nature*, Jul. 2011. DOI: 10.1038/nature10261.

[22] S. Etaki, M. Poot, I. Mahboob, K. Onomitsu, H. Yamaguchi, and H. S. J. van der Zant, "Motion detection of a micromechanical resonator embedded in a d.c. squid," *Nature Physics*, Aug. 2008. DOI: 10.1038/nphys1057.

[23] A. de los Ríos Sommer, N. Meyer, and R. Quidant, "Strong optomechanical coupling at room temperature by coherent scattering," *Nature Communications*, Jan. 2021. DOI: 10.1038/s41467-020-20419-2.

[24] A. Nunnenkamp, K. Børkje, and S. M. Girvin, "Single-photon optomechanics," *Physical Review Letters*, Aug. 2011. DOI: 10.1103/physrevlett.107.063602.

[25] S. Weis *et al.*, "Optomechanically induced transparency," *Science*, Dec. 2010. DOI: 10.1126/science.1195596.

[26] F. Marquardt, J. P. Chen, A. A. Clerk, and S. M. Girvin, "Quantum theory of cavity-assisted sideband cooling of mechanical motion," *Physical Review Letters*, Aug. 2007. DOI: 10.1103/physrevlett.99.093902.

[27] W. P. Bowen, *Quantum Optomechanics*. CRC Press, Nov. 2015. DOI: 10.1201/b19379.

[28] S. Mancini, D. Vitali, and P. Tombesi, "Optomechanical cooling of a macroscopic oscillator by homodyne feedback," *Phys. Rev. Lett.*, 4 Jan. 1998. DOI: 10.1103/PhysRevLett.80.688.

[29] J. Chan *et al.*, "Laser cooling of a nanomechanical oscillator into its quantum ground state," *Nature*, Oct. 2011. DOI: 10.1038/nature10461.

[30] J. B. Clark, F. Lecocq, R. W. Simmonds, J. Aumentado, and J. D. Teufel, "Sideband cooling beyond the quantum backaction limit with squeezed light," *Nature*, Jan. 2017. DOI: 10.1038/nature20604.

[31] M. Asjad, S. Zippilli, and D. Vitali, "Suppression of stokes scattering and improved optomechanical cooling with squeezed light," *Physical Review A*, Nov. 2016. DOI: 10.1103/physreva.94.051801.

[32] H.-K. Lau and A. A. Clerk, "Ground-state cooling and high-fidelity quantum transduction via parametrically driven bad-cavity optomechanics," *Phys. Rev. Lett.*, 10 Mar. 2020. DOI: 10.1103/PhysRevLett.124.103602.

[33] Y.-C. Liu, Y.-F. Xiao, X. Luan, Q. Gong, and C. W. Wong, "Coupled cavities for motional ground-state cooling and strong optomechanical coupling," *Physical Review A*, Mar. 2015. DOI: 10.1103/physreva.91.033818.

[34] J.-Y. Yang *et al.*, "Ground-state cooling of mechanical oscillator via quadratic optomechanical coupling with two coupled optical cavities," *Optics Express*, Jul. 2019. DOI: 10.1364/oe.27.022855.

[35] L. F. Deeg, D. Zoepfl, N. Diaz-Naufal, M. L. Juan, A. Metelmann, and G. Kirchmair, *Optomechanical backaction in the bistable regime*, 2024.

[36] N. Diaz-Naufal *et al.*, *Kerr enhanced optomechanical cooling in the unresolved sideband regime*, 2024.

[37] H.-P. Breuer and F. Petruccione, *The Theory of Open Quantum Systems*. Oxford University PressOxford, Jan. 2007. DOI: 10.1093/acprof:oso/9780199213900.001.0001.

[38] A. Rivas and S. F. Huelga, *Open Quantum Systems: An Introduction*. Springer Berlin Heidelberg, 2012. DOI: 10.1007/978-3-642-23354-8.

[39] C. Gardiner and P. Zoller, *Quantum Noise: A Handbook of Markovian and Non-Markovian Quantum Stochastic Methods with Applications to Quantum Optics* (Springer Series in Synergetics). Springer, 2004.

[40] N. Diaz-Naufal, "Optomechanical system in an unconventional bath," Master's thesis, Freie Universität Berlin, Berlin, Germany, 2020.

[41] J. v. Neumann, "Wahrscheinlichkeitstheoretischer aufbau der quantenmechanik," *Nachrichten von der Gesellschaft der Wissenschaften zu Göttingen, Mathematisch-Physikalische Klasse*, 1927.

[42] H. J. Carmichael, *Statistical Methods in Quantum Optics 1*. Springer Berlin Heidelberg, 1999. DOI: 10.1007/978-3-662-03875-8.

[43] G. Lindblad, "On the generators of quantum dynamical semigroups.," *Math. Phys.*, 1976. DOI: 10.1007/BF01608499.

[44] C. W. Gardiner and M. J. Collett, "Input and output in damped quantum systems: Quantum stochastic differential equations and the master equation," *Physical Review A*, Jun. 1985. DOI: 10.1103/physreva.31.3761.

[45] J. Kepler, *De Cometis*. 1619.

[46] A. Einstein, "On the present status of the radiation problem," *Physikalische Zeitschrift*, 817 1909.

[47] K. J. Vahala, "Optical microcavities," *Nature*, Aug. 2003. DOI: 10.1038/nature01939.

[48] H. G. Craighead, "Nanoelectromechanical systems," *Science*, Nov. 2000. DOI: 10.1126/science.290.5496.1532.

[49] C. M. Caves, "Quantum-mechanical noise in an interferometer," *Phys. Rev. D*, 8 Apr. 1981. DOI: 10.1103/PhysRevD.23.1693.

[50] K. Jacobs, I. Tittonen, H. M. Wiseman, and S. Schiller, "Quantum noise in the position measurement of a cavity mirror undergoing brownian motion," *Phys. Rev. A*, 1 Jul. 1999. DOI: 10.1103/PhysRevA.60.538.

[51] "LIGO laser interferometer gravitational-wave observatory." Accessed: 2024-04-22. ().

[52] "The virgo collaboration." (1987), [Online]. Available: https://www.virgo-gw.eu/ (visited on 04/22/2024).

[53] A. B. Braginsky V. B. & Manukin, "Ponderomotive effects of electromagnetic radiation," *Sov. Phys. JETP*, Oct. 1967.

[54] V. B. Braginsky, A. B. Manukin, and G. M. Keiser, "Measurement of weak forces in physics experiments," *American Journal of Physics*, Feb. 1978. DOI: 10.1119/1.11161.

[55] M. Vogel, C. Mooser, K. Karrai, and R. J. Warburton, "Optically tunable mechanics of microlevers," *Applied Physics Letters*, Aug. 2003. DOI: 10.1063/1.1600513.

[56] A. Dorsel, J. D. McCullen, P. Meystre, E. Vignes, and H. Walther, "Optical bistability and mirror confinement induced by radiation pressure," *Phys. Rev. Lett.*, 17 Oct. 1983. DOI: 10.1103/PhysRevLett.51.1550.

[57] T. J. Kippenberg, H. Rokhsari, T. Carmon, A. Scherer, and K. J. Vahala, "Analysis of radiation-pressure induced mechanical oscillation of an optical microcavity," *Phys. Rev. Lett.*, 3 Jul. 2005. DOI: 10.1103/PhysRevLett.95.033901.

[58] H. Rokhsari, T. J. Kippenberg, T. Carmon, and K. J. Vahala, "Radiation-pressure-driven micro-mechanical oscillator," *Opt. Express*, Jul. 2005. DOI: 10.1364/OPEX.13.005293.

[59] T. Carmon, H. Rokhsari, L. Yang, T. J. Kippenberg, and K. J. Vahala, "Temporal behavior of radiation-pressure-induced vibrations of an optical microcavity phonon mode," *Phys. Rev. Lett.*, 22 Jun. 2005. DOI: 10.1103/PhysRevLett.94.223902.

[60] O. Arcizet, P.-F. Cohadon, T. Briant, M. Pinard, and A. Heidmann, "Radiation-pressure cooling and optomechanical instability of a micromirror," *Nature*, Nov. 2006. DOI: 10.1038/nature05244.

[61] S. Gigan *et al.*, "Self-cooling of a micromirror by radiation pressure," *Nature*, Nov. 2006. DOI: 10.1038/nature05273.

[62] A. Schliesser, P. Del'Haye, N. Nooshi, K. J. Vahala, and T. J. Kippenberg, "Radiation pressure cooling of a micromechanical oscillator using dynamical backaction," *Phys. Rev. Lett.*, 24 Dec. 2006. DOI: 10.1103/PhysRevLett.97.243905.

[63] T. Corbitt *et al.*, "An all-optical trap for a gram-scale mirror," *Phys. Rev. Lett.*, 15 Apr. 2007. DOI: 10.1103/PhysRevLett.98.150802.

[64] J. D. Thompson, B. M. Zwickl, A. M. Jayich, F. Marquardt, S. M. Girvin, and J. G. E. Harris, "Strong dispersive coupling of a high-finesse cavity to a micromechanical membrane," *Nature*, Mar. 2008. DOI: 10.1038/nature06715.

[65] S. Barzanjeh, A. Xuereb, S. Gröblacher, M. Paternostro, C. A. Regal, and E. M. Weig, "Optomechanics for quantum technologies," *Nature Physics*, Dec. 2021. DOI: 10.1038/s41567-021-01402-0.

[66] C.-H. Bai, D.-Y. Wang, H.-F. Wang, A.-D. Zhu, and S. Zhang, "Classical-to-quantum transition behavior between two oscillators separated in space under the action of optomechanical interaction," *Scientific Reports*, May 2017. DOI: 10.1038/s41598-017-02779-w.

[67] F. Marquardt, A. Clerk, and S. Girvin, "Quantum theory of optomechanical cooling," *Journal of Modern Optics*, Nov. 2008. DOI: 10.1080/09500340802454971.

[68] J. D. Teufel *et al.*, "Circuit cavity electromechanics in the strong-coupling regime," *Nature*, Mar. 2011. DOI: 10.1038/nature09898.

[69] S. Mancini, D. Vitali, and P. Tombesi, "Optomechanical cooling of a macroscopic oscillator by homodyne feedback," *Physical Review Letters*, Jan. 1998. DOI: 10.1103/physrevlett.80.688.

[70] P. F. Cohadon, A. Heidmann, and M. Pinard, "Cooling of a mirror by radiation pressure," *Phys. Rev. Lett.*, 16 Oct. 1999. DOI: 10.1103/PhysRevLett.83.3174.

[71] D. Kleckner and D. Bouwmeester, "Sub-kelvin optical cooling of a micromechanical resonator," *Nature*, Nov. 2006. DOI: 10.1038/nature05231.

[72] C. Genes, D. Vitali, P. Tombesi, S. Gigan, and M. Aspelmeyer, "Ground-state cooling of a micromechanical oscillator: Comparing cold damping and cavity-assisted cooling schemes," *Phys. Rev. A*, 3 Mar. 2008. DOI: 10.1103/PhysRevA.77.033804.

[73] D. Vitali, S. Mancini, L. Ribichini, and P. Tombesi, "Mirror quiescence and high-sensitivity position measurements with feedback," *Phys. Rev. A*, 6 May 2002. DOI: 10.1103/PhysRevA.65.063803.

[74] G.-L. Schmid, C. T. Ngai, M. Ernzer, M. B. Aguilera, T. M. Karg, and P. Treutlein, "Coherent feedback cooling of a nanomechanical membrane with atomic spins," *Phys. Rev. X*, 1 Jan. 2022. DOI: 10.1103/PhysRevX.12.011020.

[75] J. Guo and S. Gröblacher, "Coherent feedback in optomechanical systems in the sideband-unresolved regime," *Quantum*, Nov. 2022. DOI: 10.22331/q-2022-11-03-848.

[76] M. Ernzer *et al.*, "Optical coherent feedback control of a mechanical oscillator," *Phys. Rev. X*, 2 May 2023. DOI: 10.1103/PhysRevX.13.021023.

[77] A. Naik *et al.*, "Cooling a nanomechanical resonator with quantum back-action," *Nature*, Sep. 2006. DOI: 10.1038/nature05027.

[78] E. Verhagen, S. Deléglise, S. Weis, A. Schliesser, and T. J. Kippenberg, "Quantum-coherent coupling of a mechanical oscillator to an optical cavity mode," *Nature*, Feb. 2012. DOI: 10.1038/nature10787.

[79] D. Kleckner, B. Pepper, E. Jeffrey, P. Sonin, S. M. Thon, and D. Bouwmeester, "Optomechanical trampoline resonators," *Optics Express*, Sep. 2011. DOI: 10.1364/oe.19.019708.

[80] W. P. Bowen, *Quantum Optomechanics*. CRC Press, Nov. 2015. DOI: 10.1201/b19379.

[81] D. Mason, J. Chen, M. Rossi, Y. Tsaturyan, and A. Schliesser, "Continuous force and displacement measurement below the standard quantum limit," *Nature Physics*, May 2019. DOI: 10.1038/s41567-019-0533-5.

[82] B. C. Barish and R. Weiss, "Ligo and the detection of gravitational waves," *Physics Today*, 1999. DOI: 10.1063/1.882861.

[83] C. M. Caves, K. S. Thorne, R. W. P. Drever, V. D. Sandberg, and M. Zimmermann, "On the measurement of a weak classical force coupled to a quantum-mechanical oscillator. i. issues of principle," *Rev. Mod. Phys.*, 2 Apr. 1980. DOI: 10.1103/RevModPhys.52.341.

[84] E. E. Wollman *et al.*, "Quantum squeezing of motion in a mechanical resonator," *Science*, Aug. 2015. DOI: 10.1126/science.aac5138.

[85] A. Zivari, R. Stockill, N. Fiaschi, and S. Gröblacher, "Non-classical mechanical states guided in a phononic waveguide," *Nature Physics*, May 2022. DOI: 10.1038/s41567-022-01612-0.

[86] B. D. Hauer, J. Combes, and J. D. Teufel, "Nonlinear sideband cooling to a cat state of motion," *Physical Review Letters*, May 2023. DOI: 10.1103/physrevlett.130.213604.

[87] M.-A. Lemonde, N. Didier, and A. A. Clerk, "Nonlinear interaction effects in a strongly driven optomechanical cavity," *Physical Review Letters*, Aug. 2013. DOI: 10.1103/physrevlett.111.053602.

[88] S. Mancini, V. Giovannetti, D. Vitali, and P. Tombesi, "Entangling macroscopic oscillators exploiting radiation pressure," *Phys. Rev. Lett.*, 12 Mar. 2002. DOI: 10.1103/PhysRevLett.88.120401.

[89] C. F. Ockeloen-Korppi *et al.*, "Stabilized entanglement of massive mechanical oscillators," *Nature*, Apr. 2018. DOI: 10.1038/s41586-018-0038-x.

[90] S. Kotler *et al.*, "Direct observation of deterministic macroscopic entanglement," *Science*, May 2021. DOI: 10.1126/science.abf2998.

[91] V. Giovannetti, S. Mancini, and P. Tombesi, "Radiation pressure induced einstein-podolsky-rosen paradox," *Europhysics Letters (EPL)*, Jun. 2001. DOI: 10.1209/epl/i2001-00284-x.

[92] C. A. Regal, J. D. Teufel, and K. W. Lehnert, "Measuring nanomechanical motion with a microwave cavity interferometer," *Nature Physics*, May 2008. DOI: 10.1038/nphys974.

[93] G. Via, G. Kirchmair, and O. Romero-Isart, "Strong single-photon coupling in superconducting quantum magnetomechanics," *Physical Review Letters*, Apr. 2015. DOI: 10.1103/physrevlett.114.143602.

[94] D. Zoepfl, M. L. Juan, C. M. F. Schneider, and G. Kirchmair, "Single-photon cooling in microwave magnetomechanics," *Physical Review Letters*, 2 Jul. 2020. DOI: 10.1103/physrevlett.125.023601.

[95] T. Luschmann *et al.*, "Mechanical frequency control in inductively coupled electromechanical systems," *Scientific Reports*, Jan. 2022. DOI: 10.1038/s41598-022-05438-x.

[96] I. C. Rodrigues, D. Bothner, and G. A. Steele, "Cooling photon-pressure circuits into the quantum regime," *Science Advances*, Oct. 2021. DOI: 10.1126/sciadv.abg6653.

[97] B. A. Moores, L. R. Sletten, J. J. Viennot, and K. W. Lehnert, "Cavity quantum acoustic device in the multimode strong coupling regime," *Physical Review Letters*, May 2018. DOI: 10.1103/physrevlett.120.227701.

[98] T. T. Heikkilä, F. Massel, J. Tuorila, R. Khan, and M. A. Sillanpää, "Enhancing optomechanical coupling via the josephson effect," *Physical Review Letters*, May 2014. DOI: 10.1103/physrevlett.112.203603.

[99] A. N. Cleland, J. S. Aldridge, D. C. Driscoll, and A. C. Gossard, "Nanomechanical displacement sensing using a quantum point contact," *Applied Physics Letters*, Aug. 2002. DOI: 10.1063/1.1497436.

[100] N. E. Flowers-Jacobs, D. R. Schmidt, and K. W. Lehnert, "Intrinsic noise properties of atomic point contact displacement detectors," *Physical Review Letters*, Mar. 2007. DOI: 10.1103/physrevlett.98.096804.

[101] M. Blencowe, "Nanoelectromechanical systems," *Contemporary Physics*, Jul. 2005. DOI: 10.1080/00107510500146865.

[102] A. D. O'Connell *et al.*, "Quantum ground state and single-phonon control of a mechanical resonator," *Nature*, Mar. 2010. DOI: 10.1038/nature08967.

[103] O. Arcizet, V. Jacques, A. Siria, P. Poncharal, P. Vincent, and S. Seidelin, "A single nitrogen-vacancy defect coupled to a nanomechanical oscillator," *Nature Physics*, Sep. 2011. DOI: 10.1038/nphys2070.

[104] S. Kolkowitz *et al.*, "Coherent sensing of a mechanical resonator with a single-spin qubit," *Science*, Mar. 2012. DOI: 10.1126/science.1216821.

[105] F. Marquardt and S. Girvin, "Optomechanics," *Physics*, May 2009. DOI: 10.1103/physics.2.40.

[106] M. Aspelmeyer, S. Gröblacher, K. Hammerer, and N. Kiesel, "Quantum optomechanics—throwing a glance [invited]," *Journal of the Optical Society of America B*, May 2010. DOI: 10.1364/josab.27.00a189.

[107] F. Marquardt, "The gentle cooling touch of light," *Nature*, Oct. 2011. DOI: 10.1038/478047a.

[108] R. Feynman, R. Leighton, and M. Sands, *The Feynman Lectures on Physics, Vol. II: The New Millennium Edition: Mainly Electromagnetism and Matter* (The Feynman Lectures on Physics). Basic Books, 2011.

[109] U. Vool and M. Devoret, "Introduction to quantum electromagnetic circuits," *International Journal of Circuit Theory and Applications*, Jun. 2017. DOI: 10.1002/cta.2359.

[110] P. Krantz, M. Kjaergaard, F. Yan, T. P. Orlando, S. Gustavsson, and W. D. Oliver, "A quantum engineer's guide to superconducting qubits," *Applied Physics Reviews*, Jun. 2019. DOI: 10.1063/1.5089550.

[111] C. M. M. Schneider, "Magnetic coupling between superconducting circuits and a cantilever," PhD thesis, Unversität Innsbruck, 2021.

[112] D. Zoepfl, "Demonstration of nonlinear enhanced backaction cooling in microwave magnetomechanics," PhD thesis, Unversität Innsbruck, 2022.

[113] M. Poot and H. S. van der Zant, "Mechanical systems in the quantum regime," *Physics Reports*, Feb. 2012. DOI: 10.1016/j.physrep.2011.12.004.

[114] D. Bothner, I. C. Rodrigues, and G. A. Steele, "Four-wave-cooling to the single phonon level in kerr optomechanics," *Communications Physics*, Feb. 2022. DOI: 10.1038/s42005-022-00808-3.

[115] A. Vinante, "Superconducting inductive displacement detection of a microcantilever," *Applied Physics Letters*, Jul. 2014. DOI: 10.1063/1.4891173.

[116] A. N. Cleland, *Foundations of Nanomechanics*. Springer Berlin Heidelberg, 2003. DOI: 10.1007/978-3-662-05287-7.

[117] K. L. Ekinci and M. L. Roukes, "Nanoelectromechanical systems," *Review of Scientific Instruments*, May 2005. DOI: 10.1063/1.1927327.

[118] D. M. Karabacak, V. Yakhot, and K. L. Ekinci, "High-frequency nanofluidics: An experimental study using nanomechanical resonators," *Physical Review Letters*, Jun. 2007. DOI: 10.1103/physrevlett.98.254505.

[119] G. D. Cole, I. Wilson-Rae, K. Werbach, M. R. Vanner, and M. Aspelmeyer, "Phonon-tunnelling dissipation in mechanical resonators," *Nature Communications*, Mar. 2011. DOI: 10.1038/ncomms1212.

[120] J. Rieger, A. Isacsson, M. J. Seitner, J. P. Kotthaus, and E. M. Weig, "Energy losses of nanomechanical resonators induced by atomic force microscopy-controlled mechanical impedance mismatching," *Nature Communications*, Mar. 2014. DOI: 10.1038/ncomms4345.

[121] A. Einstein, "Über einen die erzeugung und verwandlung des lichtes betreffenden heuristischen gesichtspunkt," *Annalen der Physik*, Jan. 1905. DOI: 10.1002/andp.19053220607.

[122] A. A. Clerk, M. H. Devoret, S. M. Girvin, F. Marquardt, and R. J. Schoelkopf, "Introduction to quantum noise, measurement, and amplification," *Rev. Mod. Phys.*, 2 Apr. 2010. DOI: 10.1103/RevModPhys.82.1155.

[123] A. Clerk, "Quantum noise and quantum measurement," in *Quantum Machines: Measurement and Control of Engineered Quantum Systems*. Oxford University PressOxford, Jun. 2014. DOI: 10.1093/acprof:oso/9780199681181.003.0002.

[124] H. B. Callen and T. A. Welton, "Irreversibility and generalized noise," *Physical Review*, Jul. 1951. DOI: 10.1103/physrev.83.34.

[125] U. Marconi, A. Puglisti, L. Rondoni, and A. Vulpianti, "Fluctuation–dissipation: Response theory in statistical physics," *Physics Reports*, Jun. 2008. DOI: 10.1016/j.physrep.2008.02.002.

[126] A. Nunnenkamp, K. Børkje, and S. M. Girvin, "Cooling in the single-photon strong-coupling regime of cavity optomechanics," *Physical Review A*, May 2012. DOI: 10.1103/physreva.85.051803.

[127] C. Gerry and P. Knight, *Introductory Quantum Optics*. Cambridge University Press, 2004. DOI: 10.1017/CBO9780511791239.

[128] S. Aldana, C. Bruder, and A. Nunnenkamp, "Equivalence between an optomechanical system and a kerr medium," *Phys. Rev. A*, 4 Oct. 2013. DOI: 10.1103/PhysRevA.88.043826.

[129] A. K. Sarma and S. Kalita, *Tutorial: Cavity quantum optomechanics*, 2022.

[130] A. A. Clerk, M. H. Devoret, S. M. Girvin, F. Marquardt, and R. J. Schoelkopf, "Introduction to quantum noise, measurement, and amplification," *Reviews of Modern Physics*, Apr. 2010. DOI: 10.1103/revmodphys.82.1155.

[131] M. Tsang and C. M. Caves, "Coherent quantum-noise cancellation for optomechanical sensors," *Physical Review Letters*, Sep. 2010. DOI: 10.1103/physrevlett.105.123601.

[132] M. H. Wimmer, D. Steinmeyer, K. Hammerer, and M. Heurs, "Coherent cancellation of backaction noise in optomechanical force measurements," *Physical Review A*, May 2014. DOI: 10.1103/physreva.89.053836.

[133] M. T. Jaekel and S. Reynaud, "Quantum limits in interferometric measurements," *Europhysics Letters (EPL)*, Oct. 1990. DOI: 10.1209/0295-5075/13/4/003.

[134] A. Luis and L. Sánchez-Soto, "Breaking the standard quantum limit for interferometric measurements," *Optics Communications*, May 1992. DOI: 10.1016/0030-4018(92)90147-j.

[135] S. E. Harris, J. E. Field, and A. Imamo ğlu, "Nonlinear optical processes using electromagnetically induced transparency," *Phys. Rev. Lett.*, 10 Mar. 1990. DOI: 10.1103/PhysRevLett.64.1107.

[136] S. E. Harris, "Electromagnetically induced transparency," *Physics Today*, Jul. 1997. DOI: 10.1063/1.881806.

[137] A. H. Safavi-Naeini *et al.*, "Electromagnetically induced transparency and slow light with optomechanics," *Nature*, Mar. 2011. DOI: 10.1038/nature09933.

[138] F. Massel *et al.*, "Microwave amplification with nanomechanical resonators," *Nature*, Dec. 2011. DOI: 10.1038/nature10628.

[139] X.-Y. Lü, W.-M. Zhang, S. Ashhab, Y. Wu, and F. Nori, "Quantum-criticality-induced strong kerr nonlinearities in optomechanical systems," *Scientific Reports*, Oct. 2013. DOI: 10.1038/srep02943.

[140] I. C. Rodrigues, D. Bothner, and G. A. Steele, "Coupling microwave photons to a mechanical resonator using quantum interference," *Nature Communications*, Nov. 2019. DOI: 10.1038/s41467-019-12964-2.

[141] J. D. Teufel, T. Donner, M. A. Castellanos-Beltran, J. W. Harlow, and K. W. Lehnert, "Nanomechanical motion measured with an imprecision below that at the standard quantum limit," *Nature Nanotechnology*, Nov. 2009. DOI: 10.1038/nnano.2009.343.

[142] A. Dorsel, J. D. McCullen, P. Meystre, E. Vignes, and H. Walther, "Optical bistability and mirror confinement induced by radiation pressure," *Phys. Rev. Lett.*, 17 Oct. 1983. DOI: 10.1103/PhysRevLett.51.1550.

[143] T. Carmon, M. C. Cross, and K. J. Vahala, "Chaotic quivering of micron-scaled on-chip resonators excited by centrifugal optical pressure," *Physical Review Letters*, Apr. 2007. DOI: 10.1103/physrevlett.98.167203.

[144] F. Marquardt, J. G. E. Harris, and S. M. Girvin, "Dynamical multistability induced by radiation pressure in high-finesse micromechanical optical cavities," *Physical Review Letters*, Mar. 2006. DOI: 10.1103/physrevlett.96.103901.

[145] A. Gozzini, I. Longo, S. Barbarino, F. Maccarrone, and F. Mango, "Light-pressure bistability at microwave frequencies," *Journal of the Optical Society of America B*, Nov. 1985. DOI: 10.1364/josab.2.001841.

[146] C. Fabre, M. Pinard, S. Bourzeix, A. Heidmann, E. Giacobino, and S. Reynaud, "Quantum-noise reduction using a cavity with a movable mirror," *Physical Review A*, Feb. 1994. DOI: 10.1103/physreva.49.1337.

[147] S. Mancini and P. Tombesi, "Quantum noise reduction by radiation pressure," *Physical Review A*, May 1994. DOI: 10.1103/physreva.49.4055.

[148] R. Ghobadi, A. R. Bahrampour, and C. Simon, "Quantum optomechanics in the bistable regime," *Physical Review A*, Sep. 2011. DOI: 10.1103/physreva.84.033846.

[149] S. Aldana, C. Bruder, and A. Nunnenkamp, "Equivalence between an optomechanical system and a kerr medium," *Physical Review A*, Oct. 2013. DOI: 10.1103/physreva.88.043826.

[150] A. D. Buckingham, "Birefringence resulting from the application of an intense beam of light to an isotropic medium," *Proceedings of the Physical Society. Section B*, Mar. 1956. DOI: 10.1088/0370-1301/69/3/309.

[151] M. Takatsuji, "Quantum theory of the optical kerr effect," *Physical Review*, Mar. 1967. DOI: 10.1103/physrev.155.980.

[152] M. J. Collett and D. F. Walls, "Squeezing spectra for nonlinear optical systems," *Physical Review A*, Nov. 1985. DOI: 10.1103/physreva.32.2887.

[153] R. M. Shelby, M. D. Levenson, D. F. Walls, A. Aspect, and G. J. Milburn, "Generation of squeezed states of light with a fiber-optic ring interferometer," *Physical Review A*, Jun. 1986. DOI: 10.1103/physreva.33.4008.

[154] J. F. Roch, G. Roger, P. Grangier, J.-M. Courty, and S. Reynaud, "Quantum non-demolition measurements in optics: A review and some recent experimental results," *Applied Physics B Photophysics and Laser Chemistry*, Sep. 1992. DOI: 10.1007/bf00325017.

[155] G. J. Milburn, "Quantum optical fredkin gate," *Physical Review Letters*, May 1989. DOI: 10.1103/physrevlett.62.2124.

[156] S. L. Braunstein and P. van Loock, "Quantum information with continuous variables," *Reviews of Modern Physics*, Jun. 2005. DOI: 10.1103/revmodphys.77.513.

[157] M. Dykman, *Fluctuating Nonlinear Oscillators: From Nanomechanics to Quantum Superconducting Circuits*. Oxford University Press, Jul. 2012. DOI: 10.1093/acprof:oso/9780199691388.001.0001.

[158] B. Yurke *et al.*, "Observation of 4.2-k equilibrium-noise squeezing via a josephson-parametric amplifier," *Physical Review Letters*, Feb. 1988. DOI: 10.1103/physrevlett.60.764.

[159] M. A. Castellanos-Beltran, K. D. Irwin, G. C. Hilton, L. R. Vale, and K. W. Lehnert, "Amplification and squeezing of quantum noise with a tunable josephson metamaterial," *Nature Physics*, Oct. 2008. DOI: 10.1038/nphys1090.

[160] S. Puri, S. Boutin, and A. Blais, "Engineering the quantum states of light in a kerr-nonlinear resonator by two-photon driving," *npj Quantum Information*, Apr. 2017. DOI: 10.1038/s41534-017-0019-1.

[161] S. Zhao *et al.*, *Fast and robust cat state preparation utilizing higher order nonlinearities*, 2023. DOI: 10.48550/ARXIV.2312.05218.

[162] A. G. White, P. K. Lam, D. E. McClelland, H.-A. Bachor, and W. J. Munro, "Kerr noise reduction and squeezing," *Journal of Optics B: Quantum and Semiclassical Optics*, Aug. 2000. DOI: 10.1088/1464-4266/2/4/315.

[163] B. Yurke and E. Buks, "Performance of cavity-parametric amplifiers, employing kerr nonlinearites, in the presence of two-photon loss," *Journal of Lightwave Technology*, Dec. 2006. DOI: 10.1109/jlt.2006.884490.

[164] A. Krasnok, P. Dhakal, A. Fedorov, P. Frigola, M. Kelly, and S. Kutsaev, "Superconducting microwave cavities and qubits for quantum information systems," *Applied Physics Reviews*, Jan. 2024. DOI: 10.1063/5.0155213.

[165] P. Bertet *et al.*, *Circuit quantum electrodynamics with a nonlinear resonator*, 2011.

[166] R. Gross and A. Marx, *Festkörperphysik*. München: De Gruyter Oldenbourg, 2014. DOI: doi:10.1524/9783110358704.

[167] A. I. B. John Clarke, *The SQUID Handbook: Fundamentals and Technology of SQUIDs and SQUID Systems*. Wiley-VCH, May 2004. DOI: 10.1002/3527603646.

[168] H. J. Carmichael, G. J. Milburn, and D. F. Walls, "Squeezing in a detuned parametric amplifier," *Journal of Physics A: Mathematical and General*, Feb. 1984. DOI: 10.1088/0305-4470/17/2/031.

[169] G. J. Walls D. F. & Milburn, *Quantum Optics*. Springer Berlin Heidelberg, 2008. DOI: 10.1007/978-3-540-28574-8.

[170] M. Müller and I. Rotter, "Exceptional points in open quantum systems," *Journal of Physics A: Mathematical and Theoretical*, Jun. 2008. DOI: 10.1088/1751-8113/41/24/244018.

[171] T. Ojanen and K. Børkje, "Ground-state cooling of mechanical motion in the unresolved sideband regime by use of optomechanically induced transparency," *Physical Review A*, Jul. 2014. DOI: 10.1103/physreva.90.013824.

[172] J. B. Clark, F. Lecocq, R. W. Simmonds, J. Aumentado, and J. D. Teufel, "Sideband cooling beyond the quantum backaction limit with squeezed light," *Nature*, Jan. 2017. DOI: 10.1038/nature20604.

[173] S. Huang and G. S. Agarwal, "Enhancement of cavity cooling of a micromechanical mirror using parametric interactions," *Physical Review A*, Jan. 2009. DOI: 10.1103/physreva.79.013821.

[174] J.-H. Gan, Y.-C. Liu, C. Lu, X. Wang, M. K. Tey, and L. You, "Intracavity-squeezed optomechanical cooling," *Laser Photonics Reviews*, Oct. 2019. DOI: 10.1002/lpor.201900120.

[175] B. Xiong, X. Li, S.-L. Chao, Z. Yang, R. Peng, and L. Zhou, "Strong squeezing of duffing oscillator in a highly dissipative optomechanical cavity system," *Annalen der Physik*, Mar. 2020. DOI: 10.1002/andp.201900596.

[176] M. Asjad, N. Etehadi Abari, S. Zippilli, and D. Vitali, "Optomechanical cooling with intracavity squeezed light," *Optics Express*, Oct. 2019. DOI: 10.1364/oe.27.032427.

[177] P. D. Nation, M. P. Blencowe, and E. Buks, "Quantum analysis of a nonlinear microwave cavity-embedded dc squid displacement detector," *Phys. Rev. B*, 10 Sep. 2008. DOI: 10.1103/PhysRevB.78.104516.

[178] C. Laflamme and A. A. Clerk, "Quantum-limited amplification with a nonlinear cavity detector," *Phys. Rev. A*, 3 Mar. 2011. DOI: 10.1103/PhysRevA.83.033803.

[179] P. Schmidt *et al.*, "Sideband-resolved resonator electromechanics based on a nonlinear josephson inductance probed on the single-photon level," *Communications Physics*, Dec. 2020. DOI: 10.1038/s42005-020-00501-3.

[180] O. Shevchuk, G. A. Steele, and Y. M. Blanter, "Strong and tunable couplings in flux-mediated optomechanics," *Phys. Rev. B*, 1 Jul. 2017. DOI: 10.1103/PhysRevB.96.014508.

[181] D. Zoepfl, P. R. Muppalla, C. M. F. Schneider, S. Kasemann, S. Partel, and G. Kirchmair, "Characterization of low loss microstrip resonators as a building block for circuit qed in a 3d waveguide," *AIP Advances*, Aug. 2017. DOI: 10.1063/1.4992070.

[182] M. L. Gorodetsky, A. Schliesser, G. Anetsberger, S. Deleglise, and T. J. Kippenberg, "Determination of the vacuum optomechanical coupling rate using frequency noise calibration," *Optics Express*, Oct. 2010. DOI: 10.1364/oe.18.023236.

[183] H. J. Carmichael, G. J. Milburn, and D. F. Walls, "Squeezing in a detuned parametric amplifier," *Journal of Physics A: Mathematical and General*, Feb. 1984. DOI: 10.1088/0305-4470/17/2/031.

[184] S. Lang, *Complex Analysis*. Springer New York, 1999. DOI: 10.1007/978-1-4757-3083-8.

[185] M. Asjad, S. Zippilli, and D. Vitali, "Suppression of stokes scattering and improved optomechanical cooling with squeezed light," *Phys. Rev. A*, 5 Nov. 2016. DOI: 10.1103/PhysRevA.94.051801.

[186] Y.-C. Liu, Y.-F. Xiao, X. Luan, and C. W. Wong, "Dynamic dissipative cooling of a mechanical resonator in strong coupling optomechanics," *Physical Review Letters*, Apr. 2013. DOI: 10.1103/physrevlett.110.153606.

[187] X. Wang, S. Vinjanampathy, F. W. Strauch, and K. Jacobs, "Ultraefficient cooling of resonators: Beating sideband cooling with quantum control," *Physical Review Letters*, Oct. 2011. DOI: 10.1103/physrevlett.107.177204.

[188] T. Rocheleau, T. Ndukum, C. Macklin, J. B. Hertzberg, A. A. Clerk, and K. C. Schwab, "Preparation and detection of a mechanical resonator near the ground state of motion," *Nature*, Dec. 2009. DOI: 10.1038/nature08681.

[189] M. Asjad, N. E. Abari, S. Zippilli, and D. Vitali, "Optomechanical cooling with intracavity squeezed light," *Optics Express*, Oct. 2019. DOI: 10.1364/oe.27.032427.

[190] J. B. Clark, F. Lecocq, R. W. Simmonds, J. Aumentado, and J. D. Teufel, "Observation of strong radiation pressure forces from squeezed light on a mechanical oscillator," *Nature Physics*, Mar. 2016. DOI: 10.1038/nphys3701.

[191] J. Monsel *et al.*, "Optomechanical cooling with coherent and squeezed light: The thermodynamic cost of opening the heat valve," *Phys. Rev. A*, 6 Jun. 2021. DOI: 10.1103/PhysRevA.103.063519.

[192] S. M.
bibinitperiod Z. S., *Quantum Optics*. Cambridge University Press, 1997.

[193] H. Yuen and J. Shapiro, "Optical communication with two-photon coherent states–part i: Quantum-state propagation and quantum-noise," *IEEE Transactions on Information Theory*, Nov. 1978. DOI: 10.1109/tit.1978.1055958.

[194] U. L. Andersen, T. Gehring, C. Marquardt, and G. Leuchs, "30 years of squeezed light generation," *Physica Scripta*, Apr. 2016. DOI: 10.1088/0031-8949/91/5/053001.

[195] A. Szorkovszky, A. A. Clerk, A. C. Doherty, and W. P. Bowen, "Detuned mechanical parametric amplification as a quantum non-demolition measurement," *New Journal of Physics*, Apr. 2014. DOI: 10.1088/1367-2630/16/4/043023.

[196] S. Ma, M. J. Woolley, and I. R. Petersen, "A derivation of moment evolution equations for linear open quantum systems," in *2018 33rd Youth Academic Annual Conference of Chinese Association of Automation (YAC)*, IEEE, May 2018. DOI: 10.1109/yac.2018.8405797.

[197] F. Caruso, J. Eisert, V. Giovannetti, and A. S. Holevo, "Multi-mode bosonic gaussian channels," *New Journal of Physics*, Aug. 2008. DOI: 10.1088/1367-2630/10/8/083030.

[198] L.-M. Duan, G. Giedke, J. I. Cirac, and P. Zoller, "Inseparability criterion for continuous variable systems," *Physical Review Letters*, Mar. 2000. DOI: 10.1103/physrevlett.84.2722.

[199] J. Fiurášek and N. J. Cerf, "How to measure squeezing and entanglement of gaussian states without homodyning," *Physical Review Letters*, Aug. 2004. DOI: 10.1103/physrevlett.93.063601.

[200] N. R. Davis and C. D. Cantrell, "Squeezed states in the context of langevin equations and non-positive-definite diffusion coefficients," *Journal of the Optical Society of America B*, Jan. 1989. DOI: 10.1364/josab.6.000074.

[201] G. Milburn and D. Walls, "Production of squeezed states in a degenerate parametric amplifier," *Optics Communications*, Nov. 1981. DOI: 10.1016/0030-4018(81)90232-7.

[202] A. Szorkovszky, A. C. Doherty, G. I. Harris, and W. P. Bowen, "Mechanical squeezing via parametric amplification and weak measurement," *Physical Review Letters*, Nov. 2011. DOI: 10.1103/physrevlett.107.213603.

[203] M. G. A. Paris, F. Illuminati, A. Serafini, and S. De Siena, "Purity of gaussian states: Measurement schemes and time evolution in noisy channels," *Physical Review A*, Jul. 2003. DOI: 10.1103/physreva.68.012314.

[204] J. Aasi *et al.*, "Enhanced sensitivity of the ligo gravitational wave detector by using squeezed states of light," *Nature Photonics*, Jul. 2013. DOI: 10.1038/nphoton.2013.177.

[205] J. Abadie, B. P. Abbott, R. Abbott, e. a. Abbott, and T. L. S. Collaboration, "A gravitational wave observatory operating beyond the quantum shot-noise limit," *Nature Physics*, 2011. DOI: 10.1038/nphys2083.

[206] M. Tse, H. Yu, and et al., "Quantum-enhanced advanced ligo detectors in the era of gravitational-wave astronomy," *Phys. Rev. Lett.*, 23 Dec. 2019. DOI: 10.1103/PhysRevLett.123.231107.

[207] J. Guo, Q. He, and M. Fadel, "Quantum metrology with a squeezed kerr oscillator," *Physical Review A*, May 2024. DOI: 10.1103/physreva.109.052604.

[208] K. Jähne, C. Genes, K. Hammerer, M. Wallquist, E. S. Polzik, and P. Zoller, "Cavity-assisted squeezing of a mechanical oscillator," *Phys. Rev. A*, 6 Jun. 2009. DOI: 10.1103/PhysRevA.79.063819.

[209] H. J. Carmichael, "Quantum trajectory theory for cascaded open systems," *Phys. Rev. Lett.*, 15 Apr. 1993. DOI: 10.1103/PhysRevLett.70.2273.

[210] J. R. Johansson, G. Johansson, and F. Nori, "Optomechanical-like coupling between superconducting resonators," *Physical Review A*, Nov. 2014. DOI: 10.1103/physreva.90.053833.

[211] C. Eichler and J. R. Petta, "Realizing a circuit analog of an optomechanical system with longitudinally coupled superconducting resonators," *Physical Review Letters*, May 2018. DOI: 10.1103/physrevlett.120.227702.

[212] D. Bothner, I. C. Rodrigues, and G. A. Steele, "Photon-pressure strong coupling between two superconducting circuits," *Nature Physics*, Aug. 2020. DOI: 10.1038/s41567-020-0987-5.

[213] A. Nunnenkamp, K. Børkje, J. G. E. Harris, and S. M. Girvin, "Cooling and squeezing via quadratic optomechanical coupling," *Physical Review A*, Aug. 2010. DOI: 10.1103/physreva.82.021806.

[214] M. Asjad, G. S. Agarwal, M. S. Kim, P. Tombesi, G. D. Giuseppe, and D. Vitali, "Robust stationary mechanical squeezing in a kicked quadratic optomechanical system," *Physical Review A*, Feb. 2014. DOI: 10.1103/physreva.89.023849.

[215] J. C. Sankey, C. Yang, B. M. Zwickl, A. M. Jayich, and J. G. E. Harris, "Strong and tunable nonlinear optomechanical coupling in a low-loss system," *Nature Physics*, Jun. 2010. DOI: 10.1038/nphys1707.

[216] M. Bhattacharya, H. Uys, and P. Meystre, "Optomechanical trapping and cooling of partially reflective mirrors," *Physical Review A*, Mar. 2008. DOI: 10.1103/physreva.77.033819.

[217] R. Schack and A. Schenzle, "Moment hierarchies and cumulants in quantum optics," *Physical Review A*, Apr. 1990. DOI: 10.1103/physreva.41.3847.

[218] C. Navarrete-Benlloch, E. Roldán, Y. Chang, and T. Shi, "Regularized linearization for quantum nonlinear optical cavities: Application to degenerate optical parametric oscillators," *Optics Express*, Sep. 2014. DOI: 10.1364/oe.22.024010.

[219] P. Degenfeld-Schonburg, C. Navarrete–Benlloch, and M. J. Hartmann, "Self-consistent projection operator theory in nonlinear quantum optical systems: A case study on degenerate optical parametric oscillators," *Physical Review A*, May 2015. DOI: 10.1103/physreva.91.053850.

[220] J. D. W. Alexander L. Fetter, *Quantum theory of many-particle systems* (Pure and Applied Physics), First Edition. Mcgraw-Hill, 1971.

[221] J. Johansson, P. Nation, and F. Nori, "Qutip 2: A python framework for the dynamics of open quantum systems," *Computer Physics Communications*, Apr. 2013. DOI: 10.1016/j.cpc.2012.11.019.

[222] S. Huang and G. S. Agarwal, "Electromagnetically induced transparency from two-phonon processes in quadratically coupled membranes," *Physical Review A*, Feb. 2011. DOI: 10.1103/physreva.83.023823.

[223] K. Børkje, A. Nunnenkamp, J. D. Teufel, and S. M. Girvin, "Signatures of nonlinear cavity optomechanics in the weak coupling regime," *Physical Review Letters*, Aug. 2013. DOI: 10.1103/physrevlett.111.053603.

[224] R. Loudon and P. Knight, "Squeezed light," *Journal of Modern Optics*, Jun. 1987. DOI: 10.1080/09500348714550721.